ISSN 1694-7398
journals.manas.edu.kg

JUNE 2023
Volume 11, Issue 1

MANAS JOURNAL OF ENGINEERING

MJEN

BISHKEK 2022

KYRGYZ TURKISH MANAS UNIVERSITY
MANAS JOURNAL OF ENGINEERING (MJEN)

ISSN: 1694- 7398
Year: 2023
Volume: 11
Special Issue: 1
http://journals.manas.edu.kg
journals@manas.edu.kg

PUBLICATION PERIOD

Manas Journal of Engineering (MJEN) is published twice year, MJEN is a peer reviewed journal.

CORRESPONDENCE ADDRESS
Kyrgyz Turkish Manas University
Chyngyz Aitmatov Avenue 56 Bishkek, KYRGYZSTAN
URL: http://journals.manas.edu.kg
e-mail: journals@manas.edu.kg
Tel : +996 312 492763- Fax: +996 312 541935

KYRGYZ TURKISH MANAS UNIVERSITY
MANAS JOURNAL OF ENGINEERING (MJEN)

Content

MANAS Journal of Engineering
ISSN 1694-7398 | e-ISSN 1694-7398

Volume 11, Issue 1, (2023) Pages 1-7
https://doi.org/10.51354/mjen.955930

Investigation and analysis of interleaved dc-dc boost converter for grid-connected photovoltaic energy system

Mehmet Büyük

Adıyaman University, Electrical and Electronics Engineering, 02300, Adıyaman, Türkiye, mbuyuk@adiyaman.edu.tr, ORCID: 0000-0003-3026-4034

ABSTRACT

The installation of photovoltaic energy system has been increasing in recent years with the increment of the demand to the electrical power. PV system can be installed as either standalone or grid-connected. Grid-connected PV systems are more attractive because of not requiring a storage system. In this study, a three-leg interleaved boost converter for grid-connected PV system is proposed. In the proposed system, a grid-connected PV system is designed and modelled in a simulation environment. The proposed model is analysed in comparison with the conventional dc-dc boost converter topology under variations of irradiance and temperature. The comparison of two systems is performed according to input current ripple ratio and THD value of the grid current. The simulation results show that the proposed topology has lower current ripple and THD value comparing with the conventional topology.

ARTICLE INFO

Research article

Received: 26.10.2022
Accepted: 16.12.2022

Keywords:
dc/dc converter, interleaved boost converter, grid-connected PV system, current ripple, THD.

1. Introduction

In today's life, the applications of renewable energy sources have come into prominence by reduction of the fossil fuels and increasing greenhouse gas emissions [1, 2]. Photovoltaic (PV) panel systems attract further attention since their simple implementation and low maintenance cost. In addition, the power generation capacity of PV systems can be improved via implementation of industry 4.0 [3]. Besides, the systems are applicable for houses, industrial plants and commercial power plants [4-7]. Furthermore, the installed PV system capacity over the world has been increasing significantly in recent years [8]. Although standalone and grid-connected PV panel systems are available in applications, the grid-connected systems are more efficient and highly preferred systems in applications [5-7]. In general, a dc/dc converter and an inverter are used to connect the PV panels to the grid [9]. The dc/dc converter is applied to obtain the suitable dc voltage level with the maximum power of PV panel [1, 10, 11]. The inverter is utilised to converter dc voltage into ac voltage [12].

There are several dc/dc converter topologies implemented in the grid-connected PV systems. However, a boost converter is usually preferred as a dc/dc converter in PV system and renewable energy systems [2, 13-16]. There are also a few boost converter circuits in literature studies and applications [13, 17, 18]. In earlier studies, conventional boost converter topology is used with PV system. However, the PV current has a high ripple ratio when the conventional boost converter is used [10, 11, 19, 20]. The high current ripple ratio in PV side effects total harmonic distortion (THD) value of current injected to the grid. Besides, the high ripple degrades the PV lifetime and overall system efficiency.

In this study, a three-leg interleaved boost converter is applied for the grid-connected PV system. The proposed system is modelled and analysed through a simulation environment. A grid-connected PV system in the rating of 10.6 kW is designed and constructed in the simulation environment, and the constructed model is simulated for conventional boost converter and IBC systems. The modelled system is examined under different irradiance and temperature values. The simulation results are presented by considering current ripple ratio and THD value.

The rest of the manuscript is organized as follows. In Section 2, the PV system model of the simulated system and its characteristics are introduced. In Section 3, the structure of the proposed system is presented. By this way, the model of the proposed system is explained in detail. In addition, the current ripple ratios are given for the conventional boost converter and IBC. In Section 4, the simulation results of the proposed system with the conventional boost converter and IBC topologies are presented. The results of IBC topology are discussed and compared with the results of the conventional topology. The conclusion is discussed in Section 5.

2. PV system model and characteristic

A PV module consists of small solar cells (approximately 1-2 W) to generate high output power and voltage. As well known that an ideal solar cell is modelled as a current source with parallel a diode. Besides, series and parallel resistors are included to ideal model to demonstrate power losses. The widespread equivalent circuit model of a single PV cell/module is illustrated in Figure 1. This model is called a single diode model and includes five parameters to be determined. The $I-V$ characteristic of the single diode model is acquired through Eq. (1) [21].

$$I = I_{pv} - I_0\left[\exp\left(\frac{V+IR_s}{aV_T}\right)-1\right]-\frac{V+IR_s}{R_{sh}} \quad (1)$$

Where,

I_{pv} : PV current
I_0 : Saturation current
R_s : Series resistor
R_{sh} : Shunt resistor
V_T : Diode thermal voltage

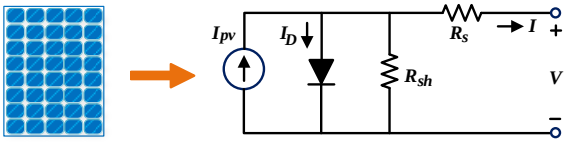

Figure 1. *A single PV module and its equivalent circuit scheme*

The parameters of the model are obtained by equations of short circuit, open circuit, MPP circuit and zero derivative for MPP circuit. The parameters for a single module are shown in Table 1. According to these parameters, PV current, series and shunt resistors and diode saturation current are obtained. Then, the $I-V$ and $P-V$ curves of this model are drawn for different irradiance values at 25 ^0C, as shown in Figure 2.

Table 1. *The parameters for a single PV modüle*

Parameter	Description	Value
P_{mp}	Maximum power	305.2 W
V_{oc}	Open circuit voltage	64.14 V
V_{mp}	Voltage at MPP	54.7 V
N_{cell}	# of cell per module	96
I_{sc}	Short-circuit current	5.94 A
I_{mp}	Current at MPP	5.56 A

The voltage level of the single module is low during the grid connection. Thus, in the present work, seven in series and five in parallel modules are connected to create a PV array with sufficient voltage level and high current value. The $I-V$ and $P-V$ curves of PV array are drawn for different irradiance values at 25 ^0C, as demonstrated in Figure 3.

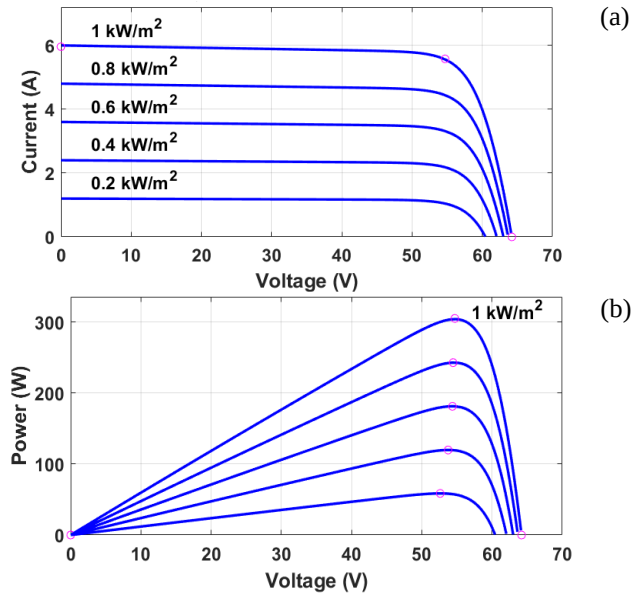

Figure 2. *The $I-V$ and $P-V$ curves of single PV module under different irradiances*

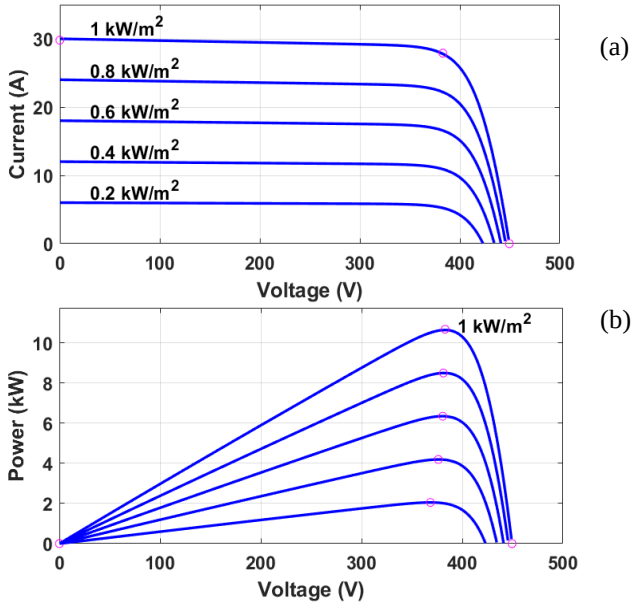

Figure 3. *The $I-V$ and $P-V$ curves of PV array under different irradiances*

3. Structure and control of the proposed system model

The general representation of the proposed system is demonstrated in Fig. 4. The proposed system consists of a PV array transferring solar energy into electric energy, a three-leg boost converter with MPPT controller, and a three-phase DC-AC inverter with the current controller and output LCL filter. Incremental conductance MPPT algorithm is applied to acquire maximum power [22,23].

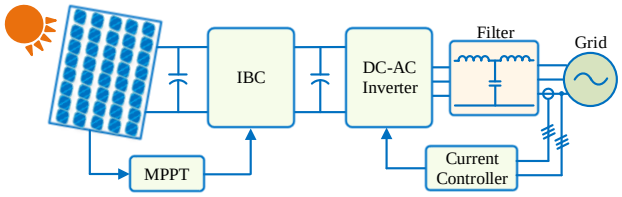

Figure 4. *General structure scheme of the proposed system*

3.1. Interleaved boost converter

The conventional boost converter and IBC structures with pulses and PV currents are shown in Figure 5. The structure and pulse signal of the conventional converter are demonstrated in Figure 5(a) and Figure 5(c). Besides, the structure and pulse signals of IBC topology are shown in Figure 5(b) and Figure 5(d).

The relation between input voltage and output voltage of the conventional boost converter is given in (2). The current flowing on the inductor is increasing once the switching component turns on and decreasing when turns off. The difference between the lower and upper points of the current is ripple current that has drawbacks on the PV system and output voltage. The ripple current is obtained by Eq. (3). To lessen the ripple current, the inductance value or switching frequency can be increased. However, higher inductance value results in bulky system and high switching frequency leads to efficiency degradation. In this study, instead, a three-leg boost converter is proposed to reduce the inductor current ripple and its negative effect [13, 24].

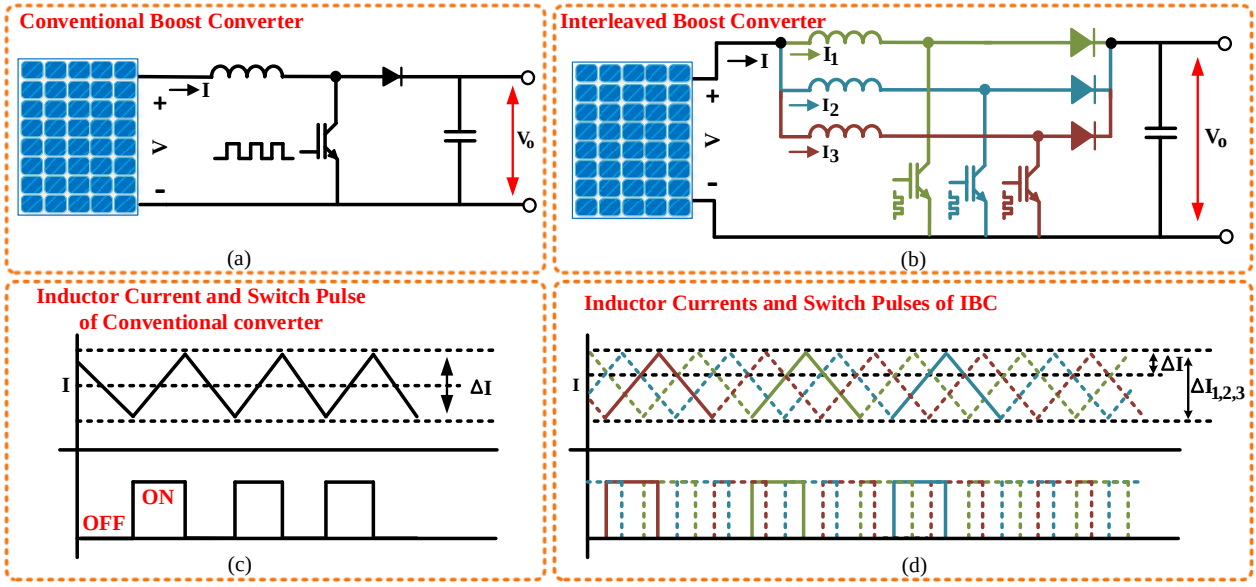

Figure 5. *The structures, currents and pulse waveforms of the conventional boost converter and IBC*

$$V_o = \frac{1}{(1-D)}V \tag{2}$$

$$\Delta I = \frac{DT_s}{L}V \tag{3}$$

Where, D is duty cycle and T_s is switching time.

In this study, a three-phase IBC is preferred to convert DC voltage level. Three parallel converters are used in this topology, as shown in Figure 5(b). The operation of IBC is based on applying identical pulses with shifting the pulses of the switches by 120^0 [19,24]. The switching signals and inductor currents are demonstrated in Figure 5(d). The switching signals may overlap depending on duty cycle, as shown in Figure 5(d). It is proposed to select the duty cycle higher than 1/3 in order to obtain boosted input voltage. The input ripple current is obtained as Eq. (4). The input ripple current is obtained according to the duty cycle ratio [10].

$$\Delta I = \begin{cases} 0.34 < D < 0.66\ ; & \frac{VT_s d}{3L}\left(\frac{2-3D}{D'}\right) \\ 0.67 < D < 1 \quad ; & \frac{VT_s d}{L}\left(\frac{1-D}{D'}\right) \end{cases} \tag{4}$$

Where, d is the ratio of input current rising time to its period (t_r/τ).

3.1. DC/AC conversion

The PV system is connected to the grid through a DC-AC inverter. In this study, a three-phase inverter is used to convert DC voltage into AC voltage. The inverter includes three half-bridge inverter legs. The switching components of the inverter are modulated by SPWM method. The rms voltage value of

inverter is obtained as in (5) for the fundamental component [25]. The circuit diagram of the grid-connected inverter is demonstrated in Figure 6. An LCL filter is tied between the inverter and the grid to effectively degrade the ripple harmonics generated from the modulation of the inverter [26]. Besides, a simple resistor connected in series with the filter capacitor suppresses the filter resonance.

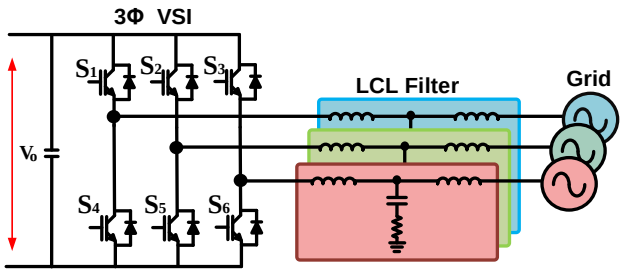

Figure 6. *The circuit diagram of the three-phase grid-connected inverter*

$$V_i = \frac{M}{2\sqrt{2}} V_o \quad (5)$$

Where, M index represents the modulation ratio of the reference sine signal to the carrier signal. $\boldsymbol{V_i}$ and $\boldsymbol{V_o}$ are inverter output fundamental voltage and capacitor dc voltage, respectively. The constant $\boldsymbol{M/(2\sqrt{2})}$ gives the inverter gain value [25].

4. Case studies and discussion

The proposed system is modelled and analysed though a simulation program environment. The system parameters of the modelled system are given in Table 2. The proposed system is tested under various irradiance and temperature values. The changes in irradiance and temperature are shown in Figure 7. Besides, the mean powers obtained from PV array according to the irradiance and temperature variations for conventional boost converter and IBC are illustrated in Figure 8. The mean power obtained by the IBC topology is always higher than the conventional topology.

The modelled system is examined for conventional boost converter and three-phase IBC topologies. Figure 9 shows the current and voltage waveforms once the conventional boost converter and three-phase IBC are applied. It is obvious that the output current has high ripple current when the conventional method is used. On the other hand, the ripple current is reduced to almost 1/3 ratio with IBC technique.

Table 2. *The system parameters of the proposed system*

Parameter	Description	Value
$\boldsymbol{V_g}$	Grid voltage	380 V
$\boldsymbol{f_g}$	Grid frequency	50 Hz
$\boldsymbol{V_o}$	DC link voltage	750 V
$\boldsymbol{P_{pv}}$	Max. PV power	10.6 kW
$\boldsymbol{f_{sd}}$	IBC switching freq.	5 kHz
$\boldsymbol{f_{si}}$	Inverter switching freq.	5 kHz

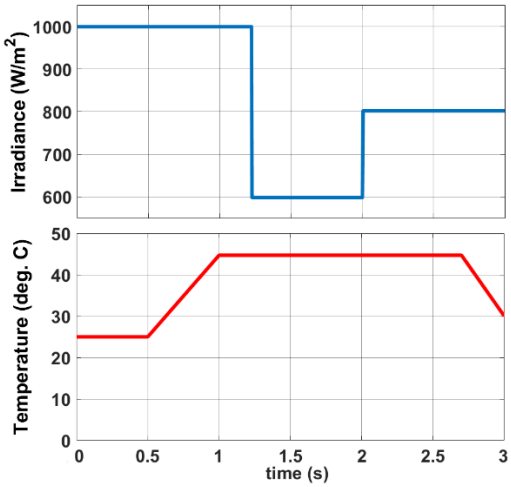

Figure 7. *The changes in irradiance and temperature*

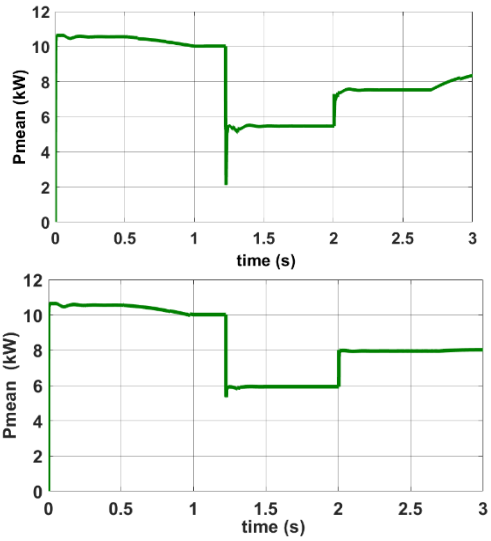

Figure 8. *Mean power behaviour of PV array under irradiance and temperature changes for conventional converter and (b) IBC topology*

The grid voltage and current supplied by PV to the grid under the variation of the irradiance and temperature are shown in Figure 10. This result is illustrated only for IBC based topology. It can be seen from the figure that the supplied current decreases with irradiance reduction and temperature increment.

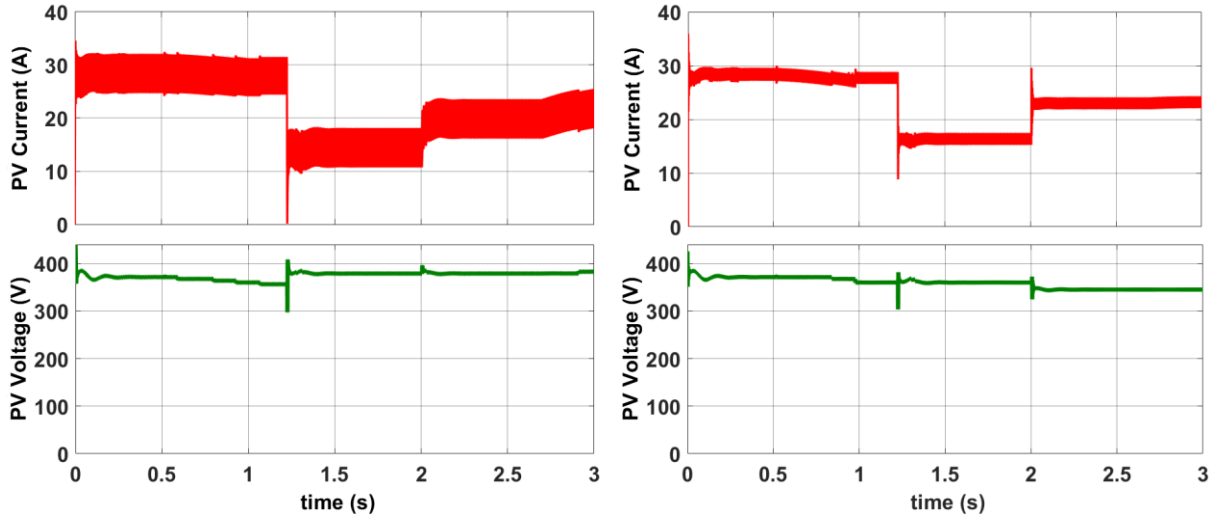

Figure 9. *Output current and voltage waveforms of PV array for (a) conventional boost converter and (b) IBC*

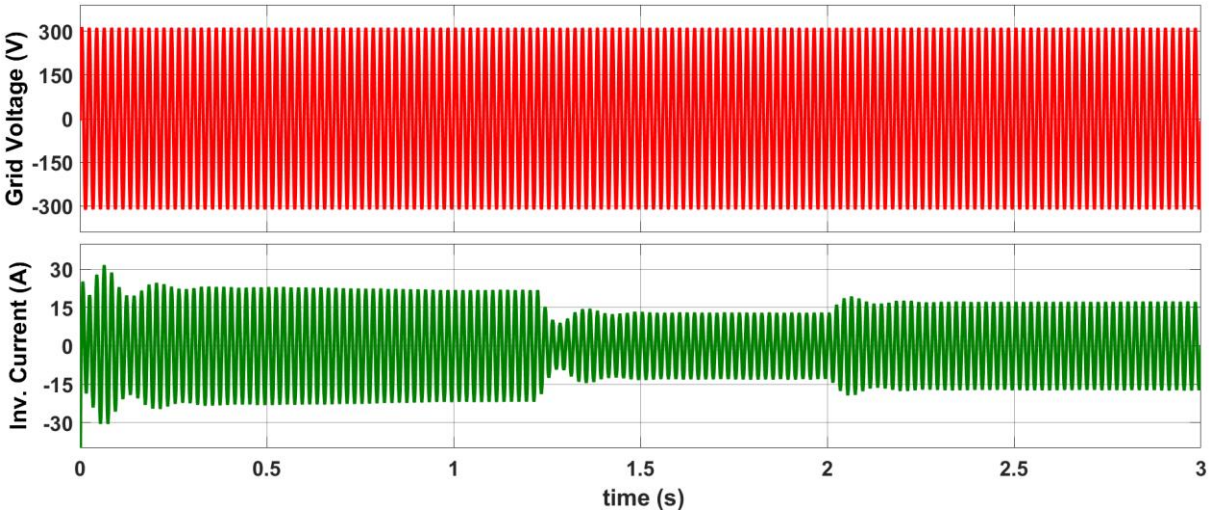

Figure 10. *The waveforms of grid voltage and inverter current*

The grid-side current waveforms with their harmonic spectra and THDs are shown in Figure 11. The results for conventional and IBC methods are given in Figure 11(a) and Figure 11(b), respectively. The THD values of the grid-side currents are 0.94 % and 0.87 % for the conventional method and IBC method, respectively. It is obvious from the simulation results that the proposed system injects current to the grid with lower THD value.

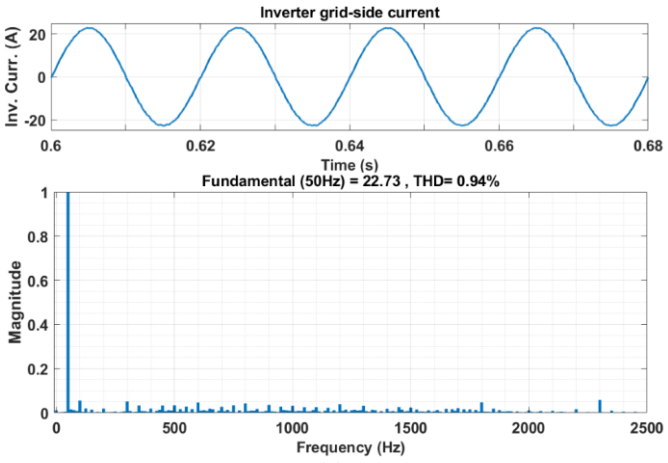

(a)

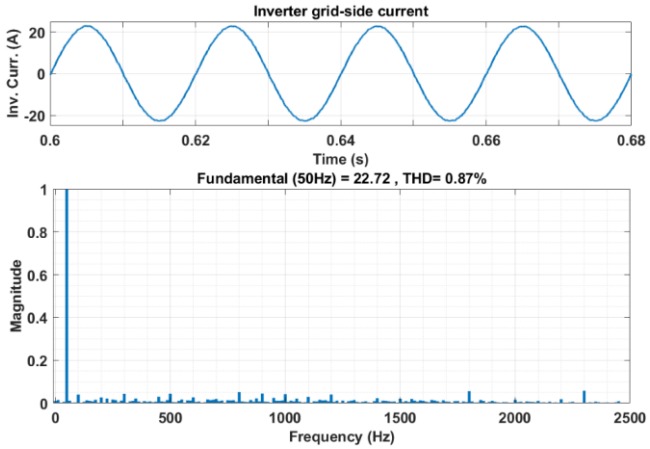

(b)

Figure 11. *Waveforms of grid currents and FFTs with (a) conventional method and (b) IBC structure*

5. Conclusion

A grid-connected PV system with IBC has been proposed in this study. In the proposed study, IBC is used as dc/dc converter to reduce the current ripple ratio. The IC MPPT algorithm is applied to obtain the maximum power from the PV array. A 10.6 kW grid-connected PV system is designed in this study. The proposed system has been modelled in simulation environment, and it is examined under variation of irradiance and temperature. The proposed system is compared with the conventional boost converter model. It is shown from the simulation results that the IBC topology has a lower PV current ripple in comparison with the conventional boost converter. The current ripple values are 7.2V and 2.1V for the conventional boost converter and the IBC topologies, respectively. Moreover, the THD values of the grid current are 0.94% and 0.87% for the conventional boost converter and the IBC topologies, respectively. It is obvious from the results that the current ripple and THD value are reduced by the IBC model.

References

[1]. M. İnci, "Interline fuel cell (I-FC) system with dual-functional control capability," International Journal of Hydrogen Energy, vol. 45, pp. 891-903, 2020/01/01/ 2020.

[2]. Sudha R., Abishri P., and U. S., "Review of Coupled Two and Three Phase Interleaved Boost Converter (IBC) and Investigation of Four Phase IBC for Renewable Application," International Journal of Renewable Energy Research, vol. 6, 2016.

[3]. H. H. Çoban, "Accelerating renewable energy generation over industry 4.0 " MANAS Journal of Engineering, vol. 7, pp. 114-120, 2019.

[4]. X. Cao, C. Zhang, Y. Zhang, Z. Gan, H. Li, W. Ni, et al., "The simulation study of the modulation method for PV grid-connected system," Energy Procedia, vol. 145, pp. 122-127, 2018/07/01/ 2018.

[5]. M. İnci, "Design and Analysis of Dual Level Boost Converter Based Transformerless Grid Connected PV System for Residential Applications," in 2019 4th International Conference on Power Electronics and their Applications (ICPEA), 2019, pp. 1-6.

[6]. F. Sedaghati, A. Nahavandi, M. A. Badamchizadeh, S. Ghaemi, and M. Abedinpour Fallah, "PV Maximum Power-Point Tracking by Using Artificial Neural Network," Mathematical Problems in Engineering, vol. 2012, p. 506709, 2012/03/01 2012.

[7]. S. Zhang and Y. Tang, "Optimal schedule of grid-connected residential PV generation systems with battery storages under time-of-use and step tariffs," Journal of Energy Storage, vol. 23, pp. 175-182, 2019/06/01/ 2019.

[8]. M. K. A. Rödl , H. Schaumburg, "Strategy For A Large Scale Introduction Of Solar Energy In Central Asia," MANAS Journal of Engineering vol. 5, pp. 48-56, 2017.

[9]. M. S. Aygen and M. İnci, "Zero-sequence current injection based power flow control strategy for grid inverter interfaced renewable energy systems," Energy Sources, Part A: Recovery, Utilization, and Environmental Effects, pp. 1-22, 2020.

[10]. G.-Y. Choe, J. Kim, H.-S. Kang, and B.-K. Lee, "An Optimal Design Methodology of an Interleaved Boost Converter for Fuel Cell Applications," Journal of Electrical Engineering & Technology vol. 5, pp. 319-328, 2010.

[11]. M. Elsied, A. Oukaour, H. Chaoui, H. Gualous, R. Hassan, and A. Amin, "Real-time implementation of four-phase interleaved DC–DC boost converter for electric vehicle power system," Electric Power Systems Research, vol. 141, pp. 210-220, 2016/12/01/ 2016.

[12]. M. İnci, "Performance Analysis of T-type Inverter Based on Improved Hysteresis Current Controller," Balkan Journal of Electrical and Computer Engineering, vol. 7, pp. 149-155, 2019.

[13]. J. Seok and A. Parastar, "Modeling and Control of the Average Input Current for Three-Phase Interleaved Boost Converters," IEEE Transactions on Industry Applications, vol. 51, pp. 2340-2351, 2015.

[14]. R. Seyezhai and B. L. Mathur, "Design and implementation of interleaved boost converter for fuel cell systems," International Journal of Hydrogen Energy, vol. 37, pp. 3897-3903, 2012/02/01/ 2012.

[15]. F. Slah, A. Mansour, M. Hajer, and B. Faouzi, "Analysis, modeling and implementation of an interleaved boost DC-DC converter for fuel cell used in electric vehicle," International Journal of Hydrogen Energy, vol. 42, pp. 28852-28864, 2017/11/30/ 2017.

[16]. P. Thounthong, P. Sethakul, S. Rael, and B. Davat, "Design and Implementation of 2-Phase Interleaved Boost Converter for Fuel Cell Power Source," in 2008 4th IET Conference on Power Electronics, Machines and Drives, 2008, pp. 91-95.

[17]. R. Saadi, M. Y. Hammoudi, O. Kraa, M. Y. Ayad, and M. Bahri, "A robust control of a 4-leg floating interleaved boost converter for fuel cell electric vehicle application," Mathematics and Computers in Simulation, vol. 167, pp. 32-47, 2020/01/01/ 2020.

[18]. J. Choi, H. Cha, and B. Han, "A Three-Phase Interleaved DC–DC Converter With Active Clamp for Fuel Cells," IEEE Transactions on Power Electronics, vol. 25, pp. 2115-2123, 2010.

[19]. D. S. G. Krishna and M. Patra, "Modeling of multi-phase DC-DC converter with a compensator for better voltage regulation in DC micro-grid application," in 2016 International Conference on Signal Processing, Communication, Power and Embedded System (SCOPES), 2016, pp. 989-994.

[20]. M. Rezvanyvardom, E. Adib, and H. Farzanehfard, "New interleaved zero-current switching pulse-width modulation boost converter with one auxiliary switch," IET Power Electronics, vol. 4, pp. 979-983, 2011.

[21]. J. Cubas, S. Pindado, and C. De Manuel, "Explicit Expressions for Solar Panel Equivalent Circuit Parameters Based on Analytical Formulation and the Lambert W-Function," Energies, vol. 7, pp. 4098-4115, 2014.

[22]. S. Motahhir, A. El Hammoumi, and A. El Ghzizal, "The most used MPPT algorithms: Review and the suitable low-cost embedded board for each algorithm," Journal of Cleaner Production, vol. 246, p. 118983, 2020/02/10/ 2020.

[23]. A. Loukriz, M. Haddadi, and S. Messalti, "Simulation and experimental design of a new advanced variable step size Incremental Conductance MPPT algorithm for PV systems," ISA Transactions, vol. 62, pp. 30-38, 2016/05/01/ 2016.

[24]. S. Sakulchotruangdet and S. Khwan-on, "Three-phase Interleaved Boost Converter with Fault Tolerant Control Strategy for Renewable Energy System Applications," Procedia Computer Science, vol. 86, pp. 353-356, 2016/01/01/ 2016.

[25]. M. Nabil, S. M. Allam, and E. M. Rashad, "Modeling and design considerations of a photovoltaic energy source feeding a synchronous reluctance motor suitable for pumping systems," Ain Shams Engineering Journal, vol. 3, pp. 375-382, 2012/12/01/ 2012.

[26]. M. Büyük, A. Tan, M. Tümay, and K. Ç. Bayındır, "Topologies, generalized designs, passive and active damping methods of switching ripple filters for voltage source inverter: A comprehensive review," Renewable and Sustainable Energy Reviews, vol. 62, pp. 46-69, 2016/09/01/ 2016..

MANAS Journal of Engineering
ISSN 1694-7398 | e-ISSN 1694-7398

Volume 11, Issue1, (2023) Pages 8-24
https://doi.org/10.51354/mjen.1055315

Investigation of production of spare parts in agricultural industry in industry 4.0 through an example system edit

Damla Tuğrul [1,*], Aydın Şık [2]

[1] Beykent Üniversitesi Mühendislik-Mimarlık Fakültesi Endüstriyel Tasarım Bölümü, İstanbul, TÜRKİYE, tugruldamla@gmail.com, ORCID:0000-0003-3357-7781

[2] Gazi Üniversitesi Mimarlık Fakültesi, Endüstriyel Tasarım Bölümü, Ankara, TÜRKİYE, aydins@gazi.edu.tr, ORCID:0000-0002-8977-9094

ABSTRACT

The search for maximum efficiency which was formed as a result of the digital transformation, which was founded in the 1970s, brought Industry 4.0, which means the change of production strategies and business models, in 2011. In this new age which predicts the use of smart factories using unmanned cutting-edge smart robots; it is claimed that resource efficiency will increase, costs will decrease, the speed of product launching will improve and energy savings will be achieved thanks to dark production. It is a fact that the competition in the market will increase with this new age in the world. Turkey's success in holding on to this global market seems to depend on adaptation to newly created technologies, hosting and support processes. Especially the adaptation of SMEs, which constitute a large share of entrepreneurship activities, to this process is important. For this reason, in this study, by examining the production flow of "Kan Metal", which makes small scale production; it has been adapted to Industry 4.0 setup. Thus, by comparing the current system with the predicted one; advantages and disadvantages are identified and changes in the transformation process are revealed.During the examination of the production system, firstly, an information questionnaire was sent to the company, a visit was made to the company, information was exchanged with the company official with the semi-structured interview technique in the light of the information obtained from the questionnaires, and the production line was examined and photographed with the observation method. The current system was analyzed in the light of these data and adapted to the industry 4.0 system with the literature review method and a fictional model was designed.As a result, industry 4.0 means many advantages for the market, such as increased productivity, reduced costs, ease of use of resources and space, tracking the production flow from order to supply, and creating sensitive products. However, the high costs and unqualified personnel of the establishment of new technologies constitute the biggest disadvantages for SMEs. Transition to the new system seems possible only if these companies are supported in terms of infrastructure, education and capital.

ARTICLE INFO

Research article

Received: 9.01.2022
Accepted: 16.01.2023

Keywords:

Industry 4.0,
production methods,
small scale production,
smart factories

**Corresponding author*

1. Introduction

Until today, 4 different breaks have occurred in the industry and these are called industrial revolutions. The first of the first 3 Industrial Revolutions, which lasted about 200 years, began in the 1780s, with the replacement of mechanical looms by steam engines and the foundation of mechanical production systems, based in England. Thus, there was an extreme increase in productivity in fabric production that moved from private workshops to central factories. [9]. Approximately 100 years later, the period corresponding to the beginning of the 20th century indicates the second Industrial Revolution. In this period, which is also called the technology revolution, production was completely steam-powered and the construction of railways has started. While this situation supports the increase in steel production; on the other hand, it has transformed it into need. In addition, the development of industrial activities has increased the demand for energy resources and started the transition towards oil and electricity by separating resource use from steam power. With the introduction of electrical energy in assembly lines, the development of mass production and division of labor has created high efficiency. In the same way, electrical

communication has developed and the possibility of communication by telegraph has emerged[3, 17].

Advances in electricity and information technologies in the early 1970s, brought a radical change based on information technology, communication and energy. Production based on mechanical and electronic technology has begun to change with digital technology, and automation has become widespread. The rapid development of computers and the Internet, along with Digital Technology, has brought about the development of information processing, communication and micro-electronic techniques. In the 3rd industrial period, when developments based on micro-electronic technologies such as atom energy, computers, fiber-optics and chips were experienced, the use of solar energy, wind energy, hydroelectric and geothermal power plants became prominent as the concepts of sustainability and sustainable energy became important [17, 27]. All these industrial revolutions have triggered the formation of new generation technologies, smart objects and factories that can communicate with each other. Thus, in the 2000s, the fourth industrial revolution, called industry 4.0, came to the fore. For this period, which is considered as a transition phase of the world, it is predicted that a production cycle in which much higher productivity is aimed at lower costs will develop and thus a new system and social structure will be formed.

2. Industry 4.0

After first mention of forth industrial revolution in Hannover Fair in 2011, Germany Government build a research group to investigate forth industrial revolution in 2012. The research group published a result report in 2013. According to report, nowadays we have been experiencing the transition process of Industry 4.0 and to success of this process 8 step must be completed: 1st step is detection of reference hardware architecture and providing standardization, 2nd step is administration of complex systems, 3rd step is usage of wide-ranging and high-speed communication infrastructure in industry, 4th step is safety and security, 5th step is organization of study and design, 6th step is permanent education and development of professional education, 7th step is adaptation of current regulation, 8th and last step is providing efficiency of source in application [17]. In new industry era, main aim is usage of all sources including human in optimal level and getting result in the most efficient way. For this purpose, a system that consist of simultaneous usage of all technological developments is conceptualized.

A research group including The German Research Center for Artificial Intelligence and Siemens and 20 industrial partners run an application about working principles of a smart factory in Kaiserslautern. Soap bottles with radio frequency identification [RFID]. labels are used with the purpose of observation of the interaction between product and machines. These labels give information about colors, size, and volume of the bottles to machines. After giving information, smart machines recognize the bottles and then classify and fill them. In this cyber-physical system working style, information transfer completed by using radio frequencies and transferred information is stored in digital environment in each step [2]. Moreover, these labels create information clouds during production process. These clouds and continuing of the information process will be used to enable the communication between producer and consumer. Using this system consumer will be able to rate the producer performance, give feedback during the working process and producer will be able to follow the process in breakdown situations.

Pioneer technologies of Industry 4.0 are examined in cloud computing system, augmented reality, simulation, autonomous robots, large data, cyber-physical systems, smart factories, integration of system, internet of objects, three dimensional printers categories [26].

Smart Factories: Smart factories are defined as environments which do not include human factor except extraordinary situations, and consist of machines, robots, and equipment which are working in interaction with each other autonomously [23].

Internet of Objects: The network models which connecting internet with help of additional sensors. They are placed in internal system. Purpose of these models is enabling objects to gather and distribute data.

Cyber-Physical Systems: They are defined as interaction systems between physical world and cyber environments with the help of internet. There are sensors in these systems. These whole systems enable us to define the physical movements in cyber environment. Moreover, it enables communication between objects [16].

Cloud-Computing Technologies: The data held by companies stored in a cloud system that defined as virtual server and accessible for share and usage by any devices with internet connection is provided by a technology. The infrastructure that makes mentioned technology useful is defines the cloud computing system using the software and data of the main source and enable the distribution through IT network [22].
Large Data: Gathering and analyzation statistics of internet, social media, kinds of sensors, GSM records, corporate and consumer-based administration data, and similar kind of data is defined as large data. Moreover, to define it as large data, standardization of simultaneous decision process is required. Optimization of task and decision matcher operation modes increases the quality and efficiency of production. In addition, it helps energy-saving, maintenance of equipment [21].

Simulation: Simulation is defined as a three-dimensional virtual model, which is prepared using real time information, of product, material, and production steps during design

process. It imitates the process and system in the real world. By using this imitation, it defines the objects and relationships of object [29].

System Integration: It is integration of production and administration of business to each other. This integration enables the parts work with harmony with each other. As a result, consumer, supplier, distribution channels work with harmony with each other. The whole system is defined as system integration. System integration makes it possible to have footprint of machines, components, material that used in production process [8].

Three-Dimensional Printers: They print three dimensional objects in real world using three-dimensional data created computers. Mechanical parts except motors and electronic devices can be produced by them. 3D printers also used to surface improvement and modelling. They are used in medicine, industry, food, town planning, genetics, and IT technologies areas [33]. Another important advantage of them is, they decrease the costs of production which results in an increase of accessibility of products. Application of this process to different materials is continuing.

Augmented Reality: They are technologies which bring together the data of real and virtual objects [15]. An advantage of this technology is it make it possible to virtually adaptation of new features to real objects. By using possible it is easier to save time, workload and do not lose contact with the real world.

Autonomous Robots: They are electro-mechanic devices that can carry out tasks with previously programmed software. They can be controlled by operators or by software. Nowadays, these robots are commonly used and human workload replaced with autonomous robots' day by day [5, 8].

2.1. The Place of Industry 4.0 in the World and Turkey

According to 2020 IFR World Robotics report, with 12% increase, 2.7 million industrial robots are used in the world which is a world record [14]. In last ten years, in especially automotive industry and respectively electronics, metal, machine, plastic, chemical product, and food industries an increase of usage of industrial robots are observed. Two-thirds of the global market of production industrial robots are occupied by new built robots in Asia. The biggest operational stock in the area is announced as China with the 21% increase and 783 000 pieces in 2019. The European market which has Germany as main user, showed 7% increase with 580 000 pieces in 2019. European companies especially which includes SMEs, focus on systems with smart sensors to detect glitch and faults in the production process. Moreover, they also support to educate engineers in that area [10].

While corporation of human and robots has been increasing worldwide, Cobot [collaborative robot]. organization has increased %11 unlike traditional robots. While suppliers of these robots are increasing, application range of them are expand and currently their share in the industrial market is 4.8% [14].

When we check the place of Turkey in the OECD countries and chosen countries, Turkey is 35th in the research and development in 2018 [23]. According to 2019 reports, the share of research and development has increased to 1.06% in gross domestic product [31].

When we look at the perception of sector to fourth industrial revolution in Turkey, results indicate that there are legal loopholes, shortage of qualified workman and problems at research and development necessity, learning necessities, problems in system designs, financial difficulties, and dependency to abroad. In addition, with the industry 4.0 there might be disadvantages for Turkey due to cultures of business, the situation of industry in Turkey, working conditions, high costs, and comprehensive software. According to reports, often used applications of industry 4.0 are system integrations, big data, internet of objects, cloud computing systems and another result is that there is an awareness of new technologies in the companies which use advanced technology [13].

SME are very important in transition to industry 4.0. In 2019, the share of SMEs is99.8% in new business attempts in Turkey. 72.4% of employment is encountered by SMEs. According to classification of SMEs; although 56.9% of SMEs are working with low technology, the rate of large-scale initiatives is 49% [32]. According to predictions, SMEs are very important in the process of adaptation of advanced technology to production if conditions are suitable.

3. Aim and method

The main aim of the study is the detection of the tendency of the transition of industry 4.0 and especially to observe the effects of the SMEs' advanced technology integration to production. To achieve this aim, a questionnaire which is about company information, strategies, structure of organization, sources, information systems, and culture of organization are e-mailed to Kan Metal which is a company in Ostim, Ankara (cf. Annex-1). According to data taken from questionnaire additional questions about production and mechanism directed to companies (cf. Annex-2). Finally, by visiting companies, production mechanism is observed, photographed, and semi-structured interview technique, which is one of the qualitative data collection techniques, was carried out. At the end of the research, production mechanism at Kan Metal, and steps of production are examined and edited with the technologies which are predicted to be used with industry 4.0 by using the literature review method.

4. Findings and application

4.1. Company Info

Kan Metal, which is a company built to produce automotive spare parts and marketing in 1958 in Ostim-Ankara, produces spare parts of agricultural machinery since 1982. The company consist of 1 engineer, 2 bachelors, 11 workers and the company is a relatively small SME. They participate fairs in Germany and Italy twice in a year for advertising activity, and they export agricultural machines to Italy, Spain, Germany, Greece, Bulgaria, Serbia, Russia, Ukraine, Hungary, Azerbaijan, Uzbekistan, Iran, Taiwan, and more countries. While the company takes accounting services from outside of the company, they handle their web service. They own 7 machines which can be controlled manually and numerically, and they take painting and baking services from outside of the company.

In 2016, they bought their neighbors' place and their place doubled. In 10 years, they are planning to move a 4-storey factory in Ankara-Kazan. According to this plan, settlement plan of machines will change and painting, baking services will be added up to production process.

The product range of Kan Metal, which produces to order, consists of two groups as vibrating crank and drum blade. In this study, the production stages of the vibrating crank are examined.

4.2. Production Line

The steps of the production of the vibrating crank are explained respectively.

Work order and design: Due to the production to order method, material control is carried out according to the product chosen by the customers from the catalog. 6 meters long round steel solid shafts with diameters ranging from 25 to 42 mm are supplied as raw material. Since the priority is the delivery time, if they do not have the material, an order is placed from a supplier from Ankara and Istanbul who will deliver the material first regardless of the cost.

If the customer requests a special non-catalog vibrator crank production, the part is sent as a sample. After the sample is measured and the technical drawing is created, it is sent back to the company.

Raw Material Warehouse: 6-meter shafts are kept in the entrance that has a maximum capacity of 75 tons. Materials and storage times vary according to diameters. The purpose of storage is stated as shortening the supply time and meeting the demand during busy periods. Stock control is done manually with Excel program based on orders.

Picture 1. *Raw material storage area and Saw*

Saw: The 6-meter shafts are cut according to the dimensions of the ordered product.

CNC lathe: Center holes are drilled on one end of the cut shafts to be used in the lathe machine in the next stages.

Picture 2. *CNC lathe - raw material - lathed product*

Twisting: Due to the costs of special production machines, the fourth generation twisting machine designed by Kan Metal, twists the shafts according to the desired details.

Picture 3. *Kan Metal twisting machine*

Cut to length machine: The twisted products are cut from the ends according to the final length measurement.

Picture 4. *Cut to length machine*

Dimension control: The dimensions and oscillations of all products are individually measured and controlled.

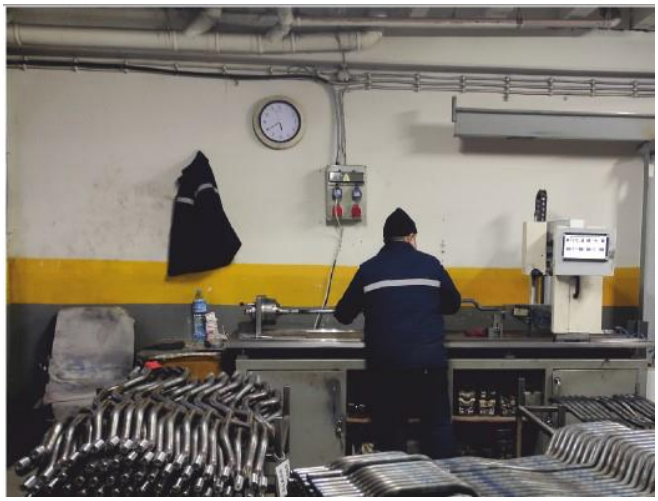

Picture 5. Bench for dimension control

Universal lathe: 1 mm of the end parts of the cranks are removed from the diameter in order to obtain more precise

measurements in CNC lathes.

Picture 6. *Universal lathe*

CNC lathe: The ends of the cranks where the bearings will be seated are turned according to the bearing tolerances.

Picture 7. *CNC lathe*

Attachment assembly: The cranks are divided into 4 groups at this step. Screwing, pressing and welding processes are performed according to the order. If the order is requested without attachment parts or if the product is manufactured for stock, no action is taken to the part.

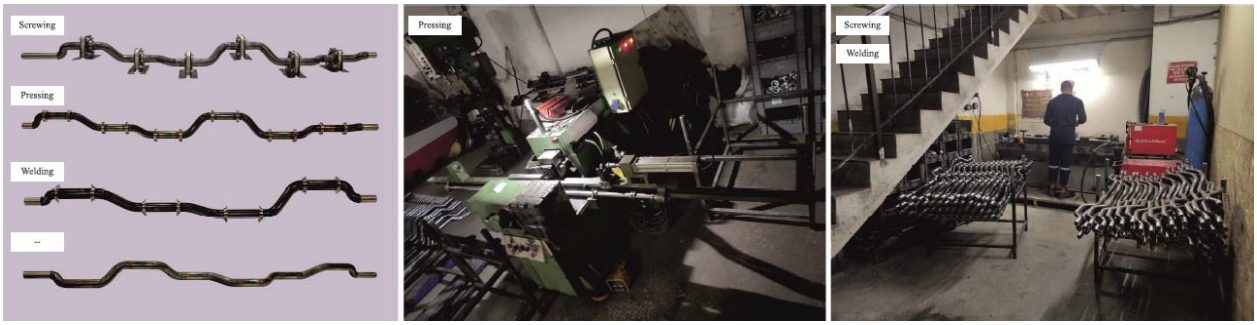

Picture 8. *Types of vibrating cranks – Press machine – screw and welding workbench*

Machining center: Wedge channels are opened to turned parts in the machining center so that they can fit into the machine.

Picture 9. *Machining center*

Painting and firing: At this step, the parts are taken by forklifts to another company located on the same street and undergo static painting and firing processes.

Packing: Tops of the parts are wrapped with nets to prevent damage to the parts and the parts are dressed with logo nylon films.

Product warehouse: It is the last step where intermediate and final products are stored until the order is received or until the shipment date. As indoor transportation is not convenient forklifts cannot be used in this area, and parts can only be stored in a single or double storeys with of pallet trucks.

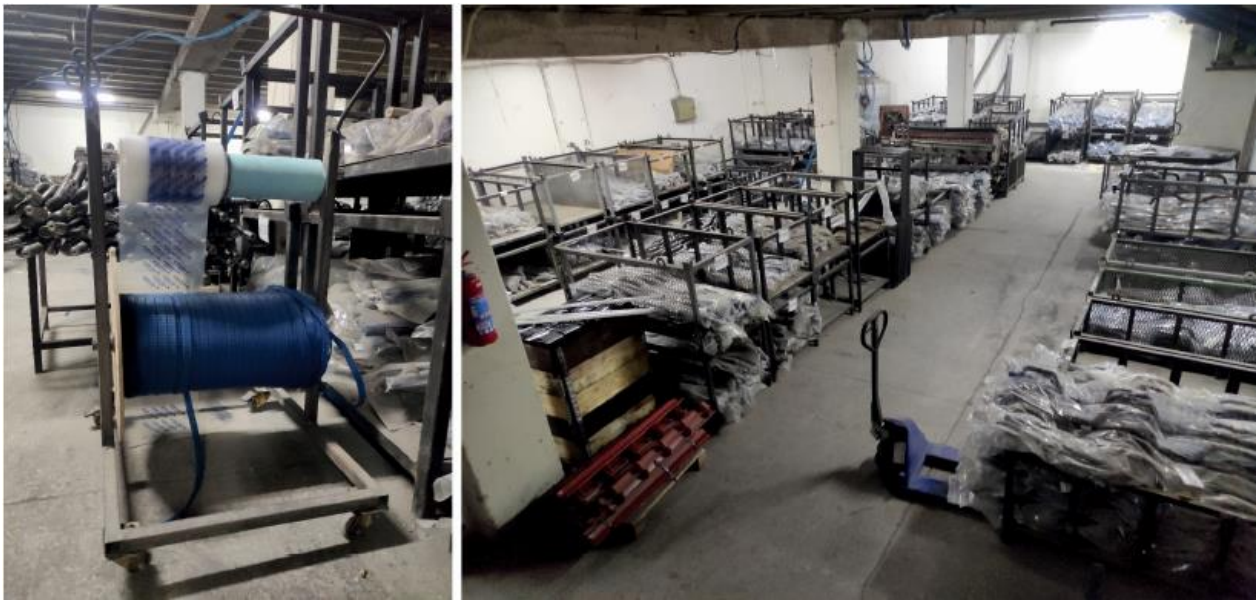

Picture 10. *Packaging and warehouse*

4.3. Current Production Line Evaluation

When the production stages of the shaking crank were examined, it was observed that there were no fully automatic machines included in the process and the production mainly relied on manpower. When the advantages of this mode of production are examined, it is observed that improvements can be made with low capital, and flexible working can be achieved by shifting workers from line to line according to work load. In addition, the company does not have difficulty in meeting the demand and can apply overtime during busy order periods.

The disadvantages of the current production line can be listed as follows:

- Insufficient raw material warehouse space,
- Irregular charges of supply,
- Inventory tracking is not actively conducted,
- Unnecessary circulation time between production machines,
- Accumulating parts in each process step and switching to a new process,
- Dependency to operators,
- Since the final product warehouse is on the lower floor, there is no forklift, only one-floor material can be stored.

In the production of vibrating cranks Kan Metal constantly employs 2 personnel and additional 4 personnel who are shifted from other productions based on the need. Considering that the existing conditions of the enterprise, where the daily production rate is maximum 30, will be improved, it is foreseen to add another one of the CNC lathe machine in Step 8, which determines the daily production amount. In this case, the speed of the twisting machine, which has a daily production capacity of 40-60 pieces in the 4th step, can be slow.

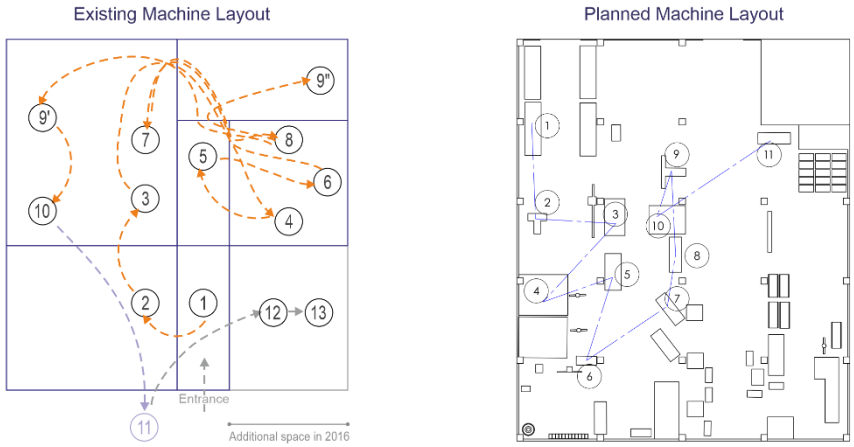

Picture 11. *Production flow available and planned machine layouts*

It is contemplated that the production can reach the maximum level of its own conditions by doubling the production if dyeing and firing units are added to a vibrating crank line, which is thought to have pairs of CNC lathe and twisting machines at the factory that is located on a larger area as planned in Picture 13. In this case, if 2 people are added to the new machines, 2 people are added to the painting and packaging steps, 1 person is added as support to the additional parts assembly and processing center, and 1 person is added as accounting, a total of 6 people will be included and the production line will be able to work at full capacity as planned.

4.4. Fictional Industry4.0 Factory Model

In order for the vibrator crank part used in combine harvesters to be healthy and long-lasting, it is important that it does not make any secretions while turning, and therefore it requires sensitive production. In the current flow, machining parts in the universal lathe before CNC turning lathe in steps 7 and 8 are an extra step to achieve greater precision. Considering this sensitivity and the machines used, the company is seen as having a very convenient production flow for the application of Industry 4.0 technologies.

In case of transition to Industry 4.0 model, it is foreseen that simulation, smart robots, internet of things, horizontal/vertical software integration and cloud technologies will be included in the system. In this case, the flow is set up as in Picture 14.

According to the Industry 4.0 setup, with the horizontal/vertical software integration that can be included in the system, raw material order and stock control, which is one of the most priority problems of the enterprise, will be resolved according to the production flow. In addition, the delivery time will be determined and customers will be able to control the order, production and delivery processes of the products and provide feedback. By creating a simulation of the part instead of sending a sample, additional shipping charges and extra workload will be avoided. Part drawings, quality control documents, company documents and inter-company contracts can be stored in the cloud and used when needed.

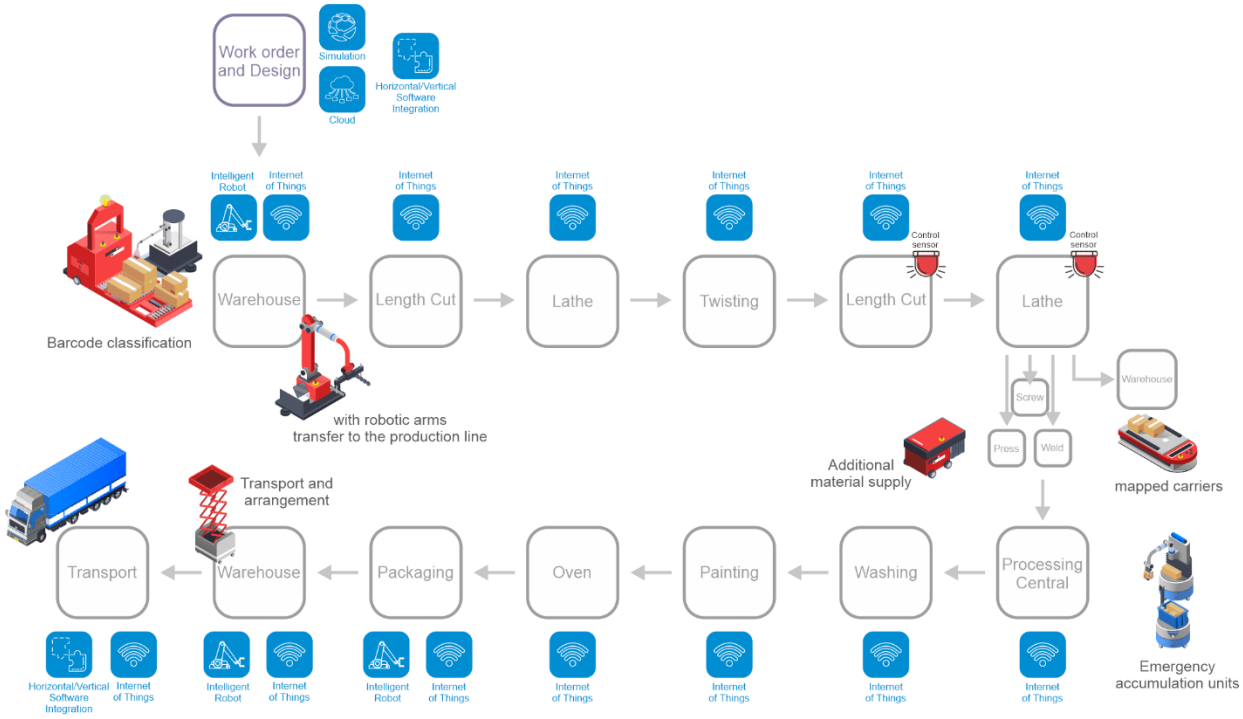

Picture 12. *Production flow available and planned machine layouts*

While the raw materials that arrive at the company are loaded into the warehouse via smart robots, they can be classified according to their diameters thanks to smart barcodes. In addition, it is foreseen that the internet of things will enable entering the raw material stock system that arrives and a warning can be sent for the order in case the products decrease on the shelf. After the raw materials are transferred to the production line by the means of robot arms, thanks to the internet of things, each product will be able to move on to the next process after completing its process.

In cut-to-length and turning steps where quality control is important, intermediate products will be checked before proceeding to the next step through control sensors, and if there is any mistake, transfer will be provided after fixing it. In the lathe step that requires precise processing, after the first measurement is done, it will be controlled and reduced to a fine tolerance, so that the two processes will be combined to ensure that the dimensions are suitable for the final product.

In the additional processing stage, intermediate products will be processed according to the order with the help of the internet of things, and if the product is to be stored as an intermediate product, it can be taken to the warehouse by means of mapped carriers.

Products will progress with the help of even the same technologies, including paint and oven, and when it comes to the packaging step, it will be done with the help of smart robots. After this step, the final products will be transported to the shipment or warehouse thanks to their smart tags. In case the shipment takes place, thanks to the software integration, the carrier company will be notified and the products will be sent without losing time. The customer will receive information that the products are ready and on the way.
In the case of a malfunction in the machines within the system flow, it is designed that support can be provided with smart emergency material suppliers and the machines can repair themselves. In addition, it is foreseen that the production line can be prevented from stopping by creating emergency accumulation units.

4.5. Advantages and Disadvantages of the Fictional Industry 4.0 Factory Model for Kan Metal

The proposed technologies are fundamental innovations, not remedial methods for the company. Re-establishing a factory with these technologies requires large capital, as it will be costly. but Kan Metal, a small-scale SME, aims to develop itself by investing its resources in technology in a balanced way.

When the current production flow is examined, it has been determined that the stage that slows down the daily production amount is the CNC machine specified in Step 8. The fact that there is only one of these machines, which has a daily production capacity of 30, causes the company's daily production capacity to be 30. For this reason, one more CNC machine was added to the new diagram. Thus, assuming that the production rate will remain constant, the number of

products to be sent to the twisting machine with a daily production capacity of 40-60 units and the total production amount are expected to be doubled.

The company, which has a production capacity of 60 vibrating cranks with a daily working time of 9 hours, will increase its capacity to 160 products (60 pieces x 24 hours / 9 hours) considering that the production will be uninterrupted for 24 hours under the new conditions. While 180 items (6 days x 30 items) are produced per month in traditional production, it is calculated that the weekly production (7 days x 160 items) will be 1,120 items in the case of 7 days of uninterrupted production with Industry 4.0. Thus, when the new situation is compared with the existing production capacities, it is observed that the production rate will increase by 622.2%.

More production means either more product than demand or the necessity of finding new markets. This means that the company gains approximately 6 times more customers compared to its customer portfolio. The necessity of reaching new markets and customers brings with it the necessity of increasing the number of personnel or their skills working in the company.

It is thought that 7 machine equipment in the company will evolve into 11 machines and mapped carriers, emergency accumulation units and robotic placement units if Industry 4.0 is adopted. In this case, it is foreseen that there will be no business areas where 11 blue-collar workers out of 14 working in the company can work. Considering that the accounting services are outsourced, it has been determined that 2 people who are partners of the company and the only engineer in the company will adapt to the new system and deal with processes such as order approval, advertising activities and emergency controls, so that the company's production can be carried out with a total of 3 people.

Establishing a staff of 20 with the plan to include 6 more personnel, which was observed in the company's short-term development plan, will also increase personnel costs and the margin of human error. According to the newly calculated situation, the profitability rate of the company will increase with a total of 3 people and standard quality products will be obtained.

In order to include new parts in production, the company requests sample parts from its customers and starts production by measuring on each part. Thanks to the developing 3D scanning technologies, the samples will be saved to the cloud system before they are sent, and they will be delivered, edited and stored. This will both increase the company and customer communication, reduce transportation costs and create a platform where the company can securely store and share production details and drawings and make arrangements interactively with the customer. In addition, 3D printers will enable the production of samples that can be checked and sent to the customer before the parts go into mass production. Thus, in the current system, the interaction of the international company with the customer will increase, and the company will easily reach new customers and increase its market share, with the ease of designing customer-specific parts with reduced shipping costs.

One of the biggest advantages of the new model is that the company will find solutions to the problems that cause inefficient use and cost losses, such as forgetting materials in the storage area, which is currently experiencing difficulties, with the help of smart tags, smart carriers with maps and elevators, and moving lines.

Thanks to the technologies brought by Industry 4.0, shaky cranks will be produced uninterruptedly despite the current or planned new order in Kan Metal, and the factory will have used its resources in the most efficient way. Thanks to the control of the production flow with the internet of things and the horizontal/vertical system integration, raw material arrival-end product output and producer-customer balances will be able to be adjusted according to the order without any problems. In addition, stock follow-ups will be kept up-to-date and the cost will be reduced by making the raw material orders at the right time. In addition, the necessary additional material and material support in the production line will be kept under control automatically, thus preventing the disruptions in the workflow.

Since there is a minimum use of manpower in the dark factory system, the negative effects of the employees and the environment in production will be minimized. In addition, all data from order to distribution will be pulled from the cloud and system assurance will be provided in the data flow.

5. Conclusion and recommendations

In the study, the the vibrating crank production methods of Kan Metal, a small-scale SME company located in Ankara, were examined and applied to Industry 4.0. It is foreseen that the company, which produces 30 pieces with 9 hours of work per day, will produce twice [60 items in 9 hours]. in the same time by adding one more CNC lathe, which determines the production amount under new conditions. In addition, since uninterrupted production will be started throughout the day, the daily production amount will increase to 160 units. Working 6 days a week, the company can produce a total of 180 products, while in the new fictional system, it will be able to produce 1120 vibratory cranks 7 days a week. In this way, it has been calculated that approximately 622.2% efficiency will be achieved with Industry 4.0. In addition, it has been revealed that there will be no need for blue-collar stuff as the worker-dominated production style is replaced by faultless production.

In current studies the implementation of Industry 4.0 in

Turkey is seen as a process that will bring a lot of efficiency, especially for SMEs [6, 34]. While the final products of the companies are perfected in many aspects such as products that require precise measurement, supply costs, production continuity, efficient use of storage units, worker defects and safety, uninterrupted data flow, the production flow will be designed at an optimum level. In addition, it is foreseen that internal and inter-firm communication will be provided at a high level thanks to system integrations.

When the results of the survey and the results obtained in the research are compared with similar studies [20, 34], it is observed that SME companies do not have enough information about Industry 4.0, do not support personnel training in this direction, and provide a shy attitude due to the technical knowledge and cost necessary to create the system. In addition, factories and therefore countries must have certain infrastructures such as internet, electricity, water and communication. However, despite these negativities, the advantages that come with the technologies that will be implemented in the long term are of great importance for both capital owners and the country's industry. These advantages are mainly envisaged as follows:

- With the discrete production method, production will become uninterrupted and productivity will increase due to unit product cost, in factories that work only during working hours or in shifts and where mass production is not possible.
- Information storage and processing processes during the design and ordering stages of the products will be provided by cloud systems and the internet of things, samples can be measured with 3D scans and approval from the customer can be obtained by simulation method, and easy sample creation will be possible thanks to 3D printers. Thanks to these steps, shipping costs will decrease and customer satisfaction and trust will be ensured. Thus, small firms will be able to compete with large enterprises and it will be easier to open up to new markets.
- Raw material supply and storage will be controlled thanks to horizontal/vertical integration, so that negative situations such as order delays will be eliminated.
- By minimizing human use, human errors will decrease, personnel expenditures will decrease, production will accelerate and occupational health and safety violations will be prevented.
- Accessibility and transparency of production processes will facilitate remote control for managers and will be important for customers for monitoring and reliability.
- Thanks to digitalized machines and cloud storage, new product types and revisions will be included in production at low cost as soon as possible, and products will be produced with minimum waste and standard quality.

Considering the costs of transition to Industry 4.0 and the shortage of qualified personnel, it is necessary for Turkey to increase the share of the budget spent on R&D and to train qualified personnel in order to compete with the enterprises in the world. In addition, technology departments and robot laboratories in universities should be given importance, and robot development should be supported with TUBITAK projects. Legal, infrastructural, financial and educational support should be given to SMEs and the transition to the new system should be facilitated with state support.

Acknowledgments

We would like to thank Kan Metal and Güray Kan for their valuable contributions.

References

[1] Akben, İ. and Avşar, İ. İ. (2018). Endüstri 4.0 ve Karanlık Üretim: Genel Bir Bakış. Türk Sosyal Bilimler Araştırmaları Dergisi /Journal of Turkish Social Sciences Research 3(1), 27-37.

[2] Aksoy, S. (2017). Değişen teknolojiler ve endüstri 4.0: endüstri 4.0'ı anlamaya dair bir giriş. SAV Katkı, 4, 34-44.

[3] Alfred, D. and Chandler, Jr. (1994). Scale and Scope: The Dynamics Of Industrial Capitalism, The Belknap Press of Harvard University Press, Harvard.

[4] Ashton, K. (2009). That 'internet of things' thing. RFID Journal, 22(7), 97-114.

[5] Berger, R. (2014). Industry 4.0 The New İndustrial Revolution. Maschinenbau Engineered Products High Tech Branchenexpertise.

[6] Bulut, E., and Akçacı, T. (2017). Endüstri 4.0 ve inovasyon göstergeleri kapsaminda Türkiye analizi. ASSAM Uluslararası Hakemli Dergi, 4(7), 55-77.

[7] Coleman, D. C. (1956). Industrial Growth and Industrial Revolutions. Economica, 23(89), 1-22.

[8] Davutoğlu, N. A., Akgül, B., and Yıldız, E. (2017). İşletme Yönetiminde Sanayi 4.0 Kavramı İle Farkındalık Oluşturarak Etkin Bir Şekilde Değişimi Sağlamak. ASOS JOURNAL-Akademik Sosyal Araştırmalar Dergisi, 52, 544–567.

[9] Drath, R. and Horch, A. (2014). Industrie 4.0: Hit or Hype. IEEE Industrial Electronics Magazine, 8(2), 56-58.

[10] EFFRA (2013). Factories Of The Future, Multi Annual Roadmap For The Contractual PPP Under Horizon 2020. Available:https://ec.europa.eu/research/industrial_technologies/pdf/ppp-factories-of-the-future-strategic-

multiannual-roadmap-info-day_en.pdf [Accessed: 19 January 2021].

[11] Ertuğrul, İ., and Deniz, G. (2018). 4.0 Dünyası: Pazarlama 4.0 ve Endüstri 4.0. Bitlis Eren Üniversitesi Sosyal Bilimler Dergisi, 7(1), 143-170.

[12] Faulds, D. J., and Raju, P. S. (2019). An interview with Chuck Martin on the Internet of Things. Business Horizons, 62(1), 27–33.

[13] Göv, S. A., and Erdoğan, D. Dördüncü Endüstri Devriminin (Endüstri 4.0) Neresindeyiz?. İstanbul Gelişim Üniversitesi Sosyal Bilimler Dergisi, 7(2), 299-318.

[14] IFR (2020, 24 Eylül), World Robotics Report. Available:https://ifr.org/downloads/press2018/Presentation_WR_2020.pdf [Accessed: 19 January 2021].

[15] İçten, T and Bal, G. (2017). Artırılmış Gerçeklik Üzerine Son Gelişmelerin ve Uygulamaların İncelenmesi. Gazi Üniversitesi Fen Bilimleri Dergisi Part C: Tasarım ve Teknoloji , 5 (2) , 111-136 .

[16] Jazdi, N. (2014). Cyber Physical Systems in The Context Of Industry 4.0. In 2014 IEEE international Conference On Automation, Quality And Testing, Robotics (pp. 1–4). IEEE.

[17] Kagermann, H., Wahlster, W. and Helbig, J. (Eds.). (2013). Recommendations for implementing the strategic initiative Industrie 4.0: Final report of the Industrie 4.0 Working Group, Frankfurt, April.

[18] Kesayak, B. (2015). Available:"Endüstri Tarihine Kısa Bir Yolculuk" http://www.endustri40.com/endustri-tarihine-kisa-bir-yolculuk/ [Accessed: 19 January 2021].

[19] Kılıç, S., and Alkan, R. M. (2018). Dördüncü sanayi devrimi Endüstri 4.0: Dünya ve Türkiye değerlendirmeleri. Girişimcilik İnovasyon ve Pazarlama Araştırmaları Dergisi, 2(3), 29-49.

[20] Kureş, T., & ŞIK, A. (2022). Yangın Söndürme Tüpü Üretiminin Endüstri 4.0'da Örnek Vaka Uygulaması Üzerinden İncelenmesi. Online Journal of Art and Design, 10(3).

[21] Lee, J., Kao, H.-A. and Yang, S. (2014). Service Innovation And Smart Analytics For İndustry 4.0 And Big Data Environment. Procedia Cirp, 16, 3–8.

[22] Lu, Y. (2017). Industry 4.0: A Survey On Technologies, Applications And Open Research İssues. Journal of ındustrial ınformation ıntegration.

[23] Motyl, B., Baronio, G., Uberti, S., Speranza, D., and Filippi, S. (2017). How will Change the Future Engineers' Skills in the Industry 4.0 Framework? A Questionnaire Survey. Procedia Manufacturing, 11(June), 1501–1509.

[24] OECD (2020). Main Science and Technology Indicators R&D Highlights in the February 2020 Publication. Available: https://www.oecd.org/sti/msti2020.pdf.[Accessed: 19 January 2021].

[25] Oğrak, Z., and Şık, A. (2020). Plastik Üretiminin Endüstri 4.0'da Örnek Vaka Uygulaması Üzerinden İncelenmesi. Tykhe Sanat ve Tasarım Dergisi, 5(8), 35-57.

[26] Ötleş, S. and Özyurt, V. H. (2016). Endüstri 4.0: Gıda sektörü perspektifi. Dünya Gıda Dergisi, 89-96.

[27] Redclift, M. (2005). Sustainable Development (1987–2005): An Oxymoron Comes of Age. Sustainable Development, 13(4), 212-227.

[28] Roblek, V., Mesko, M. and Krapez, A. (2016). A Complex View of Industry 4.0. SAGE Open, 6(2), 1-11.

[29] Rodič, B. (2017). Industry 4.0 and the new simulation modelling paradigm. Organizacija, 50(3), 193-207.

[30] Shrouf, F., Ordieres, J. and Miragliotta, G. (2014). Smart Factories in Industry 4.0: A Review of the Concept and of Energy Management Approached in Production Based on the Internet of Things Paradigm. IEEE International Conference on Industrial Engineering and Engineering Management, 697-701.

[31] Türkiye İstatistik Kurumu, 2019-a, Araştırma-Geliştirme Faaliyetleri Araştırması. 23 Ekim 2020 Haber Bülteni. Available: https://tukweb.tuk.gov.tr/PreHaberBultenler.do?d=33676# [Accessed: 19 January 2021].

[32] Türkiye İstatistik Kurumu, 2019-b, Küçük ve Orta Büyüklükteki Girişim İstatistikleri. 28 Aralık 2020 Haber Bülteni. Available: https://tukweb.tuk.gov.tr/HbPrnt.do?d=37548 [Accessed: 19 January 2021].

[33] Vaidya, S., Ambad, P., and Bhosle, S. (2018). Industry 4.0–a glimpse. Procedia Manufacturing, 20, 233-238.

[34] Yıldız, A. (2018). Endüstri 4.0 and akıllı fabrikalar. Sakarya Üniversitesi Fen Bilimleri Enstitüsü Dergisi, 22(2), 546-556.

Annex-1:

COMPANY INFORMATION SURVEY
What is your company's NACE code?
What is the total number of employees in your company?
How is the differentiation of employees in your company according to their education level?
Doctorate : ..... Post graduate: ..... Licence:..... Associate degree: ..... High school: ..... Vocational high school: ..... Primary education: .....
How many engineers are working in your company?
Do you have an R&D department in your company? Yes ☐ No ☐
Do you have R&D employees? If yes, indicate how many staff there are.
Do you have an engineer or employee who works/can work in the field of Industry 4.0? (software, electronics, mechatronics etc.) Please explain if any.
What is your company's industry?
☐ Agriculture ☐ Tourism ☐ Plastic Machine Metal ☐ Energy ☐ Mine ☐ Food ☐ Health ☐ Forest Products ☐ Other
What is the scope of activity of your company?
☐ Local / Regional Scale ☐ National Scale ☐ International Scale ☐ World Scale ☐ Other
1. STRATEGY
1.1.What is your company vision?

1.2.What is your company mission?											
1.3.Do you have a company strategy (written, unwritten, short/long term goals)? Please specify if any.											
1.4.Do you have a defined R&D and Innovation strategic goal(s)? Please specify if any.											
1.5. Is a defined Industry 4.0 strategy among your target(s)? Please specify if any.											
1.6. If you have defined strategic goals, are they known to your top and middle managers and employees? If your answer is yes, please explain											
2. ORGANIZATIONAL STRUCTURE											
2.1. Do your employees have applicable job descriptions (written, verbal, defined, master-apprentice relationship)? Please specify if any.											
Current state							Importance for the Firm				
Often.....Never							Important .Unimportant				
5	4	3	2	1	**2.2**.How often do your employees take part in project-based interdisciplinary work within the scope of business objectives? How important is it for your employees to engage in project-based interdisciplinary work?		5	4	3	2	1
5	4	3	2	1	**2.3**.How often do your employees work in different departments and develop competence? How important is it for your employees to work in different departments and develop competence?		5	4	3	2	1
High.....Low							High.....Low				
5	4	3	2	1	**2.4**.What is the decision/initiative level of your employees in operational processes in your business?		5	4	3	2	1
5	4	3	2	1	**2.5**.What is the effect level of these decisions on central government decisions?		5	4	3	2	1
5	4	3	2	1	**2.6**.What is the impact level of your employees' mistakes on business operations?		5	4	3	2	1
5	4	3	2	1	**2.7**.What is the level of knowledge of company managers on concepts such as smart factory / product / production?		5	4	3	2	1
2.8. Does your organization provide training on new technologies?											
2.9. Do you have feedback mechanisms (customer, employee, market, competitor, etc.) in your business? Please specify if any.											

Often.....Never						Important .Unimportant				
5	4	3	2	1	**2.10**.How often does the business receive feedback from customers?	5	4	3	2	1
5	4	3	2	1	**2.11**.How often is customer feedback used in product development processes?	5	4	3	2	1
2.12 Evaluate the suitability of your organizational structure for fast or flexible production methodologies.										

Often.....Never						Important .Unimportant				
5	4	3	2	1	**2.13**.To what extent can you fulfill/find solutions to your customers' demands/ problems by using certain technologies and methods?	5	4	3	2	1
5	4	3	2	1	**2.14**.What is the level of competence to adapt to changing market conditions?	5	4	3	2	1
2.15. Flexible hours, taking initiative, etc.) If yes, please specify.										
2.16.Are there incentive motivation systems in the business to increase the self-confidence of your employees? Please specify if any.										
2.17.Do you plan to make improvements in light of the questions in this section? If your answer is yes, give an example.										
3. RESOURCES										
3.1. Financial Infrastructure										
3.1.1.Do you have financing/credit opportunities that you can allocate to invest in new technologies?										
3.1.2.Would you consider investing in sectors outside of your field of work? If your answer is yes, give an example.										
3.2.Do you have machines compatible with Industry 4.0? (Can he work without a human being?)										
Often.....Never						Important .Unimportant				
5	4	3	2	1	3.2.1.What is the level of horizontal formal communication channels between your employees?	5	4	3	2	1
5	4	3	2	1	3.2.2.What is the level of vertical formal communication channels between your employees?	5	4	3	2	1
3.3. Physical Infrastructure										
3.3.1.Can you extract data from your operations through communication ports? If your answer is yes, give an example.										
3.3.2.Do you have machines compatible with Industry 4.0? (Can he work without a human being?)										

Often.....Never						Important .Unimportant				
5	4	3	2	1	**3.3.3**.What is your level of using the communication ports of your devices?	5	4	3	2	1
5	4	3	2	1	**3.3.4**.What is your level of knowledge on data collection with your machines in their current state or with integrated sensors?	5	4	3	2	1
5	4	3	2	1	**3.3.5**. Is fault detection and calibration performed independently and automatically by the machines in pre-production and production processes?	5	4	3	2	1
3.3.6.Do you use sensors in your operational processes related to production? If your answer is yes, give an example.										

High. . . . . Low						Important .Unimportant				
5	4	3	2	1	**3.3.7**.Can your employees use the data produced by digital tools (sensors, etc.) for strategic decision making?	5	4	3	2	1
5	4	3	2	1	**3.3.8**.Is the production processes monitored with smart sensors/RFID and the data collected is automatically transformed to feed the decision support systems?	5	4	3	2	1
3.3.9. Are there intermediate elements/systems (hardware, wireless connection systems, etc.) that will provide information transfer between employees and machines?										
3.3.10.Do you plan to make improvements in light of the questions in this section? If your answer is yes, give an example.										
4. INFORMATION SYSTEMS										
4.1.Data Integration										
4.1.1. Does your company have a database management system? Please specify if any.										
4.1.2.Does your company use software such as ERP? If your answer is yes, give an example.										
Often. . . . . Never						Important .Unimportant				
5	4	3	2	1	**4.1.3**.What is the level of effective use of information systems?	5	4	3	2	1
5	4	3	2	1	**4.1.4**.What is the level of integration of data produced in different units?	5	4	3	2	1
5	4	3	2	1	**4.1.5**.What is the standardization level of data produced from information sources?	5	4	3	2	1
5	4	3	2	1	**4.1.6**.What is the level of precaution taken for cyber security in your institution?	5	4	3	2	1
Often. . . . . Never						Important .Unimportant				
5	4	3	2	1	**4.1.7**.What is the level of user identification, administrative user separation and data flow (IEC62443 standard etc.) in the processes where information technologies are used?	5	4	3	2	1
5	4	3	2	1	**4.1.8**.What level of automatic information is provided to those responsible (manager, operator, etc.) of operations (logistics, production, marketing, etc.) carried out within the scope of company activities, about the operation and critical processes of the operation, through software applications?	5	4	3	2	1
4.2 Data Use in Decision Making Processes										
High. . . . . Low						Important .Unimportant				
5	4	3	2	1	**4.2.1**.What is the level of instant data capture from operations from business functions (production, logistics, service, R&D and marketing)?	5	4	3	2	1
5	4	3	2	1	**4.2.2.**If instant data can be drawn from business functions, what is the level of real-time monitoring of the captured data?	5	4	3	2	1
5	4	3	2	1	**4.2.3**.What is the level of making the produced data meaningful and using it in planning?	5	4	3	2	1
5	4	3	2	1	**4.2.4**What is the level of task-based use of the produced data?	5	4	3	2	1
Often. . . . . Never						Important .Unimportant				
5	4	3	2	1	**4.2.5**.How often do your employees use personalized methods (signs, voice commands, etc.) for data entry?	5	4	3	2	1
4.2.6. Do you have information technology infrastructure such as physical server, cloud-based server, system backup information (NAS etc.)?										

High..... Low						Important .Unimportant				
5	4	3	2	1	**4.2.7.** What is your remote access activity level to business data?	5	4	3	2	1
4.2.8 Do you plan to make improvements in light of the questions in this section? If yes, give an example.										
5. CULTURE										
High..... Low										
5	4	3	2	1	**5.1.** What is the intra-firm diffusion level of mechanisms for compensating employee errors in the operation of company functions?	5	4	3	2	1
5	4	3	2	1	**5.2.** What is the level of your employees adapting to a new practice/method?	5	4	3	2	1
5	4	3	2	1	**5.3.** What is the level of competence of your employees in information technologies (technology developed for data recording, transfer, manipulation, use and interpretation)?	5	4	3	2	1
5	4	3	2	1	**5.4.** At what level do the causes of the problems experienced in the company operations spread within the company?	5	4	3	2	1
5	4	3	2	1	**5.5** What is the level of trust of your employees in the decisions made by the information systems?	5	4	3	2	1
Often..... Never						Important .Unimportant				
5	4	3	2	1	**5.6.** How often do your employees submit training requests to management to critique new competencies?	5	4	3	2	1
5	4	3	2	1	**5.7** How often do your employees receive proposals to change the business structure/actions on global innovations related to the business's industry?	5	4	3	2	1
					5.8. How often are urgent/rapid decisions taken for company strategy and operation based on the feedback of your employees?					
5.9. Do you plan toimake improvements in light of the questions in this section? If your answer is yes, give an example.										

Annex-2:
Additional Survey Questions:

1. How many employees does the company have?
2. Which departments does the company get external help from?
3. Could you share the process diagram and describe the process flow?
4. What is the daily capacity of the company?
5. Does the company have machines working in shifts in the production flow?
6. What are the additional machines for working full capacity? How many workers does the company need in the case of full capacity?
7. What are your criteria for choosing the suppliers? Who pays the delivery costs?

MANAS Journal of Engineering
ISSN 1694-7398 | e-ISSN 1694-7398

Volume 11, Issue 1, (2023) Pages 25- 52
https://doi.org/10.51354/mjen. 1074008

A review study on the use of dimethyl ether in diesel engines: effects on CO_2 emissions

İsmet Sezer

Department of Mechanical Engineering, Gümüşhane University, Gümüşhane, Turkey, isezer@gumushane.edu.tr, ORCID: 0000-0001-7342-9172

ABSTRACT

Emissions from vehicles and other fuel combustion systems can alter the composition of the atmosphere and augment its capacity to absorb heat. These gases, which are effective at trapping heat, are known as greenhouse gases and include all gases found in vehicle emissions. Reducing the emissions of carbon dioxide (CO_2) has become an urgent necessity around the world, and many countries have imposed limits on their CO2 output. Using biofuels in automotive engines is an effective way of reducing greenhouse gas emissions. The CO_2 emissions emitted from the combustion of biofuels are absorbed as trees and plants grow. Biofuels can be used either as pure fuels or blended with conventional fuels. Most research has declared that the most effective way to reduce greenhouse emissions is the use of various biofuels. Therefore, it is essential to assess the outcomes of research regarding alternate fuels or fuel additives to determine their proper utilization. Using of diesel engines can also help reduce CO_2 emissions as they emit less CO_2 emissions than gasoline engines. This review study investigates the effects the using of dimethyl ether on CO_2 emissions in diesel engines. The results showed that CO_2 emissions decrease when using the pure DME and DME blends with diesel and LPG fuels due to the oxygen content and the lower carbon to hydrogen ratio of DME. The decrements in CO_2 emissions for pure DME, diesel–DME blends and LPG–DME blend are about 5.2–18.3%, 3–41.6% and 10.6–16.4%, respectively.

ARTICLE INFO

Review article

Received: 15.02.2022
Accepted: 14.02.2023

Keywords:

CO2 emissions
diesel engines
dimethyl ether
fuel additives

*Corresponding author

1. Introduction

Diesel engines are the dominant power sources among automobile engines due to their superior performance, fuel economy and lower emission of hydrocarbons (HCs), carbon monoxide (CO) and carbon dioxide (CO2) compared to gasoline engines [1]. However, diesel engines are currently known to emit higher levels of particulate matter (PM) and nitrogen oxides (NOx) emissions than those of gasoline engines. Therefore, to reduce emissions from diesel engines, numerous researches have been conducted, and progressive studies on alternative fuels have been carried out [2]. Among the various alternatives, DME stands out from the standpoint of energy security, as it can be industrially synthesized from coal, natural gas, and numerous types of biomass [3]. However, the physical properties of DME such as lower viscosity, lubricity, combustion enthalpy, and boiling point require modifications to the diesel engine structures and components. The technology for using pure DME in compression ignition (CI) namely diesel engines and vehicles are still in the development stage. However, DME can be used as an additive in diesel fuel or other alternative fuels [4]. It is essential to evaluate the results of different studies concerning the use of DME in diesel engines together in order to apply them in practice. Therefore, this review study aims to investigate the effects of dimethyl ether on CO2 emission in diesel engines.

2. Characteristics of dimethyl ether

DME is the simple ether with the chemical formula of CH3–O–CH3 (C2H6O) as seen in the Fig. 1. In general, the physical properties of DME are very similar to those of the liquefied petroleum gas (LPG). Therefore, the requirements of the storage, fuel handling and transportation for DME are similar to those of LPG [3].

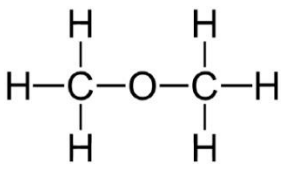

Figure 1. *Chemical structure of DME [5]*

DME can be produced using indirect or direct synthetic methods as seen in Fig. 2. DME is generated through a dehydration reaction after the synthetic reaction of methanol in the indirect synthetic method, while it is directly produced from natural gas in the direct synthetic method [5]. The production cost of DME is less than diesel fuel or gasoline on an energy equivalent basis. The economics of DME production are similar to compressed natural gas (CNG) or liquefied natural gas (LNG), when the large scale plants are considered [6]. DME is gaseous and almost non–toxic at atmospheric pressure and room temperature. Therefore, it needs to be pressurized over 0.5 MPa to keep it in a liquid state under ambient temperature and pressure conditions. The fuel delivery pressure should be increased to 1.7–2.0 MPa under engine operating conditions to prevent vapor lock in the fuel injection system [7, 8].

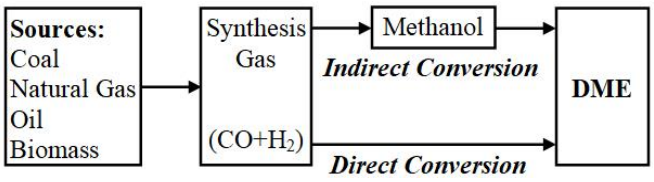

Figure 2. *Production methods of DME [9]*

The properties of DME and diesel fuel are tabulated in Table 1. It can be seen that the properties of DME are quite different from those of diesel fuel. DME has the high vapor pressure and low boiling temperature, which is a gas fuel at room temperature and atmospheric pressure. The heating value of DME is significantly lower than conventional diesel fuel. Therefore, the fuel supply system, injection system and combustion system of the engine should be redesigned or modified for the use of DME [10]. However, the cetane number of DME is higher than that of diesel fuel, which demonstrates good ignition capability. The latent heat of evaporation of DME is much higher than diesel fuel, which is beneficial for reducing the mixture temperature and increasing engine volumetric efficiency.

Table 1. *The properties of DME and diesel fuel [8]*

Property	DME	Diesel
Chemical formula	$CH_3–O–CH_3$	C_xH_y
Molecular weight, g/mol	46.07	170
Boiling point, °C	–24.9	180–360
Vapor pressure, kPa	530	<<10
Liquid density, kg/m^3	668	840
Liquid viscosity, cP	0.15	4.4–5.4
Lower heating value, kJ/kg	28430	42500
Ignition temperature, °C	235	250
Cetane number	55–60	40–55
Stoichiometric air/fuel ratio	9	14.6
Modulus of elasticity, N/m^2	6.37x10^8	1.486x10^9
Mass fraction of carbon	52.2	86
Mass fraction of hydrogen	13	14
Mass fraction of oxygen	34.8	0

DME has only C–H and C–O bonds, without C–C bonds, and contains about 34.8% oxygen. Because of these properties, DME combustion produces almost zero PM emission and the low noise level. It can tolerate a higher EGR rate to reduce NOx emissions greater extent than with conventional diesel fuel [6]. The other advantage of DME is that it is non–corrosive to the fuel system structure and metal surfaces [5]. The low viscosity of DME causes leakage in the fuel supply system, which relies on small clearances for sealing. Its lower lubricity characteristics result in intensified surface wear on the moving parts within the fuel injection system. Therefore, adding of proper additives is essential to prevent leakage and surface wear during the using of DME. The compressibility of DME is generally higher than that of diesel, so DME requires more compression pump work compared to the diesel. In general, DME deteriorates the rubber seals mainly due to its corrosive nature. For that reason, all existing rubber seals in injection systems should be replaced with non–corrosive materials [1].

3. Problems with dimethyl ether

DME has the favorable properties described above; there are some problems encountered in the practical use of DME such as below [4, 5].

- DME fuel feed pump and high pressure pump should be designed according to the requirements of the desired DME fuel system, engine power, and vehicle type. The design needs to account for the distinctive physical properties of DME, including its high vapor pressure, high compressibility, low viscosity, and its capacity to dissolve rubber and certain plastics.
- Due to its low viscosity, DME has poor lubricity which can cause frictional wear and internal leakage problems. To counter these issues, proper additives should be added to DME fuel. Furthermore, its high vapor pressure combined with its low viscosity can cause vapor locks and cavitations in fuel systems.
- DME has a lower heating value and density than diesel fuel, so more fuel needs to be injected to generate the same amount of heat. This means an increased injection rate and duration are necessary for DME compared to diesel fuel. This could, however, result in increased fuel line back pressure. Additionally, the use of larger fuel injectors, fuel pumps, and fuel tanks is essential when using of DME.
- The current ultra–high injection technology used for diesel fuel does not apply to DME injection due to the

superior atomization and vaporization characteristics of DME. Additionally, the o appropriate injector nozzle and combustion chamber geometry for DME should be determined for an optimum injection strategy.

- The fuel heating may occur when engine temperature becomes high, which could result in a decrease in fuel density and an increase in compressibility. As a result, it becomes more difficult to supply the required amount of fuel to stabilize the DME engine operation. To mitigate this, the fuel cooling or temperature control unit is essential to the fuel supply and injection system in DME fuelled engines.

The ability to operate without causing black smoke makes DME a viable option in direct injection diesel engines. The only significant changes that need to be made are installing a high pressure (injection pressure no higher than 300 bar) fuel injection system, typically with an electronic control, in order to optimize the injection timing and duration. A turbocharger and an EGR system must be also added to take advantage of all the benefits of using DME. Finally, a suitable fuel storage and supply system must be put in place. These modifications can be done at a low cost without replacement of major engine components. Although optimization of the fuel injection equipment for overcoming issues such as low density, low lubricity, and corrosiveness is necessary for mass production, DME can be used with diesel or the other alternative fuels as an environmental friendly and renewable alternative fuel [4].

4. Researhes on dimethyl ether

There have been numerous studies conducted on the production technologies, fuel properties, combustion characteristics, engine performance, and exhaust emissions of DME. The different production methods were examined and compared in terms of cost in the studies of production technologies [9, 11, 12]. Moreover, the studies of fuel properties focused on features of DME which are different to diesel fuel, such as oxygen content, low density, low viscosity, and low lubricity [5, 13–15]. Additionally, the effects of DME on parameters such as injection characteristics [16–23], ignition delay, combustion duration, cylinder temperature, and pressure were investigated in the combustion studies [13, 24–36]. The studies of engine performance analyzed the impacts of DME on parameters such as torque, engine power, brake thermal efficiency, and fuel consumption [37–58]. Further, the emission studies investigated the effects of DME on emissions of CO, HC, PM or soot, NOx, and CO2 [59–80]. The lower CO2 emissions are anticipated during the use of DME and its blends, since the combustion equations of DME and diesel fuels at stoichiometric conditions are as Eqs. (1) and (2) [13].

$$\text{DME: } C_2H_6O + 3[O_2 + 3.76N_2] \rightarrow 2CO_2 + 3H_2O + 3(3.76)N_2 \quad (1)$$

$$\text{Diesel: } C_{12}H_{24} + 18[O_2 + 3.76N_2] \rightarrow 12CO_2 + 12H_2O + 18(3.76)N_2 \quad (2)$$

Therefore, the potential of dimethyl ether on reducing of CO2 emissions in diesel engines was investigated in this review study based on literature.

5. Combustion characteristics of dimethyl ether

The 664 K can provide thermal reactivity energy for the breaking up of DME into CH4, H2 and CO. Comparing the combustion and decomposition of DME; it can be observed that the decomposition process occurs at different temperatures and pressures with varying speeds, while combustion takes place at cylinder temperature of approximately 1000 K. According to Eq. (3), which shows the decomposition of DME, each mole of DME is broken down into one mole of CH4, H2, and CO. The decomposition speed of DME is related to temperature; such as, chemical kinetic modeling of DME demonstrates that 99% of it is broken down in around 0.1 s when it is heated to 973 K, with the process being faster at higher pressures [81].

$$CH_3OCH_3 \rightarrow CH_4 + H_2 + CO \quad (3)$$

It is declared that the ignition of DME in combustion chambers occurs earlier than that of diesel or biodiesel fuels in CI engines, owing to its lower ignition temperature and higher cetane number. Effects of DME on the parameters related to the combustion of DME such as heat release, combustion pressure and temperature are presented below. Additionally, DME combustion is soot–free because of its lack of C–C bonds, and it has lower HC and CO emissions than those of diesel combustion. NOx emission from DME combustion can be reduced by applying exhaust gas recirculation ratio (EGR), as well as with the multiple injection strategy and premixed combustion [13].

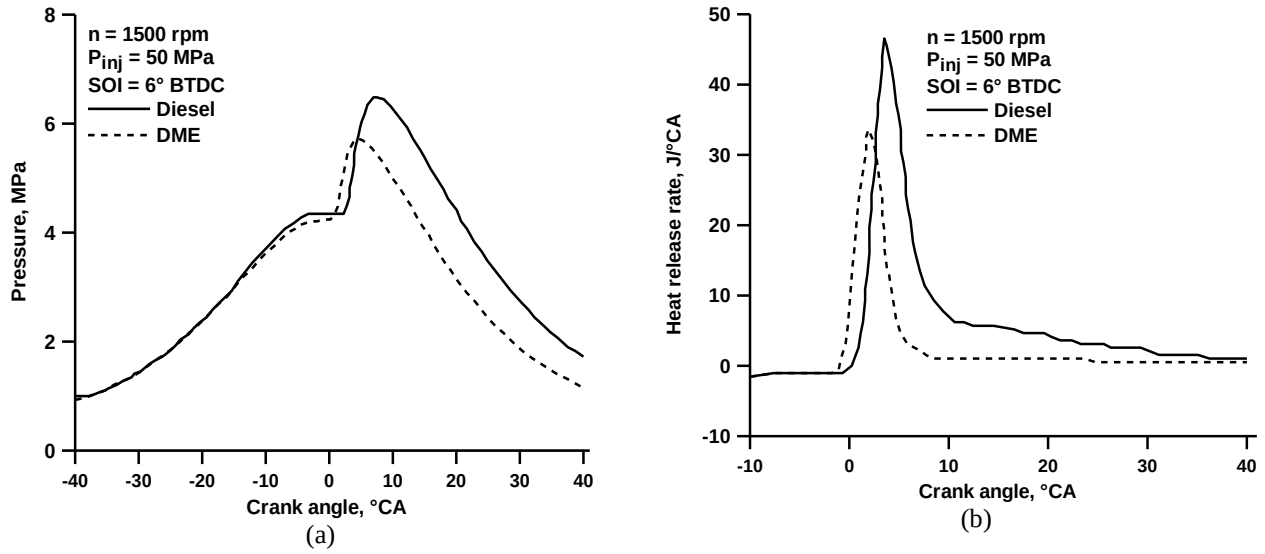

Figure 3. *Variation of a) pressure and b) heat release rate for Diesel and DME fuels [5]*

Fig. 3(a) and (b) show the combustion pressure and heat release rate (HRR) of DME and diesel fuels at engine speed of 1500 rpm, injection pressure of 50 MPa, start of injection (SOI) of 6° BTDC (before top dead center), and an injection fuel mass of 8 mg/cycle. The peak pressure of diesel fuel was higher than that of DME at the same injection quantity due to its higher lower heating value (LHV) of 42.5 MJ/kg compared to that of DME's 28.43 MJ/kg. However, it is declared that an increased amount of injected DME should match that of diesel to improve the combustion characteristics such as combustion pressure and heat release [5].

Fig. 4 (a) and (b) show the combustion characteristics of DME and diesel fuels for a single–cylinder engine with constant energy input at 50 MPa of injection pressure. In the case of DME fuel, the combustion pressure and heat release rate of the engine resulted in a higher peak compared to that of diesel fuel at injection timing of 2° BTDC as seen in Fig. 4 (a) and (b). Comparing the ignition characteristics of both DME and diesel fuel, DME combustion showed earlier ignition than diesel combustion because the cetane number of DME is higher than that of diesel fuel. The gap in the ignition delay between diesel and DME was about 1.3–2.3° CA (crank angle). Therefore, the shorter ignition delay and the faster ignition of DME created an excessive rise in pressure and heat release rate compared to diesel fuel, as seen in the combustion pressure profile and heat release pattern [13].

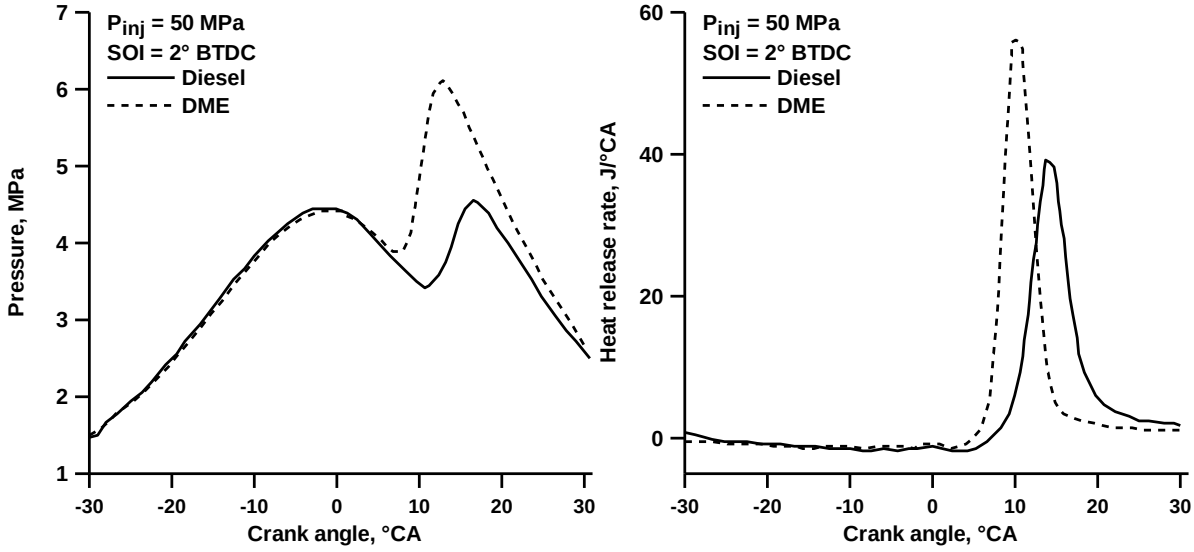

Figure 4. *Variation of a) pressure and b) heat release rate for Diesel and DME fuels [13]*

Fig. 5 shows a comparison of the combustion characteristics at baseline condition. It can be seen that the combustion pressure and heat release rates of diesel fuel have lower peaks than those of the DME fuel with the same calorific value due to the different combustion properties. In addition, the ignition timing of the DME fuel is more advanced than that of diesel fuel, as it has a higher cetane number and faster evaporation. Accumulated heat release (AHR) of DME fuel is also higher than that of diesel fuel due to the greater injected fuel amount. Finally, the accumulated heat releases of DME and diesel fuel become stable from 5° and 30° ATDC (after top dead center), respectively. This is due to the more rapid combustion of DME fuel resulting from its faster evaporation compared to diesel fuel [77].

Fig. 6 shows the comparison of combustion pressure and heat release rate for diesel, GTL (Gas to Liquid) and DME at the maximum torque point and 9° CA injection timing. It can be seen in 6(a) that the peak pressures of diesel, GTL, and DME were 13.9, 13.4, and 11.2 MPa respectively, with the maximum combustion pressures of GTL and DME being lower than that for diesel by 3.6% and 17.2% respectively. This is attributed to the significantly high cetane number of GTL and DME, leading to a shortened ignition delay period during which less combustible mixture is formed and the maximum combustion pressure drops. In addition, Fig. 6(b) reveals that the peak value of heat release rate with GTL is lower than that for diesel by 3.0%. The location of GTL heat release rate peak value is slightly delayed compared to diesel. The peak heat release rate of DME is also lower than that for the diesel engine and its peak heat release rate is later than that for diesel. This is due to the longer pressure wave propagation for GTL and DME in comparison to diesel, which results in a longer fuel injection delay for GTL and DME than for diesel. Consequently, the effect of the injection delay of GTL and DME is more pronounced and causes the lagged maximum pressure, even though GTL and DME, with high cetane numbers, should have a prompt combustion [67].

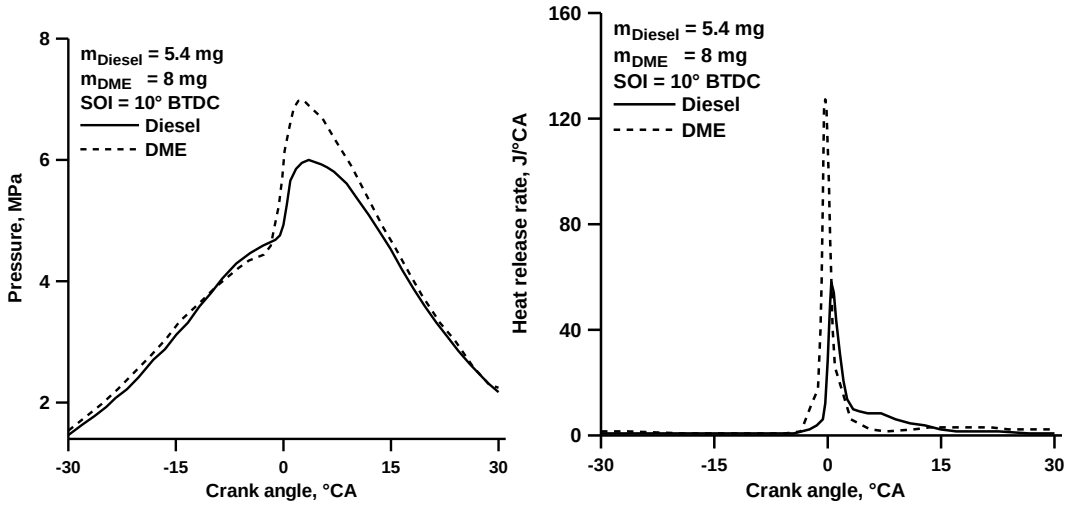

(a) (b)

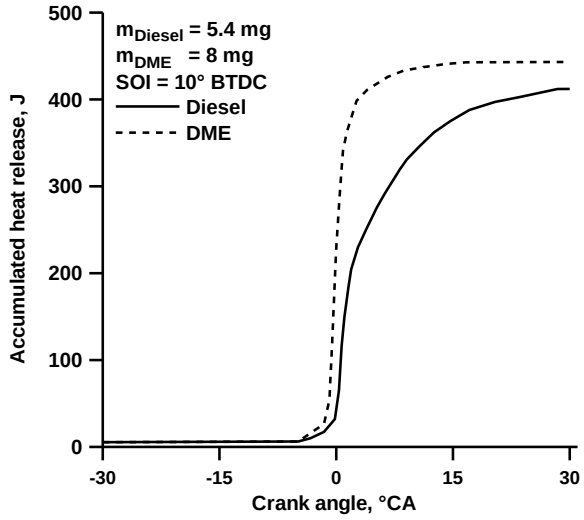

(c)

Figure 5. *Variation of a) pressure, b) heat release rate and c) accumulated heat release for Diesel and DME fuels [77]*

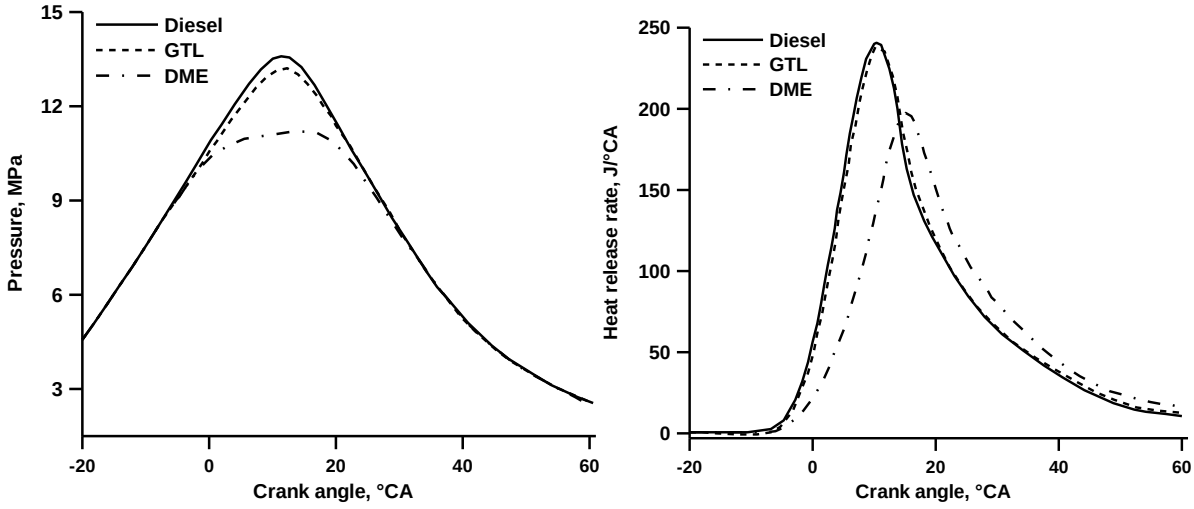

(a) (b)

Figure 6. *Variation of a) pressure and b) heat release rate for Diesel, DME and GTL fuels [67]*

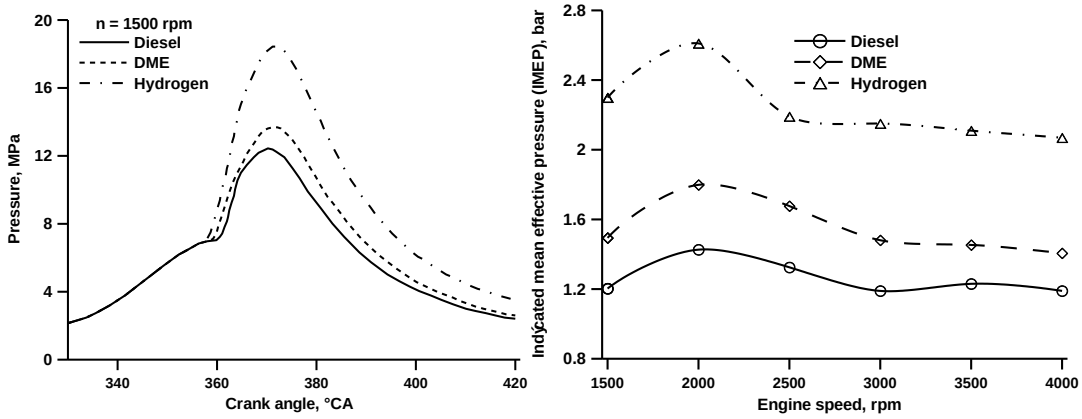

(a) (b

Figure 7. *Variation of a) pressure and b) IMEP for Diesel, DME and Hydrogen fuels [49]*

Fig. 7(a) compares the pressure for different fuels at 1500 rpm crank angle. Fig. 7(a) shows that hydrogen fuel combustion produces higher pressure and temperature within the cylinder in comparison to the other fuels. This higher temperature and pressure contributes to higher engine efficiency. Furthermore, Fig. 7(b) indicates that hydrogen fuel can create a higher IMEP (indicated mean effective pressure) compared to the other fuels. However, a decreasing trend of IMEP can be observed after 2000 rpm as the engine speed increases. At 4000 rpm, 46.8% and 18% IMEP increase of hydrogen to DME and DME to diesel application were obtained, respectively. The higher IMEP of hydrogen can be attributed to its higher latent enthalpy and chemical composition. Consequently, higher mean effective pressure results in shorter energizing time and prolonged premixed combustion duration [49].

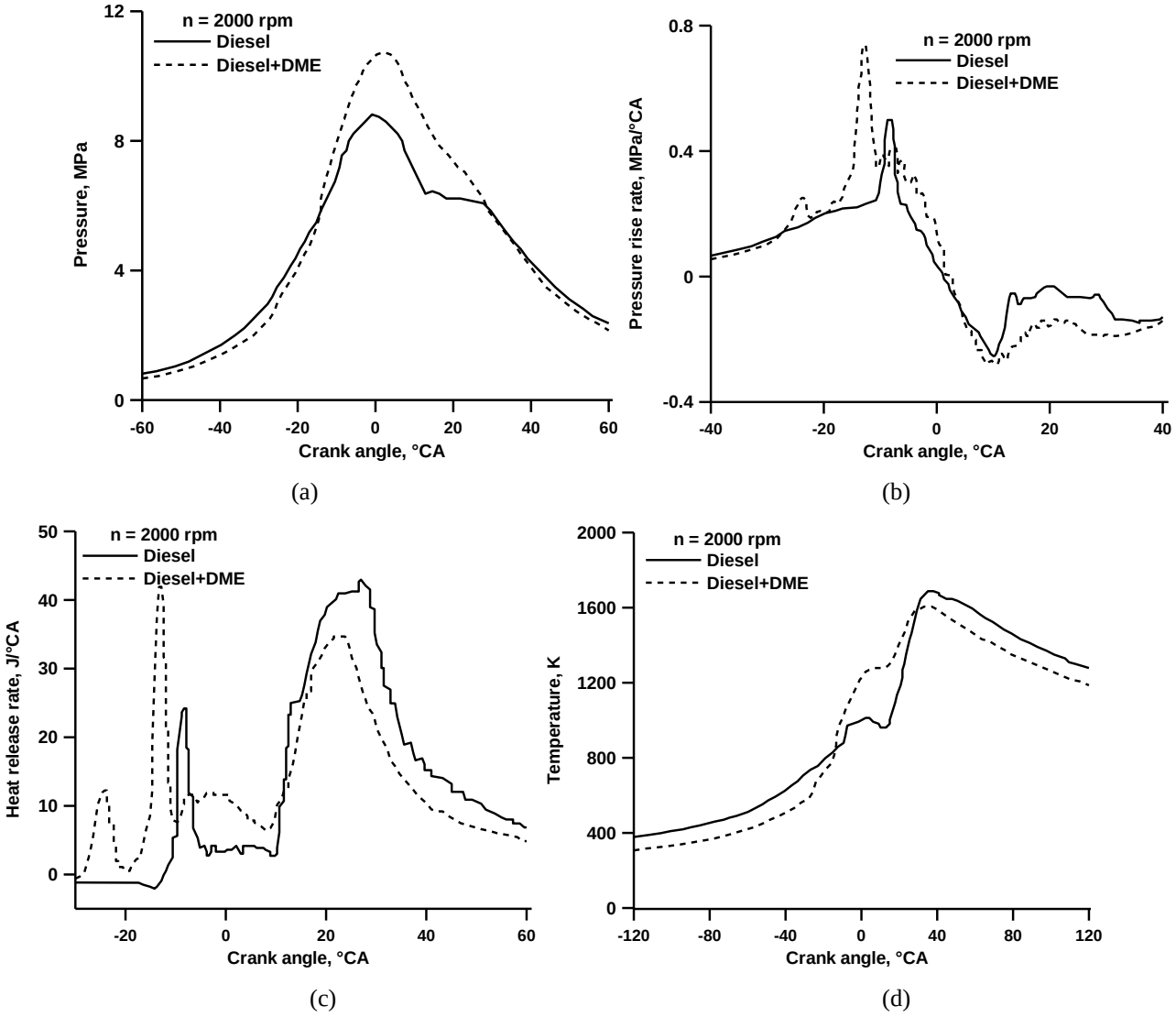

Figure 8. *Variation of a) pressure, b) pressure rise rate, c) heat release rate and d) temperature for Diesel and Diesel–DME blend [7]*

Fig. 8(a) shows that in premixed charge compression ignition (PCCI) composite combustion mode of Diesel–DME blend and direct injection (DI) combustion of diesel fuel, the maximum pressure is 10.7 MPa and the corresponding crank angle of 1.9° ATDC for Diesel–DME, which is higher than the peak pressure of 9.0 MPa for DI combustion at 0.6° ATDC. However, the maximum pressure appears slightly delayed due to DME forming a homogeneous mixture before entering the cylinder and its low ignition temperature causing early combustion at the end of the compression stroke. Fig. 8(b) illustrates the difference between Diesel–DME and diesel fuel pressure rise rate, where the peak pressure rise rate of Diesel–DME is 0.732 MPa/°CA and that of diesel fuel is 0.527 MPa/°CA, with the peak rate moving from 8.2° BTDC to 12.7° BTDC. It is therefore important to pay attention to the supply amount of DME when running the engine in the composite combustion mode. Otherwise, power performance and fuel economy will be adversely affected. Fig. 8(c) shows the variation of heat release rate between two combustion modes. It is seen that a great difference exists between the heat release rate of the composite combustion mode and the diesel DI combustion mode. The heat release in the composite combustion mode comprises three stages. The first stage involves low temperature combustion at compression pressures between 30° and 20° BTDC. The second stage, with the cylinder temperature increasing, involves the mixing and ignition of DME and pilot diesel injection, with the corresponding compression pressure being between 20° and 10° BTDC. This is mainly a short duration combustion process with a higher heat release peak. The third stage involves combustion after diesel injection. The heat released by the diesel DI combustion consists of two parts: the first part is released by the pilot injection of the first stage, the second part by the main injection. Fig. 8(d) illustrates that the cylinder

temperature in the composite combustion mode is lower than in the diesel DI mode before 15° BTDC. The cylinder temperature in the composite combustion mode is higher than that in the diesel DI mode between 15° BTDC and 30° ATDC. The cylinder temperature of the composite combustion mode is lower than that of the diesel DI mode after than around 30° ATDC. The maximum average cylinder temperature in both combustion modes occurs when the CA of 30° ATDC. The maximum temperature of the diesel DI mode is 1650 K, which is higher than 1600K of composite combustion mode [7].

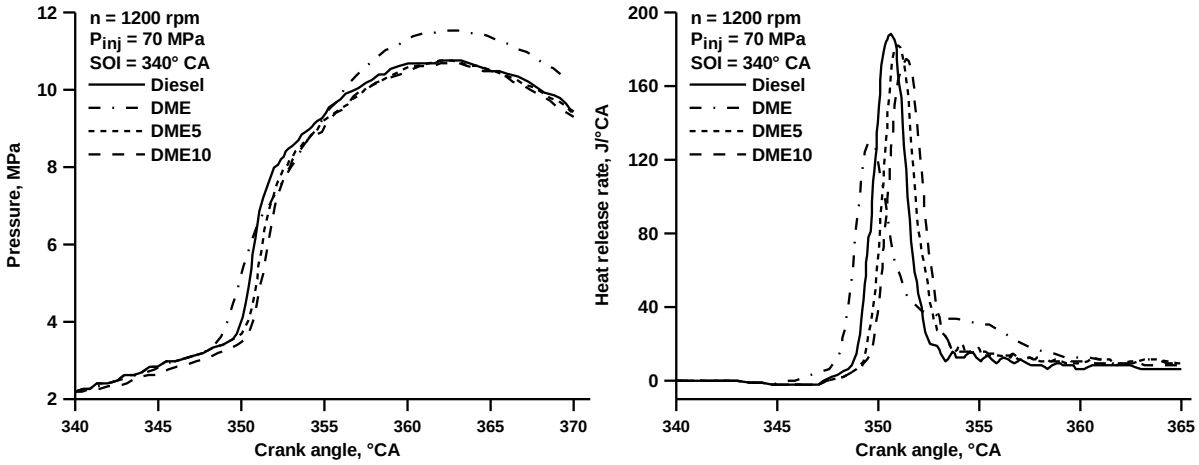

(a) (b)

Figure 9. *Variation of a) pressure and b) heat release rate for Diesel–DME blends [20]*

Fig. 9(a) and (b) show the cylinder pressure and heat release rate traces for diesel fuel, DME and diesel–DME blends at injection timing of 340° CA. It is seen that the peak pressure with DME was higher by 1 MPa than those of the diesel fuel and DME blends. This is attributed to the rapid vaporization, high cetane number and good mixing of DME. The peak cylinder pressures for the DME blends were similar to that for diesel fuel. In terms of the slope of the pressure curve, the diesel fuel had the steepest one, whereas the slope of the pressure curve for DME blends became smoother as the DME ratio increased. The ignition delay of DME is shorter than that of the diesel fuel due to fast vaporization as seen in heat release rate graph. However, ignition delay was longer than that of the diesel fuel when the DME blends were injected into the cylinder. This can be explained that the diesel fuel and air in the cylinder were inhibited by the earlier vaporization of the DME fuel. Additionally, the ascending order of the slope of the heat release rate was diesel fuel, DME5, DME10 and DME, with the heat release rate curve gradient for the diesel fuel being the steepest [20].

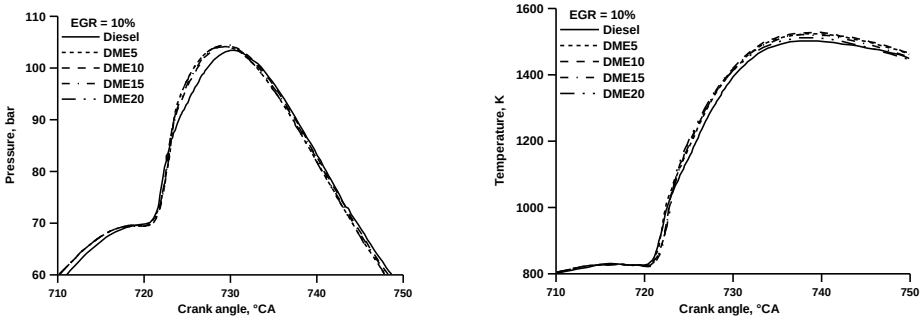

(a) (b)

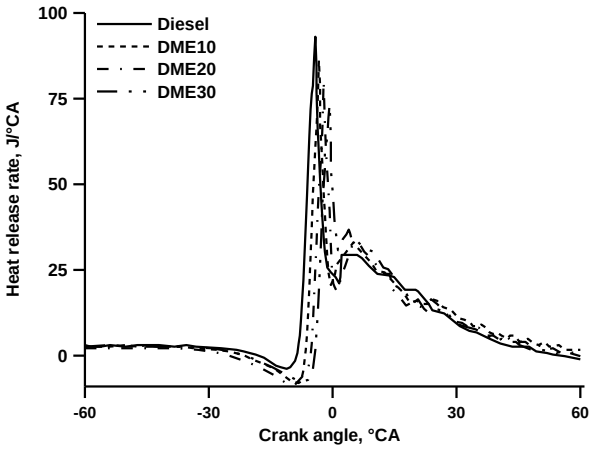

(c)

Figure 10. *Variation of a) pressure and b) temperature for Diesel and Diesel–DME blends [33] and c) heat release rate for Diesel and Diesel–DME blends [66]*

Fig. 10(a) depicts the impact of various diesel–DME blends on cylinder pressure, with peak pressure increasing as the ratio of DME in diesel blend increases due to a decrease in ignition delay. Fig 10(b) illustrates the effect of various diesel–DME blends on cylinder temperature, which is higher for higher DME blend ratio as DME is being combusted more efficiently [33]. Fig. 10(c) illustrates the heat release rate of four different fuels. It is observed that the amount of heat released during the premixed combustion stage when using diesel–DME blends is lower than that of diesel fuel. This decrease in heat release leads to a reduction in combustion pressure and temperature, consequently resulting in lower NOx emission. With an increase in DME content, there is a decrease in the amount of heat release during the premixed combustion stage due to the improved auto–ignition and atomization properties of DME in the diesel–DME blends, consequently improving engine combustion [66].

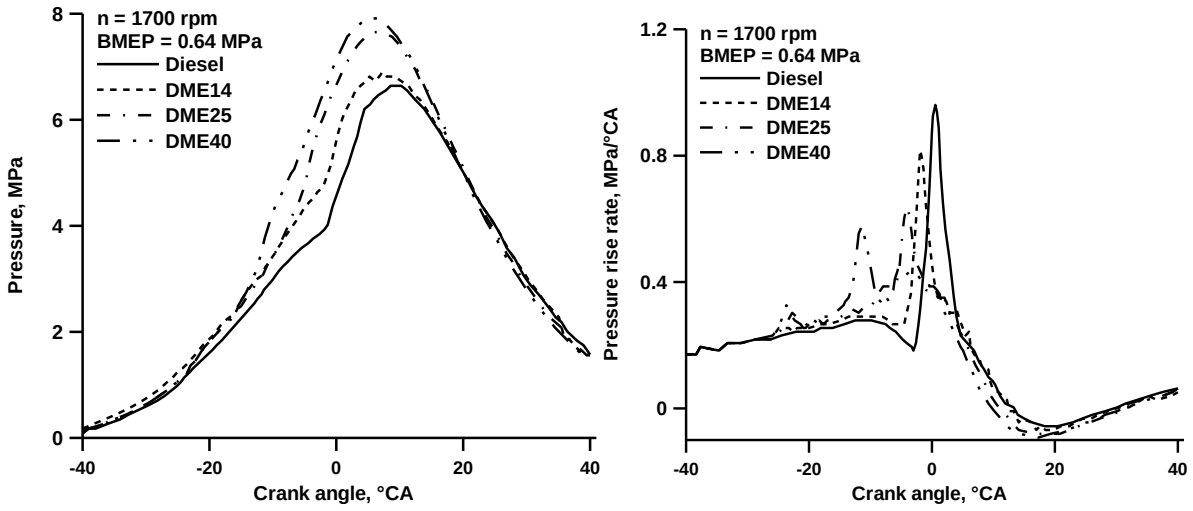

(a) (b)

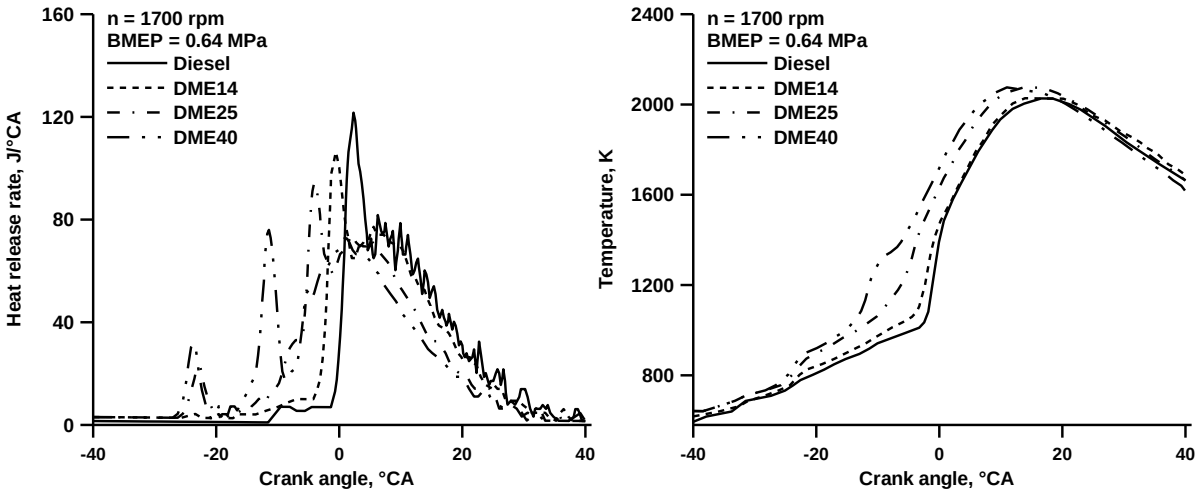

Figure 11. *Variation of a) pressure, b) pressure rise rate, c) heat release rate and d) temperature for Diesel and Diesel–DME blend [45]*

Fig. 11(a) shows based on analysis of measured indicator diagrams, the remarkable distinctions in values and positions of maximum pressure (pmax) under various port DME energy ratios. It is clear that, due to the DME's ability to auto–ignite easily when mixed with intake air, the ignition timing of DME is prior to that of diesel and the initial combustion occurs in a homogenous charge compression ignition (HCCI) process. This is seen in the cylinder pressure curves, which display an increased pressure peak as well as an advanced position of that peak when DME is fumigated in the intake air. For both port inspiration and in–cylinder injection DME, pmax increases with the amount of DME–premixed. Fig. 11(b) reveals the relationship between pressure rise rate and DME energy ratio. This curve displays the level of pressure oscillations as well as other combustion characteristics. For conventional direct injection compression ignition (DICI), only one peak is present in the rate of pressure rise curve. However, as DME–diesel dual fuel PCCI combustion occurs sequentially between HCCI and DICI, more peaks than one are visible in the rate of pressure rise curve. The first peak, during cool flame process, stays relatively constant in crank angle, but increases with the DME energy ratio. The peak moves to an earlier crank angle and decreases in value as more DME is added during the diffusive combustion process. The heat release curves of DME–diesel dual fuel PCCI combustion cases were complex, unlike typical DICI combustion. As shown in Fig. 11(c), the heat release process consisted of three stages: cool flame, HCCI combustion, and diffusive combustion. It was observed that the timing of the cool flame was almost consistent regardless of the DME energy ratio. Moreover, the negative temperature coefficient region shortened and the HCCI combustion was advanced as more DME was added. Simultaneously, maximum heat release rate of DME cool flame and high temperature reaction increased but maximum heat release rate of diesel diffusion decreased with increase in DME energy ratio. In Fig. 11(d), the in–cylinder temperatures were shown to be higher due to the DME HCCI combustion, as the DME energy ratio increased [45].

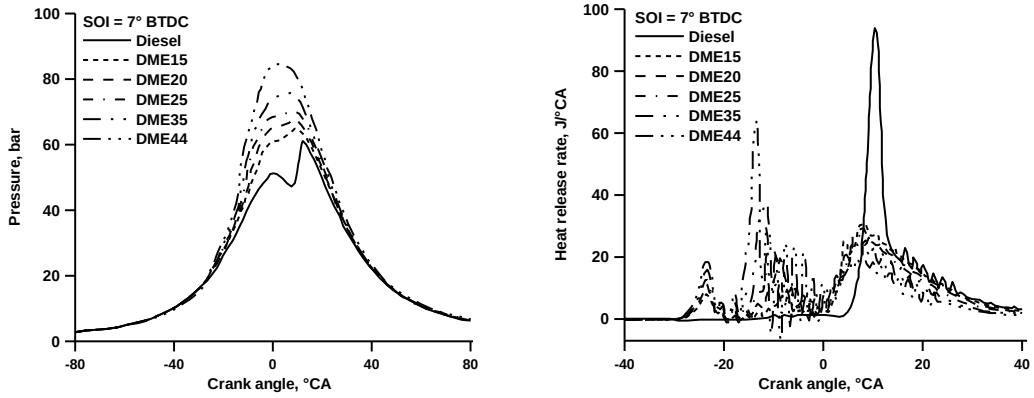

Figure 12. *Variation of a) pressure and b) heat release rate Diesel–DME blends [34]*

Fig. 12(a) shows the variation of cylinder pressure with the increasing of DME ratio. As DME is injected in the intake air, it undergoes a premixed combustion process, which leads to an earlier start of combustion, and an increased peak pressure, as evidenced by the pressure trace. This is further supported by the heat release rate in Fig. 12(b). Without DME addition, no heat release is observed until the mild premixed ignition at around 2° BTDC, while with DME addition, there is an early start of combustion at 32° BTDC, bringing with it low temperature heat release, which intensifies with increasing DME fumigation. A second stage of DME oxidation, starting between 22° BTDC and 5° BTDC and mostly in advance of the diesel fuel injection event at 7° BTDC, is also noted. At 15% DME ratio, the second stage of DME oxidation begins just as the diesel fuel injection starts at 7° BTDC, while at 20% DME ratio, it happens earlier at around 10° BTDC. This second stage oxidation further moves to earlier timing and increasing peak heat release rate with more DME added, which leads to a substantial increase in peak cylinder pressure of 33% at 44% DME ratio [34].

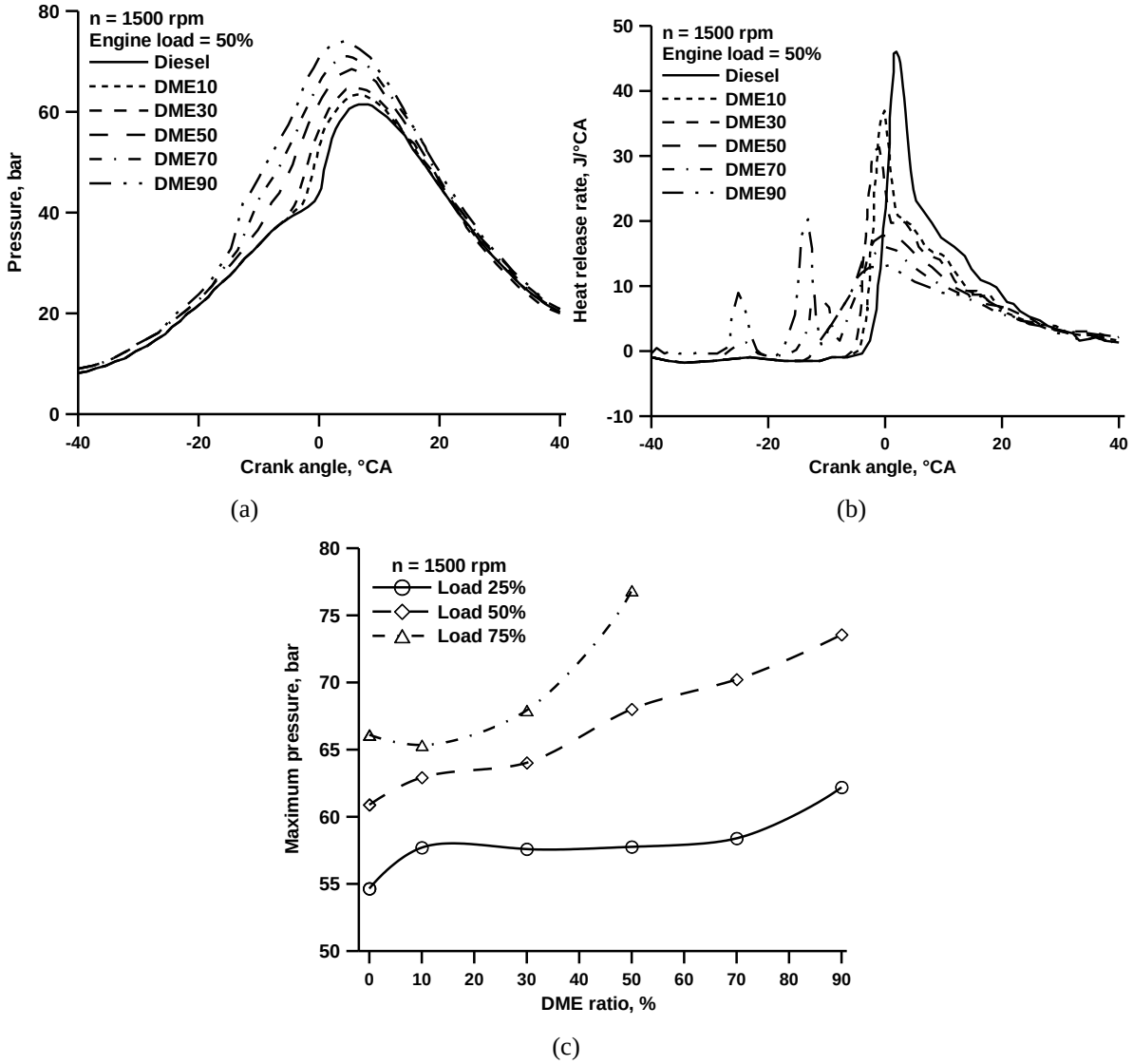

Figure 13. *Variation of a) pressure, b) heat release rate and c) maximum pressure for Diesel and Diesel–DME blends [52]*

The effect of PCCI with dual fuel (DME and diesel) on cylinder pressure and heat release rate characteristics are depicted in Fig. 13(a) and (b). The 100 consecutive engine cycles analysis, which included peak engine cylinder pressure and heat release rate, was conducted to analyze entire HCCI and diffusion combustion characteristics. In DME–diesel dual fuel mode of PCCI engine, two peak heat release rate curves were observed. The first peak pressure was due to the low–temperature combustion induced by DME injection. This HCCI combustion, which was characterized by high cetane number and auto–ignition temperature, was suitable for the application. The reaction occurred from 29° BTDC to 24°

BTDC, in which DME was combusted at the appropriate temperature. Higher DME concentration led to increased peak heat release rate in the low temperature combustion, without significant differences with the engine load. The second peak pressure was a result of diffusion combustion of diesel fuel. The second peak of heat release rate from diffusion combustion decreased with larger amount of DME pre–mixing ratio, due to the reduced diesel fuel concentration. The maximum peak pressure at 50% load was closely at top dead center (TDC), when the DME ratio was 90%. The ignition delay was reduced in comparison to neat diesel fuel, resulting in advanced peak pressure with any given engine speed and load. Fig. 13(c) illustrates that the maximum cylinder pressure varies depending on engine load and DME ratio. The high proportion of DME pre–mix increases the maximum peak pressure at all engine load conditions, as the pre–mix enhances combustion in the cylinder. At high load of 75% of maximum load however, it was found that the engine becomes unstable when using the high DME ratio (>50%) in port injection, due to the unmodified compression ratio; this can lead to engine knock. Thus, a low compression ratio is required for high DME ratio under high engine load conditions [52].

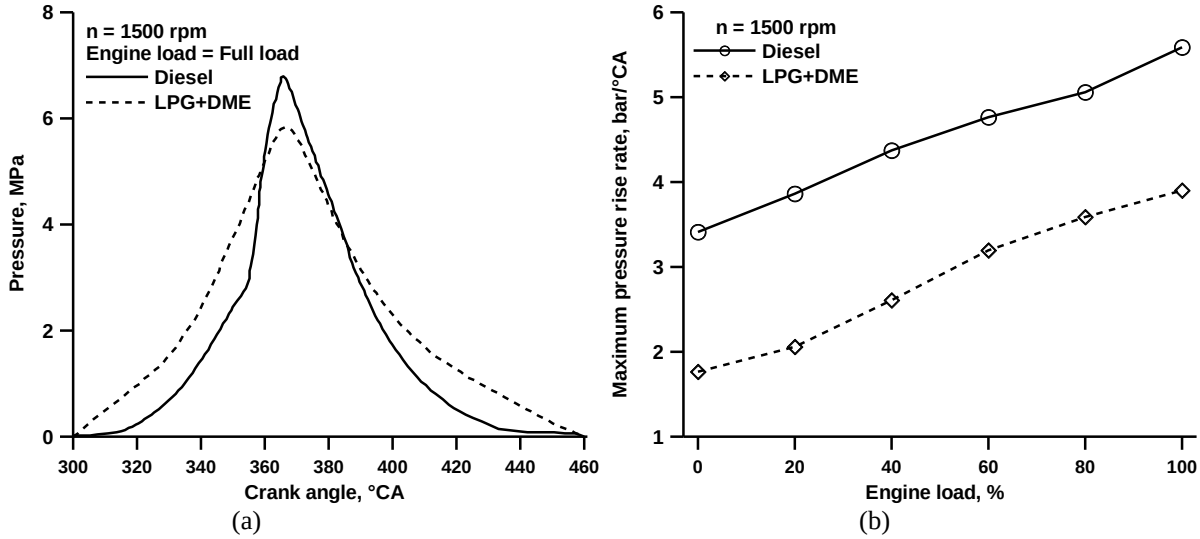

Figure 14. *Variation of a) pressure and b) rate of maximum pressure rise for Diesel and LPG–DME blend [24]*

The pressure crank–angle data for both diesel and LPG–DME operation at full load condition is depicted in Fig. 14(a). It is observed that diesel operation obtains a maximum cycle pressure of around 68 bar, while the maximum cycle pressure for LPG–DME operation is 44 bar. The reduced pressure in the LPG–DME fuel operation can be attributed to the decrease in heat release after TDC due to lower cylinder–gas temperature, which results in a decreased peak pressure. Fig. 14(b) shows the rate of maximum pressure rise for both diesel and LPG–DME operation. Diesel operation has a higher pressure rise rate compared to that of LPG with DME operation. This can be explained by the DME cooling of the intake charge and the consequently lower cylinder gas temperature, which leads to a lower pressure rise rate [24].

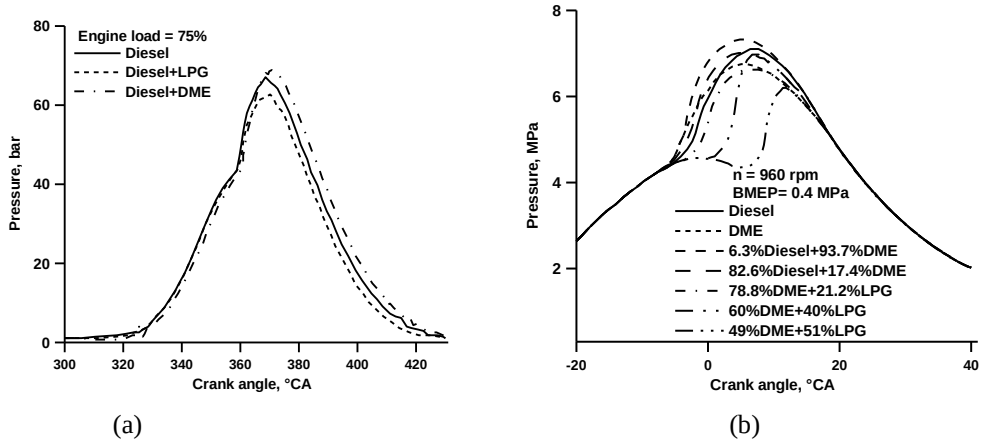

Figure 15. *Variation of pressure a) for Diesel, Diesel–LPG and LPG–DME blends [32] and b) for Diesel, Diesel–DME and DME–LPG blends [71]*

The cylinder pressure of diesel with DME and LPG without EGR, as reflected in Fig. 15(a), is positioned between diesel with DME and diesel with LPG due to the fuel physical and chemical properties such as density, viscosity, cetane number, boiling point and latent heat of vaporization, which can significantly affect combustion patterns. The lower boiling point and higher cetane number of DME can lead to improved combustion characteristics, such as advanced peak pressure of up to 2° CA compared to diesel. Fig. 15(b) reveals the improved performance of DME blended diesel and LPG engines in terms of pressure against crank angle. The pressure characteristics of diesel engine is observed to remain unaffected, even slightly improved, while combustion properties are seen to be considerably improved with increased concentration of DME blended with LPG [71].

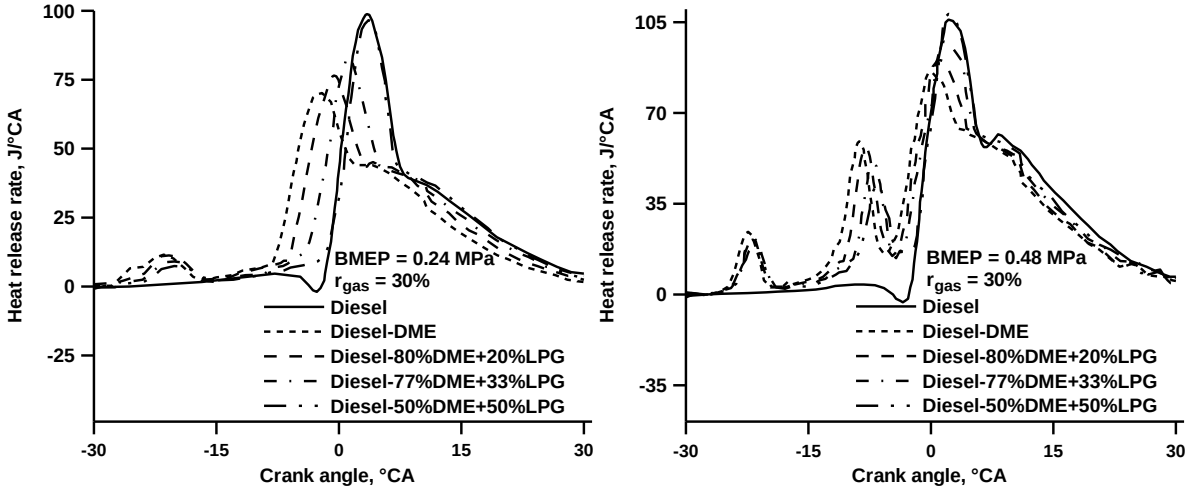

(a) (b)

Figure 16. *Variation of heat release rate for Diesel–DME+LPG blends at a) BMEP of 0.24 MPa and b) BMEP of 0. 48 MPa [81]*

Fig. 16(a) gives the heat release process for a dual–fuel PCCI combustion engine with varying ratios of LPG at BMEP of 0.24 MPa and a gas fuels (DME and LPG) energy ratio of 30%. It can be seen that the heat release process consists of DME low temperature reaction (LTR) and conventional diffusion–controlled CI combustion. The ignition timing of the DME LTR combustion remains essentially constant (around 24–25° BTDC) regardless of the amount of premixed charge, as seen in Fig. 18(a). This is due to the fact that the initial combustion temperature of DME LTR combustion is usually around 700–750 K, and the ignition timing is mainly determined by the cylinder temperature, with the rise of temperature mainly influenced by the compression of the charge; this causes the ignition timing of the DME LTR combustion to be relatively unaffected by the quantity of premixed charge. The maximum value of the heat release rate during the DME LTR process decreases slightly with an increase in LPG ratio, as the quantity of DME available for auto–ignition reduces. Meanwhile, it can be observed that the start of CI combustion is postponed with a higher LPG ratio, as the premixed LPG prevents DME from auto–ignition and part of the energy or radicals released from the DME cool–flame are used to ignite the LPG when its quantity increases. Additionally, the maximum value of the heat release rate increases slightly with the gas fuels ratio due to the higher lower heating value of LPG compared to DME. Fig. 16(b) shows the heat release process of the dual–fuel PCCI combustion engine with different LPG ratios at a BMEP of 0.48 MPa and a gas fuels energy ratio of 30%. It can be seen that with an increase in the amount of port fumigation DME, high temperature reaction (HTR) becomes more noticeable compared to that at a BMEP of 0.24 MPa and a gas fuels energy ratio of 30% and the heat release process of the dual–fuel combustion consists of LTR, HTR, and a conventional diffusion–controlled CI combustion. Similar to Fig. 18(a), the timing of LTR onset is nearly the same, and the maximum value of heat release rate during the DME LTR process slightly decreases with an increase in LPG ratio. Additionally, the onset of HTR is delayed, and the maximum value of heat release rate decreases slightly with a rise in LPG ratio due to the suppression of LPG addition on DME auto–ignition. The start of diffusion–controlled combustion is also delayed with a rise in LPG ratio, but the maximum value of heat release rate during this stage slightly increases due to the higher heating value of LPG [81].

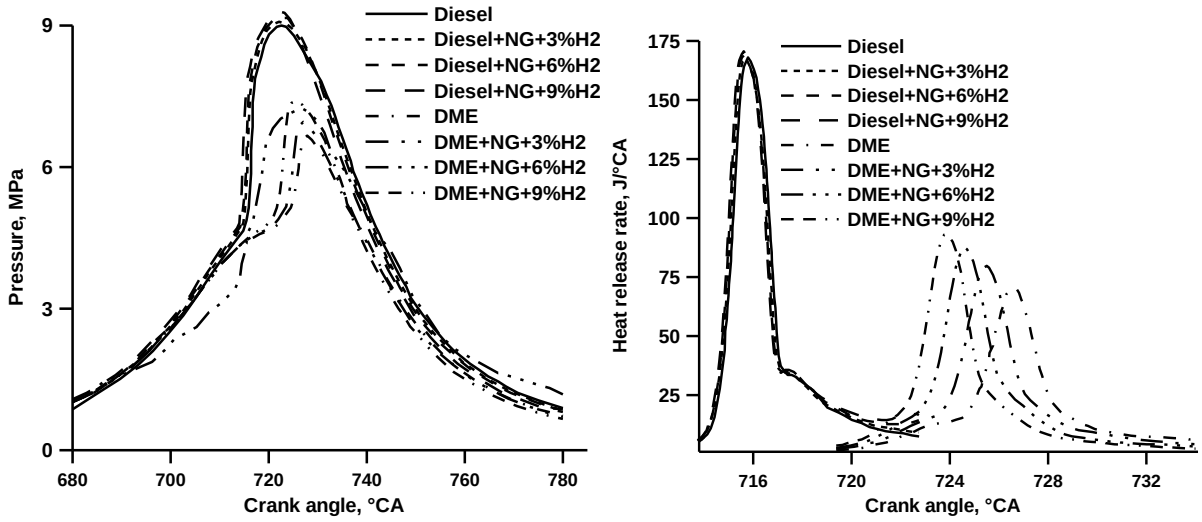

(a) (b)

Figure 17. *Variation of a) pressure and b) heat release rate for Diesel–NG–H2 and DME–NG–H2 blends [82]*

Fig. 17(a) displays the combustion pressure for the hydrogen (H2) addition to NG–Diesel and NG–DME cases, from which it is clear that the NG–DME mixture is more sensitive against the addition of hydrogen; the increases in pressure for the NG–DME and NG–Diesel cases being 11.1% and 2.8%, respectively. According to this study, the maximum temperature showed the advancement with the addition of hydrogen for both NG–DME and NG–Diesel mixtures. This advancement was also noted in the pressure of all cases, as seen in Fig. 19(a). The cylinder temperatures of diesel and DME cases displayed a different behavior against the addition of hydrogen as an enhancer additive. The addition of hydrogen was found to have a greater influence on the cylinder temperature in DME cases, however, all temperatures in diesel cases were observed to be higher than the same case in NG–DME fuel mixtures. These results are also represented in the heat release rate diagram in Fig. 19(b), where the addition of hydrogen resulted in advancement in the start of combustion (SOC). Fig. 17(b) shows the heat release rate for various hydrogen additions to the NG–Diesel and NG–DME fuels. It is evident from the figure that adding hydrogen has a different effect on the NG–DME fuel mixture in comparison to the NG–Diesel. As discussed, hydrogen addition is more effective on the NG–DME fuel mixture, which is also seen in the HRR diagrams. There are two different behaviors against the addition of hydrogen with respect to the maximum cumulative heat release (CHR). Hydrogen has a greater effect on the NG–DME fuel mixture, with the maximum CHR increasing by about 7.6% for a 9% addition to the fuel mixture. This process is different for the NG–Diesel mixture, with the trend of increasing maximum CHR decreasing as hydrogen is added. In each case, the CHR of NG–Diesel is higher than that of NG–DME, by 31%, 27%, 24%, and 22% respectively. These differences show the higher effect of hydrogen on the NG–DME fuel mixture, reducing the difference in combustion quality between NG–Diesel and NG–DME; the decrease in combustion quality with the use of DME is due to the in–cylinder behavior of DME, which breaks up into CH4, CO and H2 [82].

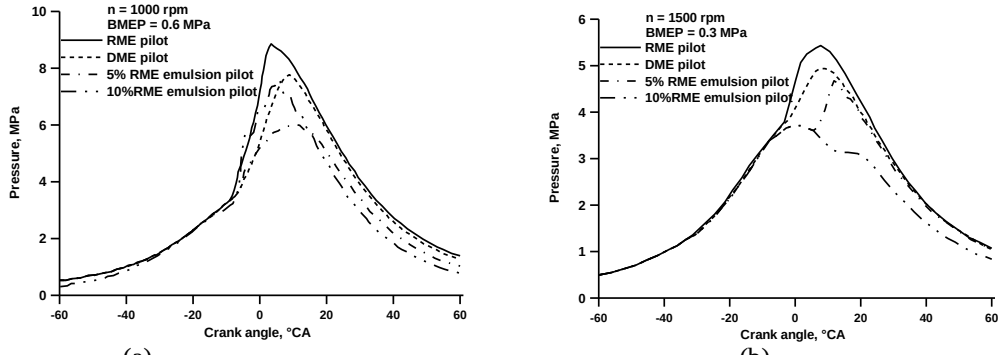

(a) (b)

Figure 18. *Variation of pressure at a) 1000 rpm and 0.6 MPa and b) 1500 rpm and 0.3 MPa conditions for various pilot injection fuels in dual fuel natural gas engine [39]*

Fig. 18(a) shows the variation of pressure for all tested pilot fuels at 1000 rpm and BMEP of 0.6 MPa. It is observed that the 10% emulsion pilot and DME pilot fuel have similar peak pressure levels, but the peak of the DME occurs about 3.5° CA later than that of the 10% emulsified pilot. It is probable that the slightly extended ignition delay and comparatively slower rate of combustion of the DME pilot fuel are responsible for this retardation. Meanwhile, both emulsion pilot fuels and DME pilot produce lower peak pressures than the rapeseed–oil methyl ester (RME) pilot. For the emulsion pilot fuels, this is likely due to the cooling effect caused by the water vaporizing in the pilot fuel mixture, while the low combustion enthalpy of DME can explain its lower peak value. It is also noted that the rate of pressure rise for the 10% emulsion is highest in comparison with the other pilot fuels. This can be attributed to the micro explosion phenomenon occurring on a larger scale than the 5% emulsion, resulting in a better distribution of fuel across the combustion chamber. This would enable ignition to take place in more areas, accelerating combustion. This could be because the 5% emulsion does not contain enough water suspended in the atomized droplets, which impedes the number and intensity of micro explosions. The ignition delay of RME was the shortest (2.3 ms, while ignition started at 10.7° BTDC), followed by the 10% emulsion pilot fuel (2.6 ms, with ignition starting at 8.9° BTDC), then the 5% emulsion pilot fuel (2.7 ms, with ignition starting at 8.3° BTDC), and finally the DME pilot fuel (2.8 ms, with ignition starting at 7.7° BTDC). The emulsification of RME extended the pilot fuel's ignition delay by roughly 10–15% in comparison to neat RME at this engine speed. This can be attributed to the DME's higher auto–ignition temperature and its evaporation during injection, which would cool the charge mixture. Furthermore, with increasing natural gas flow rate, the mass flow rate of the emulsion pilot fuels slightly increased while the mass flow rate of DME was consistently greater than the other liquid pilot fuels due to its comparatively lower combustion enthalpy. Fig. 18(b) shows the pressure crank angle data for all pilot fuels at 1500 rpm and a BMEP of 0.3 MPa. Neat RME has the highest peak pressure, followed by the DME pilot and then the 5% emulsified pilot fuel, with the 10% emulsified pilot fuel having the lowest peak pressure. At this speed and load condition, DME has a shorter ignition delay (2.3 ms, ignition starting at 3.8° ATDC) than the neat RME pilot (2.1 ms, starting at 5.6° ATDC). The 5% emulsified pilot fuel follows with an ignition delay of 3.3 ms (starting at 5.2° ATDC), and the 10% emulsified pilot fuel has the longest ignition delay at 3.8 ms (starting at 9.7° ATDC). It seems that the comparatively low combustion temperatures for dual–fuelling at this engine speed and load make it difficult for the micro explosion phenomenon to manifest. The higher concentration of water in the 10% emulsion appears to significantly impede combustion, which explains why the 5% and 10% emulsified pilot fuels reversed places compared to 1000 rpm. Different trends at 1000 and 1500 rpm may be attributed to the quality of emulsions. Before reaching the engine, the emulsions and neat RME were mixed in the emulsifying circuit and then entered a fuel measuring flask. As the engine consumed the fuel, it stayed undisturbed in the flask, downstream of which was a fuel line of about 60 cm in length, after which the emulsions went into the engine's fuel system. This fuel line contained water during operation, so there was a risk that the injected volume of emulsion did not contain the necessary amount of water. RME and DME pilots both account for about 40% of combustion enthalpy, whereas emulsions provide only about 34%. The higher mass flow rate of DME participating in combustion can explain its relatively short ignition delay at this engine speed. Furthermore, at the highest natural gas flow rate corresponding to this condition, the mass flow rate of the emulsified pilot fuels decreases slightly compared to lower load conditions. It is clear that the mass flow rate of DME is consistently higher than the liquid pilot fuels. At 1500 rpm, the amount of natural gas inducted per cycle is lower than at 1000 rpm. This is because the flow rate of natural gas is held constant for both engine speeds while entering the engine intake manifold. As a result, the reduced amount of natural gas coupled with the cooling effect of the emulsified pilot fuels leads to noticeably lower and significantly delayed peak pressures. Furthermore, the engine was stalling at high load in dual–fuel mode when using the emulsified pilot fuel. This was because the emulsion was separating in the fuel line. Due to these factors, the same load ranges visible at 1000 rpm couldn't be reproduced [39].

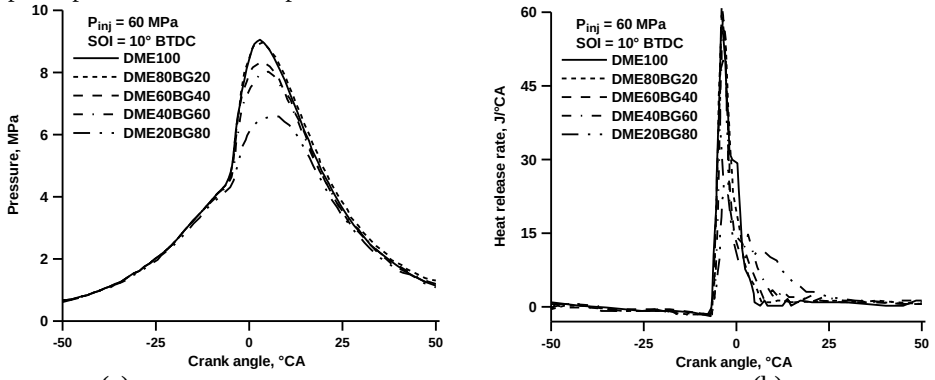

Figure 19. *Variation of a) pressure and b) heat release rate for DME–BG (biogas) blends [75]*

Fig. 19(a) and (b) shows the combustion pressure and heat release rate characteristics for different DME–biogas (BG) blends in DME–fueled diesel engines with common–rail injection systems, compared in the range of injection timing from 10° BTDC to 40° BTDC with an interval of 10° CA. It can be seen from Fig. 19(a) that the peak combustion pressure tended to decrease with increasing mixing ratio of biogas at the same injection timing. The test fuel with biogas ratio of 0.2 still had so much DME compared to pure DME combustion, so it showed a similar pressure trajectory with DME. However, higher mixing ratio conditions (biogas ratio of 0.8) showed different combustion behavior, especially at BTDC 40°, where misfire occurs. At the same injection timing, the increase in mixing ratio of biogas caused an increase in the coefficient of variation for the peak combustion pressure, retardation of ignition timing, and a decrease in the rate of combustion pressure increase. An advance in injection timing induced a visible trajectory of combustion pressure according to changes in the mixing ratio of biogas. The time difference to reach the same combustion pressure increased with an advance in the injection timing between DME and a higher mixing ratio fuel with a biogas ratio of 0.6, as shown in the pressure diagram of Fig. 19(a). For example, at an injection timing of 10° BTDC, 0.3 degree difference was observed between DME and biogas ratio of 0.6 test fuels to reach 6 MPa combustion pressure. Whereas, at 40° BTDC, 30° BTDC, and 20° BTDC, an increase to 7.5, 5.5, and 1.4 degrees was required, respectively. In this case, it is important to understand why the distribution of DME as an ignition source in the combustion chamber changed as the injection timing was advanced. When the injection timing was close to TDC, the injected DME spray was mainly distributed in the piston bowl. Thus, the injected DME mixed with the biogas that flowed into the combustion chamber through the intake port. In addition, this mixture of biogas and DME can react with the oxygen in the combustion chamber for ignition and combustion. However, when DME fuel is injected from 30° BTDC to 40° BTDC into crevice and squish regions, the ignition and combustion are less active due to low utilization of oxygen. On the other hand, when the biogas ratio is 0.8, composed of 80% intake biogas and 20% direct injection DME, the ignition and combustion characteristics are found to be unstable. Thus, it is determined that the biogas ratio of 0.8 is not suitable [75].

Fig. 20(a) and (b) compare cylinder pressure and heat release rate data for DME–NH3 blends. The injection timings are 10°, 20°, and 18° BTDC for 100%DME, 60%DME–40%NH3, and 40%DME–60%NH3, respectively. As shown in Fig. 22(a), the cylinder pressure history of 40%DME–60%NH3 is distinct from those of 100%DME and 60%DME–40%NH3. The pressure trace of 40%DME–60%NH3 is slightly higher during the compression process, and lower during the expansion process, despite the heat release rate indicating no combustion before TDC. 100%DME exhibits diesel combustion with its premixed combustion, mixing–controlled combustion, and late combustion phases identified in conventional compression ignition engines and its ignition delay is 4° CA. For 60%DME–40%NH3, a longer ignition delay of 19.5° CA is observed; causing a very significant premixed combustion and a late combustion phase is visible from the heat release rate data. With very early injection timing, 40%DME–60%NH3 has a homogeneous combustion phase with short combustion duration, like that seen in HCCI combustion. It is assumed that the early injection of 40%DME–60%NH3 causes complete evaporation of the fuel during the intake and compression process, causing the rise of pressure in the cylinder due to the increase of vapor pressure. This early injection also gives the fuel and air enough time to mix completely, resulting in homogeneous combustion. However, 100%DME and 60%DME–40%NH3 demonstrate typical diesel combustion and maintain higher cylinder pressure during the expansion process compared to 40%DME–60%NH3, due to its lower combustion temperature, which reduces the pressure in the expansion stroke. Fig. 20(c) shows the cumulative heat release fraction (i.e., mass burn fraction) corresponding to the conditions in Fig. 20(c). It can be seen that combustion of 100%DME steadily advances until 140° ATDC, indicating slow diffusion combustion during the later stage. On the other hand, 60%DME–40%NH3 has 90% heat release within 40° CA after ignition and continues to release heat through 70° ATDC, exhibiting greater premixed combustion phase and smaller mixing controlled combustion phase, similar to PCCI. Lastly, 40%DME–60%NH3 has extremely short combustion duration of 20° CA, which is attributed to the early fuel injection timing and indicates HCCI combustion [41].

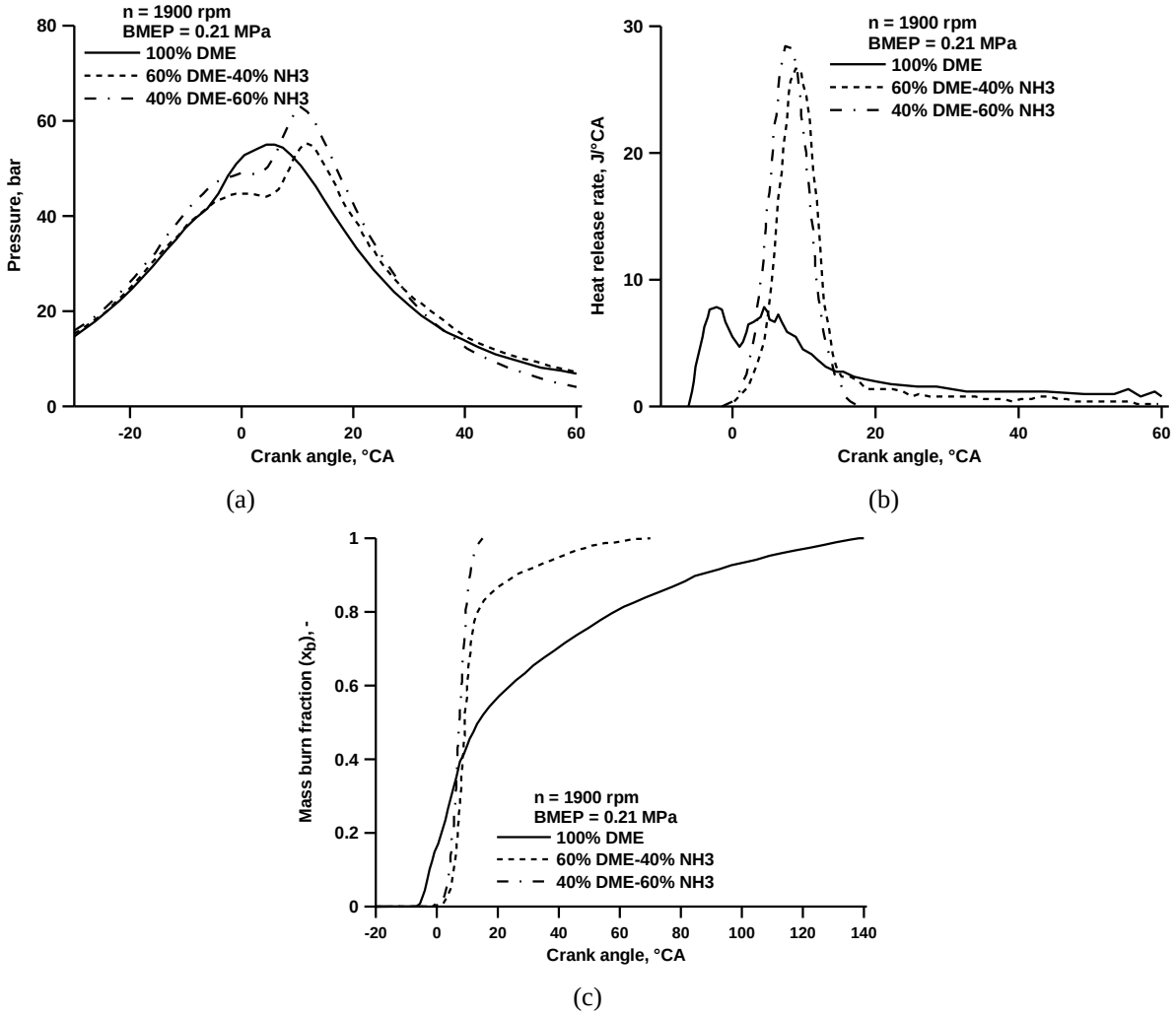

Figure 20. *Variation of a) pressure, b) heat release rate and c) mass burn fraction for DME–NH3 blends [41]*

Fig. 21 shows the combustion pressure and pressure rise rate at various crank angles for injection timing of 20° BTDC. As shown in Fig. 21(a), the motoring combustion pressure before injection timing of 20° BTDC decreases with increasing ethanol fraction. This decrease is due to heat absorption by ethanol evaporation. The polytrophic index calculated for the test conditions of 100% DME was about 1.26, whereas the DME–ethanol dual–fuel cases had lower values of 1.23–1.25. Generally, the polytrophic index for adiabatic compression of air is 1.4, and lower values are the result of heat loss to the cylinder walls or the heat absorbed by fuel vaporization. Hence, it is assumed that ethanol evaporation induced the lower motoring combustion pressure before injection. After injection, the ignition timing was retarded as the ethanol fraction increased; consequently, the ignition delay was prolonged. This increase in the ignition delay with increasing ethanol fraction caused an increase of the combustion pressure rising rate. Thus, the PRR increased with increasing ethanol fraction, as shown in Fig. 21(b) [61].

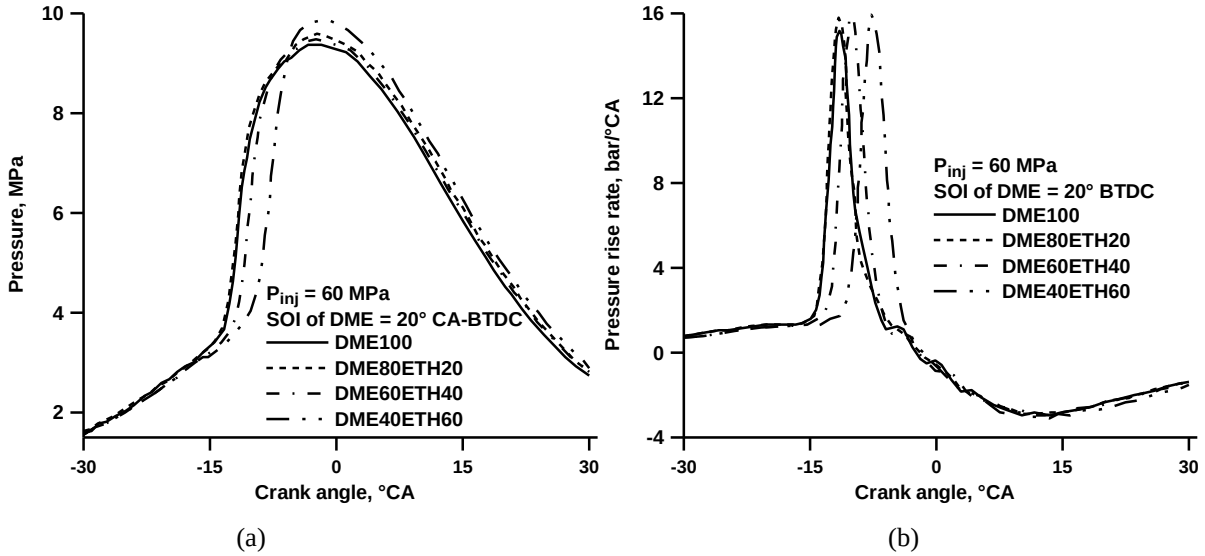

(a) (b)

Figure 21. *Variation of a) pressure and b) heat release rate for DME–ethanol (ETH) blends [61]*

Fig. 22 shows the cylinder pressure, heat release rate, cylinder temperatures, and pressure rise rate at 1.52 MPa brake mean effective pressure (BMEP). With the increase of DME proportion, the peak pressure decreases and its phase retards as seen in Fig. 22(a). The cylinder pressure peaks are 12.5 MPa at 14.5° ATDC, 11.7 MPa at 14.5° ATDC, 10.9 MPa at 16° ATDC, and 10.1 MPa at 1.5° BTDC. The cetane number of biodiesel is lower than DME, resulting in a longer ignition delay period and more fuel accumulation in the cylinder during this delay. Therefore, the maximum pressure of Biodiesel, DME50, DME70, and DME100 progressively decrease. It is clear that the combustion of DME–biodiesel blends shows the diffusion combustion mode without premixed combustion. The pressure rise rate decreases and its phase are retarded with the increasing DME proportion as seen in Fig. 24(b). The pressure rise rate reflects the combustion rate and heat release rate; thereby, a larger pressure rise rate implies a cruder engine operation. Accordingly, DME blending can ensure a more stable engine operation. The intake air temperature and pressure of a turbocharged engine are higher at full load, thus resulting in a shorter ignition delay [25].

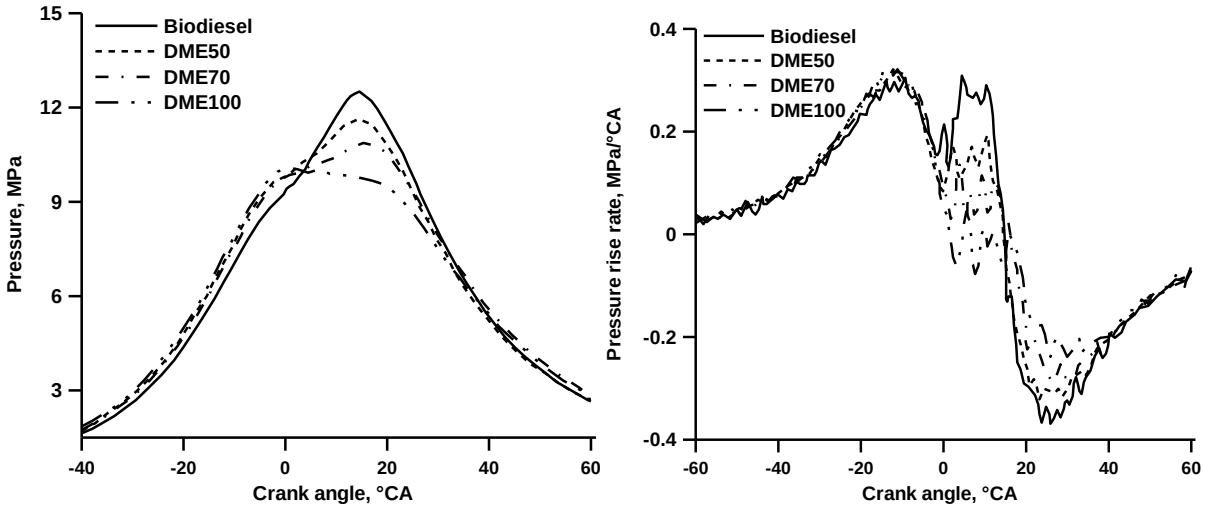

(a) (b)

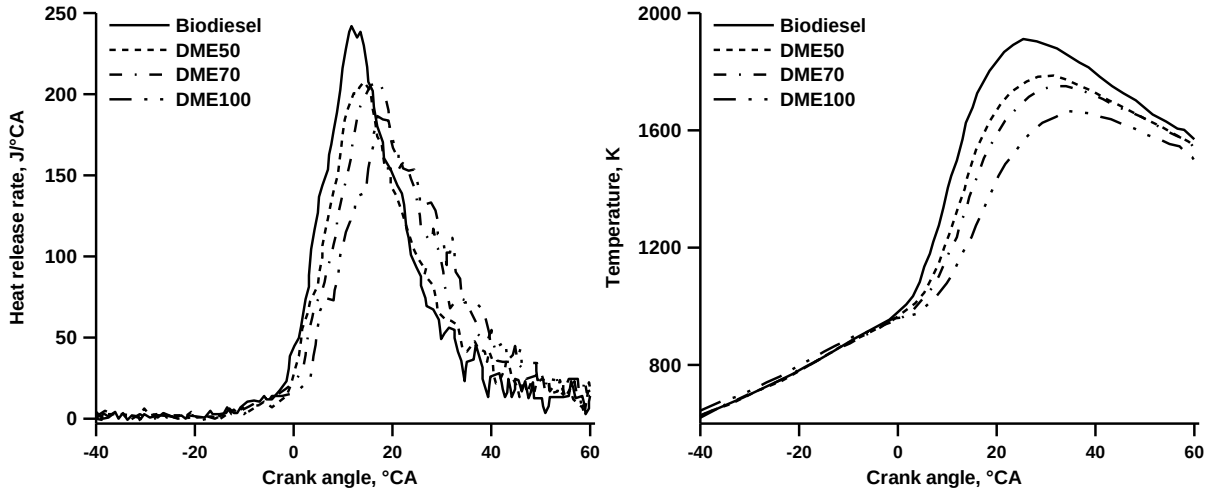

(c) (d)

Figure 22. *Variation of a) pressure, b) pressure rise rate, c) heat release rate and d) temperature for biodiesel–DME blends [65]*

As seen in Fig 22(c), the ignition timing retards, and the peak heat release rate decreases while its phase retards with the increase of the DME proportion. Specifically, the peak heat release rate of biodiesel, DME50, DME70, and DME100 are respectively 241.9 J/°CA at 11.5° ATDC, 210.7J/°CA at 12.5° ATDC, 208.8 J/°CA at 17° ATDC, and 186.9 J/°CA at 19° ATDC. Although the cetane number of DME is higher than that of biodiesel, its ignition delay is shorter due to its lower propagation velocity of fuel pressure wave in the pipe and longer fuel injection delay. Consequently, the peak heat release rate drops and its phase retards. With the increase of DME proportion, the peak cylinder temperature decreases and its phase is delayed as seen in Fig. 22(d). The peak cylinder temperature of biodiesel, DME50, DME70 and DME100 are 2097 K, 1954 K, 1914 K, and 1838 K, respectively, and the corresponding phases are 26° CA, 30.5° CA, 32.5° CA and 39.5° CA. The later ignition and combustion is attributed to the higher latent heat of vaporization of DME compared to biodiesel, which leads to more heat absorption during vaporization [65].

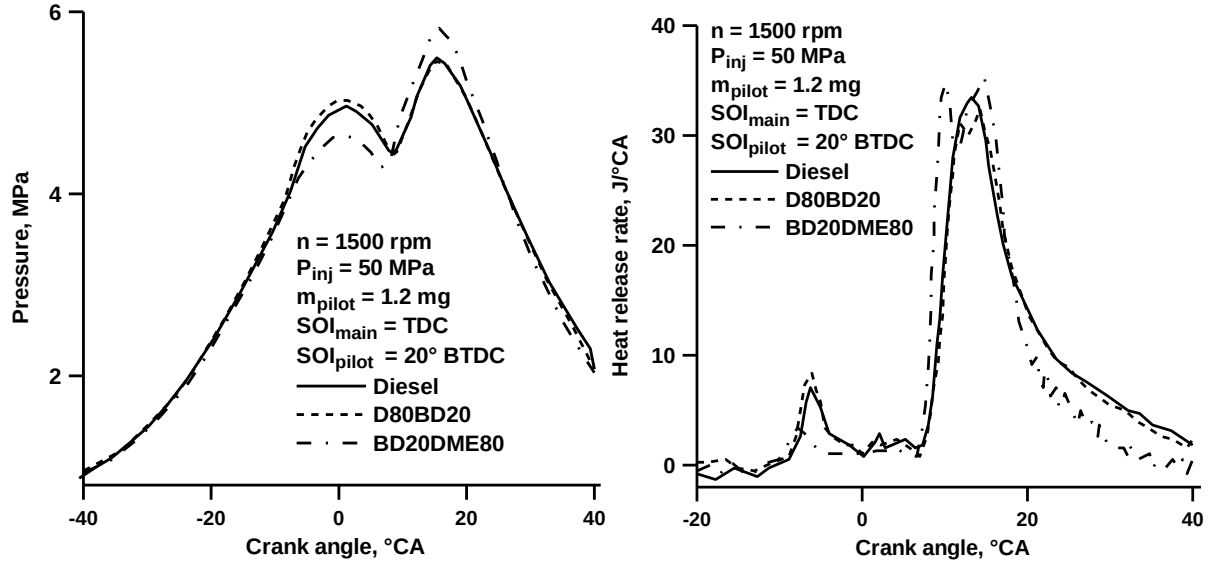

(a) (b)

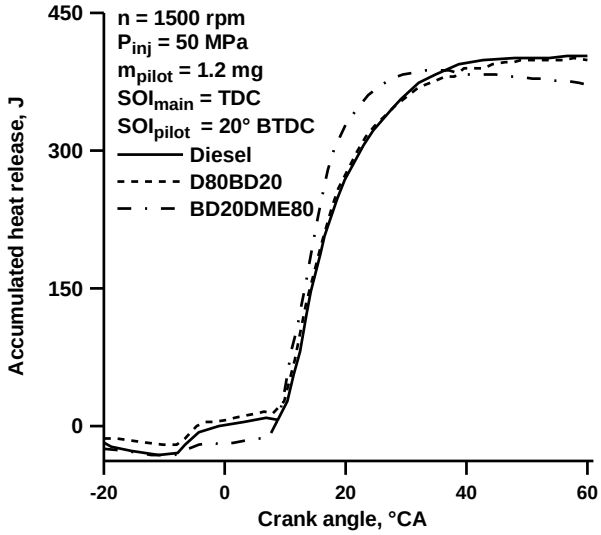

(c)

Figure 23. *Variation of a) pressure, b) heat release rate and c) accumulated heat release for diesel–biodiesel–DME blends [73]*

Fig. 23 shows the effect of *DME*–biodiesel blend (DME80BD20), diesel–biodiesel blend (D80BD20), and diesel (D), on the combustion pressure, heat release rate, and accumulated heat release in a CI engine at 1500 rpm with various pilot injection timings. The combustion characteristics were investigated with a fuel injection pressure of 50 MPa, pilot injection quantity of 1.2 mg, and a main injection timing of top dead center (TDC) [73]. As illustrated in Fig. 23(a), the DME–biodiesel blend (DME80BD20) had a higher peak pressure than that of the diesel–biodiesel blend (D80BD20) and conventional diesel fuel. This could be attributed to the lower bulk modulus of DME fuel than conventional diesel fuel at the same temperature in a closed system. Thus, the higher compressibility and low heating value of DME required higher energy input and fuel quantity than that of diesel fuel, resulting in a higher peak pressure at a constant engine load. The pressure rise near TDC is similar for diesel and D80BD20 fuels, while DME80BD20 blend exhibited lower values than that of the other fuels; primarily due to its low lower heating value (LHV). The LHV of DME80BD20 is 29.92 MJ/kg, and those of diesel and D80BD20 fuel are 42.5 MJ/kg and 41.83 MJ/kg, respectively. For the same injection quantity, a lower peak from the DME–biodiesel blend combustion was observed because of the relatively low LHV of DME. On the other hand, the heat release rate of DME80BD20 indicates that heat release in the pilot injection occurred at approximately 10° BTDC. The heat release of the main injection showed the advanced burning of DME80BD20 fuel when compared to diesel and D80BD20 fuel. Thus, the conventional diesel and diesel–biodiesel blend (D80BD20) resulted in higher pressure at the TDC region, while the DME80BD20 fuel exhibited lower pressure than D80BD20 [73].

6. Effects of dimethyl ether on air–fuel ratio

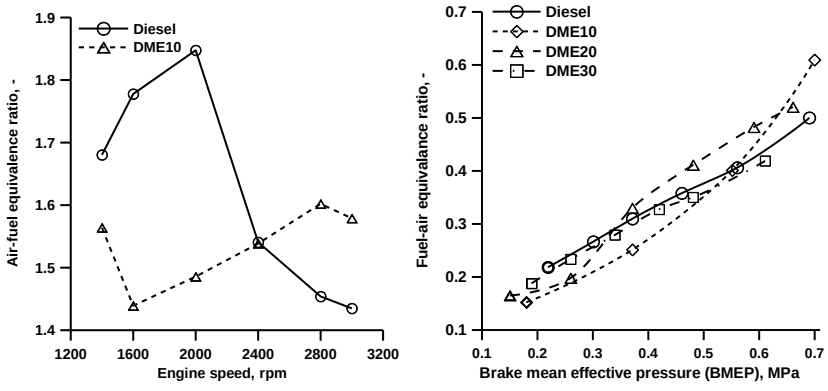

(a) (b)

Figure 24. *Variation of air–fuel equivalence ratio for DME blend a) [55] and b) [66]*

Fig. 24(a) compares the air–fuel equivalence ratio of diesel (D) and DME10 blend. It can be seen from the figure that the air–fuel ratio of DME10 blend is lower at low engine speed and higher at high engine speeds than diesel fuel. This is due to the higher amount of fuel delivery for higher output torque at low engine speeds and the lower amount of fuel injection by decreasing engine load at high engine speeds. As a result of this, the lower air–fuel ratio is obtained with DME10 blend at low engine speeds [55]. It is also seen from Fig. 24(b) the DME10 blend has lower fuel–air equivalence ratio than those of diesel fuel, DME20 and DME30blends, especially at low engine loads [66].

7. Effects of dimethyl ether on exhaust gas temperature

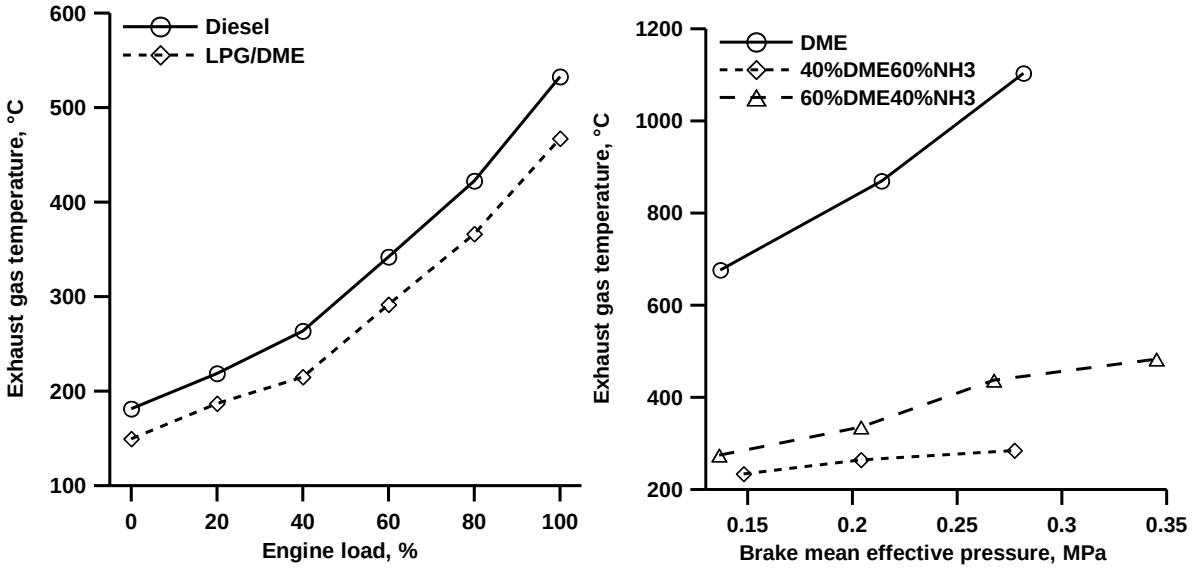

(a) (b)

Figure 25. *Variation of exhaust gas temperature for a) Diesel and LPG–DME blend [24] and b) DME and DME–NH_3 blends [41]*

Fig. 25(a) depicts the variation of exhaust gas temperature (EGT) under different engine loads. It can be seen from the Fig. 25(a) that EGT is found to be lower by about 40–50 °C in the case of LPG–DME operation throughout the load spectrum as compared to diesel operation. It is declared that the higher latent heat of vaporization of DME cools the intake charge, which reduces the peak temperature of the combustion in the engine cylinder and also EGT [24]. Fig. 25(b) shows the comparison of EGT versus brake mean effective pressure (BMEP). It is seen in the figure that EGT values for 100% DME are higher than those for both 60%DME–40%NH_3 and 40%DME–60%NH_3 blends. It is noted that EGT decreases as the ammonia (NH_3) concentration is increased in the blend. It is commended that the reduction in EGT is due to the loss in energy of the combustion process caused by the high latent heat of ammonia. It also stated that this is especially evident in case of 40%DME–60%NH_3 blend where the fuel charge has sufficient time to fully evaporate, drawing the full latent heat energy out of the in–cylinder air [41].

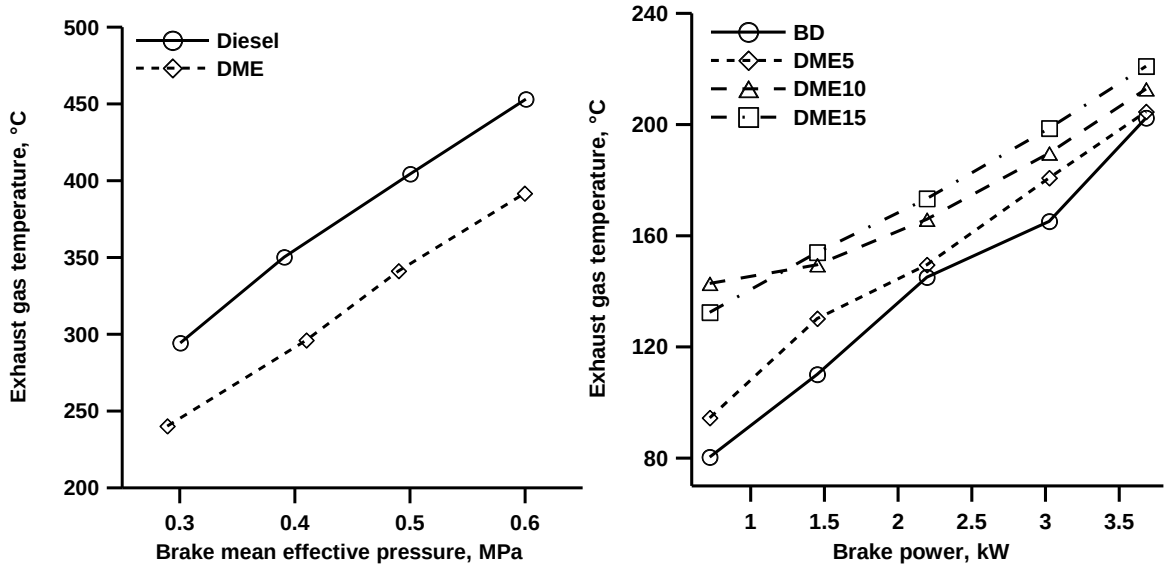

(a) (b)

Figure 26. *Variation of exhaust gas temperature for a) Diesel and DME [54] and b) Biodiesel and Biodiesel–DME blends [63]*

Fig. 26(a) shows a comparison of the EGT between DME and diesel fuel. The exhaust gas temperature is plotted against brake mean effective pressure (BMEP). It seen from the Fig. 26(a) that EGT is lower for DME by around 50 °C compared to diesel fuel. It is declared that the reason of this reduction in EGT is the lower energy content of DME [54]. Fig. 28(b) illustrates that EGT for the biodiesel (BD) and its blends with DME namely DME5, DME10 and DME15. It is seen from the Fig. 26(b), EGT are increased for all the fuels with the increase of engine load and DME blends give the higher EGT values than BD fuel. Additionally, EGT increases with the increase of DME ratio so DME15 blend gives higher EGT values than DME5 and DME10 blends at all engine loads. It is declared that increases in EGT when using of DME blends is sourced from the enhanced combustion due the higher oxygen content and the other fuel properties improved the combustion of DME. It is also stated that another reason for increase of EGT may be the shortened combustion period because of the higher flame velocity of DME [63].

8. Effects of dimethyl ether on CO_2 emissions

Fig. 27(a) illustrates the NOx and CO2 emissions for DME compared with diesel fuel from a six–cylinder turbocharged–intercooler heavy–duty diesel engine operating in the Japanese JE–05 test mode. It is seen from the figure that DME provides the significant reduction in CO2 emissions compared to diesel fuel. It is also declared the reduction in NOx and CO2 emissions that can be achieved with DME at a similar fuel economy. It is stated that CO2 emissions is about 10% less than that of diesel fuel when using DME due to based on the difference between the C/H ratio of fuels [56]. Fig. 27(b) gives the CO2 emissions characteristics when DME10 and DME20 blends are used. It is seen the figure that compared to diesel fuel there is obvious reduction in CO2 emissions for DME10 and DME20 blends at most BMEP values. It is declared that the possible reason of this reduction in CO2 emissions is the low C/H ratio and oxygen content of the DME blends [34].

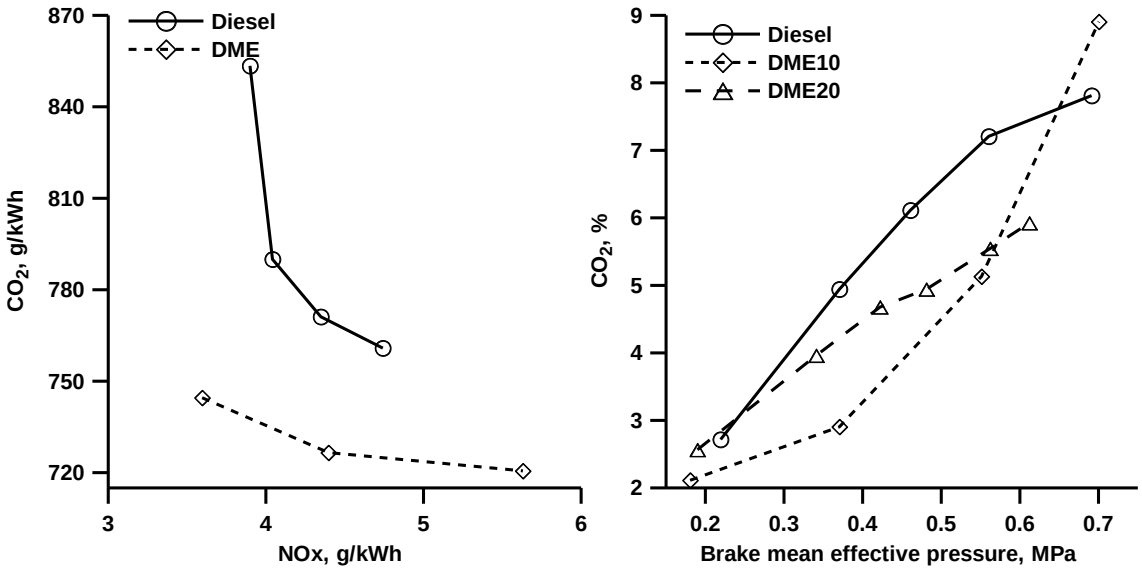

(a) (b)

Figure 27. *a) Variation of CO_2 emissions for a) Diesel and DME [56] and b) Diesel and Diesel–DME blends [34]*

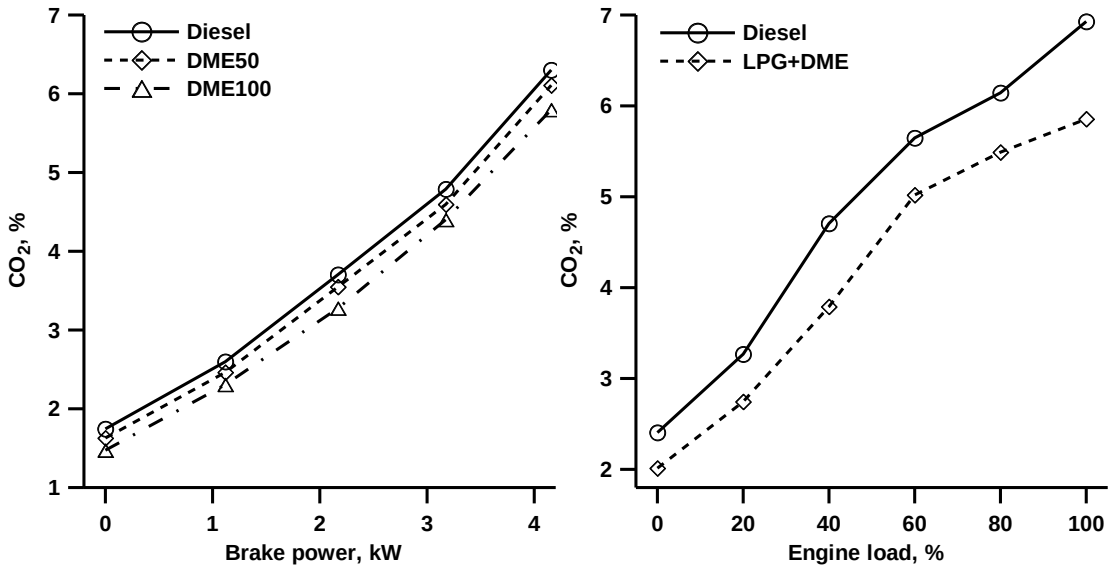

(a) (b)

Figure 28. *Variation of CO_2 emissions for a) Diesel and Diesel–DME blend [53] and b) Diesel and LPG–DME blend [24]*

It can be also observed from Fig. 28(a) that CO_2 emissions are lower for pure DME (DME100) and DME50 blend than diesel fuel because of the same reasons [53]. The variation of CO_2 emissions levels for diesel fuel and LPG–DME blend at different loads is shown in Fig. 28(b). It is seen from the figure that CO_2 emission level is lower for LPG–DME blend compared to diesel fuel. It is explained that the reduction in CO_2 emissions due to lower carbon to hydrogen ratio of DME compared to LPG [24].

Table 2. The variations in the results obtained with using of DME

Base Fuel–Blend	Reference	Air–Fuel Ratio	EGT	CO_2 Emissions
		Variation (%)		
D–LPG+DMEX	[24]	–	↓12–18.3	↓10.6–19.4
D–DME10	[34]	–	–	↓41.6–↑14.1
D–DME20	[34]	–	–	↓5.8–31.8
DME–40DME60NH3	[41]	–	↓60.2–61.8	–
DME–60DME40NH3	[41]	–	↓65.6–69.8	–
D–DME50	[53]	–	–	↓3–7.7
D–DME100	[53]	–	–	↓8.5–18.3
D–DME100	[54]	–	↓13.6–18.6	–
D–DME10	[55]	↓19.6–↑10.2	–	–
D–DME100	[56]	–	–	↓5.2–5.7
BD–DME5	[63]	–	↑1.7–17.3	–
BD–DME10	[63]	–	↑4.9–70.8	–
BD–DME15	[63]	–	↑9–59	–
D–DME10	[66]	↓30.2–↑21.8	–	–
D–DME20	[66]	↓25.7–↑18.7	–	–
D–DME30	[66]	↓8.5–16.2	–	–

9. Conclusions

The effects the use of dimethyl ether on CO_2 emissions in diesel engines are examined in this review study. The following conclusions can be summarized as obtained findings of the study.

- The use of dimethyl ether significantly affected the combustion characteristics such as pressure, temperature and heat release in diesel engines. The use of pure dimethyl ether caused to decreases in the combustion characteristics at the same amount of fuel input, while the combustion characteristics were improved with increased dimethyl ether fuel at the same amount of energy input compared diesel fuel. The use of dimethyl ether together with the liquid fuels such as diesel, biodiesel and ethanol generally improved the combustion characteristics, while the combustion characteristics can be adversely affected when the use of dimethyl ether together with the gaseous fuels such as LPG, natural gas, biogas and hydrogen. However, the negative changes in combustion characteristics are quite low and do not prevent the use of dimethyl ether.
- Air–fuel equivalence ratio decreases when using the diesel–DME blend, especially at low engine speeds, providing high engine torque, because of the lower stoichiometric air–fuel ratio of DME. However, air–fuel equivalence ratio increases when using the diesel–DME blend at high engine speeds and loads because of the increased fuel injection. The decrement in air–fuel equivalence ratio for DME10 blend is about 30.2%, while the increment is about 21.8%.
- Exhaust gas temperature decreases when using the pure DME and its blends with diesel, LPG and NH_3 fuels due to lower heating value of DME, while DME and its blends with biodiesel gives the higher exhaust gas temperature than biodiesel due to enhanced combustion. The decrements in exhaust gas temperature for pure DME, diesel–DME blends, LPG–DME blend and DME–NH_3 blends are about 13.6–18.6%, 12–18.3% and 60.2–69.8%, respectively, while the increments for biodiesel–DME blends are about 1.7–59%.
- CO_2 emissions decrease when using the pure DME and DME blends with diesel and LPG fuels due to the oxygen

content and the lower carbon to hydrogen ratio of DME. The decrements in CO_2 emissions for pure DME, diesel–DME blends and LPG–DME blend are about 5.2–18.3%, 3–41.6% and 10.6–16.4%, respectively.

References

[1]. Yoon SH, Cha JP Lee CS. An investigation of the effects of spray angle and injection strategy on dimethyl ether (DME) combustion and exhaust emission characteristics in a common–rail diesel engine. Fuel Processing Technology 2010; 91: 1364–1372.

[2]. Youn IM, Park SH, Roh HG, Lee CS. Investigation on the fuel spray and emission reduction characteristics for dimethyl ether (DME) fueled multi–cylinder diesel engine with common–rail injection system. Fuel Processing Technology 2011; 92: 1280–1287.

[3]. Alam M, Kajitani S. DME as an alternative fuel for direct injection diesel engine. 4th International Conference on Mechanical Engineering 2001; 87–92.

[4]. Maji S, Ahmed S, Siddiqui WA, Kumar A. Impact of di–methyl ether (DME) as an additive fuel for compression ignition engine in reduction of urban air pollution. International Journal of Innovative Research in Science, Engineering and Technology 2014; 3(11): 17221–17228.

[5]. Park SH, Lee CS. Applicability of dimethyl ether (DME) in a compression ignition engine as an alternative fuel. Energy Conversion and Management 2014; 86: 848–863.

[6]. Wattanavichien K. Implementation of DME in a small direct injection diesel engine. International Journal of Renewable Energy 2009; 4(2): 1–12.

[7]. Duan J, Sun Y, Yang Z, Sun Z. Combustion and emissions characteristics of diesel engine operating on composite combustion mode of DME and diesel. Proceedings of International Conference on Mechanical Engineering and Material Science 2012; 27: 463–466.

[8]. Kowalewicz A, Wojtyniak M. Alternative fuels and their application to combustion engines. Journal of Automobile Engineering 2005; 219: 103–125.

[9]. Azizi Z, Rezaeimanesh M, Tohidian T, Rahimpour MR. Dimethyl ether: A review of technologies and production challenges. Chemical Engineering and Processing 2014; 82: 150–172.

[10]. Huang Z, Qiao X, Zhang W, Wu J, Zhang J. Dimethyl ether as alternative fuel for CI engine and vehicle. Frontiers of Energy and Power Engineering in China 2009; 3(1): 99–108.

[11]. Lecksiwilai N, Gheewala SH, Sagisaka M, Yamaguchi K. Net energy ratio and life cycle greenhouse gases (GHG) assessment of bio–dimethyl ether (DME) produced from various agricultural residues in Thailand. Journal of Cleaner Production 2016; 134: 523–531.

[12]. Inayat A, Ghenai C, Naqvi M, Ammar M, Ayoub M, Hussin MNB. Parametric study for production of dimethyl ether (DME) as a fuel from palm wastes. Energy Procedia 2017; 105: 1242–1249.

[13]. Park SH, Lee CS. Combustion performance and emission reduction characteristics of automotive DME engine system," Progress in Energy and Combustion Science 2013; 39: 147–168.

[14]. Teng H, McCandless JC, Jeffrey BS. Thermochemical characteristics of dimethyl ether alternative fuel for compression–ignition. Society of Automotive Engineers 2001; Paper no 2001–01–0154.

[15]. Maji S, Ahmed S, Siddiqui WA, Aggarwal S, Kumar A. Impact of di–methyl ether (DME) as an additive fuel for compression ignition engine in reduction of urban air pollution. American Journal of Environmental Protection 2015; 3(2): 48–52.

[16]. Guangxin G, Zhulin Y, Apeng Z, Shenghua L, Yanju W. Effects of fuel temperature on injection process and combustion of dimethyl ether engine. Journal of Energy Resources Technology 2013; 135: 1–5.

[17]. Jalanapurkar M, Patel K, Patel T, Rathod G, Granipa H. A literature review on combine effect of di–methyl ether (DME) as an additive & the injection pressure on the performance & emission of 4 stroke C.I engine. International Journal of Advance Engineering and Research Development 2015; 2(1): 262–266.

[18]. Kim HJ, Park SH, Lee KS, Lee CS. A study of spray strategies on improvement of engine performance and emissions reduction characteristics in a DME fueled diesel engine. Energy 2011; 36: 1802–1813.

[19]. Xu S, Wang Y, Zhang X, Zhen X, Tao C. Development of a novel common–rail type dimethyl ether (DME) injector. Applied Energy 2012; 94: 1–12.

[20]. Lim OT, Iida N. A study on the spray and engine combustion characteristics of diesel–dimethyl ether fuel blends. Journal of Automobile Engineering 2015; 229(6): 782–792.

[21]. Suh HK, Lee CS. Experimental and analytical study on the spray characteristics of dimethyl ether (DME) and diesel fuels within a common–rail injection system in a diesel engine. Fuel 2008; 87: 925–932.

[22]. Genbao L, Jianming C, Minglong L, Yuhua Q, Zhaoyang C. Experimental study on the size distribution

characteristics of spray droplets of DME/diesel blended fuels. Fuel Processing Technology 2012; 104: 352–355.

[23]. Mohan B, Yang W, Yu W, Tay KL. Numerical analysis of spray characteristics of dimethyl ether and diethyl ether fuel. Applied Energy 2017; 185: 1403–1410.

[24]. El–Hagar MME–G. Effect of diethyl ether and dimethyl ether with liquefied petroleum gas on combustion and emissions characteristics of diesel engine. International Journal of Computer Science and Engineering 2014; 2(3): 193–198.

[25]. Wang Y, Xiao F, Zhao Y, Li D, Lei X. Study on cycle–by–cycle variations in a diesel engine with dimethyl ether as port premixing fuel. Applied Energy 2015; 143: 58–70.

[26]. Jeon J, Kwon S, Park YH, Oh Y, Park S. Visualizations of combustion and fuel/air mixture formation processes in a single cylinder engine fueled with DME. Applied Energy 2014; 113: 294–301.

[27]. Baskaran R. Analysis on synthesis, storage & combustion characteristics of DME as fuel in CI engines. International Journal for Research in Applied Science & Engineering Technology 2015; 3(1): 133–140.

[28]. Park S. Optimization of combustion chamber geometry and engine operating conditions for compression ignition engines fueled with dimethyl ether. Fuel 2012; 97: 61–71.

[29]. Benajes J, Novella R, Pastor JM, Hernández–López A, Kokjohn SL. Computational optimization of the combustion system of a heavy duty direct injection diesel engine operating with dimethyl–ether. Fuel 2018; 218: 127–139.

[30]. Oda Y, Osafune Y, Ueda H, Fujimura K. Clean combustion technology in diesel engines operated with dimethyl ether. Mitsubishi Heavy Industries Ltd. Technical Review 2004; 40(6): 1–5.

[31]. Song J, Huang Z, Qiao X, Wang W. Performance of a controllable premixed combustion engine fueled with dimethyl ether. Energy Conversion and Management 2004; 45: 2223–2232.

[32]. Khunaphan S, Hartley UW, Theinnoi K. Characterization and potential of dimethyl ether (DME) as dual fuel combustion in a compression ignition engine. International Journal of Engineering Science and Innovative Technology 2013; 2(3): 79–85.

[33]. Lamani VT, Yadav AK, Narayanappa KG. Influence of low–temperature combustion and dimethyl ether–diesel blends on performance, combustion, and emission characteristics of common rail diesel engine: a CFD study. Environmental Science and Pollution Research 2017; 24: 15500–15509.

[34]. Chapman EM, Boehman AL. Pilot ignited premixed combustion of dimethyl ether in a turbodiesel engine. Fuel Processing Technology 2008; 89: 1262–1271.

[35]. Ying W, Longbao Z, Zhongji Y, Hongyi D. Study on combustion and emission characteristics of a vehicle engine fuelled dimethyl ether. Journal of Automotive Engineering 2005; 219: 263–269.

[36]. Benajes J, Novella R, Pastor JM, Hernández–López A, Kokjohn S. Computational optimization of a combustion system for a stoichiometric DME fueled compression ignition engine. Fuel 2018; 223: 20–31.

[37]. Kropiwnicki J, Dominiczak P, Kneba Z. Analysis of the possibilities of using of DME fuel in motor boat drive systems. Combustion Engines 2017; 171(4): 74–80.

[38]. Smolec R, Idzior M, Karpiuk W, Kozak M. Assessment of the potential of dimethyl ether as an alternative fuel for compression ignition engines. Combustion Engines 2017; 169(2): 181–186.

[39]. Namasivayam AM, Korakianitis T, Crookes RJ, Bob–Manuel KDH, Olsen J. Biodiesel, emulsified biodiesel and dimethyl ether as pilot fuels for natural gas fuelled engines. Applied Energy 2010; 87: 769–778.

[40]. Jang J, Bae C. Effects of valve events on the engine efficiency in a homogeneous charge compression ignition engine fueled by dimethyl ether. Fuel 2009; 88: 1228–1234.

[41]. Ryu K, Zacharakis–Jutz GE, Kong S–C. Performance characteristics of compression– ignition engine using high concentration of ammonia mixed with dimethyl ether. Applied Energy 2014; 113: 488–499.

[42]. Semelsberger TA, Borup RL, Grene HL. Dimethyl ether (DME) as an alternative fuel. Journal of Power Sources 2006; 156: 497–511.

[43]. Li G. Dimethyl ether (DME): a new alternative fuel for diesel vehicle. Advanced Materials Research 2011; 156–157: 1014–1018.

[44]. Sezer I. Thermodynamic, performance and emission investigation of a diesel engine running on dimethyl ether and diethyl ether. International Journal of Thermal Sciences 2011; 50: 1594–1603.

[45]. Wang Y, Zhao Y, Yang Z. Dimethyl ether energy ratio effects in a dimethyl ether–diesel dual fuel premixed charge compression ignition engine. Applied Thermal Engineering 2013; 54: 481–487.

[46]. Ying W, Li H, Longbao Z, Wei L. Effects of DME pilot quantity on the performance of a DME PCCI–DI engine.

Energy Conversion and Management 2010; 51: 648–654.

[47]. Chen Z, Konno M, Kajitani S. Performance and emissions of DI compression ignition engines fueled with dimethyl ether. JSME International Journal 2000; 43(1): 82–88.

[48]. Arcoumanis C, Bae C, Crookes R, Kinoshita E. The potential of di–methyl ether (DME) as an alternative fuel for compression–ignition engines: A review. Fuel 2008; 87(7): 1014–1030.

[49]. Taghavifar H, Khalilarya S, Mirhasani S, Jafarmadar S. Numerical energetic and exergetic analysis of CI diesel engine performance for different fuels of hydrogen, dimethyl ether, and diesel under various engine speeds. International Journal of Hydrogen Energy 2014; 39: 9515–9526.

[50]. Patil KR, Thipse SS. A comparative study of performance and exhaust emissions of CI engine fuelled by neat DME and DME/DEE–diesel blends. Proceedings of International Conference on Advances in Mechanical Engineering 2013; 1–8.

[51]. Vispute KM, Pawar TJ. Study and prospects of di–methyl ether as an alternative fuel in C.I. engine: review. International Journal of Trend in Research and Development 2016; 3(4): 134–138.

[52]. Theinnoi K, Suksompong P, Temwutthikun W. Engine performance of dual fuel operation with in–cylinder injected diesel fuels and in–port injected DME. Energy Procedia 2017; 142: 461–467.

[53]. Deepak KM, Karthick M, Dineshbabu D, Srikanth P, Ramachandran MG. Investigation on the effect of dimethyl ether in compression ignition engine. International Journal of Innovative Research in Science, Engineering and Technology 2015; 4(2): 401–407.

[54]. Kajitani S. A study of low compression ratio diesel engines operated with neat dimethyl ether (DME). JSME TED Newsletter 2004; 42: 1–14.

[55]. Hewu W, Longbao Z. Performance of a direct injection diesel engine fuelled with a dimethyl ether/diesel blend. Journal of Automobile Engineering 2003; 217(9): 819–824.

[56]. Prabhakaran B, Thennarasu P, Karthick S. Performance and characteristics of a CI engine using DME (Dimethyl Ether). International Journal of Innovative Research in Science, Engineering and Technology 2015; 4(2): 31–34.

[57]. Kajitani S, Chen Z. Fundamental research on next generation fuel (dimethyl ether) engines. Journal of Scientific & Industrial Research 2003; 62: 133–144.

[58]. Abhishek, Rahul K, Santosh K, Martha O. Blending impacts of biogas and dimethyl ether (DME) on compressed ignition engine. International Research Journal of Engineering and Technology 2017; 4(4): 2174–2177.

[59]. Loganathan M, Anbarasu A, Velmurugan A. Emission characteristics of jatropha–ethanol and jatropha–dimethyl ether fuel blends on a DI diesel engine. Journal of Mechanical Engineering 2012; 42(1): 38–46.

[60]. Kim HJ, Park SH. Optimization study on exhaust emissions and fuel consumption in a dimethyl ether (DME) fueled diesel engine. Fuel 2016; 182: 541–549.

[61]. Park SH, Shin D, Park J. Effect of ethanol fraction on the combustion and emission characteristics of a dimethyl ether–ethanol dual–fuel reactivity controlled compression ignition engine. Applied Energy 2016; 182: 243–252.

[62]. Geng P, Cao E, Tan Q, Wie L. Effects of alternative fuels on the combustion characteristics and emission products from diesel engines: A review. Renewable and Sustainable Energy Reviews 2017; 71: 523–534.

[63]. Loganathan M, Anbarasu A, Velmurugan A. Emission characteristics of jatropha–dimethyl ether fuel blends on a DI diesel engine. International Journal of Scientific & Technology Research 2012; 1(8): 28–32.

[64]. Zhao Y, Wang Y, Li D, Lei X, Liu S. Combustion and emission characteristics of a DME (dimethyl ether)–diesel dual fuel premixed charge compression ignition engine with EGR (exhaust gas recirculation). Energy 2014; 72: 608–617.

[65]. Hou J, Wen Z, Jiang Z, Qiao X. Study on combustion and emissions of a turbocharged compression ignition engine fueled with dimethyl ether and biodiesel blends. Journal of the Energy Institute 2014; 87: 102–113.

[66]. Ying W, Longbao Z, Hewu W. Diesel emission improvements by the use of oxygenated DME/diesel blend fuels. Atmospheric Environment 2006; 40: 2313–2320.

[67]. Xinling L, Zhen H. Emission reduction potential of using gas–to–liquid and dimethyl ether fuels on a turbocharged diesel engine. Science of the Total Environment 2009; 407: 2234–2244.

[68]. Kim HJ, Park SH. Optimization study on exhaust emissions and fuel consumption in a dimethyl ether (DME) fueled diesel engine. Fuel 2016; 182: 541–549.

[69]. Park SH, Shin D, Park J. Effect of ethanol fraction on the combustion and emission characteristics of a dimethyl ether–ethanol dual–fuel reactivity controlled compression ignition engine. Applied Energy 2016; 182: 243–252.

[70]. Yanju W, Kun W, Wenrui W, Shenghua L, Xiao C, Yajing Y, Shanwen B. Comparison study on the emission characteristics of diesel– and dimethyl ether–originated particulate matters. Applied Energy 2014; 130, 357–369.

[71]. Wang Y, Zhao Y, Xiao F, Li D. Combustion and emission characteristics of a diesel engine with DME as port premixing fuel under different injection timing. Energy Conversion and Management 2014; 77: 52–60.

[72]. Park SH, Kim HJ, Lee CS. Effects of dimethyl–ether (DME) spray behavior in the cylinder on the combustion and exhaust emissions characteristics of a high speed diesel engine. Fuel Processing Technology 2010; 91: 504–513.

[73]. Thomas G, Feng B, Veeraragavan A, Cleary MJ, Drinnan N. Emissions from DME combustion in diesel engines and their implications on meeting future emission norms: A review. Fuel Processing Technology 2014; 119: 286–304.

[74]. Yoon SH, Han SC, Lee CS. Effects of high EGR rate on dimethyl ether (DME) combustion and pollutant emission characteristics in a direct injection diesel engine. Energies 2013; 6: 5157–5167.

[75]. Roh HG, Lee D, Lee CS. Impact of DME–biodiesel, diesel–biodiesel and diesel fuels on the combustion and emission reduction characteristics of a CI engine according to pilot and single injection strategies. Journal of the Energy Institute 2015; 88: 376–385.

[76]. Zhu Z, Li DK, Liu J, Wei YJ, Liu SH. Investigation on the regulated and unregulated emissions of a DME engine under different injection timing. Applied Thermal Engineering 2012; 35: 9–14.

[77]. Park SH, Yoon SH, Cha J, Lee CS. Mixing effects of biogas and dimethyl ether (DME) on combustion and emission characteristics of DME fueled high–speed diesel engine. Energy 2014; 66: 413–422.

[78]. Bogdan J, Nicolae B, Călin I, Vlad BN. Study of emissions for a compression ignition engine fueled with a mix of DME and diesel. Materials Science and Engineering 2017; 252: 1–9.

[79]. Kim HJ, Park SW, Lee CS. Numerical and experimental study on the combustion and emission characteristics of a dimethyl ether (DME) fueled compression ignition engine. Oil & Gas Science and Technology 2012; 67(3): 479–489.

[80]. Wang HW, Zhou LB, Jiang DM, Huang ZH. Study on the performance and emissions of a compression ignition engine fuelled with dimethyl ether. Journal of Automotive Engineering 2000; 214: 101–106.

[81]. Wang Y, Liu H, Huang Z, Liu Z. Study on combustion and emission of a dimethyl ether–diesel dual fuel premixed charge compression ignition combustion engine with LPG (liquefied petroleum gas) as ignition inhibitor. Energy 2016; 96: 278–285.

[82]. Kakoeea A, Gharehghani A. Comparative study of hydrogen addition effects on the natural–gas/diesel and natural–gas/dimethyl–ether reactivity controlled compression ignition mode of operation. Energy Conversion and Management 2019; 196: 92–104.

MANAS Journal of Engineering
ISSN 1694-7398 | e-ISSN 1694-7398

Volume 11, Issue 1, (2023) Pages 53-63
https://doi.org/10.51354/mjen.1211527

Prediction of the formation of low-molecular components, particles, and condensed phases during thermal destruction of oil-contaminated soil

Umirzak Dzhusipbekov[1], Dametken Fischer[1], Gulzipa Nurgalieva[1], Kubat Kemelov[1,*], Damira Sambaeva[3], Zarlık Maimekov[1]

[1]Institute of Chemical Sciences. Bekturova A.B., Republic of Kazakhstan, 050010, Almaty, st. Sh. Ulikhanov 106, jussipbekov@mail.ru, ORCID:0000-0002-2354-9878, zarlyk.maymekov@manas.edu.kg, ORCID: 0000-0002-9117-262X, damishka3004@gmail.com, ORCID:0000-0001-8326-1545, N_gulzipa@mail.ru, ORCID: 0000-0003-2659-3361

[2]Kyrgyz-Turkish Manas University, Department of Environmental Engineering, Bishkek, Kyrgyz Republic, kubat.kemelov@manas.edu.kg, ORCID: 0000-0001-7375-6325, zarlyk.maymekov@manas.edu.kg, ORCID: 0000-0002-9117-262X

[3]Kyrgyz State Technical University named after. I. Razzakova, Kyrgyz Republic, Bishkek, dsambaeva@gmail.com, ORCID: 0000-0002-9834-341X

ABSTRACT

In this study, thermodynamic modelling of the process of thermal destruction of oil-contaminated soil of Ozenmunaigas JSC, which includes compounds such as carbon, silicon, aluminum, iron, calcium, magnesium, sodium, potassium, chromium, phosphorus, manganese, copper, titanium, molybdenum, nickel, vanadium, and water, was carried out. The physicochemical and thermodynamic parameters of the complex system were calculated at P=0.1 MPa, T=598-3000 K. The concentration distribution of components, particles, and condensed phases in the gas phase has been established. In the process of thermal destruction of oil-contaminated soil, the formation of condensed phases was as follows: SiO_2(c), Al_2O_3(c), AlO_3H_3(c), Cu(c), Cu_2O(c), FeO(c), Fe_2O_3(c), Fe_3O_4(c), Fe_2SiO_4(c), NiO(c), MnO(c), Mn_3O_4(c), MnO_2H_2(c), Cr_2O_3(c), MoO_2(c), V_2O_3(c), V_2O_4(c), TiO_2(c), $MgSiO_3$(c), Mg_2SiO_4(c), $MgTi_2O_5$(c), $Ca_3P_2O_8$(c), Mg_2SiO_4(c), $MgTi_2O_5$(c), $Ca_3P_2O_8$(c), $CaCO_3$(c), $CaSiO_3$(c), $CaTiO_3$(c), $Na_2Si_2O_5$(c), $K_2Si_4O_9$(c). At the same time, the amount of condensed calcium silicate $CaSiO_3$(c) was significant and amounted to 3.2 mol/kg, which is due to the initial standard content of oxides of the type (g/kg): SiO_2-473,7, CaO-181,5 in oil-contaminated soil. The formation of various types of condensed phases (from 10^{-30} to 10^{-4} mol/kg) during thermal degradation can help reduce the synergism and toxicity of metal particles in oil-contaminated soils. In the process of thermal destruction of oil-contaminated soil, its carbon-containing components (mg/kg: C_{12}-6,27; C_{13}-10,98; C_{14}-15,69; C_{15}-18,82; C_{16}-23,52; C_{17}-31,37; C_{18}-27,80; C_{19}-17,25; C_{20}-29,80) were mainly converted into oxide, carbon dioxide, and water, and thereby neutralized the organic mass of the soil.

ARTICLE INFO

Research article

Received: 6.12.2022
Accepted: 24.05.2023

Keywords:
oil,
soil,
carbon,
metal,
chemical composition,
component,
particle,
thermodynamics,
modeling,
condensed phase,
neutralization

**Corresponding Author*

1. Introduction

In the process of production, pumping, and storage of oil, operation of treatment facilities, a significant amount of oil sludge, oil-contaminated soils, and asphalt-resin-paraffin deposits are formed, which leads to environmental pollution. In this regard, the problem of developing and applying technologies adapted to specific conditions remains an urgent task.

When developing technologies for cleaning soils and waters under changing weather conditions, it is necessary to take into account not only the climatic features of the region but also the properties of the oil, such as its hydrocarbon composition, and soil conditions. Therefore, one of the directions for the development of technologies for removing oil from ecosystems is the development of effective approaches that can ensure the removal of hydrocarbons from the environment. [1-17].

According to the above studies, it was noted in the works that the mechanism of ecosystem self-healing after oil pollution is rather complicated and is limited to decades [10-17]. At the same time, the authors emphasize that sorption methods for processing oily wastes are of great importance. Taking into account these circumstances, new technology has been developed for processing oily waste into useful products using an energy-accumulating substance based on humates, followed by the disposal of oil-contaminated soil. This study is a continuation of the above study [10-17], to predict the formation of low molecular weight components, particles, and condensed phases during the destruction of oil-contaminated soil under the influence of external thermal influences.

2. Material and method

The content of metals in the oil-contaminated soil in the preliminary stages of the study was determined using an AA240 spectrometer. In this case, the decomposition of the sample was carried out with a mixture of nitric, hydrofluoric, and perchloric acids until the sample was completely opened. The fractional composition of oil products present in the waste was determined by gas-liquid chromatography of a hexane extract on a mass-selective detector using an Agilent 6890 chromatograph and on a Fluorat-02 analyzer. The content of oxides of silicon, aluminum, iron, calcium, magnesium, potassium, sodium, chromium, and phosphorus was determined using a Lambda-35 spectrophotometer. Metals were determined by the decomposition of a sample and its fusion with sodium carbonate or with a mixture of sodium and potassium carbonates [16, 17].

Based on the obtained experimental data [16], the chemical matrix of oil-contaminated soil was compiled taking into account its organic and inorganic parts, as well as water. Using the chemical matrix of oil-contaminated soil, thermodynamic modeling of a complex system at the maximum entropy was carried out based on the “Terra” software package [18]. According to this program, the methodological basis of the calculation algorithm of the program allows for calculating formation in the equilibrium of gaseous, condensed substances, electrically neutral and ionized components, pure phases, and their solutions in the system under consideration. In computational experiments, the phase and elemental composition of oil-contaminated soil were calculated per 1 kg of a carrier (mol/kg). [17, 19], as well as the value of the limits of pressure and temperature of the destruction of the solid phase was in the range from 593 to 3000K (with a step of 500K).

3. Results and discussion

Oil-contaminated soil of “Ozenmunaigas” JSC consists of organic and inorganic components (mg/kg) such as C_{12}-6,27; C_{13}-10,98; C_{14}-15,69; C_{15}-18,82; C_{16}-23,52; C_{17}-31,37; C_{18}-27,80; C_{19}-17,25; C_{20}-29,80; SiO_2-473700; Al_2O_3-29400; Fe_2O_3-143100; CaO-181500; MgO-46500; Na_2O-20100; K_2O-46700; CrO-35200; P_2O_5-14700; Mn-5; Cu-12; Ti-23; Mo-12; Ni-1; V-5; H_2O-2,2 and the soil belong to substances of the 3rd hazard class. Acetylene fractions are the main danger in oil-contaminated soil [16, 17]. At the same time, the toxicity of the neutralized soil decreases due to the transfer of low-boiling acetylene oil fractions to high-boiling ones [17]. In this regard, it was of scientific interest to study the process of thermal destruction of oil-contaminated soil to predict the formation and concentration distribution of components, particles, and condensed phases, where the formation of a condensed phase promotes the transfer of toxic substances from the gas-liquid phase to the solid.

The following thermodynamic parameters were calculated: (entropy S, kJ/(kg K); enthalpy I, kJ/kg); internal energy (U, kJ/kg) and physical and chemical parameters (dynamic viscosity Mu, Pa s); heat capacity Cp, kJ/(kg K); thermal conductivity Lt, W/(m K); dimensionless Prandtl number, Pr; mass fraction of condensed phases, h) oil-contaminated soil in the temperature range T=298-3000 K at P=0.1 MPa. The values of enthalpy and internal energy (I and U) of the oil-contaminated soil were negative (Table 1, Fig. 1), which indicated the direction and course of the process of destruction of the initial mixture of complex chemical composition (mg/kg): C_{12}-6,27; C_{13}-10,98; C_{14}-15,69; C_{15}-18,82; C_{16}-23,52; C_{17}-31,37; C_{18}-27,80; C_{19}-17,25; C_{20}-29,80; SiO_2-473700; Al_2O_3-29400; Fe_2O_3-143100; CaO-181500; MgO-46500; Na_2O-20100; K_2O-46700; CrO-35200; P_2O_5-14700; Mn-5; Cu-12; Ti-23; Mo-12; Ni-1; V-5; H_2O-2,2 [12, 13].

The destruction of the oil-contaminated soil proceeded mainly with the formation of silicon-containing metal compounds (Fe, Na, Ca, Mg, K) (Fig. 1). Changes in thermodynamic (S, U, I) and physicochemical (Cp, Mu, Lt, Pr, z) parameters of oil-contaminated soil components during its thermal destruction within the temperature range of 293-3000K at P=0.1 MPa, showed the formation of a significant amount of condensed calcium silicate $CaSiO_3$(c) -3.2 mol/kg (Fig. 1).

Table 1. *Thermodynamic parameters of oil-contaminated soil at P=0.1 MPa*

T	S	I	U	Mu 10^5	Cp	Lt	Pr	z
293	0,69	-12590,3	-12590,3	-	0,77	-	-	1,00
593	1,34	-12310,7	-12311,0	2,19	1,00	0,06	0,69	1,00
1093	2,03	-11740,1	-11741,0	3,86	1,13	0,12	0,69	1,00
1593	2,49	-11124,8	-11126,2	5,3	1,16	0,17	0,69	1,00
2093	3,03	-10144,2	-10146,8	6,52	1,27	0,17	0,59	0,99
2593	3,35	-9377,9	-9386,6	7,33	1,27	0,13	0,63	0,97
2993	4,01	-7522,5	-7599,6	8,45	1,24	0,11	0,68	0,84

This amount of $CaSiO_3$(c) is due to the initial standard content of oxides of the type (mg/kg): SiO_2-473700, CaO-181500 in oil-contaminated soil. In addition to CaSiO3(c), other condensed phases were formed, as well as various components and particles (Table 2, Fig. 3).

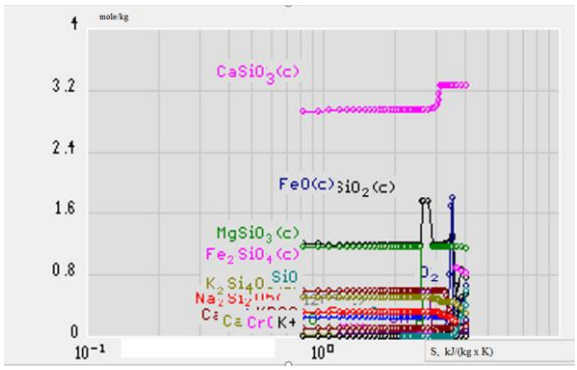

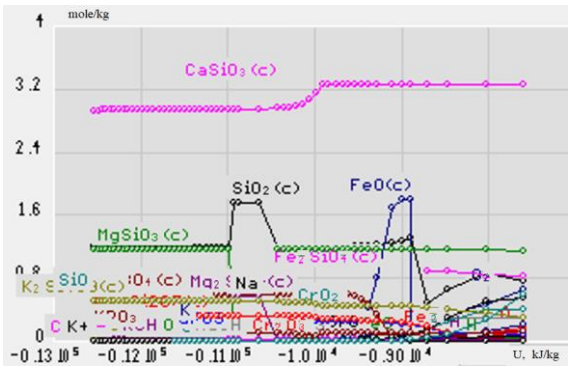

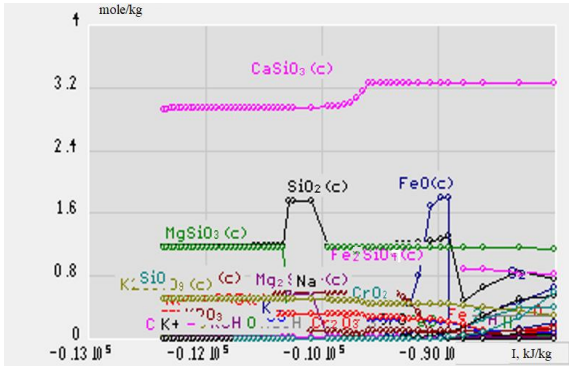

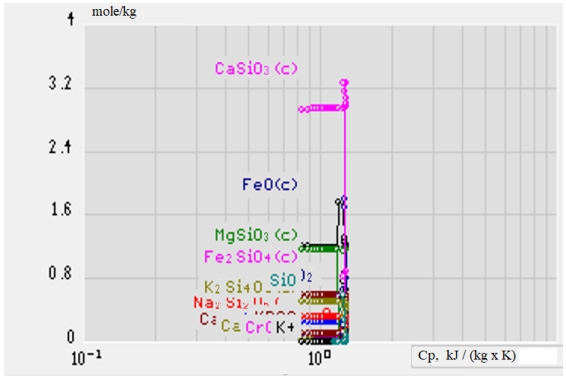

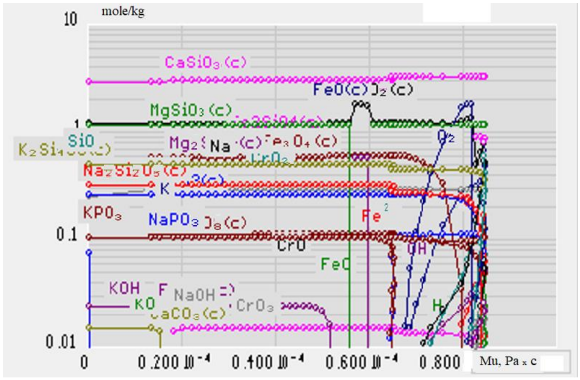

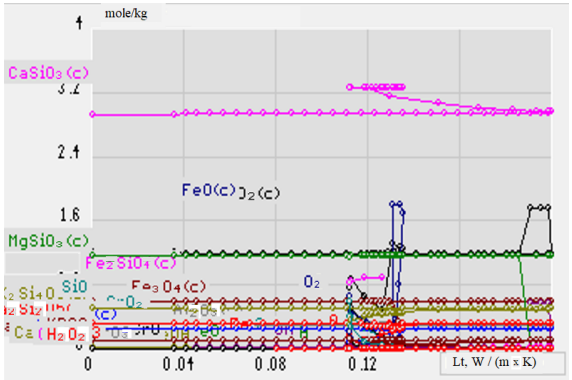

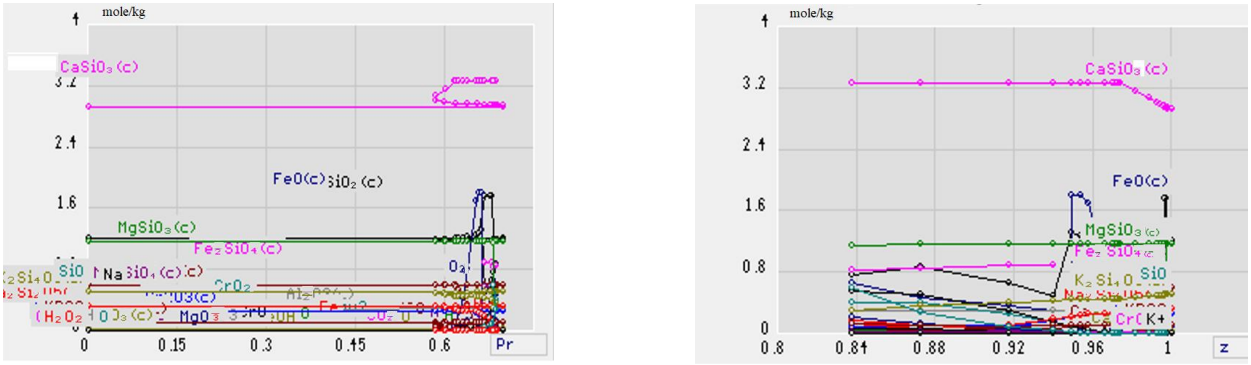

Figure.1. *Changes in thermodynamic (S, U, I) and physicochemical (Cp, Mu, Lt, Pr, z) parameters of oil-contaminated soil components during its thermal destruction within the temperature range of 593-3000K at P=0.1 MPa*

In general, the condensed phases have the following range of compounds (Fig. 2-4, Tables 2 and 3): $SiO_2(c)$, $Al_2O_3(c)$, $AlO_3H_3(c)$, Cu(c), $Cu_2O(c)$, FeO(c), $Fe_2O_3(c)$, $Fe_3O_4(c)$ $Fe_2SiO_4(c)$, NiO(c), MnO(c), $Mn_3O_4(c)$, $MnO_2H_2(c)$, $Cr_2O_3(c)$, $MoO_2(c)$, $V_2O_3(c)$, $V_2O_4(c)$, $TiO_2(c)$, $MgSiO_3(c)$, $Mg_2SiO_4(c)$, MgTi2O5(c), $Ca_3P_2O_8(c)$, $Mg_2SiO_4(c)$, $MgTi_2O_5(c)$, $Ca_3P_2O_8(c)$, $CaCO_3(c)$, $CaSiO_3(c)$, $CaTiO_3(c)$, $Na_2Si_2O_5(c)$, $K_2Si_4O_9(c)$.

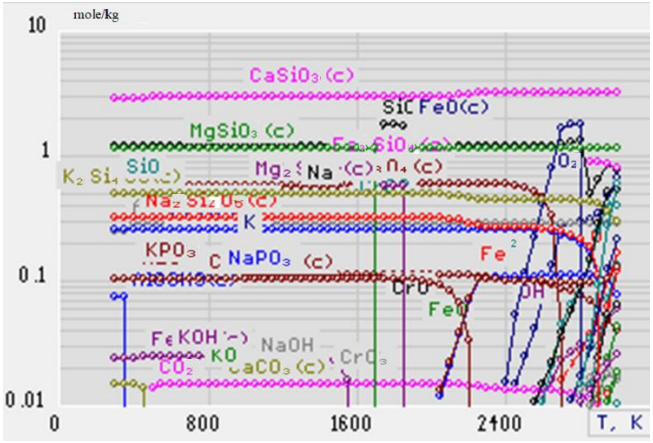

Figure 2. *Components, particles, and condensed phases formed during the destruction of oil-contaminated soil (mol/kg) depending on temperature. P=0.1 MPa.*

Table 2. *Change in the concentration of phosphorus, chromium, magnesium, iron, calcium, sodium, potassium, aluminum containing substances during the destruction of oil-contaminated soil (mol/ kg) depending on temperature. P=0.1 MPa.*

T	P	P_2	PO	PO_2	P_2O_3	P_2O_4	P_2O_5	PH	PH_2	HPO
593	1,9e-22	1,9e-22	1,9e-22	1,9e-22	1,9e-22	1,9e-22	1,9e-22	1,9e-22	1,9e-22	1,9e-22
1093	1,9e-22	1,9e-22	1,9e-22	5,1e-20	1,9e-22	1,9e-22	1,9e-22	1,9e-22	1,9e-22	1,9e-22
1593	1,9e-22	1,9e-22	1,1e-15	5,6e-12	6,1e-22	8,6e-20	1,4e-16	1,9e-22	1,9e-22	5,7e-20
2093	1,0e-13	1,0e-19	2,5e-08	1,1e-06	3,1e-12	4,9e-12	2,7e-10	7,7e-15	3,4e-16	6,3e-12
2593	1,7e-09	3,9e-14	2,1e-05	1,5e-04	2,7e-09	7,9e-10	1,6e-08	6,7e-11	1,2e-12	5,6e-09
2993	6,6e-07	3,4e-11	1,0e-03	1,6e-03	2,2e-08	1,6e-09	1,2e-08	7,1e-09	3,0e-11	1,0e-07

T	Cr	CrO	CrO2	CrO3	Cr2O3(c)	Cr2O3	CrO2H2	CrO3H3	CrO4H4
593	1,9e-22	1,9e-22	1,9e-22	1,9e-22	2,6e-01	1,9e-22	1,9e-22	1,9e-22	1,9e-22
1093	1,9e-22	1,9e-22	2,2e-17	1,5e-16	2,6e-01	1,9e-22	1,2e-16	2,6e-15	1,3e-18
1593	7,8e-18	9,2e-14	7,2e-09	1,5e-07	2,6e-01	4,7e-15	2,3e-11	6,8e-11	9,7e-14
2093	3,0e-10	6,6e-08	2,3e-05	1,0e-05	2,6e-01	7,4e-09	1,1e-07	1,2e-08	2,9e-12
2593	5,7e-06	2,9e-04	1,0e-02	1,3e-03	2,5e-01	8,4e-05	1,1e-05	1,7e-07	1,5e-11
2993	4,3e-03	6,3e-02	4,0e-01	1,6e-02	1,0e-30	8,6e-03	2,8e-05	3,9e-08	5,2e-13

T	Mg	MgO	MgH	MgOH	MgO_2H_2	$MgSiO_3(c)$	$Mg_2SiO_4(c)$	$MgTi_2O_5(c)$
593	1,9e-22	1,9e-22	1,9e-22	1,9e-22	1,9e-22	1,1e+00	1,0e-30	1,0e-30

1093	1,9e-22	1,9e-22	1,9e-22	3,4e-20	4,6e-14	1,1e+00	1,0e-30	1,0e-30
1593	4,2e-15	6,9e-14	2,7e-21	7,2e-13	5,3e-09	1,1e+00	1,0e-30	1,0e-30
2093	4,1e-09	1,0e-08	1,0e-13	2,7e-08	1,3e-06	1,1e+00	1,0e-30	2,4e-04
2593	9,1e-06	1,9e-05	8,0e-10	9,0e-06	2,3e-05	1,1e+00	1,0e-30	1,6e-04
2993	4,3e-03	5,8e-03	3,0e-07	3,7e-04	4,9e-05	1,1e+00	1,0e-30	1,0e-30

T	Fe	FeO(c)	FeO	FeO_2	Fe_2O_3(c)	Fe_3O_4(c)	FeOH	FeO_2H_2	Fe_2SiO_4(c)
593	1,9e-22	1,0e-30	1,9e-22	1,9e-22	2,4e-02	5,8e-01	1,9e-22	1,9e-19	1,0e-30
1093	7,6e-20	1,0e-30	6,8e-20	5,5e-20	2,4e-02	5,8e-01	1,5e-13	1,5e-10	1,0e-30
1593	3,1e-13	1,0e-30	7,7e-12	6,8e-11	1,2e-24	6,0e-01	2,9e-09	2,8e-07	1,0e-30
2093	2,8e-07	1,0e-30	4,4e-07	1,4e-07	1,0e-30	6,0e-01	1,4e-05	4,4e-05	1,0e-30
2593	4,5e-04	4,1e-01	3,6e-04	4,4e-05	1,0e-30	4,6e-01	9,3e-04	4,2e-04	1,0e-30
2993	1,1e-01	1,0e-30	4,2e-02	1,8e-03	1,0e-30	1,0e-30	1,0e-02	4,3e-04	8,1e-01

T	Ca	CaO	CaOH	CaO_2H_2	$Ca_3P_2O_8$(c)	$CaCO_3$(c)	$CaSiO_3$(c)	$CaTiO_3$(c)
593	1,9e-22	1,9e-22	1,9e-22	1,9e-22	1,0e-01	1,0e-30	2,9e+00	1,0e-30
1093	1,9e-22	1,9e-22	1,9e-22	1,4e-15	1,0e-01	1,0e-30	2,9e+00	1,0e-30
1593	1,3e-19	5,7e-18	2,3e-15	3,7e-10	1,0e-01	1,0e-30	2,9e+00	4,8e-04
2093	8,7e-13	2,8e-12	1,9e-10	1,2e-07	8,2e-02	1,0e-30	3,0e+00	1,0e-30
2593	6,9e-09	1,4e-08	1,1e-07	2,7e-06	1,0e-30	1,0e-30	3,2e+00	1,0e-30
2993	6,7e-06	7,1e-06	6,7e-06	6,5e-06	1,0e-30	1,0e-30	3,2e+00	1,0e-30

T	Na	NaO	Na_2O	NaOH	$Na_2O_2H_2$	$NaPO_2$	$NaPO_3$	$Na_2Si_2O_5$(c)
593	1,9e-22	1,9e-22	1,9e-22	1,1e-19	1,9e-22	1,9e-22	1,9e-22	3,2e-01
1093	7,6e-12	1,3e-17	1,9e-22	2,1e-09	9,8e-14	3,4e-21	6,1e-10	3,2e-01
1593	1,0e-07	7,4e-10	3,9e-14	5,8e-06	4,8e-10	9,5e-14	5,0e-05	3,2e-01
2093	1,4e-04	9,1e-07	8,0e-10	3,2e-04	2,7e-08	7,1e-08	2,1e-02	3,1e-01
2593	1,5e-02	2,5e-04	7,4e-07	5,2e-03	2,9e-07	1,3e-05	1,1e-01	2,6e-01
2993	5,4e-01	1,0e-02	3,5e-05	1,7e-02	1,2e-07	1,0e-04	7,8e-02	1,0e-30

T	K	K_2O	K_2O_2	KOH	$K_2O_2H_2$	KPO_3	K_2CO_3	$K_2Si_4O_9$(c)
593	1,93e-22	1,93e-22	1,93e-22	8,90e-18	1,93e-22	1,93e-22	1,93e-22	4,99e-01
1093	2,20e-12	1,93e-22	1,93e-22	1,29e-08	1,27e-13	3,29e-09	4,58e-15	4,99e-01
1593	2,05e-08	6,58e-15	6,53e-16	1,06e-05	1,97e-10	8,93e-05	2,38e-12	4,99e-01
2093	2,49e-05	6,59e-11	8,21e-13	3,44e-04	7,15e-09	2,27e-02	4,61e-11	4,88e-01
2593	2,81e-03	4,94e-08	4,94e-10	4,51e-03	7,52e-08	9,83e-02	3,30e-10	4,46e-01
2993	2,12e-01	8,36e-06	4,85e-08	2,61e-02	1,22e-07	1,27e-01	6,91e-10	3,03e-01

T	Al_2O_3(c)	Al_2O_3	HAlO	$HAlO_2$	AlO_2H_2	AlO_3H_3(c)	AlO_3H_3
593	2,9e-01	1,9e-22	1,9e-22	1,9e-22	1,9e-22	1,0e-30	1,9e-22
1093	2,9e-01	1,9e-22	1,9e-22	1,9e-22	1,3e-20	1,0e-30	8,5e-16
1593	2,9e-01	1,9e-22	1,9e-22	8,9e-15	6,3e-14	1,0e-30	1,9e-11
2093	2,9e-01	1,1e-16	3,3e-16	3,9e-10	1,7e-09	1,0e-30	3,2e-09
2593	2,9e-01	2,5e-11	9,7e-12	2,6e-07	3,2e-07	1,0e-30	3,0e-08
2993	2,9e-01	6,4e-08	5,0e-09	1,0e-05	2,6e-06	1,0e-30	1,2e-08

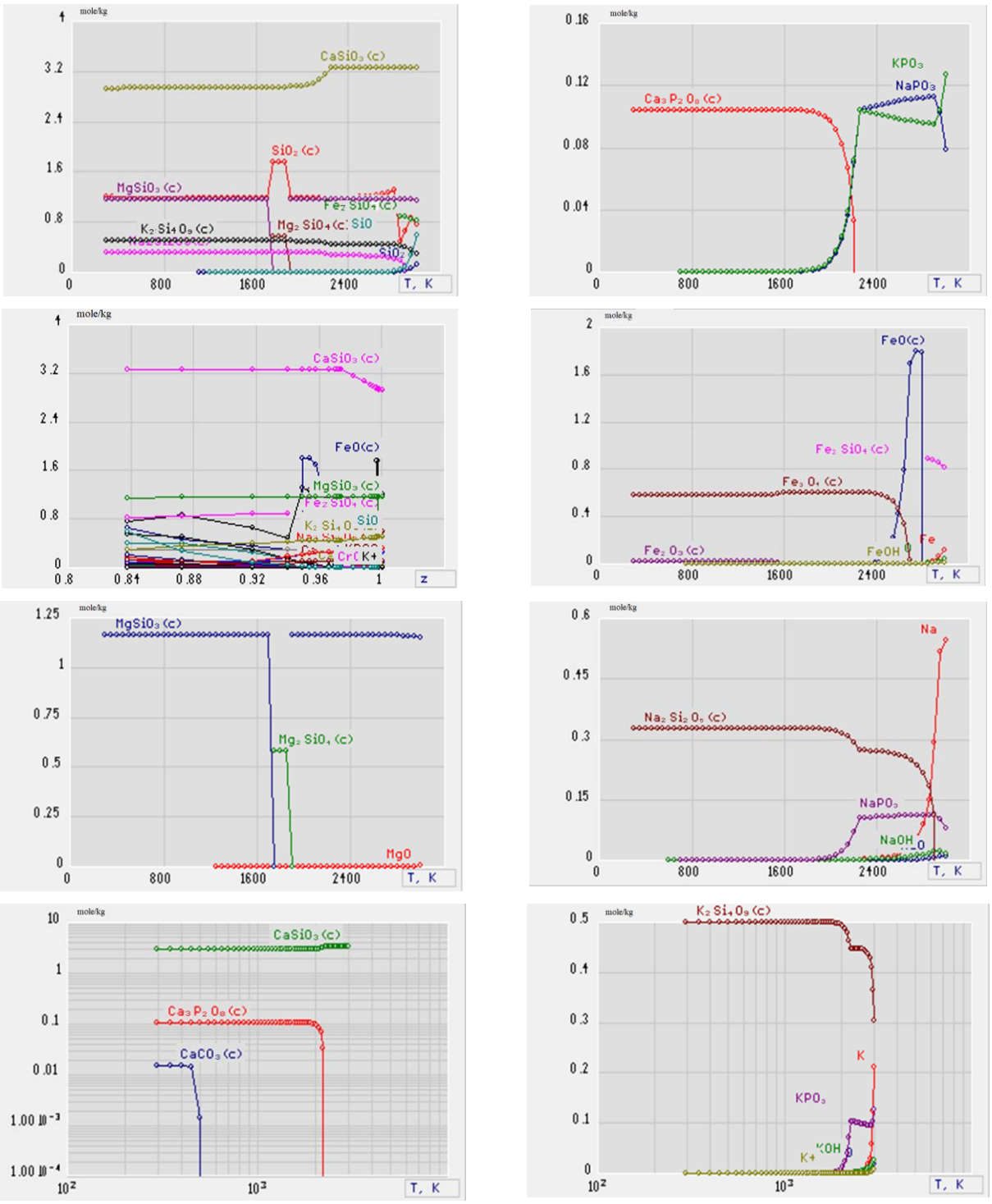

Figure 3. *Concentration change (mol/kg): silicon, iron, phosphorus, magnesium, chromium, sodium, calcium, and potassium-containing substances during the destruction of oil-contaminated soil depending on temperature. P=0.1 MPa.*

Table 3 shows the concentrations of copper, nickel, manganese, molybdenum, vanadium, titanium-containing particles, and components formed during the thermal destruction of oil-contaminated soil depending on temperature (593-2993 K). It is noted that complex redox processes occur and a wide range of substances are formed in small amounts (mol/kg): Cu(c), Cu, Cu_2, CuO, Cu_2O(c), CuH, CuOH; Ni, NiO(c), NiO, NiH, NiOH, NiO_2H_2, Mn, MnO(c), MnO, MnO_2, Mn_3O_4(c), MnH, MnOH, MnO_2H_2(c), Mo, MoO, MoO_2(c), MoO_2, MoO_3, Mo_2O_6, MoO_2H_2, MoO_3H_2, MoO_4H_2, V, VO, VO_2, V_2O_3(c), V_2O_4(c), V_4O_8, V_4O_{10}, Ti, TiO, TiO_2(c), TiO_2, TiOH (Table 3).

Table3. *Change in concentration (mol/kg): copper, nickel, manganese, molybdenum, vanadium, titanium-containing components, particles, and condensed phases during the destruction of oil-contaminated soil depending on temperature. P=0.1 MPa.*

T	Cu(c)	Cu	Cu_2	CuO	Cu_2O(c)	CuH	CuOH
593	1,9e-04	1,9e-22	1,9e-22	1,9e-22	1,0e-30	1,9e-22	1,9e-22
1093	1,9e-04	6,0e-11	8,9e-16	5,7e-16	1,0e-30	6,6e-13	9,4e-12
1593	1,0e-30	1,4e-06	4,8e-10	2,5e-08	9,4e-05	2,9e-09	3,9e-07
2093	1,0e-30	1,8e-04	1,5e-07	1,8e-06	1,0e-30	1,2e-06	5,9e-06
2593	1,0e-30	1,8e-04	6,4e-09	3,6e-06	1,0e-30	1,0e-06	1,7e-06
2993	1,0e-30	1,8e-04	2,4e-10	3,4e-06	1,0e-30	3,7e-07	2,2e-07

T	Ni	NiO(c)	NiO	NiH	NiOH	NiO_2H_2
593	1,93e-22	1,72e-05	1,93e-22	1,93e-22	1,93e-22	1,66e-19
1093	1,21e-16	1,72e-05	6,29e-18	2,41e-17	1,09e-13	6,89e-10
1593	1,88e-10	1,44e-05	5,10e-10	2,02e-12	1,34e-08	2,73e-06
2093	1,83e-06	1,00e-30	4,38e-07	3,70e-08	3,39e-06	1,15e-05
2593	1,18e-05	1,00e-30	1,78e-06	1,42e-07	2,63e-06	7,83e-07
2993	1,56e-05	1,00e-30	1,17e-06	5,69e-08	2,78e-07	5,47e-09

T	Mn	MnO(c)	MnO	MnO_2	Mn_3O_4(c)	MnH	MnOH	MnO_2H_2(c)
593	1,93e-22	9,16e-05	1,93e-22	1,93e-22	1,00e-30	1,93e-22	1,93e-22	1,00e-30
1093	2,25e-18	1,00e-30	4,19e-19	1,63e-20	3,05e-05	5,35e-18	3,73e-17	1,00e-30
1593	2,61e-12	1,00e-30	2,90e-11	4,00e-11	3,05e-05	3,62e-13	2,11e-11	1,00e-30
2093	8,94e-07	8,90e-05	9,33e-07	9,75e-08	1,00e-30	2,37e-07	4,70e-07	1,00e-30
2593	4,64e-05	1,00e-30	3,12e-05	1,93e-06	1,00e-30	7,16e-06	4,90e-06	1,00e-30
2993	6,52e-05	1,00e-30	2,21e-05	6,76e-07	1,00e-30	2,95e-06	7,18e-07	1,00e-30

T	Mo	MoO	MoO_2(c)	MoO_2	MoO_3	Mo_2O_6	MoO_2H_2	MoO_3H_2	MoO_4H_2
593	1,9e-22	1,9e-22	1,2e-04	1,9e-22	1,9e-22	1,9e-22	1,9e-22	1,9e-22	1,6e-14
1093	1,9e-22	1,9e-22	3,3e-05	9,6-18	1,6e-10	1,5e-07	1,9e-22	7,0e-14	2,4e-05
1593	1,9e-22	7,5e-20	1,0e-30	2,4e-12	1,2e-06	7,4e-06	5,0e-21	1,3e-11	6,3e-05
2093	4,6e-17	1,7e-12	1,0e-30	6,1e-08	6,1e-05	9,9e-06	4,7e-15	6,5e-09	4,0e-05
2593	3,7e-13	1,2e-09	1,0e-30	1,8e-06	1,1e-04	1,8e-07	2,0e-13	7,9e-09	2,3e-06
2993	1,2e-10	6,9e-08	1,0e-30	1,1e-05	9,6e-05	1,6e-09	2,4e-13	8,3e-10	2,9e-08

T	V	VO	VO_2	V_2O_3(c)	V_2O_4(c)	V_4O_8	V_4O_{10}
593	1,9e-22	1,9e-22	1,9e-22	4,9e-05	1,0e-30	1,9e-22	1,9e-22
1093	1,9e-22	1,9e-22	1,3e-14	1,0e-30	4,9e-05	2,6e-10	1,0e-12
1593	1,9e-22	7,6e-16	7,3e-08	1,0e-30	1,7e-29	2,0e-05	4,6e-06
2093	3,9e-15	6,0e-10	5,3e-05	1,0e-30	1,0e-30	1,1e-05	3,0e-09
2593	4,9e-12	2,9e-08	9,8e-05	1,0e-30	1,0e-30	1,1e-12	3,7e-17
2993	4,6e-10	2,9e-07	9,8e-05	1,0e-30	1,0e-30	4,4e-19	1,9e-22

T	Ti	TiO	TiO_2(c)	TiO_2	TiOH
593	1,9e-22	1,9e-22	4,8e-04	1,9e-22	1,9e-22
1093	1,9e-22	1,9e-22	4,8e-04	4,8e-21	1,9e-22
1593	1,9e-22	2,4e-19	1,0e-30	4,5e-12	6,6e-22
2093	1,1e-18	9,9e-12	1,0e-30	1,9e-07	3,3e-14
2593	9,2e-13	1,8e-07	1,0e-30	1,5e-04	2,7e-10
2993	3,6e-10	5,4e-06	1,0e-30	4,7e-04	2,0e-09

The content of condensed phases following types: Cu(c), Cu_2O(c), NiO(c), MnO(c), Mn_3O_4(c), MnO_2H_2(c), MoO_2(c), V_2O_3(c), V_2O_4(c), TiO_2(c) ranges from 10-30 to 10-4 mol per 1 kg of the gas phase. Under real conditions, synergism of these particles can take place in soils; combined effect on the components of the environment [19-22]. In the process of thermal destruction of oil-contaminated soil, the organic phase under the action of water (H_2O-2.2 mg/kg) and metal particles of the soil undergoes oxidation and destruction with the formation of oxygen-containing, hydrogen, and carbon-containing components, particles (Table 4, Fig. 4).

Table 4. *Change in concentration (mol/kg): oxygen, hydrogen, and carbon-containing substances during the destruction of oil-contaminated soil depending on temperature. P=0.1 MPa*.

T	O	O_2	H	H_2	OH	HO_2	H_2O	H_2O_2	O_3
593	1,9e-22	1,9e-22	1,9e-20	3,8e-06	6,2e-21	1,9e-22	1,1e-01	1,9e-22	1,9e-22
1093	1,0e-14	2,1e-10	1,3e-11	3,0e-06	2,1e-09	1,6e-15	1,1e-01	3,9e-14	1,9e-22
1593	3,0e-07	3,9e-03	3,6e-08	3,9e-06	3,9e-05	4,0e-08	1,1e-01	6,8e-09	2,0e-16
2093	3,6e-05	4,1e-03	2,5e-05	4,0e-04	8,1e-04	4,1e-07	1,1e-01	4,3e-08	2,9e-14
2593	4,1e-03	7,2e-02	1,2e-03	2,2e-03	1,1e-02	1,1e-05	9,8e-02	3,3e-07	3,1e-11
2993	1,6e-01	6,6e-01	1,8e-02	3,9e-03	5,9e-02	5,1e-05	4,0e-02	3,0e-07	2,0e-09

T	CO	CO_2	CH_4	CHO	CHO_2	CH_2O	CH_2O_2
593	1,6e-08	1,5e-02	1,6e-15	1,9e-22	3,3e-22	4,1e-19	1,6e-13
1093	4,0e-07	1,5e-02	1,9e-22	6,5e-19	4,6e-15	5,2e-18	3,4e-13
1593	1,6e-06	1,5e-02	1,9e-22	5,0e-16	2,3e-12	2,1e-17	6,3e-13
2093	2,6e-04	1,4e-02	1,4e-19	1,1e-11	5,0e-10	2,5e-13	6,2e-11
2593	1,9e-03	1,3e-02	2,8e-18	6,3e-10	4,7e-09	3,9e-12	1,4e-10
2993	6,4e-03	8,7e-03	6,3e-19	2,6e-09	4,5e-09	3,0e-12	2,5e-11

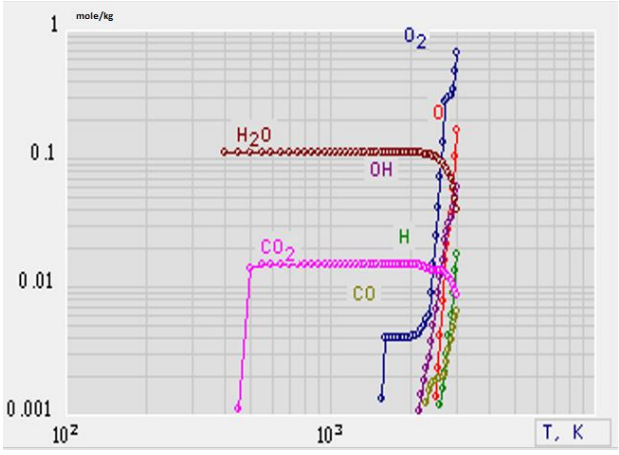

Figure 4. *Change in concentration (mol/kg): oxygen, hydrogen, carbon-containing substances during the destruction of oil-contaminated soil depending on temperature*

The content in the gas phase the concentration of compounds were: molecular oxygen =0.66 mol/kg (at 2993 K), water vapor = 0.01 mol/kg (at 593-2093 K), carbon dioxide =0.015 mol/kg (at 593-1593 K), carbon monoxide =0.0019 mol/kg (at 2593K), atomic oxygen= 0.16 mol/kg (at 2993K), atomic hydrogen= 0.018 mol/kg (at 2993K), hydroxyl = 0.059 mol/kg (at 2993K). Following types of particles: HO_2, H_2O_2, O_3, CH_4, CHO, CHO_2, CH_2O, CH_2O_2 were contained in trace amounts (Fig. 4, Table 4).

Thus, in the process of thermal degradation, the formation of various types of condensed phases can help reduce the toxicity of metal particles in oil-contaminated soils, and its carbon-containing components are mainly converted into oxide, carbon dioxide, water, and thus the neutralization of the organic mass of the soil was shown.

4. Conclusion

1. Thermodynamic modeling of the process of thermal destruction of oil-contaminated soil, consisting of carbon, silicon, aluminum, iron, calcium, magnesium, sodium,

potassium, chromium, phosphorus, manganese, copper, titanium, molybdenum, nickel, vanadium, and water, was carried out.

2. The physicochemical and thermodynamic parameters of the oil-contaminated soil were calculated at P=0.1 MPa, T=598-3000 K. The concentration distribution of components, particles, and condensed phases in the gas phase was established.
3. In the process of thermal destruction of oil-contaminated soil of "Ozenmunaigas" JSC, the formation of various condensed phases were: SiO_2(c), Al_2O_3(c), AlO_3H_3(c), Cu(c), Cu_2O(c), FeO(c), Fe_2O_3(c), Fe_3O_4(c), Fe_2SiO_4(c), NiO(c), MnO(c), Mn_3O_4(c), MnO_2H_2(c), Cr_2O_3(c), MoO_2(c), V_2O_3(c), V_2O_4(c), TiO_2(c), $MgSiO_3$(c), Mg_2SiO_4(c), $MgTi_2O_5$(c), $Ca_3P_2O_8$(c), Mg_2SiO_4(c), $MgTi_2O_5$(c), $Ca_3P_2O_8$(c), $CaCO_3$(c), $CaSiO_3$(c), $CaTiO_3$(c), $Na_2Si_2O_5$(c), $K_2Si_4O_9$(c).
4. Changes in thermodynamic (S, U, I) and physicochemical (Cp, Mu, Lt, Pr, z) parameters of oil-contaminated soil components during its thermal destruction in the temperature range of 593-3000 K and at P=0.1. MPa showed the formation of a significant amount of condensed calcium silicate $CaSiO_3$(c) - 3.2 mol/kg, which is due to the initial content of oxides of the type (mg/kg): SiO_2-473700, CaO-181500 in oil-contaminated soil. The mass fraction of all condensed phases of the system varied within Z=0.84-1.0.
5. The formation of a large number of condensed phases (from 10^{-30} to 10^{-4} mol/kg) was noted, which is very important in the processes of reducing the toxicity of various metal particles.
6. In the process of thermal destruction of oil-contaminated soil, its carbon-containing components (mg/kg): C_{12}-6,27; C_{13}-10,98; C_{14}-15,69; C_{15}-18,82; C_{16}-23,52; C_{17}-31,37; C_{18}-27,80; C_{19}-17,25; C_{20}-29,80 were mainly converted into carbon monoxide and dioxide, water, and thus the neutralization of the organic mass of the soil is achieved.

References

[1]. Ding D., Song X., Wei C., LaChance J. A review on the sustainability of thermal treatment for contaminated soils. Environmental Pollution, 253, (2019), 449-463.

[2]. Vidonish J. E., Alvarez P. J., Zygourakis K. Pyrolytic Remediation of Oil-Contaminated Soils: Reaction Mechanisms, Soil Changes, and Implications for Treated Soil Fertility. Industrial & Engineering Chemistry Research, 57(10), (2018) 3489–3500.

[3]. Bykova M.V., Pashkevich M.A.. "Engineering and ecological survey of oil-contaminated soils in industrial areas and efficient way to reduce the negative impact" in Scientific and Practical Studies of Raw Material Issues. 1st Ed, ImprintCRC Press. 2019.

[4]. Kemelov K., Maymekov U., Sambaeva D., Maymekov Z. Reducing concentrations of Benzo (a) pyrene in gas phase soot particles by using and burning water fuel emulsions. Polish Journal of Environmental Studies, 29(4), (2020), 2669-2677.

[5]. Ossai I. C., Ahmed A., Hassan A., Hamid, F. S. Remediation of soil and water contaminated with petroleum hydrocarbon: A review. Environmental Technology & Innovation, Volume, 17, (2020), 100526

[6]. Zivdar Z., Heidarzadeh N., Asadollahfardi G. Remediation of diesel-contaminated soil by low-temperature thermal desorption. Int. J. Environ. Sci. Technol., 16, (2019), 6113–6124.

[7]. Lee T., Nam I.-H., Kim J.-H., Zhang M., Jeong T. Y., Baek K., Kwon E.E. The enhanced thermolysis of heavy oil contaminated soil using CO_2 for soil remediation and energy recovery. Journal of CO_2 Utilization, 28, (2018), 367–373.

[8]. Sang Y., Yu W., He L., Wang Z., Ma F., Jiao W., Gu Q. Sustainable remediation of lube oil-contaminated soil by low temperature indirect thermal desorption: Removal behaviors of contaminants, physicochemical properties change and microbial community recolonization in soils. Environmental Pollution, 287, (2021), 117599.

[9]. Lee S. H., Kim S. O., Lee S. W., Kim M. S., Park H. Application of Soil Washing and Thermal Desorption for Sustainable Remediation and Reuse of Remediated Soil. Sustainability, 13(22), (2021), 12523.

[10]. He L., Sang Y., Yu W., Lu T., Wang F., Ma F., Jiao W. Sustainable remediation of dibenzofuran-contaminated soil by low-temperature thermal desorption: Robust decontamination and carbon neutralization. Chemosphere, 302, (2022), 134810.

[11]. Li Y., Wei M., Yu B., Liu L., Xue Q. Thermal desorption optimization for the remediation of hydrocarbon-contaminated soils by a self-built sustainability evaluation tool. Journal of Hazardous Materials, (2022), 129156.

[12]. Bykova M.V., Alekseenko A.V., Pashkevich M.A., Drebenstedt C. Thermal desorption treatment of petroleum hydrocarbon-contaminated soils of tundra,

taiga, and forest steppe landscapes. Environmental Geochemistry and Health, 43(6), (2021), 2331–2346.

[13]. Baymanov G. "Scientists of the Kyzylorda State University named after Korkyt-Ata have developed a method for cleaning oil-contaminated areas in an arid hot climate" 08/05/2017 Kyzylorda, Kazakhstan. https://www.kt.kz/rus/science/kizilordinskie_uchenie_usovershenstvovali_metod_ochistki_neftezagrjaznennih_territorij_1153644002.html https://www.kt.kz [Accessed: 20 Sept. 2022].

[14]. Dzhusipbekov U.Zh., Nurgalieva G.O., Kuttumbetov M.A., Zhumasil E., Duisenbay D., Suleimenova O.Ya. Pilot-industrial testing of the process of processing oil-contaminated soil, Chemical Journal of Kazakhstan, 3, (2015), 234-240. (in Russian)

[15]. Dzhusipbekov U.Zh., Nurgaliyeva G.O., Kuttumbetov M.A., Zhumasil E. "Neutralization of oil-contaminated soil using humate-based energy-accumulating substance" Materals Vserossiyskoy scientific and practical. conference- Nizhnekamsk, 1, 88-89, 2015. (in Russian)

[16]. Dzhusipbekov U.Zh., Nurgalieva G.O., Bayakhmetova Z.K., Aizvert L.G. Determination of the hazard class of contaminated and neutralized soil - Chemical Journal of Kazakhstan - Almaty, 1 (65), (2019), 37-49 (in Russian)

[17]. Dzhusipbekov et al. Physical and chemical bases for the restoration of oil-contaminated and disturbed soils-Almaty, 1, (2022), 162-169 (in Russian)

[18]. Trusov B. G., Badrak S. A., Turov V. P., Baryshevskaya I. M. Automated system of thermodynamic data and calculations of equilibrium states. Mathematical methods of chemical thermodynamics, Novosibirsk: Nauka, (1982), 213-219. (in Russian)

[19]. Badrul I. Petroleum sludge, its treatment and disposal: a review. Int. J. Chem. Sci.13(4), (2015), 1584-1602.

[20]. Krzhizh L., Reznik D. Technology of cleaning the geological environment from oil pollution. Ecology of production, 10, (2007), 54. (in Russian)

[21]. Ivanov A.A., Yudina N.V., Maltseva E.V., Matis E.Ya. Study of biostimulating and detoxifying properties of humic acids of various origins in oil-contaminated soil. Chemistry of vegetable raw materials, 1, (2007), 99-103. (in Russian)

[22]. Kolbasov G.A. "Assessment of the possibility of using industrial humates in the biological reclamation of oil-contaminated peat soils". Dissertation, 03.02.13. – M.: Moscow State University. M.V. Lomonosov, 2011 (in Russian)

MANAS Journal of Engineering
ISSN 1694-7398 | e-ISSN 1694-7398

Volume11, Issue 1, (2023) Pages 64-73
https://doi.org/10.51354/mjen.1217103

A new application for reading optical form with standard scanner by using image processing techniques

Fatih Taha Özcan [2], Ayşe Eldem[1,*]

[1] IT Department, Karamanoglu Mehmetbey University, Karaman, Turkey, fozcan@kmu.edu.tr, ORCID: 0000-0002-9012-0473

[2] Department of Computer Engineering, Karamanoglu Mehmetbey University, Karaman, Turkey, ayseeldem@kmu.edu.tr, ORCID: 0000-0002-5561-1568

ABSTRACT

Multiple choice exams appear as the most common method used to measure student success in education systems in Turkey and around the world. Evaluation of multiple choice exams is usually done by optical form reading systems using expensive optical forms and optical scanners. The most important reason for using optical form reading systems is to reduce the error rate to zero in the evaluation process. In this study, an alternative system is proposed for the evaluation of multiple choice exams. The designed system is a web-based software with high accuracy on evaluating that contains optical form design module, session planning module and evaluation module. The form in which the designed template will be printed on A4 paper instead of a special optical form and the system in which standard scanners will be used instead of the optical scanner, uses the image processing algorithms in the OpenCV library in the evaluation process which is an intermediate library developed in C#. The proposed system is coded to run in parallel to speed up the evaluation process. In order to determine the performance of the proposed system, the optical forms filled by 208 students studying at Karamanoğlu Mehmetbey University, Department of Computer Engineering were evaluated. The accuracy rate of the system has been determined as 99.97%. It has been determined that 1 optical evaluation time, calculated by dividing the total time obtained by running in parallel, by the number of evaluated optical forms, varies between 1.7 seconds and 15 seconds, depending on the scanning resolution.

ARTICLE INFO

Research article

Received: 10.12.2022
Accepted: 14.02.2023

Keywords:

Image preprocessing techniques,
multiple choice exam,
optical form reading,
segmentation,
thresholding

**Corresponding author*

1. Introduction

The education system is considered as a purposeful process. The process of observing a quality and showing the observation data with numbers is defined as measurement, and the process of extracting a meaning from the measured values is defined as evaluation. One of the most important processes of the education system is the measurement and evaluation phase, which includes measuring how well the information given is understood, that is, determining the extent to which the objectives have been achieved. Evaluation reveals the performance of the entire education system, including the educator. Accurate calculation of the performance of the education system is very important in terms of determining the operational and non-operational aspects of the system and perfecting the education system[1].

Multiple choice tests are used both on a large scale and on a local scale in our country. In our education system, large-scale tests were started to be applied by ÖSYM, which was established in 1974, to centralize the exams made by faculties as a result of the increase in applications to universities [2]. With the widespread use of central multiple-choice exams, multiple-choice exams have started to be held at the local scale so that students who are in the preparation stage for these exams can adapt to the exam system. The most important reason why multiple-choice exams have become so widespread is that since it is easy to answer questions in these exams, they allow more comprehensive measurement due to the fact that more questions are asked. In addition, features such as obtaining statistics on the basis of questions in multiple-choice exams provide detailed information to the educator. Since participants are charged for centrally held multiple-choice exams, it facilitates the use of optical reading systems necessary for the reading and evaluation of these exams. Educators who want to prepare their students for national multiple-choice exams generally do not have the

opportunity to demand money for the exam they have prepared themselves. Therefore, educators usually evaluate multiple-choice exams manually. Manual multiple-choice exam evaluation is prone to errors; moreover, it takes a long time to transfer the data obtained to the computer environment to get detailed statistics, which is one of the most important features of multiple-choice exams.

The aim of this study is to develop a web-based optical form evaluation system for optical forms scanned with devices such as scanners or mobile phones, which are often in the hands of the institution or educator today, instead of purchasing an optical reader required for the evaluation of multiple-choice exams and using equipment that is costly in technical maintenance. The main purpose is to reduce the cost required for the evaluation of multiple choice exams. Since the system proposed in this study includes the answer sheet design, it will allow the use of standard A4 paper. In addition, since the proposed system has a module such as creating a session plan, it will also minimize cheating, which is the biggest problem of multiple choice exams.

Information about previous studies on optical form reading is given detailed.
Nguyen et al., in their published article, worked on the evaluation with high reliability and efficiency of answer sheets scanned with a digital camera by using image processing algorithms. Nguyen et al. tested the system they designed with 10000 questions and achieved an accuracy rate of 99.74%[3]. Aydemir worked on optical form reading in his master's thesis. Aydemir tested the system he designed with 28360 questions answered by 742 students in the foreign language exam and determined the accuracy rate of the developed system as 99.94%[4]. Al-Marakeby tried to find the evaluation results by processing the exam result images scanned using a digital camera with parallel processes thanks to the multi-core processor in his published article. Finally, classifier algorithms were preferred to determine whether the box was checked or not. As a result of the tests carried out with 200 multiple choice optical forms and 24000 question answers using different light, form angle originating from scanning, the success of the system was revealed as 99.8%[5]. Fisteus et al. have worked on a low-cost and portable computer vision-based system called "Eyegrade" for multiple choice exams in their article. In order to measure the performance of the system called "Eyegrade", the results of 233 students were evaluated and they measured that system made wrong assessment on 9 students paper and revealed the success rate as 96.1%[6]. In his article Sattayakawee studied a system for the evaluation of multiple choice exams with grid type answer sheets used in Thailand. In the tests made with 300 exam papers and 16500 questions, the accuracy rate of the proposed system was measured as 99.91%[7]. In their article, Şenol and Fidan designed an exam system that evaluates the optical forms scanned with a web camera developed in C# language in order to read the optical forms used in multiple choice test systems and to provide more detailed and valuable information to the educators by making statistical analyzes. In order to measure the performance of the designed system, the answer sheets of 221 students were scanned with a web camera and errors were detected in 7 answer sheets and the performance of the system was calculated as 96.83%[8]. Patel et al., in their article published in 2015, worked on a mobile application based system they named “CheckIt”. Patel et al. tried the "CheckIt" system with 310 quizzes and tests questions and achieved a success rate of 97.48%[9]. In the article they published, Hasan and Kareem worked on a system to be used in the evaluation of multiple choice exams. Hasan and Kareem determined the accuracy rate of the artificial neural network algorithms based system as 99.96% in the test they performed with 800 answer sheets and 58000 questions[10]. Yüksel et al. have worked on a mobile application-based optical form evaluation system in the article they published. The highest success of the system was measured as 99.7% in the tests made with 1000 questions on 20 answer sheets[11]. Gyamfi and Missah worked on the optical form evaluation system they proposed for multiple choice exams in their published articles. As a result of the tests, it was revealed that the system using unsupervised learning on the basis of pixels has better performance[12]. Loke et al. proposed a new method for optical form recognition in their published paper. In the first category, 6000 questions were filled and tested by people who were not trained on how to mark, and the accuracy rate of the proposed method was measured as 99.97%. In tests with printing and scanning errors, the accuracy rate of the proposed method was measured as 99.3%[13]. Küçükkara and Tümer worked on the reading and evaluation of answer sheets for multiple choice exams in their published articles. They tested the proposed system with 105750 answer sheets in three exams attended by 35250 students in Konya and calculated the accuracy rate as 99.76%[14]. Espitia et al., in the article they published, worked on the evaluation of the answer sheets of exams such as the university entrance exam or graduation exam in Colombia using image processing algorithms. The system designed by Espitia et al. was tested with 64940 answer sheets and it was found that it achieved an accuracy rate of 99.70%[15]. In the article they published, Afifi and Hussain studied classification-based algorithms for multiple choice exams. In their tests using MATLAB, they used different classification algorithms and were able to achieve the maximum accuracy rate of 99.78% by using the CNN classification algorithm[16]. Ha and Thu studied on optical form reading using MATLAB in the article they published. They measured the success rate of the developed system as 100% in their tests using 170 optical forms[17].

In this study, a system called "Multiple Choice Examination System" is proposed instead of costly optical form reading systems, in which the optical form designed by using the system can be printed on A4 paper and standard scanners are used instead of optical scanners. The designed system is

separated from previous studies by consisting of modules such as creating a seating plan, designing optical form and evaluating optical form.

In this article, the image processing steps used during optical form evaluation are explained in the second part. The application and evaluation steps are explained in detail in the third section, and the performance of the system is explained in the fourth section.

2. Material and method

The system proposed in this study consists of a three-stage structure. The first stage consists of making the definitions including the optical form design, the second stage is the session plan and the printing of the optical forms customized according to the student and the examination, the third stage consists of scanning the marked optical forms and performing the evaluation process after uploading scanned optical forms to the system. Evaluation phase of optical forms consists of grayscale conversion, Gaussian smoothing filter, morphological opening process, thresholding and conversion to binary image, edge detection, contour extraction, and Hough circle transform, which are explained in detail below.

2.1. Convert to Grayscale

In colored images, each pixel is represented by 24-bit data. During image processing, instead of using the color values of 3 different colors in an image, a grayscale image consisting of values between 0 and 255, where a pixel can be expressed with 8-bit data without losing detail, is used. Thus, the size of the optical form image file is reduced to one third.

2.2. Gaussian Smoothing Filter

Using the Gauss function to blur the image, reduce detail and noise is called a Gaussian smoothing filter. Gaussian smoothing filter can be defined as two-dimensional convolution in general. The Gaussian smoothing filter can be expressed by the function shown in Equation (1) [18].

$$G(x) = \frac{1}{(2\pi\sigma^2)^{N/2}} e^{-(x-\mu)^2/(2\sigma^2)} \quad (1)$$

In Equation (1), "G" refers to Gaussian probability density function, "σ" refers to standard deviation of Gaussian noise, "e" refers to base of natural logarithm, "N" refers to the size of the image, "x" refers to grayscale value and "μ" refers to the mean value of Gaussian noise.

2.3. Morphological Opening

It is obtained by applying a dilation process after an erosion process. It is used to get rid of noise while preserving the properties of large shapes. Equation (2) shows the function of the morphological expansion operation.

$$\boldsymbol{A} \circ \boldsymbol{B} = (\boldsymbol{A} \boldsymbol{\theta} \boldsymbol{B}) \oplus \boldsymbol{B} \quad (2)$$

In Equation (2); "A" refers to image to open and "B" refers to the structural element that determines the shape of the opening process.

2.4. Thresholding and Conversion to Binary

Thresholding, which is one of the most basic segmentation methods, is the process of separating the objects in the image from the background of the image. The image input, which is given as grayscale, is returned as a binary image. Basically, it is aimed to change the pixels below the determined threshold value in grayscale images to black pixels, i.e. 0, and to change the pixels to white, i.e. 255, higher than the threshold value. Thresholding is also used to remove noise in the image. Here, the success of the thresholding depends on the determined threshold value. Basically, the Otsu thresholding algorithm returns a single threshold value to minimize the within-class variance and maximize the variance between classes. Equation (3) shows the variance function between classes.

$$\boldsymbol{\sigma_\omega^2(t) = \omega_0(t)\sigma_0^2(t) + \omega_1(t)\sigma_1^2(t)} \quad (3)$$

In Equation (3); "σ_w" refers to within-class variance, "*t*" refers to threshold value, weights "ω_0" and "ω_1" refer to probabilities of two classes separated by "*t*" threshold, "σ_0" and "σ_1" refer to the variance of the two classes separated by the *t* threshold.

2.5. Canny Edge Detection

Canny edge detection method is one of the most common methods used to find the edges of objects and shapes in an image. In this method, two threshold values are given as parameters. The method generally consists of 5 steps. Table 1 shows pseudocodes of the Canny edge detection algorithm.

.

Table 1. *Canny edge detection pseudocode*

Start:
Apply noise reduction with Gaussian Blur
Refine edge with non-maximum suppression
Perform pixel continuity test using double threshold value and detect strong, weak and irrelevant pixels
Convert weak pixels to strong pixels by examining neighboring pixels by edge tracking with hysteresis.
End:

2.6. Contour Extraction

Contour extraction can be defined as finding a closed curve that seamlessly connects pixels of the same color and intensity by grouping them together. Commonly contours are objects found in an image.

2.7. Hough Circle Transform

The Hough transform was found by Paul Hough in 1962 to determine whether mathematically expressible shapes exist on the picture, and if so, its location and angle. The method works with simple bit voting logic. Dana H. Ballard made improvements in 1981 for the detection of objects more general to the algorithm [19]. During the Hough transform circle detection, the functions shown in Equations (4), (5) and (6) are used.

$$\boldsymbol{r^2 = (x - a)^2 + (y - b)^2} \quad (4)$$

$$\boldsymbol{a = x - r \times cos(\theta)} \quad (5)$$

$$\boldsymbol{b = y - r \times sin(\theta)} \quad (6)$$

In Equations (4), (5) and (6); "r" refers to radius of the circle, "a" refers to coordinate of the center of the circle on the x-axis "b" refers to Coordinate of the center of the circle on the y-axis, "θ" refers to angle between (0.2π), "x" refers to coordinate of the image point on the x-axis and "y" refers to coordinate of the image point on the y-axis.

2.8. Parallel Programming

Parallel programming, the foundation of which was laid by John Cocke and Daniel Slotnick in 1958 with a computer design called SOLOMON, refers to the completion of a large and time-consuming computation in a shorter time on multiple processors simultaneously [20]. It is predicted that the size of the optical form image files to be evaluated within the scope of this study will increase as the scanning resolutions increase and the evaluation process will take longer. Therefore, in this study, parallel programming structure is used to reduce the evaluation time.

3. Application

In order to create a multiple-choice exam system, first of all, pages were designed to carry out the definition processes to be made before the exam. In these pages; user operations, unit operations, exam definition procedures, exam correct answers procedures, student procedures to take the exam, classroom procedures, session planning processes and the design of the optical form to be used in the exam are carried out. The design of these pages is shown in Figure 1.

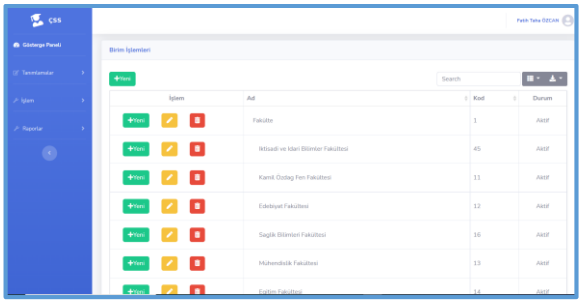

(a) Unit operations page

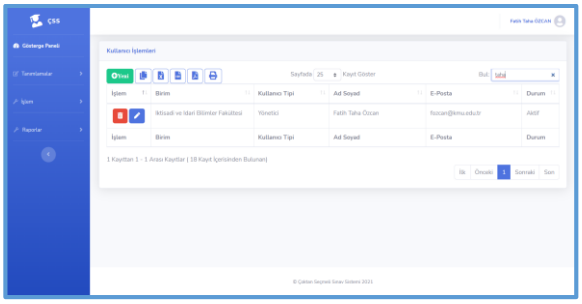

(b) User operations page

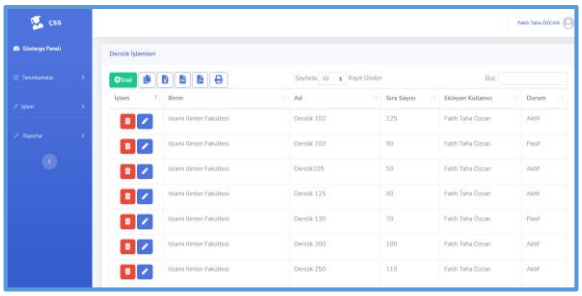

(c) Classroom operations page

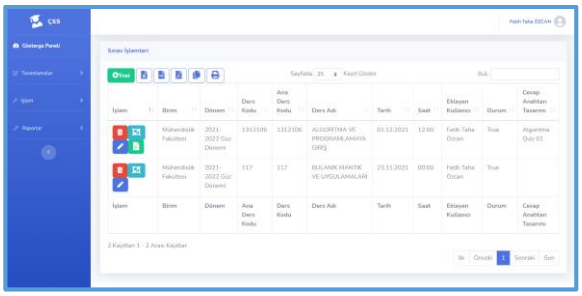

(d) Exam operations page

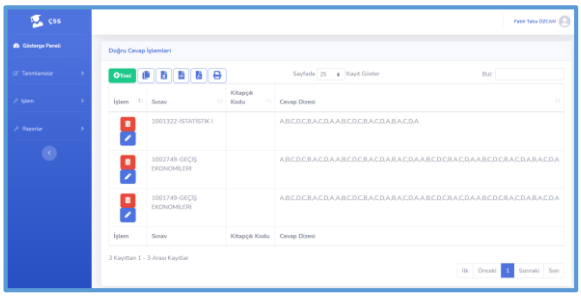

(e) Correct answer operations page

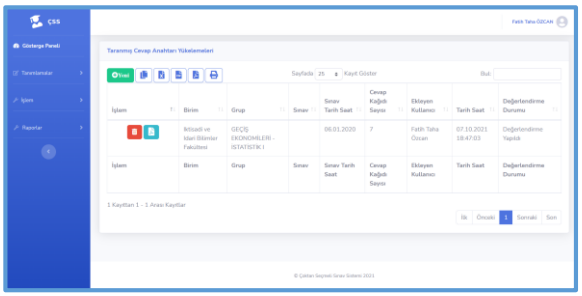

(f) Scanned optical form operations page

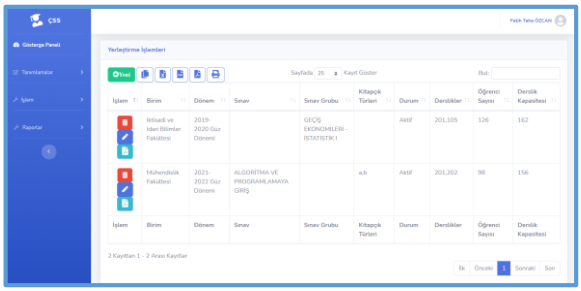

(g) Session planning operations page

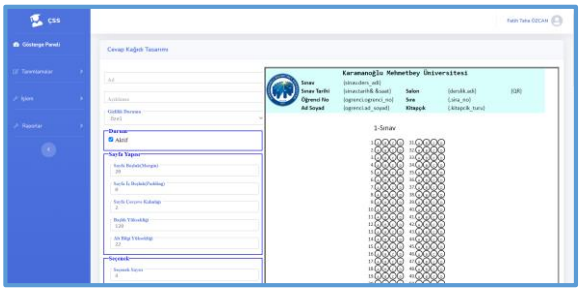

(h) Optical form design page

Figure 1. *Interface of the system*

Figure 2 shows the evaluation workflow of the system. Image file containing optical form data respectively is subjected to image processing algorithms like grayscale conversion, application of Gaussian smoothing filter to reduce noise, applying morphological opening to remove black pixel distortions, thresholding and binary level transform, angular correction, contour extraction, QR code extraction and Hough circle transform. To decide whether the option is checked, the largest square that will fit inside the circle is found, and the option is considered checked if at least 50% of the square's area is ticked.

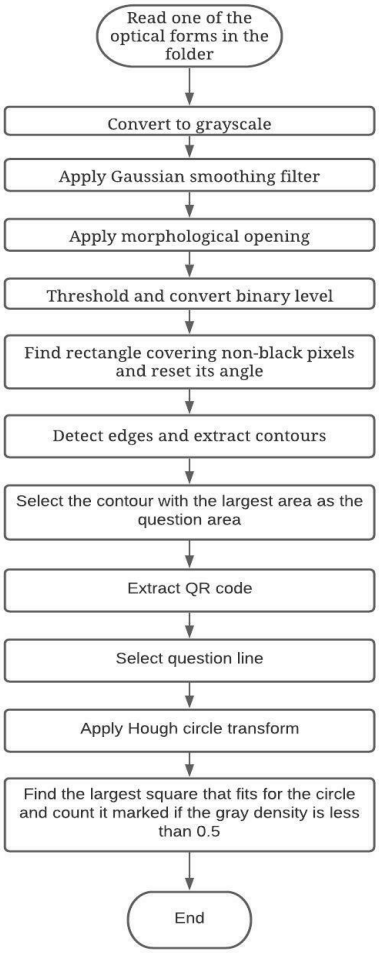

Figure 2. *Evaluation workflow*

The results obtained when the techniques mentioned are applied to the optical form are shown in Figure 3. After the aforementioned pre-processing steps, QR code extraction was performed as seen in Figure 4. According to the location of the QR code found, it is decided whether the image is inverted and, if necessary, the image is rotated 180 degrees again.

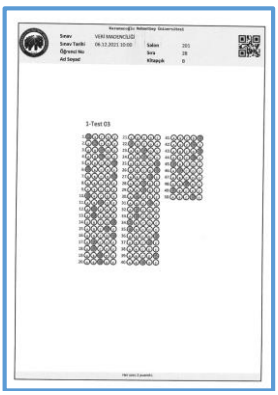

(a) Colored image is converted to grayscale image for reducing the memory space of the file.

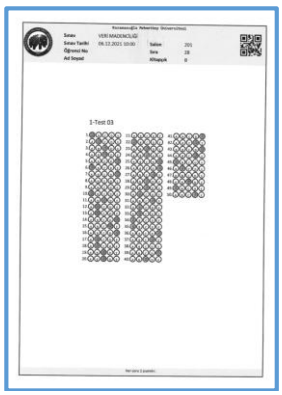

(b) Gaussian filter is applied to reduce noise.

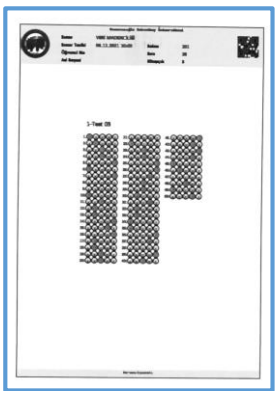

(c) Morphological opening is applied to remove the breaks in the black pixels.

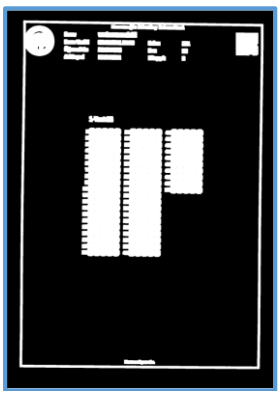

(d) Thresholding is applied to reduce noise and the image is converted to binary image. Since image processing algorithms generally perceive black pixels as background, black and white pixels are switched.

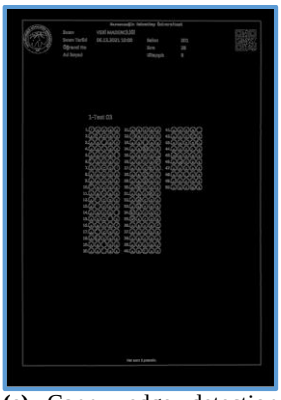

(e) Canny edge detection algorithm is applied to detect the edges in the image.

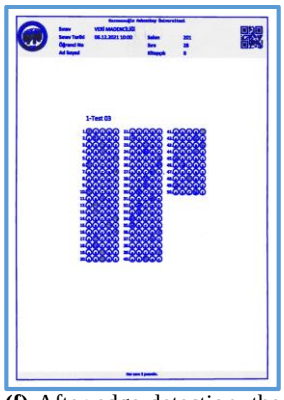

(f) After edge detection, the contours in the image are searched and the rectangular contour with the largest area is selected as the response area.

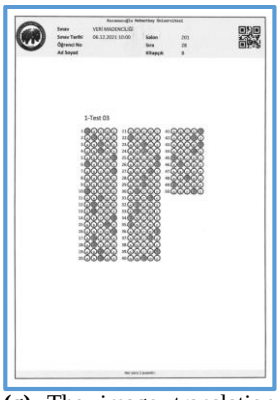

(g) The image translation algorithm is applied to reset the angle of the selected rectangle.

Figure 3. *Evaluation detailed steps*

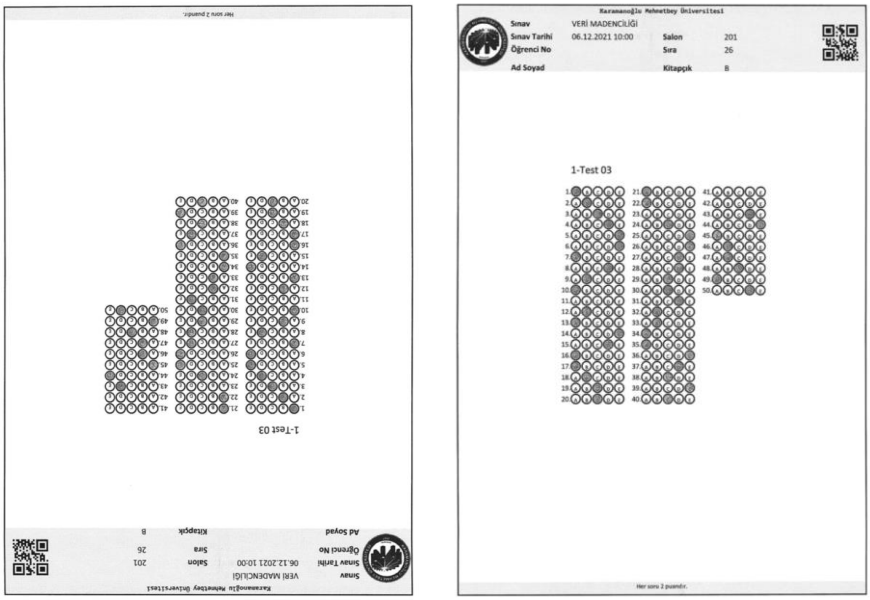

Figure 4. *QR code check*

Question evaluation steps were applied as shown in Figure 5.

(a) The question line is determined with the help of the previously calculated scale.

(b) The circles in the found question line are determined using the Hough circle transform algorithm.

(c) The largest square to fit inside the detected circles is calculated and for each option, the gray color intensity in this selected square is proportioned to 255. If the ratio is less than 0.5, the option is considered marked.

Figure 5. *Question evaluation stages*

After evaluating all the questions, the correct answers are marked in green, the wrong answers in red, the correct answers in the wrong or empty options are marked in blue, and the invalid answers are marked in purple. An orange line is used for blank questions and a purple cross for invalid questions. The resulting markings are shown in Figure 6.

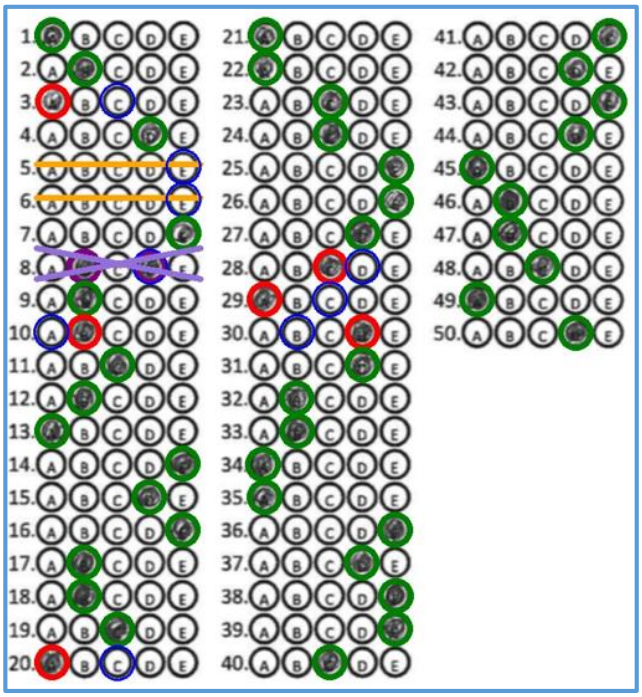

Figure 6. *Answer sheet marked by the system*

4. Result and discussion

In order to measure the accuracy and performance of the designed system, the evaluation of 5785 questions in 208 optical forms in 3 different exams of the students studying at the Computer Engineering Department of Karamanoğlu

Mehmet bey University was made at 3 different scanner resolution levels. As a result of these tests, the accuracy rate of the web-based optical form reading system was measured as 99.9%. In Figure 7, 3 different optical form designs used in exams are shown. The system designed in the study was tested with questions with 4 or 5 options, different columns and questions.

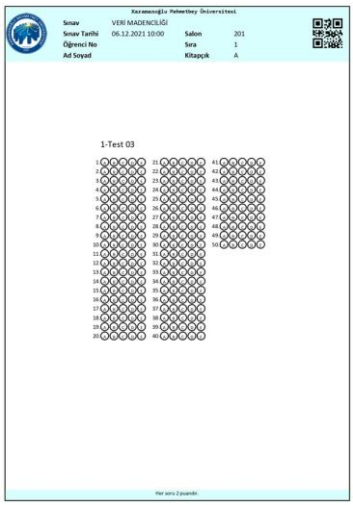

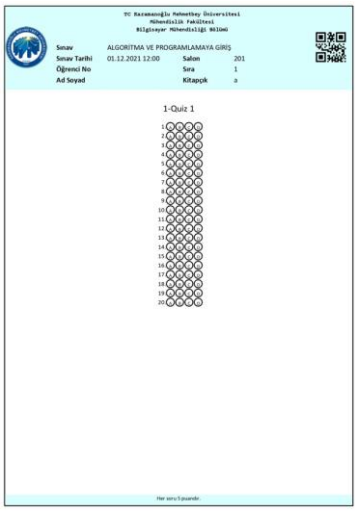

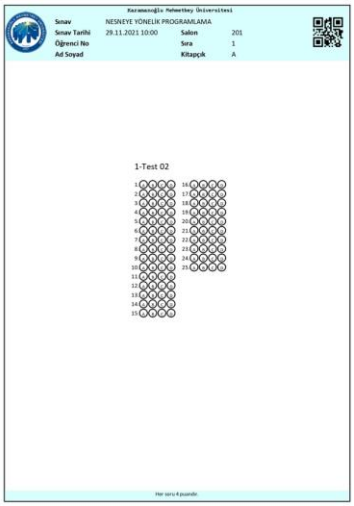

Figure 7. *Optical form designs used in exams*

In Table 2, the test results are shown in detail on the basis of scanning resolution. Since the evaluation period of the system is an important indicator in terms of performance, the tests were carried out both in parallel and in series. During the tests, the time taken to evaluate one optical form is between 2.8 seconds and 1.8 seconds when scanned at 200 DPI resolution, between 8.3 seconds and 5.8 seconds when scanned at 300 DPI resolution, and between 16 seconds and 10.9 seconds when scanned at 600 DPI resolution. In Table 3, the time performance of the system is shown in detail on the basis of scanning resolution.

Table 2. The accuracy performance of the system

		Number of Optical Forms Uploaded	Percentage of Errorless Optical Forms	Number of Questions	Percentage of Questions Read Correctly	Number of Options	Percentage of Correctly Evaluated Options
DPI	200	208	96.63%	5785	99.88%	25140	99.97%
	300	208	93.75%	5785	99.74%	25140	99.94%
	600	208	87.98%	5785	99.46%	25140	99.88%

Table 3. Time performance of the system

	Number of Optical Forms Evaluated	1 Optical Form Evaluation Time (Second)	1 Optical Form Evaluation Time (Seconds) in Parallel Mode
200 DPI	208	2.815	1.795
300 DPI	208	8.277	5.774
600 DPI	208	16.062	10.882

As a result of the test studies, it has been revealed that the most optimal performance of the system will be achieved with 200DPI scanning resolution and parallel operation. In order to increase the correct reading performance to 100%, it is thought that it will be achieved by informing the students more about marking and the use of optical form.

References

[1]. Temizkan, M. and M.E. Sallabaş, Okuduğunu Anlama Becerisinin Değerlendirilmesinde Çoktan Seçmeli Testlerle Açık Uçlu Yazılı Yoklamaların Karşılaştırılması. Dumlupınar Üniversitesi Sosyal Bilimler Dergisi, 2011(30): p. 207-220.

[2]. Çakan, M., Geniş ölçekli başarı testlerinin eğitimindeki yeri ve önemi. Eğitim ve Bilim, 2003. 28(128).

[3]. Nguyen, T.D., et al. Efficient and reliable camera based multiple-choice test grading system. 2011. IEEE.

[4]. Aydemir, F., Standart Tarayıcılarla Web Tabanlı Bilgisayar Mühendisliği. 2012.

[5]. Al-Marakeby, A., Multi Core Processors for Camera based OMR. International Journal of Computer Applications, 2013. 68(13): p. 1-5.

[6]. Fisteus, J.A., A. Pardo, and N.F. García, Grading multiple choice exams with low-cost and portable computer-vision techniques. Journal of Science Education and Technology, 2013. 22(4): p. 560-571.

[7]. Sattayakawee, N., Test scoring for non-optical grid answer sheet based on projection profile method. International Journal of Information and Education Technology, 2013. 3(2): p. 273-273.

[8]. Şenol, M. and U. Fidan, C# ile Web Kameradan Optik Form Okuma. Afyon Kocatepe University Journal of Science & Engineering, 2014. 14(2).

[9]. Patel, R., et al. CheckIt-A low cost mobile OMR system. 2015. IEEE.

[10]. Hasan, R.H. and E.I.A. Kareem, An Image Processing Oriented Optical Mark Reader Based on Modify Multi-Connect Architecture MMCA. International Journal of Modern Trends in Engineering and Research (IJMTER), 2015. 2(7).

[11]. Yüksel, A.S., et al., Mobile based optical form evaluation system. Pamukkale Üniversitesi Mühendislik Bilimleri Dergisi, 2016. 22(2): p. 94-99.

[12]. Gyamfi, E.O. and Y.M. Missah, Pixel-Based Unsupervised Classification Approach for Information Detection on Optical Markup Recognition Sheet. Advances in Science, Technology and Engineering Systems Journal, 2017. 2(4): p. 121-132.

[13]. Loke, S.C., K.A. Kasmiran, and S.A. Haron, A new method of mark detection for software-based optical mark recognition. Plos One, 2018. 13(11).

[14]. Küçükkara, Z. and A.E. Tümer, An Image Processing Oriented Optical Mark Recognition and Evaluation System. International Journal of Applied Mathematics Electronics and Computers, 2018. 6(4): p. 59-64.

[15]. Espitia, O., et al. Optical Mark Recognition Based on Image Processing Techniques for the Answer Sheets of the Colombian High-Stakes Tests. 2019. Springer.

[16]. Afifi, M. and K.F. Hussain, The achievement of higher flexibility in multiple-choice-based tests using image classification techniques. International Journal on Document Analysis and Recognition (IJDAR), 2019. 22(2): p. 127-142.

[17]. Ha, T. and N. Thu, An Application of Image Processing in Optical Mark Recognition. Vietnam Journal of Agricultural Sciences, 2020. 3(4 SE - ENGINEERING AND TECHNOLOGY).

[18]. Çayıroğlu, İ., Resim Yumuşatma (Bulanıklaştırma-Blurrıng) Filtreleri. 2021.

[19]. Ballard, D.H., Generalizing the Hough transform to detect arbitrary shapes. Pattern Recognition, 1981. 13(2): p. 111-122.

[20]. Şaan, T.G., MPI İle Paralel Programlama. 2017.

MANAS Journal of Engineering
ISSN 1694-7398 | e-ISSN 1694-7398

Volume 11, Issue 1, (2023) Pages 74-82
https://doi.org/10.51354/mjen.1223399

Analysis of the azimuth angles of a medium-scale PV system in non-ideal positions for roof application

Muharrem Hilmi Aksoy[1,*], Murat Ispir[2], Mahmud Bakirhan[3]

[1] Konya Technical University, Faculty of Engineering and Natural Sciences, Konya, Türkiye, mhaksoy@ktun.edu.tr, ORCID: 0000-0002-6509-8112

[2] Konya Technical University, Faculty of Engineering and Natural Sciences, Konya, Türkiye, mispir@ktun.edu.tr, ORCID: 0000-0001-5238-6011

[3] İmaş Makina Sanayi A.Ş., R&D Center, Konya, Türkiye, mahmut.bakirhan@imas.com.tr, ORCID: 0000-0002-7498-9646

ABSTRACT

The installation of photovoltaic (PV) panels on building roofs has seen a significant increase in recent years due to the rising cost of conventional energy sources. This shift towards renewable energy sources has been driven by the urgent need to mitigate the effects of climate change. PV applications is one of the most sustainable and cleanest sources of renewable energy, producing no greenhouse gas emissions during operation. By reducing reliance on fossil fuels, the use of PV panels can help to reduce carbon emissions and lower the overall carbon footprint of buildings. In addition to the environmental benefits, the installation of PV panels can also provide economic benefits, such as reduced energy costs and increased property value. In the past, installations were mostly made in the direction of the south, but now the roofs of the buildings facing west, east, and even north are also considered for PV panel installations.

In this study, a grid-connected PV system with an installed power of 148 kWp at the Konya Technical University (KTUN) campus is modeled by PVsyst software. The PV systems' performance on building roofs oriented in different geographical directions (north, south, east, and west) with a 30° fixed tilt angle was investigated. In the modeling, the solar irradiation coming to the surfaces of the PV panels, electricity production values, performance ratios, and their economic feasibility were calculated. The highest effective irradiation value on the panel surface was obtained from the system facing south, found as 1964.4 kWh/m². It is 20.77%, 22.87%, and 73.48% higher than the solar irradiation obtained at -90°, +90°, and 180° azimuth angles, respectively. It is concluded that the electricity generation amounts of PV systems highly depend on the azimuth angle. Similarly, the highest annual electricity production was obtained from the system installed in the 0° azimuth angle found as 254.77 MWh. The annual total electricity generation is 19.66%, 22.55%, and 69.41% higher in systems modeled toward the east, west, and north, respectively. Performance ratio, defined as the ratio of radiation coming to the panel surface and the electricity produced, has relative values between 0.843 and 0.862 for four different azimuth angles. Furthermore, as an economic analysis, the Basic Payback Period (BPP) of the projects was found as 6.92 years, 4.08 years, 4.88 years, and 5.00 years for the systems modeled in the north, south, east, and west directions, respectively. It can be concluded that the most suitable orientation is south, and the other two directions, east, and west, can also be considered feasible.

ARTICLE INFO

Research article

Received: 25.12.2022
Accepted: 16.05.2023

Keywords:
azimuth angle,
economic analysis,
photovoltaic panel,
solar energy.

*Corresponding author

1. Introduction

Renewable energy sources, such as solar and wind power, produce little to no greenhouse gas emissions, which can help to combat climate change. In addition, renewable energy can provide a reliable and stable source of electricity, particularly in remote or underserved areas. It can also help to create jobs and stimulate economic growth, particularly in rural communities where renewable energy projects are often located. Increasing the use of renewable energy can help reduce our dependence on foreign sources of fossil fuels, such as Turkey, which can have national security and economic benefits. It can also help reduce the impact of energy price fluctuations, as the cost of renewable energy sources is often

more stable than fossil fuels [1]. Although renewable energy sources are found in every country, their technical and economic feasibility varies according to geographical locations. [2,3].

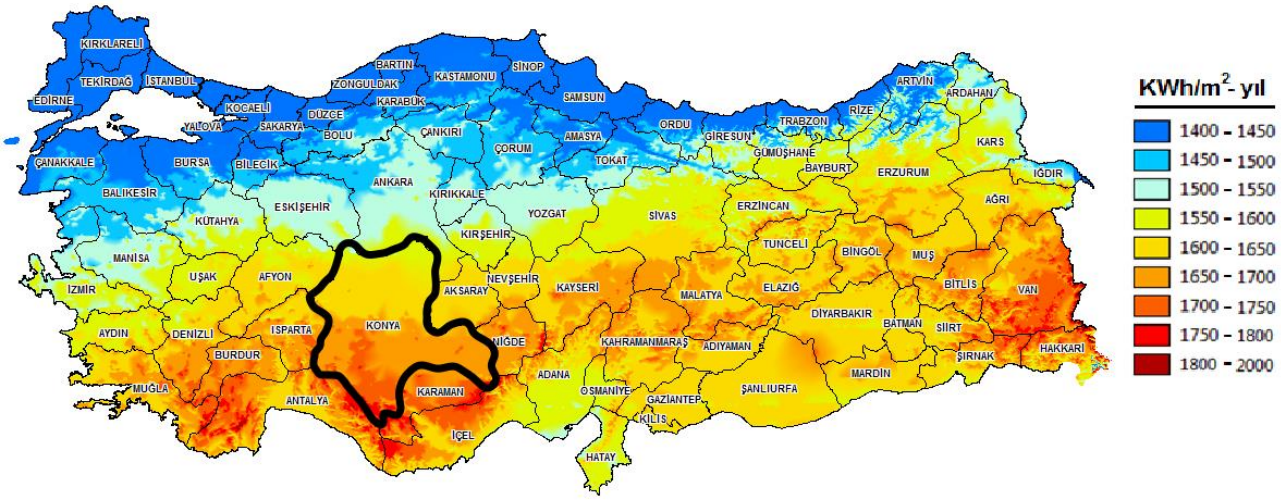

Figure 1. *The Solar Irradiation Potential of Turkey and Konya* [4,5]

Solar energy is a clean and abundant source of energy that can be harnessed in various ways, including PV cells. In addition, the cost of solar energy is decreasing, making it a more affordable option for residential and commercial users [6,7]. Solar energy systems can be used in various installation cases, including grid-connected, stand-alone, and a combination. In addition, these systems have wide application areas such as irrigation, cooling, and water pumping [8].

PV panels are devices that convert sunlight into electricity. As of 2021, the total installed capacity of PV panels worldwide is approximately 600 GW [9]. This installation represents a significant increase from previous years, as the global PV market has been growing rapidly in recent years due to falling costs and increasing demand for clean and renewable energy. Most PV panels are installed in Asia, particularly in China, which has the world's largest installed capacity at over 200 GW [10,11]. Other major PV markets include the European Union, the United States, and Japan. Due to Turkey's geographical conditions, it is in an advantageous position compared to many European countries with its 7.2 hours/day sunshine duration and 3.6 kWh/m² daily average solar radiation value [12]. The efficiency that can be achieved in Turkey also varies according to the location. As seen in Figure 1, the annual amount of radiation is higher in the southern and Mediterranean regions of Central Anatolia, including Konya, compared to other regions.

As of 2021, Turkey's total installed capacity of PV panels is approximately 7.8 GW [13]. This instillation represents a significant increase from previous years, as the Turkish government has been implementing policies to support the country's PV market growth [14]. A combination of favorable solar resources and government policies has driven the growth of the PV market in Turkey. As the country continues to transition away from fossil fuels and towards clean and renewable energy, the use of PV panels is expected to continue to grow and play an important role in meeting Turkey's energy needs. Installed power and the ratios of total installed power of PV systems between 2014 and June 2022 are given in Figures 2 and 3, respectively [15]. The figures show that the tendency to obtain electrical energy from solar energy has increased considerably in recent years in Turkey. Also, bank financings and incentives are given by the government to establish facilities play an important role in this increase [16]. In addition, a tender was made for the facility with an installed capacity of 1000 MW in the Renewable Energy Resources Area (YEKA) in Konya's Karapınar district in 2016 [17]. When the project is completed, it is expected to meet 24% of the electricity consumption of Konya and 0.6% of Turkey, with an electricity production of 2300 GWh.

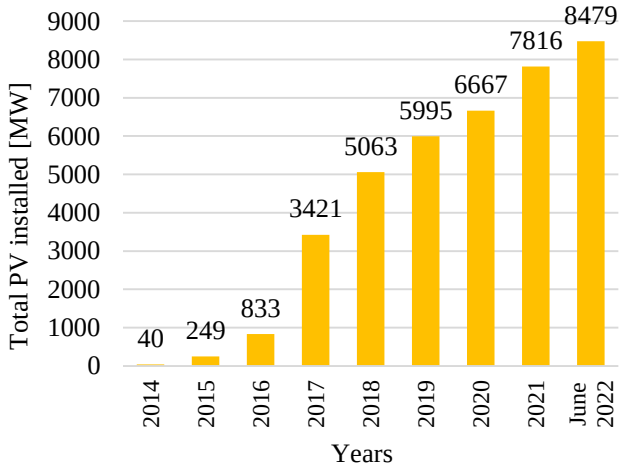

Figure 2. *Turkey's total PV installed capacity by years* [15]

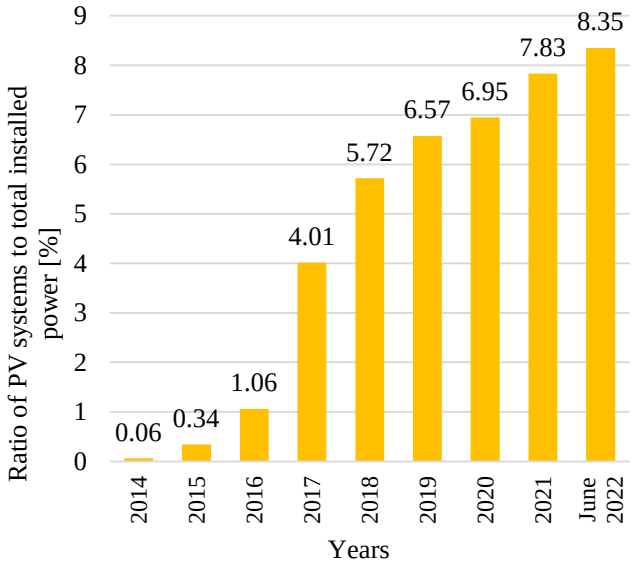

Figure 3. *The ratio of Turkey's PV systems to installed power by years* [15]

The tilt angle, known as the angle of the PV panel surface with the ground, has a very important place in the PV performance. The annual optimum value of this angle is approximately equal to the latitude angle of the place where the system will be installed. In addition, this angle changes seasonally. Since the angle of incidence of the radiation changes, the optimum tilt angle is approximately 15° smaller than the latitude angle in summer and approximately 15° greater in winter. In addition to the tilt angle, the azimuth angle, which is the angle that the panel makes in the north-south direction, also plays an important role in the PV performance [18]. The azimuth angle of the system located in the northern hemisphere and established towards the south is 0°. While this value is positive towards the west, it is negative towards the east. When these two angles are compared, the tilt angle is more important than the azimuth [19]. However, the tilt angle can be adjusted in both field and roof applications, while the azimuth angle can be adjusted in field applications but not generally in roof applications. Some studies examine the performance of the tilt and azimuth angle on the system. For example, roof models were made using four different azimuth angles as -87°, -32°, +2°, and +17° and electricity generation of the systems was examined in Huddersfield, England. The highest electricity production was obtained from the system with an azimuth angle of +2°, while the lowest was obtained with an azimuth angle of -87° [20]. Another study found that the orientation of PV panels can significantly affect their electricity-generating potential. The study found that south-facing PV panels in the northern hemisphere could generate more electricity than east- or west-facing panels and that the difference in output increased as the latitude of the panels increased [21]. Kiviluoma et al. [22] found that the angle at which PV panels are tilted can also affect their performance. The study found that tilting PV panels at an angle equal to their latitude maximized the amount of sunlight they could capture and convert into electricity and that this angle varied depending on the location of the panels. Pal et al. [23] examined the combined effect of orientation and tilt angle on the performance of PV panels. The study found that the optimal orientation and tilt for PV panels varied depending on the system's location and the time of year, but that, in general, south-facing panels tilted at an angle equal to their latitude were able to generate the most electricity. Barbón et al. [19] investigated the effects of tilt and azimuth angles on the system. Within the scope of the study, ten different cities were considered. They calculated the energy losses at different tilt angles using an azimuth angle of 0°. They calculated that 5% energy loss occurs at tilt angles between 21 and 23°, 10% at tilt angles between 31 and 33°, 15% at tilt angles between 37 and 40°, and 20% at tilt angles between 43 and 47°. They also concluded that azimuth and tilt angles have less effect in cities with low latitudes. Sun et al. [24] modeled the electricity generation obtained from the PV system at various shading percentages in Hong Kong using five different azimuth angles as -90°, -45°, 0°, 45°, and 90°, and seven different tilt angles as between 20 and 80. They obtained the most electricity production from the system with an azimuth angle of 0° and without shading. In addition, they observed that the amount of electricity decreased with the increase in the tilt angle in Hong Kong, which has a latitude of 22.57°. Aksoy et al. [25] investigated the effect of five different azimuth angles -30°, -15°, 0°, 15°, and 30° on system performance using PVsyst. In addition, they also examined the effect of shading losses on the system, which will occur from two different panel heights of 0.1 m, and 1 m and two different panel spacings of 4 m, and 8 m, and compared with no-shading systems. They obtained the highest annual electricity generation (E_G) from no-shading systems with 0° azimuth angle as 174.33 MWh and found this value to be 12.86% and 3.68% higher than for systems with 4 m and 8 m panel spacing, respectively. They also concluded that the panel heights do not affect the system performance.

The widespread adoption of PV roof applications in recent years can be attributed to several factors, including the rising cost of electricity, government incentives and regulations, advances in technology and manufacturing processes, the need for energy independence, and growing concerns about climate change. Additionally, the improved aesthetics and design options of PV panels have made them more appealing to consumers, further contributing to their widespread adoption. The roofs of houses and factories may not be positioned toward the south, and the electricity generation values of the systems installed in directions other than the south should be evaluated [26]. Therefore, in this study, PV system modeling and comparisons of different oriented systems were made using the PVsyst software with a fixed tilt angle of 30° and four different azimuth angles, -180°, 0°, -90° and 90° to the north, south, east, and west directions, respectively.

2. Material and method

PVsyst is a software program used to design and simulate PV systems. It is a commonly used tool among PV professionals and researchers, as it offers a range of features and tools for analyzing and optimizing the performance of PV systems. PVsyst allows users to create detailed models of the systems, considering factors such as the location and orientation of the panels, the type of PV cells and inverters used, and the environmental conditions at the site. The program then simulates the performance of the PV system under different conditions, allowing users to evaluate its performance and identify potential issues or areas for improvement. In addition, PVsyst also offers a range of tools for analyzing and optimizing the performance of PV systems. These tools include sizing PV systems, calculating energy yield, and estimating the financial return on investment. In the literature, studies from Turkey [27-32] and around the world [33-37] analyzed PV systems using PVsyst. For example, Aksoy et al. [38] performed performance analysis of three different cells, monocrystalline, polycrystalline, and amorphous silicon, with a fixed installed power of 300 kWp using PVsyst in Konya, Turkey. They used a tilt angle of 35° and an azimuth angle of 0° in this study. the highest electricity production was obtained from monocrystalline cells with an annual value of 513.91 MWh. This value is 1.91% and 3.07% higher than the electricity produced by polycrystalline and amorphous silicon. In addition, in the economic analysis, it was found that monocrystalline and polycrystalline systems pay for themselves in about 6 years, while amorphous silicon pays off in 9 years.

A PV system with a power of 148 kWp was modeled on the roof of any building in the KTUN campus with a latitude of 38.03 °N and longitude of 32.51 °E, which was determined by using the METEO 8.0 program, which is a part of the PVsyst software. The view of KTUN from space is given in Figure 4. Totally 528 modules, with 22 horizontal and 24 vertical, were used in all modeled systems. While the total area covered by the modeled system is 866 m², the panel surface area is 779 m². Polycrystalline cells with model number CWT280 – 60P produced by Generic were selected as PV panels.

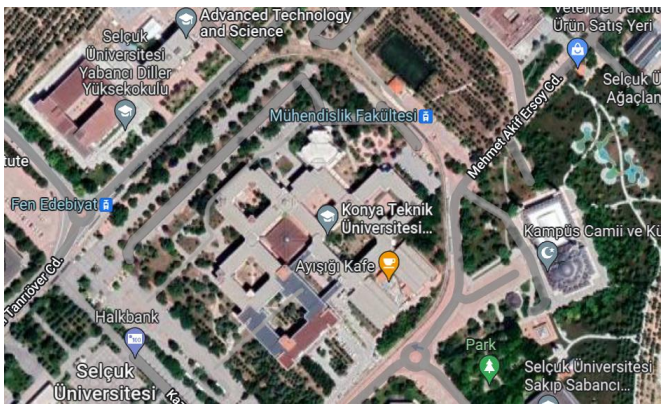

Figure 4. *The satellite view of KTUN*

Another parameter of a PV system is the performance ratio (P_R) which is calculated as the ratio of E_G to the global horizontal radiation (I_{GH}) incident on the panel surface in a system with a unit installed power [39].

$$P_R = \frac{E_G}{I_{GH} \times P_{PV}} \quad (1)$$

Where P_{PV} is the rated power of the PV system
The amount of radiation was calculated mathematically on a daily or monthly basis depending on the location. The daily radiation amount was calculated as follows [40].

$$I_{GH} = \frac{24\times3600 G_{SC}}{\pi}\left[1 + 0.033cos\left(\frac{360n}{365}\right)\right] \times cos\varphi\, cos\delta\, cos\omega_s + \frac{2\pi\omega_s}{360} sin\varphi sin\delta \quad (2)$$

Here n is the number of day, φ, δ and ω_s are the latitude angle, declination angle, and sunset time angle for the mean day of the month, respectively, and are calculated as follows.

$$\omega = 15(ST - 12) \quad (3)$$

$$\delta = 23.45\, sin\left(360\frac{284+n}{365}\right) \quad (4)$$

Where ST is local time and equals 12 at midday. Current PVsyst software uses the Perez model as the transposition method. In this model, the aim is to calculate the amount of radiation incident to the inclined plane from the horizontal radiation data. When compared with these real data, the error rate of PVsyst is less than 2% [41].

For the projects to be implemented, primarily economic analysis is required. The basic step of economic analysis is BPP is calculated as follows.

$$BPP = \frac{Initial\ investment}{Annual\ net\ cash\ inflow} \quad (5)$$

3. Result and discussion

Global solar radiation on a surface refers to the amount of solar radiation received by a surface over a period. Global solar radiation is typically measured in power units per unit area, as watts per square meter (W/m^2). The amount of global solar radiation that a surface receives depends on various factors, including the location of the surface, the time of year, and the angle at which the sun's rays strike the surface. In general, surfaces closer to the equator and receive direct sunlight for a longer period each day will receive more global solar radiation than surfaces located at higher latitudes and with less direct sunlight. The amount of irradiation coming to the panel surface affects the performance of PV systems directly. I_{GH} is the monthly average global horizontal irradiation for the location of KTUN in Konya, Turkey, given

in Figure 5. These irradiation values were analyzed with different mathematical models according to the tilt angle of the panels using PVsyst. The highest solar irradiation of all orientations occurred in July as 199.3 kWh/m², 219.8 kWh/m², 212.5 kWh/m², and 218.5 kWh/m² for north, east, west, and south, respectively. As seen in the summer months, the difference in radiation values is not so much, but in winter, the difference seems more visible. Yearly total solar radiation is obtained as 2007.4 kWh/m² from the south-oriented system. This value is annually 20.13%, 22.05%, and 66.4% higher than east, west, and north, respectively. The electricity generation values are also calculated on the inclined surface of the panels.

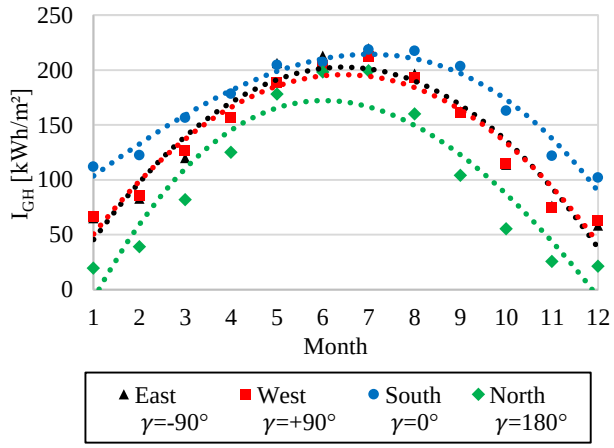

Figure 5. *Average monthly I_{GH} at various azimuth angles*

The solar irradiation is affected by losses such as shading and IAM and loses some of its energy levels. The irradiation after these loses is called Effective Global Radiation (I_{EG}). The monthly average I_{EG} reaching panel surfaces of different azimuth angles obtained with PVsyst is given in Figure 6.

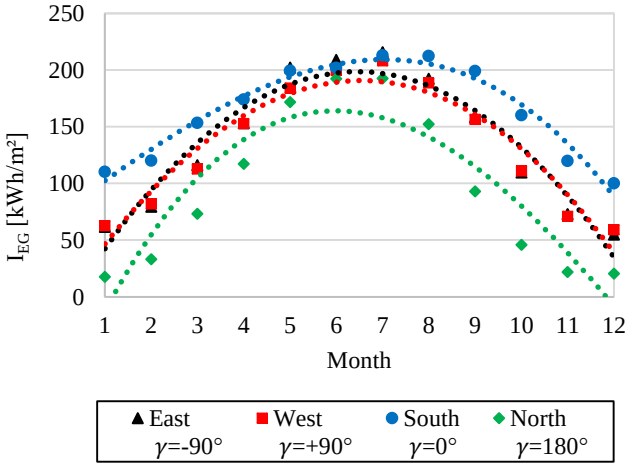

Figure 6. *Monthly average I_{EG} amounts coming into the system at various azimuth angles*

Like I_{GH}, the amount of I_{EG} is highest in the south direction and the lowest in the north direction surfaces. Systems modeled toward north, south, east, and west directions suffered radiation losses of 6.14%, 2.14%, 2.79%, and 2.66%, respectively. The lowest loss was found in the system modeled toward the south direction. Because according to KTUN, which is located in the northern hemisphere, the sun rises and sets in the southern direction. Therefore, the least loss occurs in systems modeled towards the south.

The monthly total E_G values obtained from PV systems with various azimuth angles using I_{EG} are given in Figure 7.

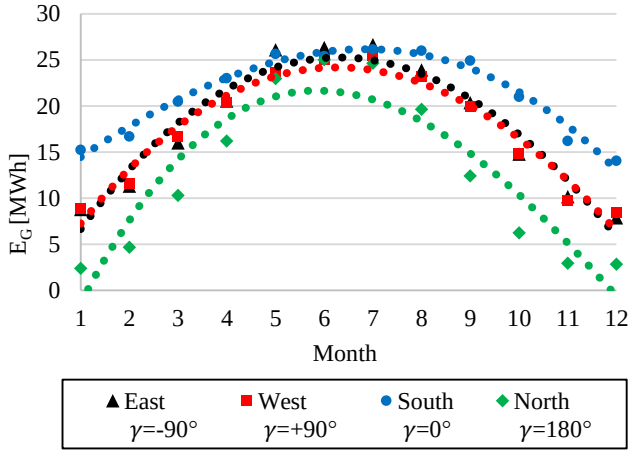

Figure 7. *Monthly average I_{EG} amounts of systems at various azimuth angles*

Since I_{EG} coming to the panel surface is higher in summer, E_G is also higher too. In addition, since I_{EG} It has the highest radiation value in the south direction, producing the highest electricity with a yearly total of 254.76 MWh. This value is 69.43%, 19.65 and 22.55% higher than the E_G by systems modeled toward north, east, and west directions, respectively. Using the values in Figures 5 and 6 and Eq. (1), P_R can be calculated. The P_R of a PV system refers to the ratio of the actual power output of the system to its theoretical maximum power output under specific operating conditions. The performance ratio can be affected by various factors, including the efficiency of the PV panels, the amount of sunlight available, and the panels' temperature. The monthly P_R values of the systems modeled in four different directions are shown in Table 1.

Table 1. *The monthly average P_R values of different oriented systems*

Months	East ($-90°$)	West ($+90°$)	South ($-0°$)	North ($\pm 180°$)
1	0.916	0.910	0.921	0.838
2	0.926	0.919	0.923	0.815
3	0.904	0.895	0.884	0.854
4	0.885	0.880	0.872	0.878
5	0.856	0.850	0.848	0.872
6	0.837	0.830	0.829	0.854
7	0.820	0.811	0.809	0.837
8	0.822	0.813	0.809	0.831
9	0.848	0.836	0.828	0.807
10	0.881	0.874	0.871	0.765
11	0.902	0.891	0.900	0.789
12	0.916	0.913	0.933	0.901
Average	0.862	0.855	0.858	0.843

It is seen that the highest P_R's are seen in the winter months. While the P_R values of the systems modeled towards the east, west, and south directions decrease towards the summer and increase towards the winter. However, since KTUN is in the northern hemisphere and is opposite to solar radiation, the situation is the opposite in the system modeled towards the north. The monthly highest P_R value of 0.933 was observed in the system modeled towards the South direction in December, while the lowest one was observed in the system modeled towards the north with a value of 0.765 in October.

The economic feasibility of a PV system depends on several factors, including the system's initial cost, the local climate and weather conditions, the amount of sunlight the system will receive, and the current and projected cost of electricity from the grid. Other factors that may affect the economic feasibility of a PV system include any available incentives or subsidies, the expected lifespan of the system, and the maintenance and repair costs over time [42-46]. The Basic Payback Period (BPB) is the time it takes for the savings generated by an investment to equal the initial cost of the investment. In the case of a PV system, also known as a solar panel system, the payback period is the length of time it takes for the savings on electricity bills to equal the initial cost of the PV system. BPP was calculated by using Eq. (5) in this study. The values listed below were used in the calculation.

- The unit investment cost of the panels is taken as 1.2 $/Wp [47].
- The operation and maintenance costs of the systems have been accepted as 2.5% of the investment cost [47].
- The electricity sales price has been determined as 0.175 $/kWh

Using the above items, the BPP values of the systems installed toward the north, south, east, and west directions were calculated as 6.92 years, 4.08 years, 4.88 years, and 5.00 years, respectively.

4. Conclusion

In conclusion, the installation of photovoltaic (PV) panels on building roofs has become increasingly common in recent years due to the urgent need to mitigate the effects of climate change and the economic benefits it offers. This study provides valuable insights into the performance and economic feasibility of PV systems on building roofs oriented in different geographical directions. The results indicate that the electricity generation amounts of PV systems are highly dependent on the azimuth angle, with south-facing systems producing the highest effective irradiation values and annual electricity production. The obtained results are given below.

- The maximum I_{GH} and I_{EG} coming on the panel surface were obtained from the model towards the south direction (azimuth angle of 0°) with values of 2007.4 kWh/m² and 1964.4 kWh/m², respectively.
- Since I_{GH} and I_{EG} on PV panels are highest, the highest annual E_G was also obtained from the system modeled toward the south with a total value of 254.76 MWh. The annual total electricity generation from the systems towards the north, east, and west directions were found to be 150.38 MWh, 212.9 MWh, and 207.88 MWh, respectively.
- It was determined that the P_Rs of the systems modeled towards the east, west, and south directions decreased towards the summer and higher in winter due to low loss due to ambient temperature.
- On the other hand, it has also been observed that the P_R values between the modeled systems are very close to each other and at a negligible level.
- The lowest BPP was obtained from the system modeled towards the south with 4.08 years. This value is 40.98%, 16.42% and 18.40% lower at the north, east and west directions, respectively.

This research underscores the importance of considering geographical orientation in the planning and implementation of PV systems to maximize their energy production and economic viability. It is recommended to make the economic analysis with Internal rate of return and Net present value methods for systems installed in different directions.

Acknowledgment

This study was orally presented at the 6th International Conference on Engineering Technologies (ICENTE'22).

References

[1]. Kabir, E., Kumar, P., Kumar, S., Adelodun, A. A., Kim, K. H., "Solar energy: Potential and future prospects". Renewable and Sustainable Energy Reviews, 82, (2018), 894-900.

[2]. Van Vuuren, D. J., Marnewick, A. L., Pretorius, J. H. C., "Validation of a Simulation-Based Pre-Assessment Process for Solar Photovoltaic Technology Implemented on Rooftops of South African Shopping Centres." Sustainability, 13(5), (2021), 2589.

[3]. Kose, F., Aksoy, M. H., Ozgoren, M., "Experimental investigation of solar/wind hybrid system for irrigation in Konya, Turkey." Thermal Science, 23(6 Part B), (2019), 4129–4139.

[4]. GEPA, "Solar Energy Potential Atlas", Republic of Turkey Ministry of Energy and Natural Resources, https://gepa.enerji.gov.tr/MyCalculator [Accessed: 25 December 2022].

[5]. Çeçen, M., Yavuz, C., Tırmıkçı, C. A., Sarıkaya, S., Yanıkoğlu, E., "Analysis and evaluation of distributed photovoltaic generation in electrical energy production and related regulations of Turkey". Clean Technologies and Environmental Policy, (2022), 1-16.

[6]. Yong, C., Desen, J., Wen, L., Yunlong, C., "Research on the cost of distributed photovoltaic plant of China based on whole life cycle perspective". IEEE Access, 7, (2019), 89379-89389.

[7]. Li, J., "Optimal sizing of grid-connected photovoltaic battery systems for residential houses in Australia." Renewable energy, 136, (2019), 1245-1254.

[8]. Rödl, A., Kaltschmitt, M., Schaumburg, H., "Strategy for A Large Scale Introduction Of Solar Energy In Central Asia." MANAS Journal of Engineering, 5(3), (2017), 48-56.

[9]. Jaxa-Rozen, M., Trutnevyte, E., "Sources of uncertainty in long-term global scenarios of solar photovoltaic technology". Nature Climate Change, 11(3), (2021), 266-273.

[10]. Kılıç, U., Kekezoğlu, B., "A review of solar photovoltaic incentives and Policy: Selected countries and Turkey". Ain Shams Engineering Journal, 13(5), (2022), 101669.

[11]. Pandey, A., Pandey, P., Tumuluru, J. S., "Solar energy production in India and commonly used technologies—An overview." Energies, 15(2), (2022), 500.

[12]. Kaya, M. N., Aksoy, M. H., Köse, F., "Renewable Energy in Turkey: Potential, Current Status and Future Aspects." Annals of Faculty Engineering Hunedoara – International Journal of Engineering Time. 15, (2017), 65–69.

[13]. Kaymak, M. K., Şahin, A. D., "The First Design and Application of Floating Photovoltaic (FPV) Energy Generation Systems in Turkey with Structural and Electrical Performance". International Journal of Precision Engineering and Manufacturing-Green Technology, 9(3), (2022), 827-839.

[14]. Çiçek, O., Mıllad, M. A. M., Erken, F. "Energy prediction based on modelling and simulation analysis of an actual grid-connected photovoltaic power plant in Turkey". European Journal of Technique (EJT), 9, (2019), 159-174.

[15]. Republic of Turkey Ministry of Energy and Natural Resources, "Solar Energy" https://enerji.gov.tr/eigm-yenilenebilir-enerji-kaynaklar-gunes, [Accessed: 25 December 2022]. (in Turkish).

[16]. Doğan S, Yağmur S. Aksoy M. H., Köse F. Solmaz O., "Solar Energy Potential in Turkey and Manufacturability Research for Equipments of Photovoltaic Panel in Konya Province" III. International Congress on Environmental Research and Technology ICERAT 2017, Belgrade, Serbia, November 08-12, 2017. pp. 35.

[17]. Enerji Atlası, "YEKA", https://www.enerjiatlasi.com/gunes/karapinar-yeka-11.html, [Accessed: 25 December 2022]. (in Turkish).

[18]. Desai, A., Mukhopadhyay, I., Ray, A. "Effect of azimuth and tilt angle on ideally designed rooftop solar PV plant for energy generation." 2021 IEEE 48th Photovoltaic Specialists Conference, PVSC 2021, pp. 522-527.

[19]. Barbón, A., Bayón-Cueli, C., Bayón, L., Rodríguez-Suanzes, C., "Analysis of the tilt and azimuth angles of photovoltaic systems in non-ideal positions for urban applications." Applied Energy, 305, (2022), 117802.

[20]. Dhimish, M., Silvestre, S., "Estimating the impact of azimuth-angle variations on photovoltaic annual energy production." Clean Energy, 3(1), (2019), 47–58.

[21]. Osmani, K., Ramadan, M., Lemenand, T., Castanier, B., Haddad, A. (2021). Optimization of PV array tilt angle for minimum levelized cost of energy. Computers Electrical Engineering, 96, 107474.

[22]. Baghoolizadeh, M., Nadooshan, A. A., Raisi, A., Malekshah, E. H. (2022). The effect of photovoltaic shading with ideal tilt angle on the energy cost optimization of a building model in European cities. Energy for Sustainable Development, 71, 505-516.

[23]. Mansour, R. B., Khan, M. A. M., Alsulaiman, F. A., Mansour, R. B. (2021). Optimizing the solar PV tilt angle to maximize the power output: A case study for Saudi Arabia. IEEE Access, 9, 15914-15928.

[24]. Sun, L., Lu, L., Yang, H., "Optimum design of shading-type building-integrated photovoltaic claddings with different surface azimuth angles". Applied Energy, 90(1), 2012, 233-240.

[25]. Aksoy, M. H., Çiylez, İ. İspir, M. "Effect of Azimuth Angle on The Performance of a Small-Scale on-Grid PV System." Turkish Journal of Nature and Science, 11(4), (2022), 42-49.

[26]. Aksoy M. H., Bakırhan M., İspir, M., "Analysis of the Azimuth Angles of a Photovoltaic System in Non Ideal Positions", VI. International Conference on Engineering Technologies, ICENTE 2022, Konya, Turkey, November, 2022. 17-19.

[27]. Aksoy, M. H. Çalık, M. K., "Performance investigation of bifacial photovoltaic panels at different ground conditions". Konya Journal of Engineering Sciences, 10(3), (2022), 704-718.

[28]. Haydaroğlu, C. Gümüş, B., "Examination of Web-Based PVGIS and SUNNY Design Web Photovoltaic System Simulation Programs and Assessment of Reliability of the Results." Journal of Engineering and Technology, 1(1), (2017), 32-38.

[29]. Çınaroğlu, M. S. "Analysis of Three Grid Connected Photovoltaic Power Plants with PVsyst Program; Sample of Kilis." El-Cezeri, 8(2), (2021), 675-687.

[30]. Özcan, Ö. İzgi, E., "Comparative performance analysis of grid-connected photovoltaic roof system. Kahramanmaras Sutcu Imam University Journal of Engineering Sciences, 23(3), (2020), 127-140.

[31]. Ozcan, O., Ersoz, F., "Project and cost-based evaluation of solar energy performance in three different geographical regions of Turkey: Investment analysis application." Engineering Science and Technology, an International Journal, 22(4), (2019), 1098-1106.

[32]. Akcan, E. , Kuncan, M. Minaz, M. R., " Modeling and Simulation of 30 kW Grid Connected Photovoltaic System with PVsyst Software." European Journal of Science and Technology, 18, (2020), 248-261(in Turkish).

[33]. Boduch, A., Mik, K., Castro, R., Zawadzki, P., "Technical and Economic Assessment of a 1 MWP floating photovoltaic system in Polish conditions." Renewable Energy, 196, (2022), 983–994.

[34]. Karki, P., Adhikary, B., Sherpa, K. Comparative study of grid-tied photovoltaic (PV) system in Kathmandu and Berlin using PVsyst." 2012 IEEE Third International Conference on Sustainable Energy Technologies (ICSET). IEEE, 2012.

[35]. Kandasamy, C. P., Prabu, P., Niruba, K. "Solar potential assessment using PVSYST software." 2013 International Conference on Green Computing, Communication and Conservation of Energy, 2013 ICGCE, pp. 667-672, IEEE.

[36]. Behera, D. D., Das, S. S., Mishra, S. P., Mohanty, R. C., Mohanty, A. M., Nayak, B. B., "Simulation of solar operated grass cutting machine using PVSYST software." Materials Today: Proceedings, 62(6), (2022), 3044-3050.

[37]. Khan, M. A., Islam, N., Khan, M. A. M., Irshad, K., Hanzala, M., Pasha, A. A., Mursaleen, M., "Experimental and simulation analysis of grid-connected rooftop photovoltaic system for a large-scale facility." Sustainable Energy Technologies and Assessments, 53, (2022), 102773.

[38]. Aksoy, M. H., Ispir, M. "Techno-Economic Feasibility of Different Photovoltaic Technologies." Applied Engineering Letters, 8(1), (2023), 1-9.

[39]. Kumar, N. M., Kumar, M. R., Rejoice, P. R., Mathew, M. "Performance analysis of 100 kWp grid connected Si-poly photovoltaic system using PVsyst simulation tool." Energy Procedia, 117, (2017), 180-189.

[40]. Shukla, K. N., Rangnekar, S., & Sudhakar, K., "Mathematical modelling of solar radiation incident on tilted surface for photovoltaic application at Bhopal, MP, India." International Journal of Ambient Energy, 37(6), (2016), 579-588.

[41]. PVsyst, Help https://www.pvsyst.com/help/models_meteo_transposition.htm [Accessed: 18 April 2023].

[42]. Duman, A. C., Güler, Ö., "Economic analysis of grid-connected residential rooftop PV systems in Turkey." Renewable Energy, 148, (2020), 697-711.

[43]. Manito, A. R., Pinto, A., Zilles, R., "Evaluation of utility transformers' lifespan with different levels of grid-

connected photovoltaic systems penetration." Renewable Energy, 96, (2016), 700-714.

[44]. Stember, L. H., Huss, W. R., Bridgman, M. S. "A methodology for photovoltaic system reliability & economic analysis." IEEE Transactions on reliability, 31(3), (1982), 296-303.

[45]. Esmaeili Shayan, M., Najafi, G., Ghobadian, B., Gorjian, S., Mazlan, M., Samami, M., Shabanzadeh, A., "Flexible photovoltaic system on non-conventional surfaces: a techno-economic analysis." Sustainability, 14(6), (2022), 3566.

[46]. Gul, E., Baldinelli, G., Bartocci, P., Bianchi, F., Domenghini, P., Cotana, F., Wang, J., "A techno-economic analysis of a solar PV and DC battery storage system for a community energy sharing." Energy, 244, (2022), 123191.

[47]. Al-Khori, K., Bicer, Y., Koç, M., "Comparative techno-economic assessment of integrated PV-SOFC and PV-Battery hybrid system for natural gas processing plants." Energy, 222, (2021), 119923.

MANAS Journal of Engineering
ISSN 1694-7398 | e-ISSN 1694-7398

Volume 11, Issue 1, (2023) Pages 83-84
https://doi.org/10.51354/mjen.1282790

Self-Assembled Short Peptide Nanostructures: Dipeptides

Emrah Dikici[1,2*], Burcu Önal Acet[2], Tuba Gök[2], Ömür Acet[3], Mehmet Odabaşı[2]

[1] Science and Technology Application and Research Center, Aksaray University, Aksaray, Turkey, emrah.dikici25@gmail.com, ORCID: 0000-0002-3086-8156

[2] Faculty of Arts and Science, Chemistry Department, Aksaray University, Aksaray, Turkey, brconl33@gmail.com, ORCID: 0000-0003-2408-8660, TubaGk34@gmail.com, ORCID: 0000-0001-7660-7587, mehmet.modabasi@gmail.com, ORCID: 0000-0002-3288-132X

[3] Vocational School of Health Science, Pharmacy Services Program, Tarsus University, Tarsus, Turkey, omuracetbio@gmail.com, ORCID: 0000-0003-1864-5694

ABSTRACT

Dipeptides are short peptide molecules formed by the peptide bond between two amino acids, and they play significant roles in various biological processes (such as protein synthesis, nutrient absorption, cellular signaling, immune response). Short peptides have a prominent place in the design of self-assembling materials. In particular, dipeptides have gained considerable attention in the field of biotechnology as a type of self-organizing nanostructure due to their low cost, simplicity of synthesis, biocompatibility, and tunability of functionality. However, there is limited knowledge about peptide and protein-based nanostructures in the literature. Therefore, more information is needed on dipeptide nanostructures, especially in terms of their potential applications for biomedical purposes. This review focuses on dipeptide nanostructures, particularly their potential uses in biomedical applications, and provides a broader perspective on the advantages, challenges, synthesis, interactions, and applications of these nanostructures.

ARTICLE INFO

Review article

Received:
Accepted:

Keywords:
Self-assembled
Nanostructures
Peptide nanomaterials
Dipeptides

**Corresponding author*

1. Introduction

Self-assembly is a natural conformation of molecules with a specific three-dimensional geometry that occurs spontaneously under certain conditions. This technique is a method in which molecules and self-assembled aggregates are arranged thermodynamically [1,2].

Stable nanostructures with different morphologies may be formed by self-assembly of peptides through non-covalent interactions such as hydrophobic, hydrogen bonding, π-π stacking, and electrostatic interactions [3]. These interactions are known to act in the fabrication of some biological structures such as dendrimers, micelles, liposomes and lipid nanocapsules [4,5].

Peptides are chains of amino acids made up of about < 50 amino acids, easy to produce, and designed to mimic the self-regulation of proteins. Peptides have great superiorities such as chemical versatility, high degree of biocompatibility and biorecognition capacities. In particular, small peptide structures have the ability to translocating cell membranes and cannot induce an immune response [3].

Peptides, and especially short peptides, are very attractive nanomaterials because of their excellent biocompatibility, ease of synthesis, functional and tunable bioactivity, and ability to adjust their structure and function to environmental conditions [6].

In recent years, it has been observed that peptides with very small structures can self-assemble in various nanomorphological structures. Therefore, they have been shown to increase their stability while minimizing the synthesis difficulty and cost. Further research in this context sought to investigate the self-assembly of peptides as small as the dipeptide structure. The first study on the self-assembly of dipeptides belongs to Gazit's group, which researched the mechanism of self-regulation of dipeptide FF [6]. FF dipeptide are highly ordered as nanotubes/microtubes [7,8,9] nanoforests [10] and nanowire [11] structures. One of the desirable properties of FF nanotubes in a material was thermal stability, a matchless property that would be desirable in any biologically inspired material [12].

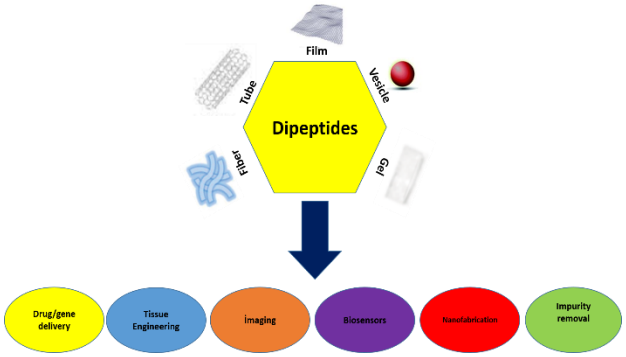

Figure.1 *Some Applications of Dipeptides*

Peptides have the ability to self-assemble in aqueous solution under different environmental conditions to form different nanostructures. In an experimental study to produce nanofibers in the literature, it has been observed that short peptides dissolve very quickly in a solution at low pH and osmotic pressure. Short peptides have outstanding properties such as versatility and flexibility for the design of self-assembly materials. These properties are convenient for understanding the structures and assembly mechanism of self-assembled peptides for the rational design of some structures [3]. Self-assembled dipeptide nanomaterials may suggest numerous potential implemantations in different fields because of their biocompatibility, easy tunability, and effortless and low-cost fabrication technique [6]. Some *a*pplications of dipeptides is shown in Figure.1. Even if there are many researches on and protein and peptide based nanostructures in literature, there is a need for a detailed review study especially on dipeptide self-assembled nanostructures. This review describes the dipeptide self-assembly mechanism, advantages, and different and important dipeptides.

2. Self-Assemble Technique

There are two methods for the fabrication of bio-based nanomaterials, known as bottom-up and top-down. For the top-down technique, nanostructured biomaterials are acquired by controlled removal of components from complex biological structures, i.e. separation of layer [13].

Supramolecular structures may be fabricated by assembling molecules for bottom-up process. It is important to know the method used in nanomaterial synthesis and the structure of each molecule existed the synthesis and the interaction of these molecules with each other. The organization of molecules occurs through weak non-covalent interactions. These interactions are electrostatic interactions, hydrogen bonds, hydrophobic interactions, and aromatic stacking [14]. These kind of interactions are in charge of the structural conformation of all biological molecules and their interaction with other molecules [5,13,14,15].

Self-assembled peptide structures include monomer sequences of short amino acid sequences or amino acid sequences that combine to form nanostructures. Peptides have different physicochemical and biochemical activities with their morphological structure, size and accessibility of surface area from a reactive point of view [16].

Molecular self-assembly defines the spontaneous union of individual molecules with thermodynamic situations into well described and quite stable supramolecule via non-covalent interactions. This case is everywhere in nature [16]. Molecular interactions keep molecules at a stable degree with low-energy status [17].

Secondary structures that allow the self-assembly of peptides are α-helices, β-sheets and β-hairpins [18,19]. α-helix is the basic secondary structure found in proteins [20].

The intrinsic thermodynamic instability phenomenon is that linear peptides with α-helical structure lose their helical structure in solution when separated from their original environment [21]. Although short α-helical peptide structures show ease of chemical synthesis and modification, it is also known that they lack stability in solution. Therefore, the novo design of peptides based on ultra-short α-helix peptides poses a problem [22].

3. The Importance of Short Peptides

Recent studies have indicated that short peptide structures have the capability of self-assembly of many different nanostructures, which can minimize the difficulties and cost of fabrication and at the same time increase their stability [23,24]. Self-assembled dipeptide nanostructures continue to be intensively investigated, especially in biomedical applications [25].

Preparation of hydrogel structures by self-assembly with short peptides was reported in one of the related synthesis methods, which self-assembled by intramolecular folding of specific peptide structures. Here, chemical crosslinking processes eliminate the need for toxic crosslinkers that are generally needed to form hydrogels from high molecular weight polymers. Another important point is that peptides with this structure are designed to respond to release. The most important features of drug carriers, such as biocompatibility, robustness and slow release ability during administration, are also expected to trigger release according to treatment needs. Therefore, the synthesis of peptides with improved therapeutic effect, responsiveness to stimuli and controlled release can be designed [26]. Oxaliplatin-peptide conjugate was formed with ultra-short peptides capable of forming hydrogels and tested in the treatment of localized

breast cancer. This conjugate showed tumor growth inhibition [27].

Cell-penetrating peptides act an significant task in drug delivery across cell membranes and translocation of genes within the nucleus. The self-assembly process is key to cell-penetrating peptides penetration mechanisms. Additionally, the self-assembly method may produce a variety of structures convenient for a particular delivery and loading of a wide variety of drugs [28]. Cell-penetrating peptides have been utilized as drug delivery tools because they have cell membrane-replacing properties [29]. Cell-penetrating peptides, which are cationic short peptides of less than 30 amino acids, and oligoarginine-based cell-penetrating peptides, 8-10 arginine residues long, have been demonstrated to have the best membrane penetration [30].

Short peptide structures are a substitute for extracellular matrix proteins. These structures are a substitute for extracellular matrix proteins. They can mimic cell adhesion and remove the complexity of extracellular matrix structural effects in cells [31]. In this sense, peptide ligands have been involved in biomaterials that may be utilized as biomimetic membranes. Examples of these are polyethylene glycol hydrogels, biodegradable polymers and self-assembled monolayers [32]. A large increase is likely to occur in peptide formulations containing polyethylene glycol, cell-penetrating peptides for intracellular delivery, and short sequence peptides as carriers [33].

It has been shown that amyloid fibrils can generally consist of polypeptides of 30-40 amino acids, but may also consist of larger proteins. Nevertheless, recent research has demonstrated the ability of much shorter peptides, namely tetra- to hexapeptides, to form typical amyloid fibrils exhibiting all the typical biophysical and ultrastructural features of amyloid fibrils [34,35].

4. Some Special Purpose Dipeptides

In their 2003 study, Gazit and colleagues reported the spontaneous self-assembly of the short dipeptide Phe-Phe. In another study [7], Wangoo et al. demonstrated the self-assembly of aliphatic single amino acids (Ala, Leu, Ile, and Val) [36].

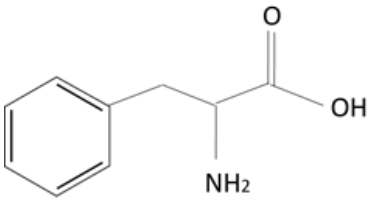

Figure.2 *Phenylalanine Structure*

Research on phenylalanine (FF), whose molecular structure is given in Figure.2 and plays an important role in the regulation of biological processes, provides new information about the biological effects, synthesis and potential applications of this amino acid. Studies have revealed novel information on FF's biological effects, synthesis, and potential applications in regulating biological processes [37].

This section of the study aims to summarize the existing knowledge on phenylalanine and its derivatives, with a particular focus on phenylalanine amide (FFA) dipeptide nanoparticles and their potential applications. The aromatic rings of FF play a crucial role in the formation of chemical and biochemical supramolecular structures by providing the necessary energetic contribution for aromatic stacking [38]. Studies on FF dipeptide have shown that this peptide can form structures in various shapes, such as spherical or tubular structures, as well as structures in the form of rings, ellipses, disks, and bowls [39].

FF is an attractive option for drug delivery systems due to its simple structure and biocompatibility. FF nanoparticles can encapsulate hydrophobic drugs to a high degree thanks to their anionic character, and drug release can be controlled by pH and glutathione. As such, FF holds great potential as a drug carrier system [40].

A study by Wang et al. on FF dipeptide nanoparticles has shown that they can be used as self-assembled nanotubes for electronic devices on graphene [41]. Liu et al. have used these nanoparticles as drug carriers due to their high biocompatibility and bioactivity [42]. In a different study conducted in 2015, FF dipeptide nanoparticles were used for nanoscale optoelectronic applications [43]. The study stated that FF dipeptide nanoparticles showed high conductivity and their optical properties could be controlled.

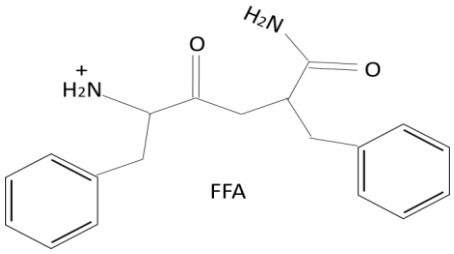

Figure.3 *Diphenylalanine amide (FFA) Dipeptide Structure*

One of the modifications made to the nanostructures formed by the FF dipeptide is the synthesis of cationic FF (H-Phe-Phe-NH2·HCl) molecules, which are obtained by replacing the -OH group in the carboxyl group with -NH2, to impart different properties [44]. The molecular structure of Diphenylalanine amide (FFA) Dipeptide is given in Figure.3. The study conducted by Yan et al. was the first to

demonstrate the potential application of cationic FF (FFA) molecules as gene and drug carriers by organizing them into nanovesicles at physiological pH [45].
The organization of cationic FF molecules into nanoparticle structures under different stimuli and conditions, and their application as carriers or sensor components, have been the subject of numerous studies [46,47]. However, the common problem in all of these studies is the instability of the resulting peptide nanoparticles, which tend to change shape to adapt to varying environmental conditions [48].

Zhang et al. were the first to develop a stable FF-based nanostructure for drug delivery. This stable nanostructure exhibits high biocompatibility and superior biodegradability properties [49].

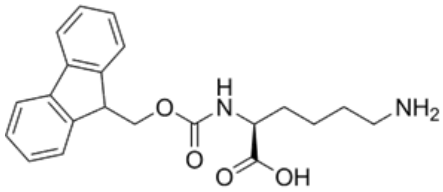

Figure.4 *Fmoc-Lys Dipeptide Structure*

Another dipeptide gaining importance is fluorenylmethoxycarbonyl lysine (Fmoc-Lys) and its molecular structure is given in Figure.4. Fmoc-Lys is a derivative of the amino acid lysine, protected with a 9-fluorenylmethoxycarbonyl protective group [49]. Lysine is a basic amino acid that is important for many biological functions. Fmoc-Lys contributes to the formation of peptides and proteins by being combined with other amino acids [50]. Typically used in solid-phase peptide synthesis, Fmoc-Lys is attached to solid support by adding an Fmoc protective group to the N-terminus. The protective group is removed with a base, such as piperidine, to extend the amino acid chain [51]. Fmoc-Lys is an important tool used in proteomic and peptidomic research, analyzing biological molecules, and designing new drugs. Additionally, Fmoc-Lys variants can be used to design peptides with increased biological activity by adding specific functions and properties to amino acid chains. Fmoc-Lys contributes to the formation of peptides and proteins by being combined with other amino acids [50,51].

When an amino acid is conjugated with a fluorenylmethoxycarbonyl (Fmoc-) group, the ability of the Fmoc functional group to form thick, tangled fibers facilitates the formation of a gel-like structure that can trap water molecules within it [52]. This property has led to the investigation and use of Fmoc-amino acids in various applications, particularly in potential areas such as drug delivery systems, tissue engineering, and wound healing. Fmoc-based hydrogels are being studied as scaffolds for tissue engineering and drug delivery vehicles [53].

Previous literature reports have shown that various Fmoc-protected amino acids exhibit gel-like properties. For example, it has been reported that amino acids such as Fmoc-F, Fmoc-M, Fmoc-Y, Fmoc-G, Fmoc-W, and Fmoc-I exhibit gel-like properties. However, it has been reported that some amino acids, such as Fmoc-alanine, Fmoc-valine, and Fmoc-leucine, do not exhibit gel-like properties due to their uncertain behaviour [52].

Recent studies by Kundu et al. have examined the self-assembly property of Fmoc-L-lysine in different organic solvents [54]. Additionally, a study by Panda et al. has demonstrated the spherical self-assembly property of Fmoc-cysteine and its applications in drug delivery [55].

5. Usage Areas of Dipeptides and Expectations

Dipeptides are widely used, especially in the field of biomedicine, for reasons such as being biocompatible and nontoxic. Dipeptides can also be used for purposes such as the determination of various substances and purification.
The accumulation of various chemicals and drugs in nature and foodstuffs has become a growing problem with the passing years. Nanoparticles are also frequently used for the detection of these residues. It is extremely important that the nanoparticle used is non-toxic. For this purpose, fluorescent nanoparticles were developed by Yan and his group. Biodegradable, tryptophan-phenylalanine dipeptide and sulfadimethoxine aptamer are combined and modified to give fluorescent properties and it has been suggested that it can be used as a reliable method for the determination of sulfadimethoxine [56]. A dipeptide and aptamer-based hybrid fluorescent platform was developed by Jin et al. for the detection of enrofloxacin, a broad-spectrum antibiotic [57].

Dipeptide-based nanocarriers have been synthesized for the release of doxorubicin enzyme-responsive, as an example for dipeptides that are also used in the design of drug delivery systems [58]. The ability to obtain nanoparticles suitable for modification with dipeptides is a feature that increases the potential of the usage areas. Tumor-targeting nanoparticles developed by Panda et al. can be included in this group [59]. In a study published last year, a new dipeptide-based cell imaging probe and tumor targeting agent were brought to the literature [60].

It is known that biocompatible nanoparticles cause fewer side effects compared to their counterparts, and even eliminate the factor that causes side effects in some cases. It has been reported that dipeptide-based nanocarriers, which exhibit antitumor activity and were developed for use in photodynamic therapy, also do not cause weight loss and unwanted immune activity [61].

Since nanoparticles can be modified to suit the preferred

purpose, it is possible to impart various properties to these nanoparticles. For example, photosensitive nanoparticles that are activated in hypoxia and designed for use in breast cancer have been developed. It has been shown that the nanoparticle prepared by combining the photosensitive pheophorbide-diphenylalanine peptide and the hypoxia-activated camptothecin prodrug, performs apoptosis by inducing ROS production after exposure to the 660 nm laser [62]. pH sensitive dipeptide-based systems are also among the systems designed to serve different usage purposes by being developed with modifications [63]. Like pH sensitivity, it is possible to develop solvent-tunable dipeptide-based nanostructures. In this way, different optoelectronic properties have been imparted to nanoparticles in different solvent environments [64]. Among the dipeptide-based nanostructures sensitized to different stimuli, redox-responsive nanostructures developed for targeted cancer therapy can be given as examples. Nanoparticles conjugated with folic acid and loaded with doxorubicin release drugs in the presence of glutathione [65].

Hydrogels are also frequently used for controlled release in drug delivery. In an article published in 2017, a biocompatible, Fmoc protected dipeptide-based hydrogel resistant to proteolysis was introduced. It has been reported that the problem of proteolysis, which is one of the most important disadvantages in the therapeutic use of peptide-based nanoparticles, is also eliminated [66]. Three-dimensional growth and functions of primary liver cells were also supported by dipeptide-based hydrogels [67]. In a recent study, biomineralized dipeptide hydrogels were found to induce bone regeneration [68]. The widespread use of dipeptide-based hydrogels in biomedical applications is due to several advantages. These include biocompatibility, availability for modifications, low cost and high stability [69]. Hydrogels are used in purification as well as biomedical applications. With the increasing importance of wastewater treatment, studies in this field have also increased. The dipeptide superhydrogel developed by Nandi et al. has enabled the removal of various toxic dyes and some heavy metals from wastewater [70].

Another usage area of dipeptide-based nanomaterials is systems in which they act as carriers for nucleic acids. They are known to be effective candidates with advantages such as easy synthesis, enzymatic stability and biocompatibility. Such a system has been designed from cationic dipeptides for gene therapy and has been reported to work successfully without any cytotoxic effect [71]. The transport of siRNAs with these systems is one of the applications that has increased in popularity in recent years. Liver-targeting dipeptide-based siRNA carrier nanoparticles that can be used therapeutically for cirrhosis have been designed. It has been reported that nanoparticles accumulate in the liver and have a therapeutic effect [72].

Due to the various advantages highlighted above, it is seen that the use of dipeptide-based nanomaterials in many areas is becoming increasingly common. It is anticipated that these nanomaterials will be used more frequently in the future, especially in biomedical applications, in the detection of antibiotics and various toxic chemicals, and in wastewater treatment in a wide range.

6. Conclusions

The examples we have covered in this review highlight dipeptides and its applications. In the past years, these dipeptide-based systems have advanced from fundamental studies of novel self-assembly principles, to initial results using in vitro systems, to in vivo models for novel therapies especially in cancer.

Peptides can self-assemble into a variety of nanostructures, which can exhibit interesting properties such as high thermostability and mechanical stability, semi-conductivity, and optical properties, which are gaining more and more attention in the biomedical and materials fields.

We believe that dipeptide-based nanostructures will be frequently encountered in the future, especially in biomedical applications, with aspects such as biocompatibility and biodegradability, as well as many other advantages discussed in this review. Its use in both in vitro and in vivo studies will increase if some of its limiting properties such as stability in physiological environments and predictability of their structures are resolved. While many challenges will be encountered in exploring dipeptide self-assembly, the future of peptide-based self-assembly nanomaterials is promising and achievable.

REFERENCES

[1]. Lee Y. S., “Self-Assembly,” In Self-Assembly and Nanotechnology: A Force Balance Approach, John Wiley & Sons: Hoboken, NJ, 2008, pp 1–19. B. and Horn P., Robot Vision. Cambridge, MA: MIT Press, 1986.

[2]. Whitesides G. M., Grzybowski, B., “Synthesis and comparison of crosslinked peptide nanoparticles based on diphenylalanine derivatives”, Science, 295, (2002), 2418.

[3]. Ma X., Xing R., Yuan C., Ogino K., Yan X., “Tumor therapy based on self-assembling peptides nanotechnology”, View, 1, (2020), 20200020.

[4]. Guyon L., Lepeltier E., Passirani C., “Self-assembly of peptide-based nanostructures: Synthesis and biological activity”, Nano Res., 11, (2018), 2315–2335.

[5]. Acet O., Dzmitry S., Victoriya Z., Pavel K., Inessa H.B., Acet B.O., Gok T., Maria B., Odabasi M., "Dipeptide nanostructures: Synthesis, interactions, advantages and biomedical applications", Colloids and Surfaces B: Biointerfaces, 222, (2023), 113031.

[6]. Panda J.J., Chauhan V.S., "Short peptide based self-assembled nanostructures: implications in drug delivery and tissue engineering", Polymer Chemistry, 5, (2014), 4418.

[7]. Reches M., Gazit E., "Casting metal nanowires within discrete self-assembled peptide nanotubes", Science, 300, (2003), 625–627.

[8]. Adler-Abramovich L., Aronov D., Beker P., Yevnin M., Stempler S., Buzhansky L., Rosenman G., Gazit E., "Self-assembled arrays of peptide nanotubes by vapour deposition", Nat. Nanotechnol, 4, (2009), 849–854.

[9]. Wang M., Du L., Wu X., Xiong S., Chu P. K., "Charged Diphenylalanine Nanotubes and Controlled Hierarchical Self-Assembly", ACS Nano, 5, (2011), 4448–4454.

[10]. Reches M., Gazit E., "Controlled patterning of aligned self-assembled peptide nanotubes", Science, 1, (2006), 195-200.

[11]. Ryu J., Park C. B.,, "High-Temperature Self-Assembly of Peptides into Vertically Well-Aligned Nanowires by Aniline Vapor", Advanced. Materials, 20, (2008), 3754–3758.

[12]. Adler-Abramovich L., Reches M., Sedman V. L., Allen S., Tendler S. J., Gazit E., "Thermal and chemical stability of diphenylalanine peptide nanotubes: implications for nanotechnological applications", Langmuir, 22, (2006), 1313–1320.

[13]. Zhang S., "Fabrication of novel biomaterials through molecular self-assembly", Nat.Biotechnol., 21, (2003), 1171–1178.

[14]. Gazit E., "Self-assembled peptide nanostructures: the design of molecular building blocks and their technological utilization", Chem. Soc. Rev., 36, (2007), 1263–1269.

[15]. Whitesides G.M., Mathias J.P., Seto C.T., "Molecular Self-Assembly and Nanochemistry: a chemical Strategy for the Synthesis of Nanostructures", Science, 254, (1991), 1312–1319.

[16]. Lee S., Trinh H. T., Yoo M., Shin J., Lee H., Kim J., Hwang E., Lim Y.B., Ryou C., "Self-Assembling Peptides and Their Application in the Treatment of Diseases ", Int. J. Mol. Sci., 20, (2019), 5850.

[17]. Han T.H., Oh J.K., Lee G.J., Pyun S.I., Sang O.K., "Hierarchical assembly of diphenylalanine into dendritic nanoarchitectures", Colloids Surf. B, 79, (2010), 440–445.

[18]. Pabo C.O., Peisach E., Grant R.A., "Design and selection of novel Cys(2)His(2) zinc finger proteins", Annu. Rev. Biochem., 70, (2001), 313–340.

[19]. Battiste J.L., Mao H.Y., Rao N.S., Tan R.Y., Muhandiram D.R., Kay L.E., Frankel, J.R. Williamson A. D., "α-helix-RNA major groove recognition in an HIV-1 Rev peptide RRE RNA complex", Science, 273, (1996), 1547–1551.

[20]. Uesugi M., Verdine G.L., "The α-helical FXX π-π motif in p53: TAF interaction and discrimination by MDM2", P. Natl. Acad. Sci., 26, (1999), 14801–14806.

[21]. Liu J., Wang D., Zheng Q., Lu M., Arora P.S., "Atomic structure of a short α-helix stabilized by a main chain hydrogen-bond surrogate", J. Am. Chem. Soc., 130, (2008), 4334–4337.

[22]. Li T., Lu X. M., Zhang M.R., Hu K., Li Z., "Peptide-based nanomaterials: Self-assembly, properties and applications", Bioactive Materials, 11, (2022), 268-282.

[23]. Chen C., Pan F., Zhang S., "Antibacterial activities of short designer peptides: a link between propensity for nanostructuring and capacity for membrane destabilization," Biomacromolecules, 11, (2010), 402–411.

[24]. Veiga A. S., Sinthuvanich C., Gaspar D., Franquelim H. G., Castanho M. A. R. B., Schneider J. P., "Arginine-rich self- assembling peptides as potent antibacterial gels," Biomaterials, 33, (2012), 8907–8916.

[25]. Gorbitz C. H., "The structure of nanotubes formed by dipheny- lalanine, the core recognition motif of Alzheimer's β-amyloid polypeptide," Chemical Communications, 22, (2006), 2332–2334.

[26]. Nagai Y., Unsworth L.D., Koutsopoulos S., Zhang S., "Slow release of molecules in self-assembling peptide nanofiber scaffold", J. Control. Release., 115, (2006), 18-25.

[27]. Reithofer M.R., Chan K. H., Lakshmanan A., Lam D.H., Mishra A., Gopalan B., Joshi M., Wanga S., Hauser C. A. E., "Ligation of anti-cancer drugs to

self-assembling ultrashort peptides by click chemistry for localized therapy", Chem. Sci., 5, (2014), 625-630.

[28]. Habibi N., Kamaly N., Memic A., Shafiee H., "Self-assembled peptide-based nanostructures: Smart nanomaterials toward targeted drug delivery", Nano Today, 11, (2016), 41-60.

[29]. Gupta B., Levchenko T., Torchilin V., "Intracellular delivery of large molecules and small particles by cell-penetrating proteins and peptides", Adv. Drug Delivery Rev., 57, (2005), 637-651.

[30]. Fuchs S.M., Raines R.T., "Internalization of cationic peptides: the road less (or more?) traveled", Cell. Mol. Life Sci., 63, (2006), 1819-1822.

[31]. Tirrell M., Kokkoli E., Biesalski M., "The Role of Surface Science in Bioengineered Materials",Surf. Sci., 500, (2002), 61-68.

[32]. Pastorino L., Habibi N., Soumetz F., Giulianelli M., Ruggiero C., "Polyelectrolyte multilayers for cell and tissue engineering", Eur. Cells Mater., 22, (2011), 66.

[33]. Davis M., Motion J., Narmoneva D., Takahashi T., Hakuno D., Kamm R., Zhang S., Lee R. T., "Injectable Self-Assembling Peptide Nanofibers Create Intramyocardial Microenvironments for Endothelial Cells", Circulation, 111, (2005), 442-450.

[34]. Tenidis K., Waldner M., Bernhagen J., Fischle W., Bergmann M., Weber M., Merkle M. L., Voelter W., Brunner H., Kapurniotu A., "Identification of a penta- and hexapeptide of islet amyloid polypeptide (IAPP) with amyloidogenic and cytotoxic properties", J. Mol. Biol., 295, (2000), 1055-1071.

[35]. Reches M., Porat Y., Gazit E., "Amyloid fibril formation by pentapeptide and tetrapeptide fragments of human calcitonin", J. Biol. Chem., 277, (2002), 35475-35480.

[36]. Singh P., Pandey S. K., Grover A., Sharma R. K., Wangoo N., "Understanding the self-ordering of amino acids into supramolecular architectures: co-assembly-based modulation of phenylalanine nanofibrils", Materials Chemistry Frontiers, 5, (2021), 1971-1981.

[37]. Basiri M. A., "Dipeptide-based nanoparticles: advances and challenges," RSC Advances, 11, (2021), 14321-14334.

[38]. Pala B. B., Vural T., Kuralay F., Cırak T., Bolat G., Abacı S., Denkbas E. B., "Disposable pencil graphite electrode modified with peptide nanotubes for Vitamin B12 analysis," Appl. Surf. Sci., 303, (2014), 37–45.

[39]. Guo C., Luo Y., Zhou R., Wei G., "Probing the Self-Assembly Mechanism of Diphenylalanine-Based Peptide Nanovesicles and Nanotubes," ACS Nano, 6, (2012), 3907-3918.

[40]. Chen C., Liu K., Li J., Yan X., "Functional architectures based on selfassembly of bio-inspired dipeptides: Structure modulation and its photoelectronic applications," Adv. Colloid Interface Sci., 225, (2015), 177-193.

[41]. Wang Q., Zhang X., "Self-assembly of diphenylalanine peptide nanotubes on graphene for electronic devices", ACS applied materials & interfaces, 8, (2016), 20125-20132.

[42]. Liu X., Wang J., Li Y., Wang X., Chen Y., "Peptide-based nanoparticles for drug delivery", Advanced drug delivery reviews, 110, (2016), 112-126.

[43]. Wang C., Wang S., Yang X., "Diphenylalanine peptide nanotubes as a platform for nanoscale optoelectronics", Advanced materials, 27, (2015), 402-427.

[44]. Yan X., He Q., Wang K., Duan L., Cui Y., Li J., "Transition of Cationic Dipeptide Nanotubes into Vesicles and Oligonucleotide Delivery," Angew. Chemie Int. Ed., 46, (2007), 2431–2434.

[45]. Yan X., Cui Y., He Q., Wang K., Li J., Mu W., Wang B., Ou-yang Z., "Reversible Transitions between Peptide Nanotubes and Vesicle-Like Structures Including Theoretical Modeling Studies," Chem. Europe, 14, (2008), 5974–5980.

[46]. Zhang H., Fei J., Yan X., Wang A., Li J., "Enzyme-Responsive Release of Doxorubicin from Monodisperse Dipeptide-Based Nanocarriers for Highly Efficient Cancer Treatment In Vitro," Adv. Funct. Mater., 25, (2015) 1193–1204.

[47]. Ma H., Fei J., Li Q., Li J., "Photo-induced Reversible Structural Transition of Cationic Diphenylalanine Peptide Self-Assembly," Small, 11, (2015), 1787–1791.

[48]. Huang C., Chen X., Lu Y., Yang H., Yang W., "Electrogenerated chemiluminescence behavior of peptide nanovesicle and its application in sensing

dopamine," Biosens. Bioelectron, 63, (2015), 478-482.

[49]. Fields G. B., Noble, R. L., "Solid phase peptide synthesis utilizing 9-fluorenylmethoxycarbonyl amino acids." International Journal of Peptide and Protein Research, 35, (1990), 161-214.

[50]. Wang, J., "Solid-phase synthesis of Fmoc-protected peptides" Journal of Visualized Experiments, 136, (2018), e57327.

[51]. Chan W. C., White, P. D., "Fmoc solid phase peptide synthesis: a practical approach." Oxford University Press. Carpino, L. A., 115, (2000), 4397-4398.

[52]. Draper E. R., Morris K. L., Little M. A., Raeburn J., Colquhoun C., Cross E. R., Mc Donald T. O., Serpell L. C., Adams D. J., "Hydrogels formed from Fmoc amino acids", Cryst.Eng.Comm., 17, (2015), 8047-8057.

[53]. Estroff L. A., Hamilton A. D., "Water gelation by small organic molecules", Chemical reviews, 104, (2004), 1201-1218.

[54]. Hashemnejad S. M., Huda M. M., Rai N., Kundu S., "Molecular insights into gelation of di-fmoc-L-lysine in organic solvent–water mixtures", ACS omega, 2, (2017), 1864-1874.

[55]. Chibh S., Katoch V., Kour A., Khanam F., Yadav A. S., Singh M., Kundu G. C., Prakash B., Panda J. J., "Continuous flow fabrication of Fmoc-cysteine based nanobowl infused core–shell like microstructures for pH switchable on-demand anti-cancer drug delivery", Biomaterials Science, 9, (2021), 942-959.

[56]. Yan R., Wen Z., Hu X., Wang W., Meng H., Song Y., Tang Y., "A sensitive sensing system based on fluorescence dipeptide nanoparticles for sulfadimethoxine determination", Food Chemistry, 405, (2023), 134963.

[57]. Jin Y., Yan R., Wang, S., Wang X., Zhang X., Tang Y., "Dipeptide nanoparticle and aptamer-based hybrid fluorescence platform for enrofloxacin determination", Microchimica Acta, 189, (2022), 96.

[58]. Zhang H., Fei J., Yan X., Wang A., Li J., "Enzyme-responsive release of doxorubicin from monodisperse dipeptide-based nanocarriers for highly efficient cancer treatment in vitro", Advanced Functional Materials, 25, (2015), 1193-1204.

[59]. Panda J. J., Kaul A., Kumar S., Alam S., Mishra A. K., Kundu G. C., Chauhan V. S., "Modified dipeptide-based nanoparticles: vehicles for targeted tumor drug delivery", Nanomedicine, 8, (2013), 1927-1942.

[60]. Sivagnanam S., Das K., Basak M., Mahata T., Stewart A., Maity B., Das P., "Self-assembled dipeptide based fluorescent nanoparticles as a platform for developing cellular imaging probes and targeted drug delivery chaperones", Nanoscale Advances, 4, (2022), 1694-1706.

[61]. Ma K., Xing R., Jiao T., Shen G., Chen C., Li J., Yan X., "Injectable self-assembled dipeptide-based nanocarriers for tumor delivery and effective in vivo photodynamic therapy", ACS Applied Materials & Interfaces, 8, (2016), 30759-30767

[62]. Sun M., Jiang H., Liu T., Tan X., Jiang Q., Sun B., Sun J., "Structurally defined tandem-responsive nanoassemblies composed of dipeptide-based photosensitive derivatives and hypoxia-activated camptothecin prodrugs against primary and metastatic breast tumors", Acta Pharmaceutica Sinica B, 12, (2022), 952-966.

[63]. Wang Y., Xing P., An W., Ma M., Yang M., Luan T., Hao A., "pH-Responsive dipeptide-based dynamic covalent chemistry systems whose products and self-assemblies depend on the structure of isomeric aromatic dialdehydes", Langmuir, 34, (2018), 13725-13734.

[64]. Xue H., Li X., Wang K., Cui W., Zhao J., Fei J., Li J., "Solvent-tunable dipeptide-based nanostructures with enhanced optical-to-electrical transduction", Chemical Communications, 55, (2019), 13136-13139.

[65]. Chibh S., Kour A., Yadav N., Kumar P., Yadav P., Chauhan V. S., Panda J. J., "Redox-responsive dipeptide nanostructures toward targeted cancer therapy", ACS omega, 5, (2020), 3365-3375.

[66]. Tiwari P., Verma R., Basu A., Christman R. M., Tiwari A. K., Waikar D., Dutt Konar A., "Proteolysis-Resistant Self-Assembled ω-Amino Acid Dipeptide-Based Biocompatible Hydrogels as Drug Delivery Vehicle", ChemistrySelect, 2, (2017), 6623-6631.

[67]. Biswas S., Vasudevan A., Yadav N., Yadav S., Rawal P., Kaur I., Chauhan V. S., "Chemically Modified Dipeptide Based Hydrogel Supports Three-Dimensional Growth and Functions of Primary Hepatocytes", ACS Applied Bio Materials, 5, (2022), 4354-4365.

[68]. Hao L., Wang A., Fu J., Liang S., Han Q., Jing Y., Yin J., "Biomineralized dipeptide self-assembled hydrogel with ultrahigh mechanical strength and osteoinductivity for bone regeneration", Colloids and Surfaces A: Physicochemical and Engineering Aspects, 657, (2023), 130622.

[69]. Kulkarni N., Rao P., Jadhav G. S., Kulkarni B., Kanakavalli N., Kirad S., Sahu B., "Emerging Role of Injectable Dipeptide Hydrogels in Biomedical Applications", ACS omega, 8, (2023), 3551-3570.

[70]. Nandi N., Baral A., Basu K., Roy S., Banerjee A., "A dipeptide-based superhydrogel: Removal of toxic dyes and heavy metal ions from waste water", Peptide science, 108, (2017), e22915.

[71]. Panda J. J., Varshney A., Chauhan V. S., "Self-assembled nanoparticles based on modified cationic dipeptides and DNA: novel systems for gene delivery", Journal of nanobiotechnology, 11, (2013), 1-13.

[72]. Biswas S., Yadav N., Juneja P., Mourya A. K., Kaur S., Tripathi D. M., Chauhan V. S., "Conformationally Restricted Dipeptide-Based Nanoparticles for Delivery of siRNA in Experimental Liver Cirrhosis", ACS omega, 7, (2022), 36811-36824.Myer R.L., "Parametric oscillators and nonlinear materials," in Nonlinear Optics, vol. 4, P. G. Harper and B. S. Wherret, Eds. San Francisco, CA: Academic, 1977, pp. 47-160.

MANAS Journal of Engineering
ISSN 1694-7398 | e-ISSN 1694-7398

Volume 11, Issue 1, (2023) Pages 92-104
https://doi.org/10.51354/mjen.1279695

Green chemistry assisted nanoscale synthesis and structural characterization of some transition metal cations

Mustafa Küyükoğlu[1], Melda Bolat Bülter[2], Dursun Ali Köse[1,*]

[1] Hitit University, Department of Chemistry, Ulukavak, Çorum/Türkiye, 19100, ORCID: 0000-0003-4767-6799

[2] Hitit University, Vocational School of Technical Sciences, OHS Program, Çorum/Turkey, 19100

ABSTRACT

Nanoparticle studies are groundbreaking today, largely due to unpredictable changes in particle size and surface properties. Therefore, nanoparticles are considered as building blocks in optoelectronics, pharmaceuticals, nuclear energy, bioengineering, biomedicine and industrial applications. Today, the importance of environmentally friendly methods is increasing. The use of the green synthesis method, which adopts an economic synthesis approach that will reduce resource and energy consumption and do not harm the environment, is also encouraged in every field. In the study, biosafe ascorbic acid was used as an alternative reagent (agent) to the chemical reduction method. The method process performed with the reagent selected for nanoparticle synthesis has ensured that it is green synthesis, which is adopted as non-toxic and environmentally friendly. In this study, nanoparticles were synthesized by reducing the sulphate, nitrate, chloride and acetate salts of Cu(II), Ni(II), Co(II), Zn(II) and Mn(II) transition metals with the reducing agent ascorbic acid compound. It is aimed to investigate the effects of the same metal cations and different anion salts on nanoparticle synthesis. Depending on the radius ratios and solubility values of metal cations and anions, the nanoparticle obtained from Ni(CH3COO)2 salt has the smallest radius. Nano metal particles with the largest radius were obtained as a result of reduction from Co(NO3)2 salt. The characterization of the synthesized nanoparticles were recorded by particle size analysis and scanning electron microscopy (SEM) images.

ARTICLE INFO

Research article

Received: 10.04.2023
Accepted: 16.05.2023

Keywords:
Transition metal,
cation,
nanoparticle,
ascorbic acid,
reduction

**Corresponding author*

1. Introduction

Nanotechnology is a science that deals with the preparation of nano-sized particles ranging from 1 to 100 nm using various synthesis strategies and particle structure and size modification. Nanoparticles have proven to be a scientific and technological boon that can be used in many different application areas such as medicine, organic chemistry, inorganic chemistry, materials science, food, electronics, fuel cells, solar cells, voltaic batteries, chemical sensors, space, sports equipment, chemical fabrics [1-9]. Due to the specific properties (size, shape, and distribution) of nanoparticles, they can be used in applications requiring advanced technology [10-12]. Nanoparticles of transition metals also have wide applications in different interdisciplinary fields due to their distinctive physicochemical properties associated with their nanometer size [5–8]. Metal oxide nanoparticles (MONs) are synthesized from all-metal precursors. These nanoparticles play an important role in many fields of physics, chemistry, and materials science. MONs have unique optoelectrical properties due to their well-known localized surface plasmon resonance properties. Nano-sized metal oxides have many outstanding properties, including high cleaning capacity and heavy metal selectivity. They hold great potential as promising adsorbents for heavy metals. Therefore, synthesis techniques mainly focus on size, morphological configuration, stability, and distribution [17-21]. The chemicals used for nanoparticle synthesis and stabilization are toxic and lead to non-biosafe by-products. Therefore, there is a growing interest in “green nanotechnology” that is environmentally friendly with the specific properties of nanoparticles [22-25]. The reduction of metal nanoparticles with the ascorbic acid compound can be said to be a green method whose process is non-toxic, low cost, and environmentally friendly [10,26-31]. When the transition metal studies in the literature are examined, it is seen that there is a focus on certain transition metals. In this study, sulphate, nitrate, chloride, and acetate salts of Cu(II), Ni(II), Co(II), Zn(II), and Mn(II) transition metal cations were combined with L-ascorbic acid (Vitamin C) using chemical reduction technique. nanoscale syntheses

were tried to be made by reducing Thus, it is aimed to investigate the effects of the same metal cations with different anion salts on nanoparticle synthesis. The synthesis of MON and anion and their effects on size will be examined. It is aimed to create a reference source for researches aiming to study nano-sized particles of specified metal cations. ZETA particle size analysis and scanning electron microscope (SEM) images were recorded for the characterization of the synthesized nanoparticles.

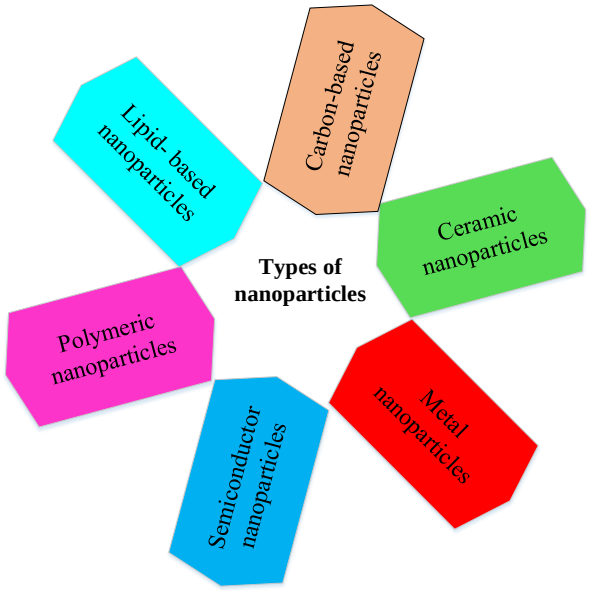

Figure 1. *Commonly used types of nanoparticles [32]*

2. Materials and methods

2.1. Materials

Sulfate, nitrate, chloride and acetate salts of copper, nickel, cobalt, zinc and manganese and ascorbic acid chemicals were procured from Sigma-Aldrich (St. Louis, USA). All other chemicals used in the study are of analytical grade. De-ionized water was also used in the study.

2.2. Synthesis of transition metal nanoparticles

In this study, metal oxide nanoparticle synthesis was performed as follows. 0.001 mol of transition metal salt and 0.011 mol of ascorbic acid were dissolved in 100 mL of de-ionized water. The pH of the solution was brought to about 6.50 with NaOH solution. The solution was then taken into a flask and placed in the assembly consisting of a water bath and a mechanical stirrer. The transition metal solution was stirred for 2.5 hours at 85°C, 700 rpm. In the last stage, the large particles and unwanted impurities settled to the bottom were filtered under vacuum and the metal nanoparticle solids remaining at the bottom of the flask after the water were removed by the evaporator device and where dried with a vacuum oven at 25 °C.

2.3. Characterization

Scanning Electron Microscope (SEM)
Surface morphology of the synthesized nanoparticles was investigated using scanning electron microscopy (SEM; FEI / Quanta 450 FEG, USA). The sample, which was attached to the SEM holder with double-sided carbon tape, was then covered under vacuum with a thin layer of gold. Then the obtained SEM sample was placed in the device and its image was taken.

Size Analysis
The size of the nanoparticles in the aqueous solution was analyzed. The scattering angle of the laser light passing through the particle depends on the particle size. As the particle size decreases, the scatter angle increases logarithmically. The scattering angles of large particles are low, the intensity of the scattered laser light is high. In small particles, the scattering angle is high and the intensity of the scattered laser light is low.

3. Results and discussions

Scanning Electron Microscopy (SEM)

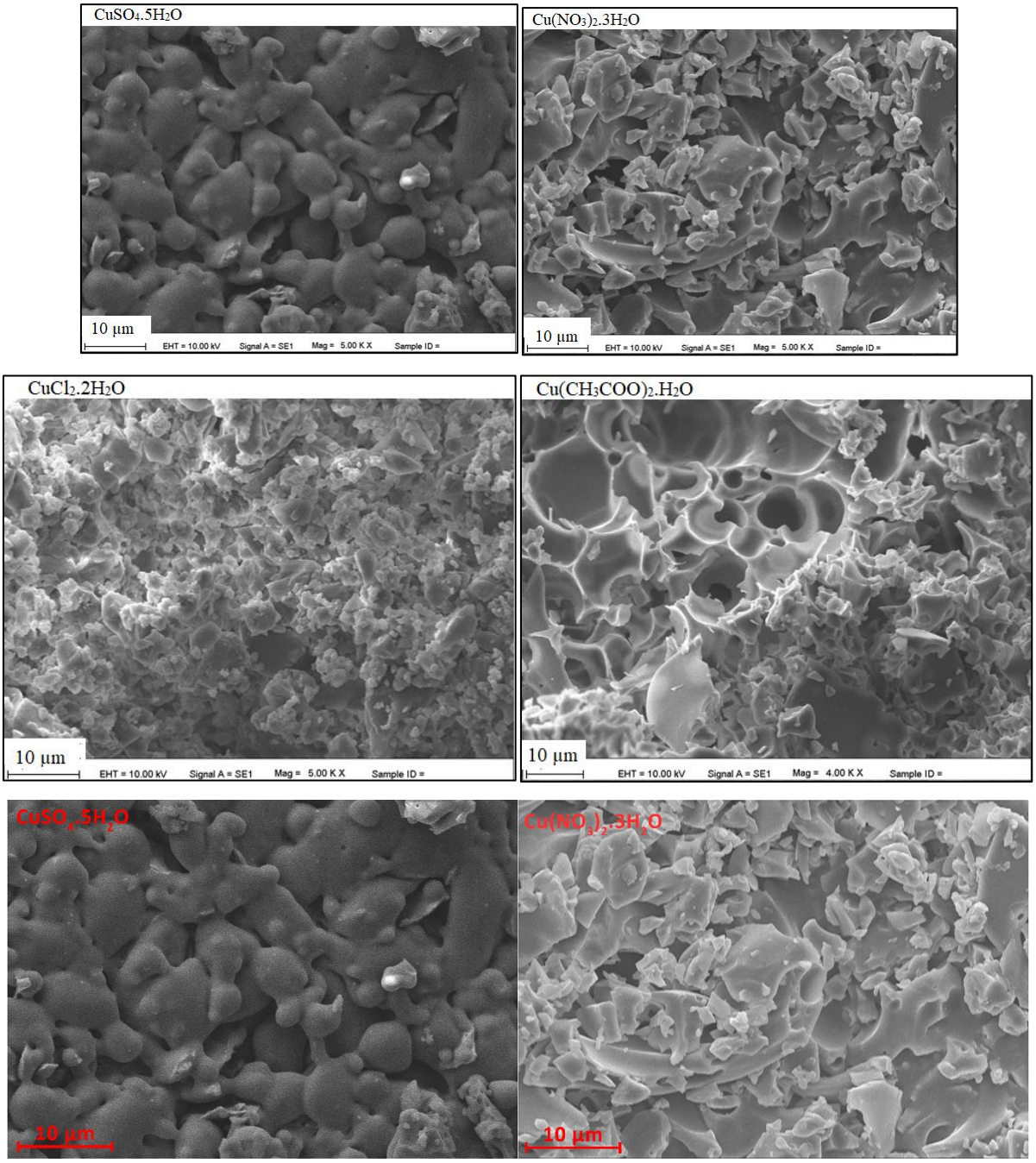

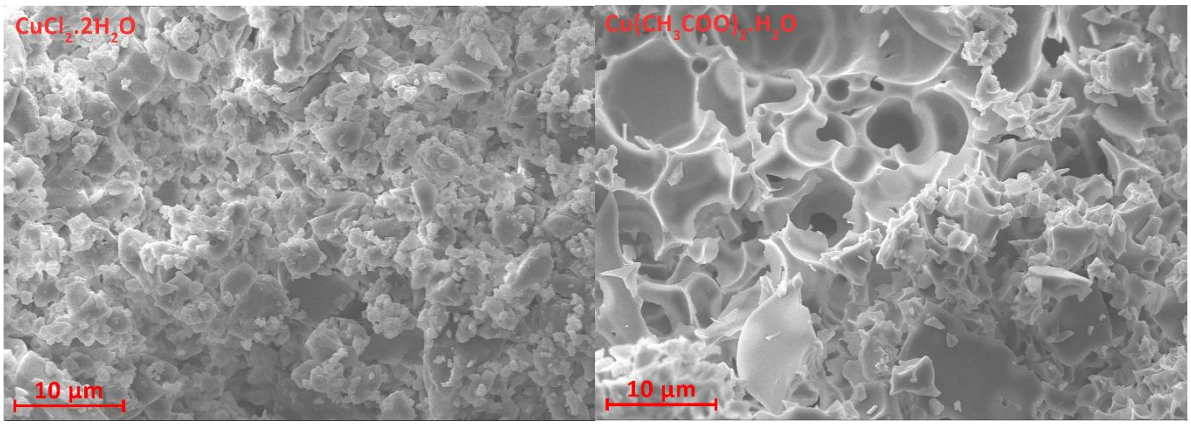

Figure 2. *SEM image of nanoparticles obtained from Cu (II) salts*

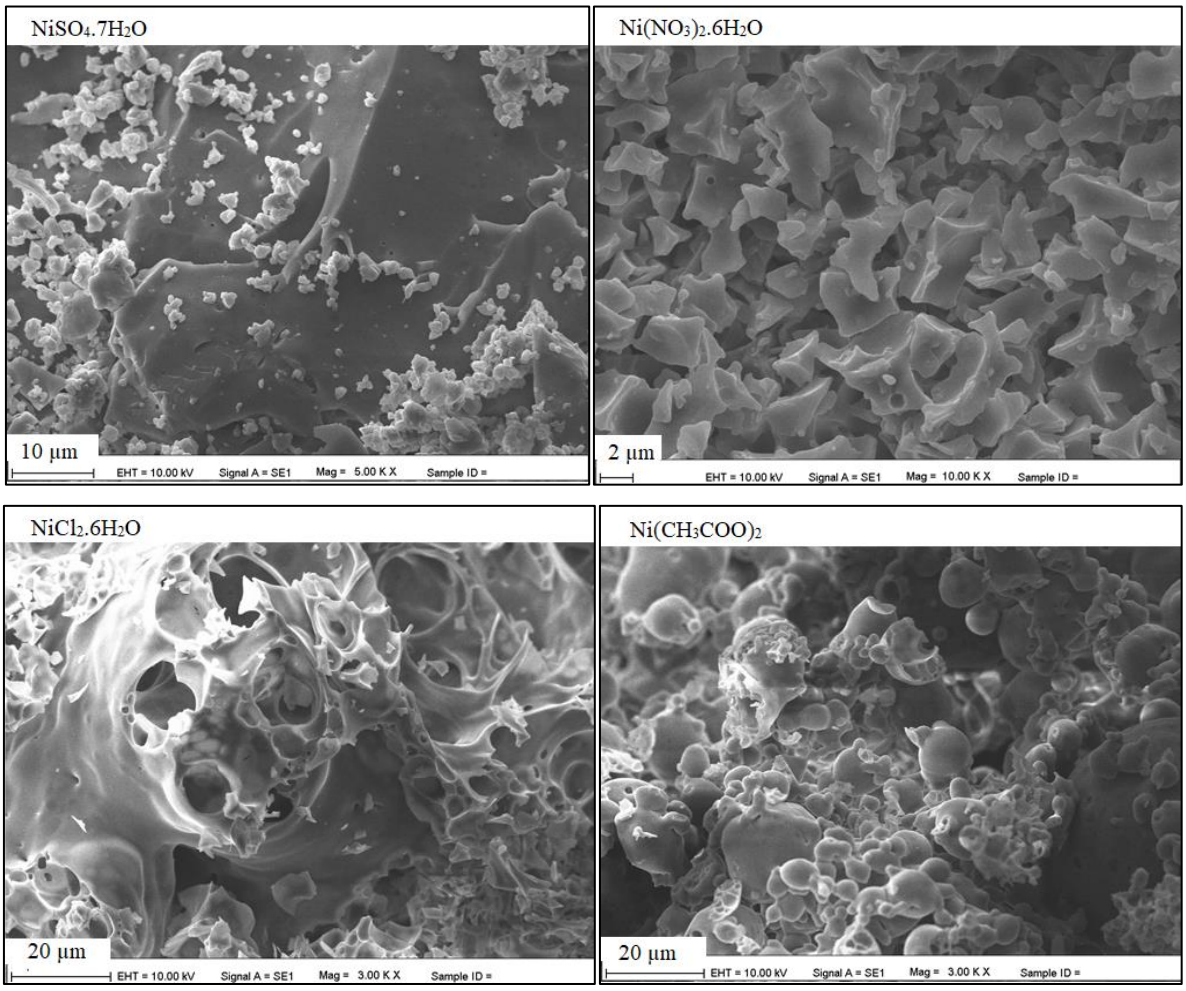

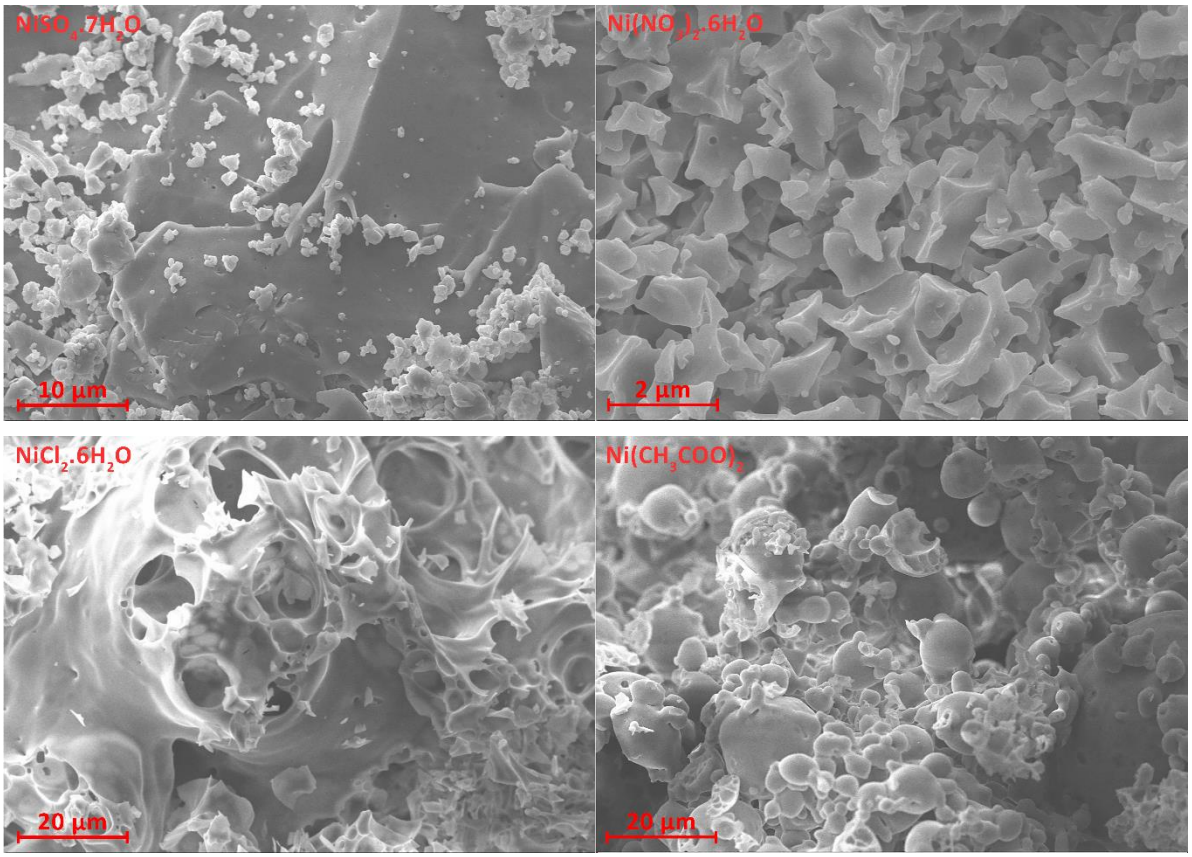

Figure 3. *SEM image of nanoparticles obtained from Ni (II) salts*

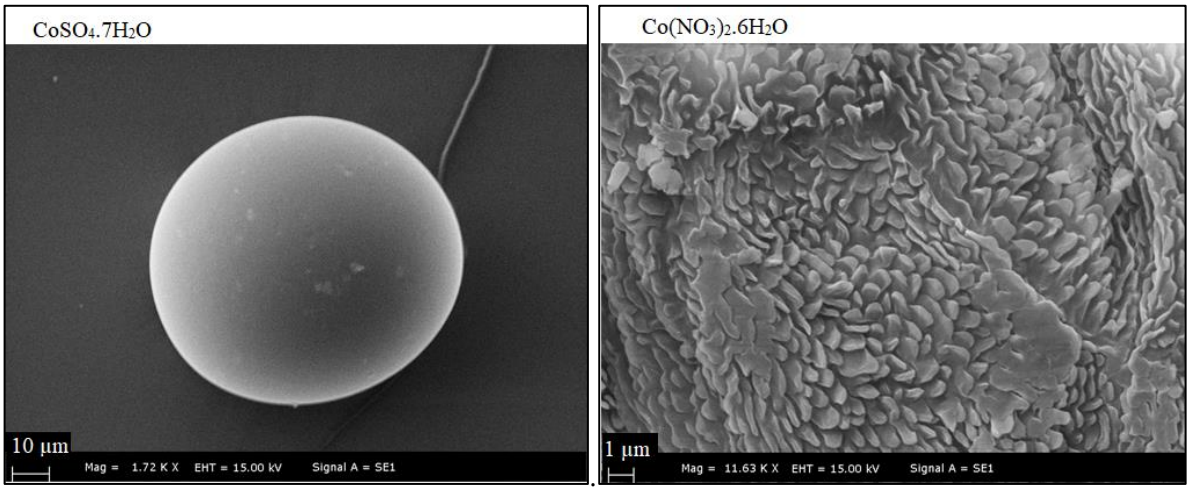

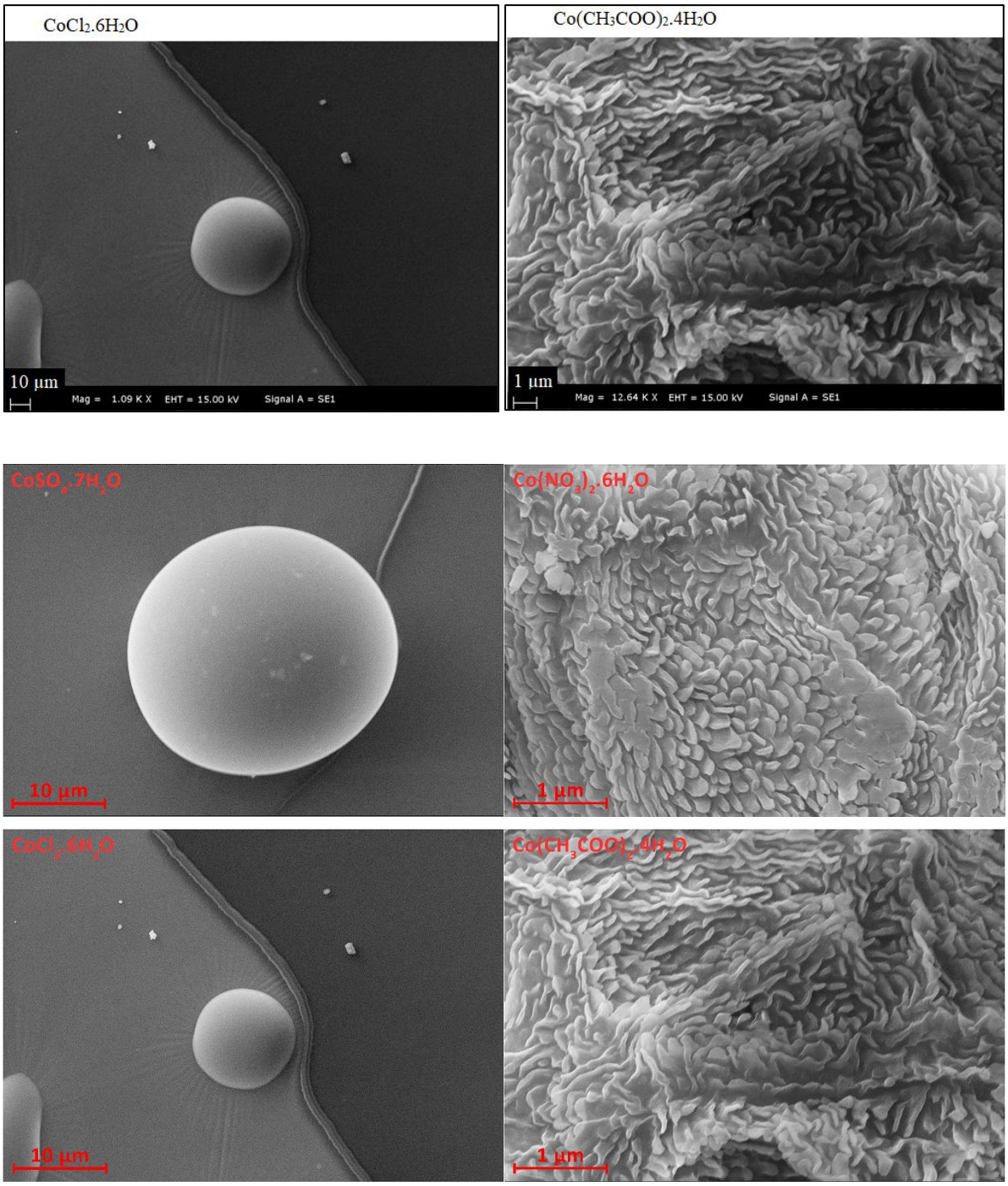

Figure 4. *SEM image of nanoparticles obtained from Co (II) salts*

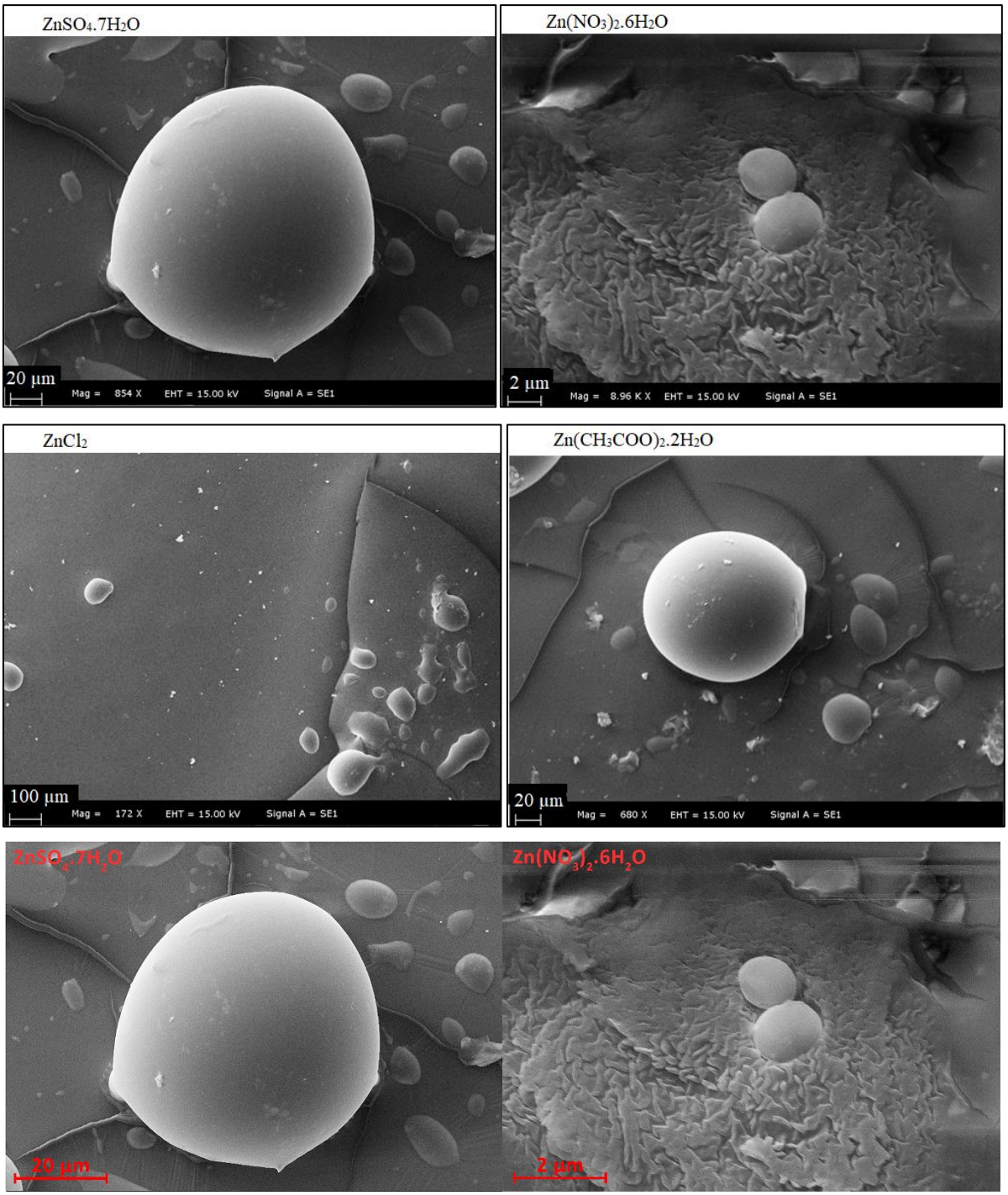
ZnSO4.7H2O
20 µm
Mag = 854 X EHT = 15.00 kV Signal A = SE1
Zn(NO3)2.6H2O
2 µm
Mag = 8.96 K X EHT = 15.00 kV Signal A = SE1
ZnCl2
100 µm
Mag = 172 X EHT = 15.00 kV Signal A = SE1
Zn(CH3COO)2.2H2O
20 µm
Mag = 680 X EHT = 15.00 kV Signal A = SE1
ZnSO4.7H2O
20 µm
Zn(NO3)2.6H2O
2 µm

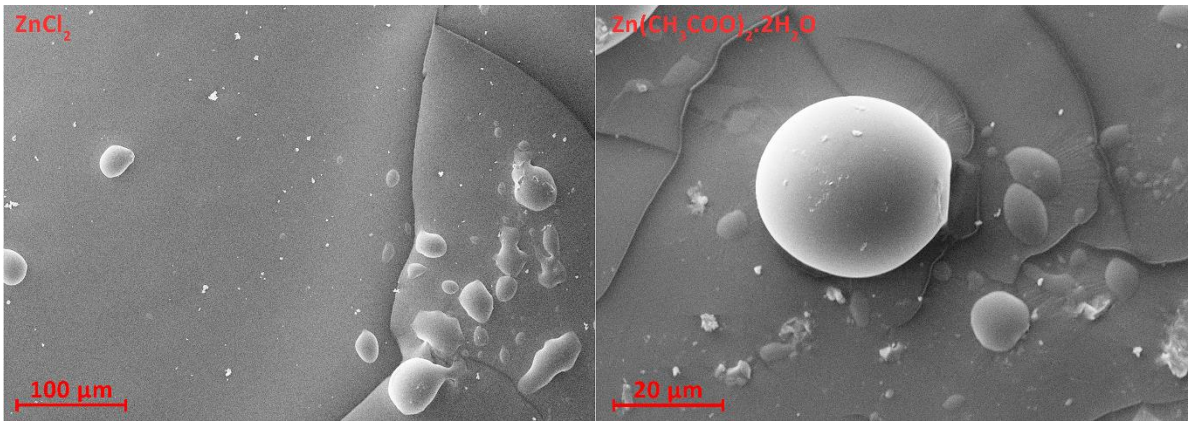

Figure 5. *SEM image of nanoparticles obtained from Zn(II) salts*

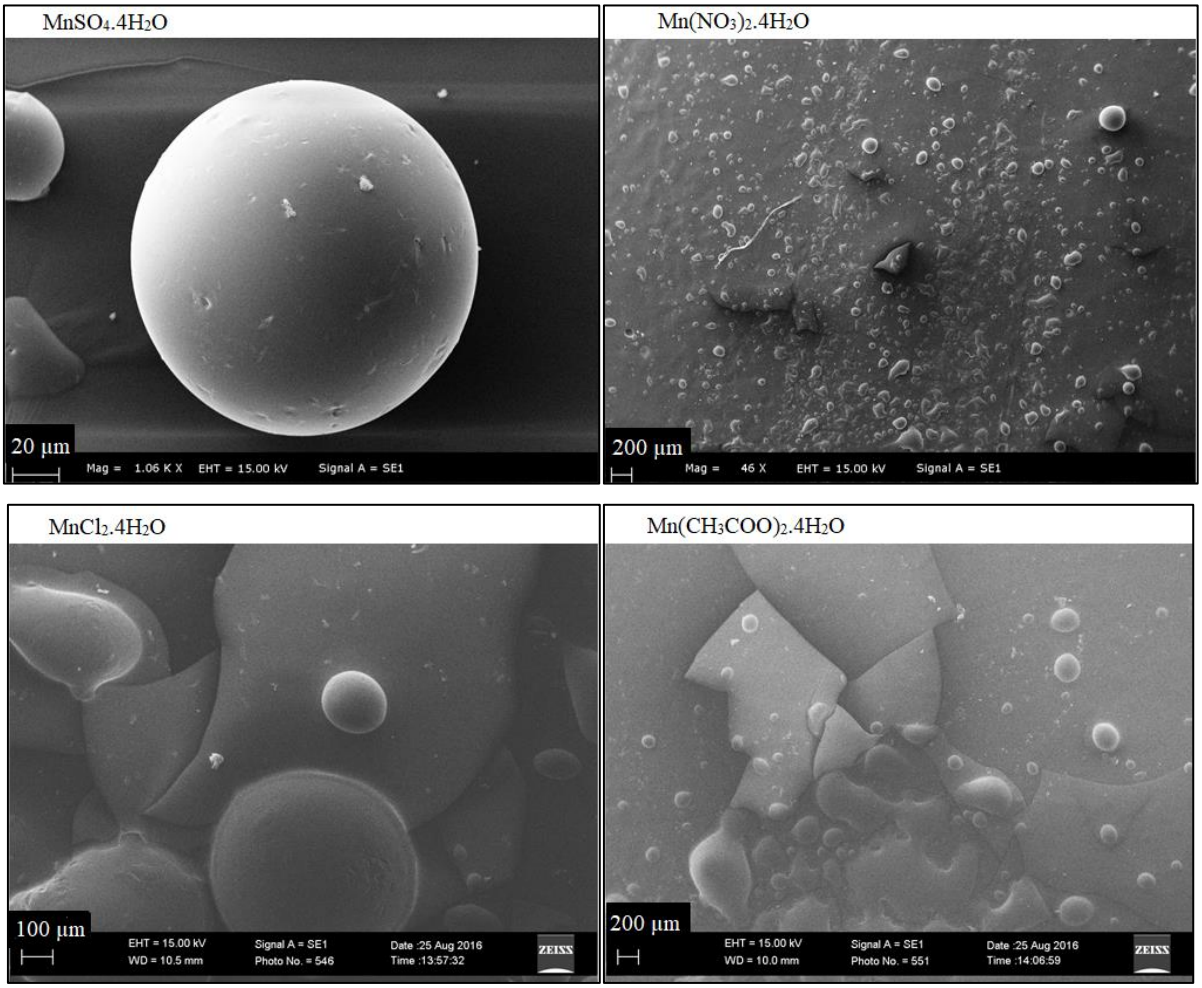

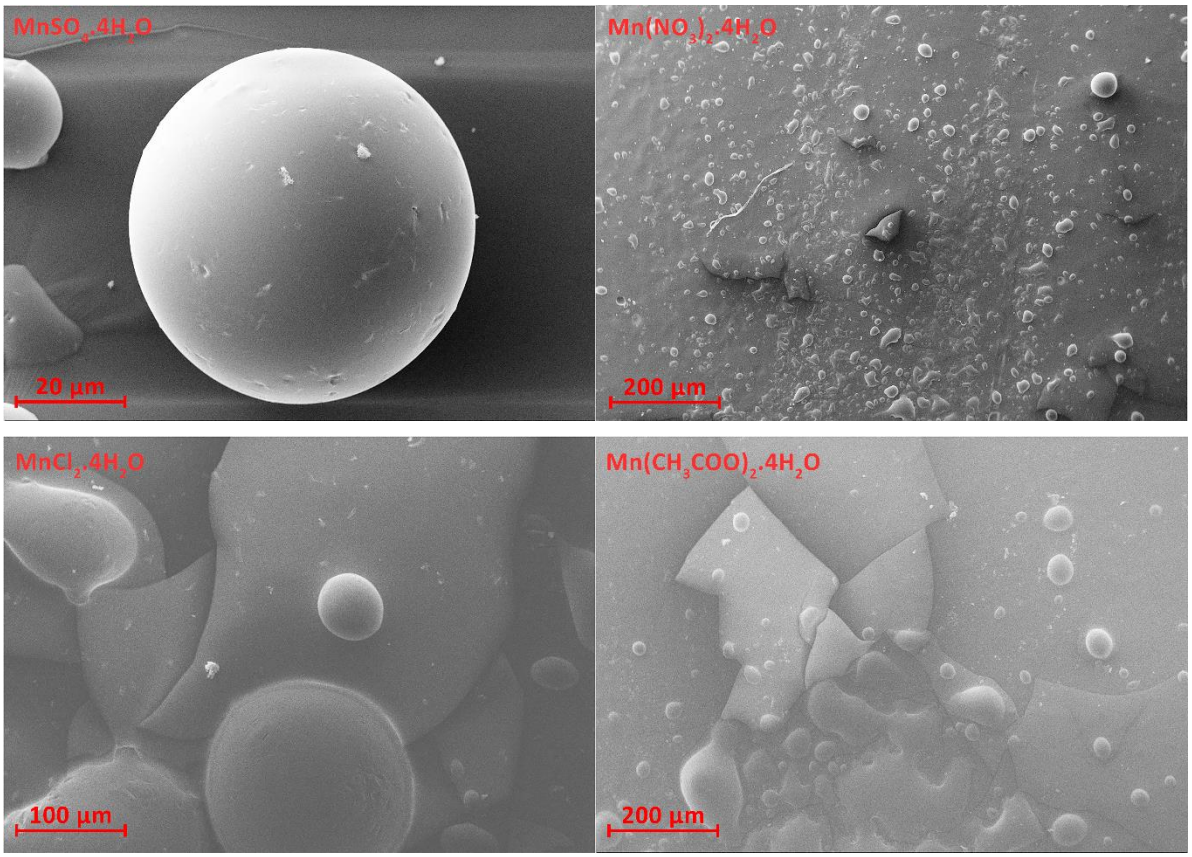

Figure 6. *SEM image of nanoparticles obtained from Mn(II) salts*

Zeta-Size chart

The size of the smallest nanoparticles was determined as $Ni(CH_3COO)_2$ and is shown in figure 7. The largest nanoparticle was determined as $Co(NO_3)_2.6H_2O$ and is shown in figure 8.

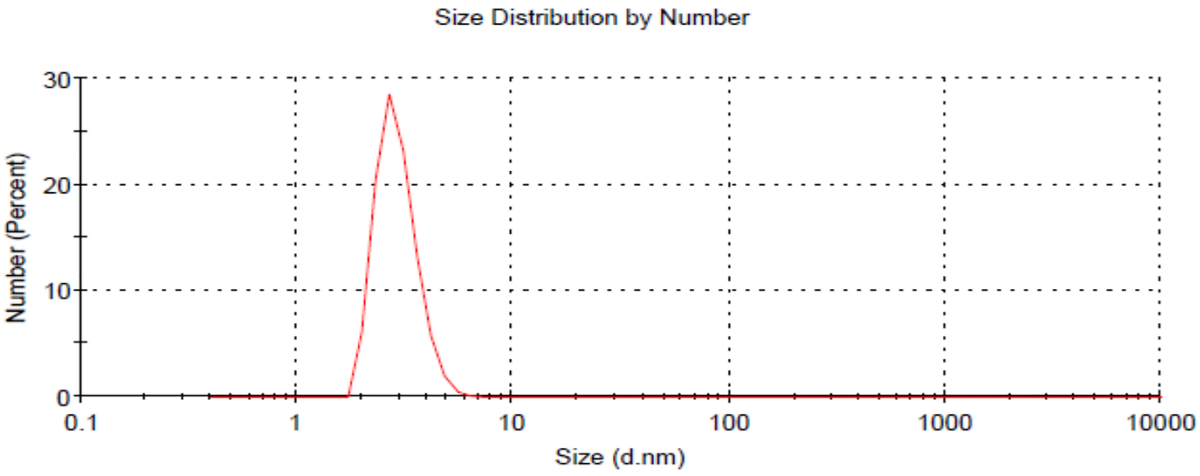

Figure 7. *Zeta-Size graph of the smallest nanoparticle $Ni(CH_3COO)_2$*

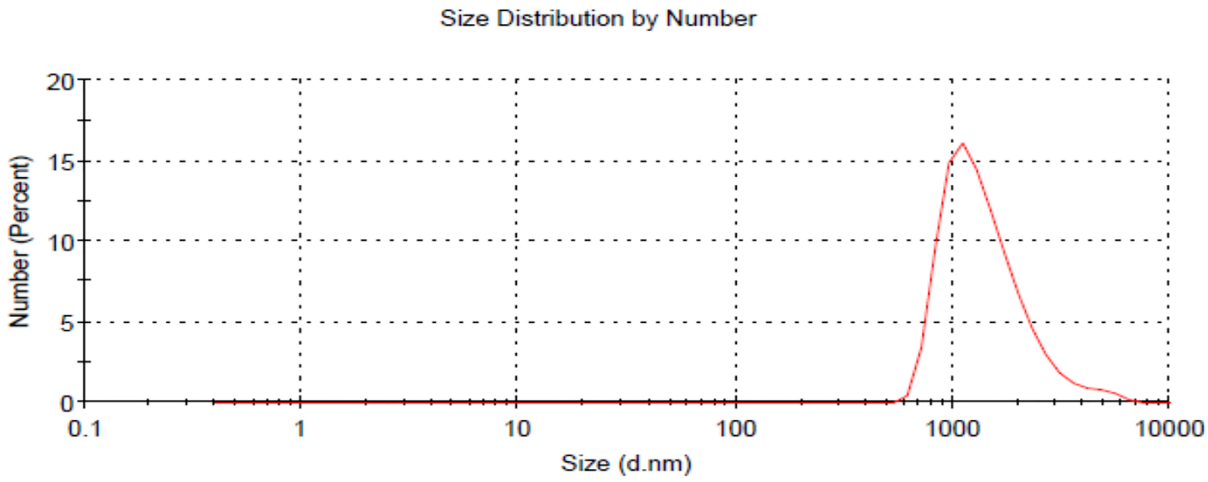

Figure 8. *Zeta-Size graph of the largest nanoparticle $Co(NO_3)_2.6H_2O$*

Table 1. Size analysis of nanoparticles based on anions and cations

Anion	Cu^{+2}(nm)	Ni^{2+} (nm)	Co^{+2} (nm)	Zn^{+2} (nm)	Mn^{+2} (nm)
Sulfate	709,6	310,8	603,9	812,6	718,3
Nitrate	635,9	145,8	1492,0	675,9	118,4
Chloride	3,421	453,7	887,3	645,8	564,4
Acetate	867,4	2,946	615,3	53,03	683,6

In the light of the data summarized in Table 1, when the size analysis of the nanoparticles is examined, the order of the salts used according to the size of the particles obtained from the small to the large is as follows: Among the cations, the smallest particle size was obtained from Ni (II) salts. It has been determined that salts with the smallest size astetate anion are formed among the anions. Accordingly, it can be said that the low solubility of nickel acetate in aqueous environment General Ranking:

compared to other salts caused the nanoparticles obtained to be smaller in size. Based on the same idea, the cobalt nitrate salt, which dissolves relatively faster in an aqueous environment, has also been identified as the largest particle. According to the results of the size analysis, the general comparisons of the particles formed by the reduction of the salts with ascorbic acid are shown below.

Ni(CH3COO)2 < CuCl2 < Zn(CH3COO)2 < Mn(NO3)2 < Ni(NO3)2 < NiSO4 < NiCl2 < MnCl2 < CoSO4 < Co(CH3COO)2 < Cu(NO3)2 < ZnCl2 < Zn(NO3)2 < Mn(CH3COO)2 < CuSO4 < MnSO4 < ZnSO4 < Cu(CH3COO)2 < CoCl2 < Co(NO3)2

When the anion-based size analysis is examined, the following sequence is formed from small to large.

Anion Rank: CH3COO- < Cl- < NO3- < SO42-

When the cation based size analysis is examined, the following sequence is formed from small to large.

Cation Rank: Ni2+ < Mn2+ < Zn2+ < Cu2+ < Co2+

When the radius values of the anions given in Table 2 are examined, it has been determined that the largest radius value is SO42- anion and the lowest value is CH3COO-

In Table 3, the radius values of the metal cations with 2+ oxidation steps are close to each other, as expected, the small value is Co2 + with low spin, and the highest value is the Zn2 + cation with d10 electronic configuration. Mn2 + d5 deviates from the periodic table bases since it has a half-filled stability electronic configuration at varying radii in accordance with the periodic table rules.

Table 2. *The radius values of anions [33]*

Anion	*Radius (nm)*
CH_3COO^-	162
NO_3^-	179
Cl^-	184
SO_4^{2-}	258

Table 3. *The radius values of anions [34]*

Cation	*Radius(pm)*
Co^{2+}	65 (ls) 74,5 (hs)
Cu^{2+}	73
Mn^{2+}	81(ls) 97 (hs)
Ni^{2+}	83
Zn^{2+}	88

ls: low spin, hs: high spin

When the solubilities of metal salts consisting of cations and anions are compared, the solubility decreases in ionic compounds (salt compounds) formed by cations and anions whose radii are close to each other due to the increasing covalent character feature. When the solubility values of the metal salts given as g/mL in an aqueous medium at 20oC in Table 4 are examined, they show the expected changes (due to periodic table exceptions), albeit small deviations.

Table 4. The solubility values of the metal salts.

Metal Salt	Solubility (g/100mL, 20°C)
$Zn(CH_3COO)_2.2H_2O$	43.0
$Zn(NO_3)_2.6H_2O$	184.0
$ZnSO_4.7H_2O$	96.0
$ZnCl_2$	395.0
$Cu(CH_3COO)_2.H_2O$	7.2
$Cu(NO_3)_2.3H_2O$	125.0
$CuSO_4.5H_2O$	32.0
$CuCl_2.2H_2O$	73.0
$Co(CH_3COO)_2.4H_2O$	38.0
$Co(NO_3)_2.6H_2O$	134.0
$CoSO_4.7H_2O$	36.2
$CoCl_2.6H_2O$	52.9
$Ni(CH_3COO)_2.4H_2O$	182.0
$Ni(NO_3)_2.6H_2O$	238.5
$NiSO_4.7H_2O$	75.6
$NiCl_2.6H_2O$	254.0
$Mn(CH_3COO)_2.4H_2O$	23.3
$Mn(NO_3)_2.4H_2O$	380.0
$MnSO_4.4H_2O$	70.0
$MnCl_2.4H_2O$	198.0

When the solubility values of the metal salts given in Table 2 and 3 are examined, it was determined that the solubility values of the metal cation and the salt compounds formed by the anion with the closest radii are the lowest as expected. However, unlike NO3-, Cl- and CH3COO- anions, all of which have a 1- oxidation step, SO42- anion, which has a 2- oxidation step, will generate a stronger electron than other anions in order to reduce the electronic stress created by the 2- charge in its structure. For this reason, the solubility of the salt compounds formed by binding to metal cations with ionic bonds with stronger covalent character compared to other anions will be lower than expected.

4. Conclusion

As seen with the anion radius order of the salts from which metal nanopowder is obtained, it is determined that salts with acetate anion form the smallest particles, although the radius of sulfate is the largest anion, its strong covalent character in binding to metal cations causes a decrease in resolution. As a result, it has been determined that the radii of metal nanopowder obtained by reduction from sulphate anion salts are the largest. This situation can be attributed to the fact that the solubility of metal salts formed by acetate anions with the closest ratio of metal cations and acetate anions is the most difficult and consequently the amount of metal cation obtained as a result of partial dissolution in water is reduced in a controlled manner and transformed into metal nanopowder. It is thought that metal nano powders obtained by reducing metal salts with higher solubility in aqueous environment very quickly with ascorbic acid increase in size as a result of agglomeration.

When the cation radius order of the salts from which the metal nano powders were examined, it was determined that the

average particle size of the nanopowder obtained from Ni2+ cations with a larger radius compared to the other cations was the smallest, and the radii of the nano metal powders obtained from Co2+ cation salts with the smallest radius were found to have the largest average. The reason for this is that the particle size of the nano powder obtained from the Ni (CH3COO)2 salt, which has the lowest solubility compared to the anion-cation ratio, is the lowest and the particle size of the nano metal powder obtained from the Co(NO3)2 salt, which has the highest solubility, is the highest. It has been determined that the particle sizes of other nano metal powders change in parallel with the change in the solubility of ionic salts (including exceptional cases).

References

[1] F. J. Heiligtag and M. Niederberger, 'The fascinating world of nanoparticle research', *Mater. Today*, vol. 16, no. 7–8, pp. 262–271, 2013, doi: 10.1016/j.mattod.2013.07.004.

[2] M. De, P. S. Ghosh, and V. M. Rotello, 'Applications of nanoparticles in biology', *Adv. Mater.*, vol. 20, no. 22, pp. 4225–4241, 2008, doi: 10.1002/adma.200703183.

[3] S. Shrivastava and D. Dash, 'Applying Nanotechnology to Human Health: Revolution in Biomedical Sciences', *J. Nanotechnol.*, vol. 2009, pp. 1–14, 2009, doi: 10.1155/2009/184702.

[4] S. S. Sana *et al.*, 'Recent advances in essential oils-based metal nanoparticles: A review on recent developments and biopharmaceutical applications', *J. Mol. Liq.*, vol. 333, p. 115951, 2021, doi: 10.1016/j.molliq.2021.115951.

[5] P. Alexandridis and M. Tsianou, 'Block copolymer-directed metal nanoparticle morphogenesis and organization', *Eur. Polym. J.*, vol. 47, no. 4, pp. 569–583, 2011, doi: 10.1016/j.eurpolymj.2010.10.021.

[6] V. Sharma *et al.*, 'Nanoparticles as Fingermark Sensors', *TrAC Trends Anal. Chem.*, vol. 143, p. 116378, 2021, doi: 10.1016/j.trac.2021.116378.

[7] A. Pawar, S. Thakkar, and M. Misra, 'A bird's eye view of nanoparticles prepared by electrospraying: advancements in drug delivery field', *J. Control. Release*, vol. 286, no. July, pp. 179–200, 2018, doi: 10.1016/j.jconrel.2018.07.036.

[8] K. McNamara and S. A. M. Tofail, 'Nanoparticles in biomedical applications', *Adv. Phys. X*, vol. 2, no. 1, pp. 54–88, 2017, doi: 10.1080/23746149.2016.1254570.

[9] M. X. Zhao and E. Z. Zeng, 'Application of functional quantum dot nanoparticles as fluorescence probes in cell labeling and tumor diagnostic imaging', *Nanoscale Res. Lett.*, vol. 10, no. 1, pp. 1–9, 2015, doi: 10.1186/s11671-015-0873-8.

[10] M. Zargar *et al.*, 'Green synthesis and antibacterial effect of silver nanoparticles using Vitex negundo L.', *Molecules*, vol. 16, no. 8, pp. 6667–6676, 2011, doi: 10.3390/molecules16086667.

[11] G. Yang *et al.*, 'Understanding the relationship between particle size and ultrasonic treatment during the synthesis of metal nanoparticles', *Ultrason. Sonochem.*, vol. 73, p. 105497, 2021, doi: 10.1016/j.ultsonch.2021.105497.

[12] Q. Zhang, Y. Zhang, Y. Li, P. Ding, S. Xu, and J. Cao, 'Green synthesis of magnetite nanoparticle and its regulatory effect on fermentative hydrogen production from lignocellulosic hydrolysate by Klebsiella sp.', *Int. J. Hydrogen Energy*, vol. 46, no. 39, pp. 20413–20424, 2021, doi: 10.1016/j.ijhydene.2021.03.142.

[13] K. Fukuda *et al.*, 'Exfoliated nanosheet crystallite of cesium tungstate with 2D pyrochlore structure: Synthesis, characterization, and photochromic properties', *ACS Nano*, vol. 2, no. 8, pp. 1689–1695, 2008, doi: 10.1021/nn800184w.

[14] U. Nithiyanantham, S. R. Ede, S. Anantharaj, and S. Kundu, 'Self-assembled NiWO4 nanoparticles into chain-like aggregates on DNA scaffold with pronounced catalytic and supercapacitor activities', *Cryst. Growth Des.*, vol. 15, no. 2, pp. 673–686, 2015, doi: 10.1021/cg501366d.

[15] L. Zhang, Y. Man, and Y. Zhu, 'Effects of Mo replacement on the structure and visible-light-induced photocatalytic performances of Bi2WO6 photocatalyst', *ACS Catal.*, vol. 1, no. 8, pp. 841–848, 2011, doi: 10.1021/cs200155z.

[16] H. Eranjaneya and G. T. Chandrappa, 'Solution Combustion Synthesis of Nano ZnWO4 Photocatalyst', *Trans. Indian Ceram. Soc.*, vol. 75, no. 2, pp. 133–137, 2016, doi: 10.1080/0371750X.2016.1181990.

[17] E. C. Dreaden, A. M. Alkilany, X. Huang, C. J. Murphy, and M. A. El-Sayed, 'The golden age: Gold nanoparticles for biomedicine', *Chem. Soc. Rev.*, vol. 41, no. 7, pp. 2740–2779, 2012, doi: 10.1039/c1cs15237h.

[18] A. Ali *et al.*, 'Synthesis, characterization, applications, and challenges of iron oxide nanoparticles', *Nanotechnol. Sci. Appl.*, vol. 9, pp. 49–67, 2016, doi: 10.2147/NSA.S99986.

[19] R. A. Ismail, S. A. Zaidan, and R. M. Kadhim, 'Preparation and characterization of aluminum oxide nanoparticles by laser ablation in liquid as passivating and anti-reflection coating for silicon photodiodes', *Appl. Nanosci.*, vol. 7, no. 7, pp. 477–487, 2017, doi: 10.1007/s13204-017-0580-0.

[20] W. M. M. Mahmoud, T. Rastogi, and K. Kümmerer, 'Application of titanium dioxide nanoparticles as a photocatalyst for the removal of micropollutants such as pharmaceuticals from water', *Curr. Opin. Green Sustain. Chem.*, vol. 6, pp. 1–10, 2017, doi: 10.1016/j.cogsc.2017.04.001.

[21] M. O. Amin, M. Madkour, and E. Al-Hetlani, 'Metal oxide nanoparticles for latent fingerprint visualization and analysis of small drug molecules using surface-assisted laser desorption/ionization mass spectrometry', *Anal. Bioanal. Chem.*, vol. 410, no. 20, pp. 4815–4827, 2018, doi: 10.1007/s00216-018-1119-2.

[22] N. Krishna, G. N. Kumar, T. Neethu, R. John, S. R. Babu, and S. Smitha Chandran, 'One Pot Green Synthesis of Silver Nanoparticles with Multiple Applications', *Mater. Today Proc.*, vol. 5, no. 9, pp. 20567–20571, 2018, doi: 10.1016/j.matpr.2018.06.435.

[23] A.T.A. Ibrahim, 'Toxicological impact of green synthesized silver nanoparticles and protective role of different selenium type on Oreochromis niloticus: hematological and biochemical response', *J. Trace Elem. Med. Biol.*, vol. 61, no. November 2019, p. 126507, 2020, doi: 10.1016/j.jtemb.2020.126507.

[24] S. P. Chandran, M. Chaudhary, R. Pasricha, A. Ahmad, and M. Sastry, 'Synthesis of gold nanotriangles and silver nanoparticles using Aloe vera plant extract', *Biotechnol. Prog.*, vol. 22, no. 2, pp. 577–583, 2006, doi: 10.1021/bp0501423.

[25] P. Rani, L. Trivedi, S. Singh, A. Singh, and G. Shukla, 'Materials Today : Proceedings Green synthesis of silver nanoparticles by Cassytha filiformis L . extract and its characterization', *Mater. Today Proc.*, no. xxxx, 2021, doi: 10.1016/j.matpr.2021.07.166.

[26] A. Umer, S. Naveed, N. Ramzan, and M. S. Rafique, 'Selection of a suitable method for the synthesis of copper nanoparticles', *Nano*, vol. 7, no. 5, 2012, doi: 10.1142/S1793292012300058.

[27] A. Umer, S. Naveed, N. Ramzan, M. S. Rafique, and M. Imran, 'A green method for the synthesis of copper nanoparticles using l-ascorbic acid', *Rev. Mater.*, vol. 19, no. 3, pp. 197–203, 2014, doi: 10.1590/S1517-70762014000300002.

[28] L. Malassis, R. Dreyfus, R. J. Murphy, L. A. Hough, B. Donnio, and C. B. Murray, 'One-step green synthesis of gold and silver nanoparticles with ascorbic acid and their versatile surface post-functionalization', *RSC Adv.*, vol. 6, no. 39, pp. 33092–33100, 2016, doi: 10.1039/c6ra00194g.

[29] D. Dutta and B. M. Das, 'Scope of green nanotechnology towards amalgamation of green chemistry for cleaner environment: A review on synthesis and applications of green nanoparticles', *Environ. Nanotechnology, Monit. Manag.*, vol. 15, no. December 2020, p. 100418, 2021, doi: 10.1016/j.enmm.2020.100418.

[30] P. Rajiv, B. Bavadharani, M. N. Kumar, and P. Vanathi, 'Synthesis and characterization of biogenic iron oxide nanoparticles using green chemistry approach and evaluating their biological activities', *Biocatal. Agric. Biotechnol.*, vol. 12, no. June, pp. 45–49, 2017, doi: 10.1016/j.bcab.2017.08.015.

[31] A. De, R. Das, P. Jain, and H. Kaur, 'Green chemistry-assisted synthesis of CuO nanoparticles: Reaction optimization, DNA cleavage, and DNA binding studies', *Mater. Today Proc.*, no. xxxx, pp. 1–4, 2020, doi: 10.1016/j.matpr.2020.10.955.

[32] T. Naseem and T. Durrani, 'The role of some important metal oxide nanoparticles for wastewater and antibacterial applications: A review', *Environ. Chem. Ecotoxicol.*, vol. 3, pp. 59–75, 2021, doi: 10.1016/j.enceco.2020.12.001.

[33] H. D. B. Jenkins and K. P. Thakur, 'Reappraisal of thermochemical radii for complex ions', *J. Chem. Educ.*, vol. 56, no. 9, pp. 576–577, 1979, doi: 10.1021/ed056p576.

[34] R.D. Shannon, 'Revised effective ionic radii and systematic studies of interatomic distances in halides and chalcogenides', *Acta Cryst.*, vol. A, no. 32, pp. 751–767, 1976, doi: 10.1107/S0567739476001551.

MANAS Journal of Engineering
ISSN 1694-7398 | e-ISSN 1694-7398

Volume 11, Issue 1, (2023) Pages 105-111
https://doi.org/10.51354/mjen.1142038

Investigation of chemical, sensory, and rheological properties of Kyrgyz ethnic fermented beverage from cereals during cold storage

Janyl Iskakova[1], Jamila Smanalieva[2]

[1] Environmental Engineering Department, Engineering Faculty, Kyrgyz-Turkish Manas University, Bishkek, Kyrgyzstan. ORCID: 0000-0002-1614-3984

[2] Department of Food Production Technology, Technology Faculty, Kyrgyz State Technical University after I. Razzakov, Bishkek, Kyrgyzstan. ORCID: 0000-0002-3929-4291

ABSTRACT

Maksym is a Kyrgyz ethnic beverage made from milled cereals such as wheat, barley, or maize, boiled in water, and then fermented using yeast and lactic acid bacteria as a starter culture. The aim of this study was to investigate the changes in the consistency and sensory properties of Maksym after industrial production during refrigerated storage. The acidity of the beverage increases and the total soluble solids decrease after 21 days. The amount of lactic acid bacteria (LAB) and yeast after production were 9.36 and 9.46 log cfu/mL, respectively. After 21 days it is indicated that the amount of both starter cultures decreased by 2 log units. In terms of acceptability, the sensory properties after 7 days of storage received the highest rating. However, the acidic taste after 21 days of storage received the lowest rating. Rheological measurements carried out at 5, 10, 20, and 30°C also revealed these changes. Four rheological models (Newtonian, Herschel-Bulkley, Ostwald De-Waele, and Casson) were used to describe the flow behaviour of the beverage. The Casson model was superior to other rheological models. The effective viscosity of Maksym was decreased from 2.66 to 1.96 mPa·s after 21 days of cold storage. The activation energy was decreased from 23.10 and 14.94 kJ/mol and indicated the thinning of viscosity of the beverage. The obtained parameters can be used to predict the shelf-life model and product labelling by its expiry period, as well as to control the quality of Maksym.

ARTICLE INFO

Research article

Received: 7.07.2022
Accepted: 16.01.2023

Keywords:
Maksym,
fermented beverage,
rheological properties,
microbiology,
sensory,
storage

**Corresponding Author*

1. Introduction

Cereal-based fermented beverages are widespread in various countries of Asia and Africa [1]. According to [2], fermented products have a lot of benefits such as eliminating unwanted factors arising from raw materials, providing a safer product with a longer shelf life. Fermentation helps to improve the organoleptic qualities of the product, facilitating digestion due to its probiotic properties compared to unfermented foods. Probiotics are products containing live microorganisms, which contribute to endoecology of the intestines of human beings as well as other animals [3]. Other functional ingredients are prebiotics, which are indigestible substances that improve the growth of probiotic microorganisms [4]. Since prebiotics support the growth and vital functions of the probiotic microbial community, there is great potential for the synergetic impact of prebiotics and probiotics. The use of prebiotic ingredients provides not only nutritional but also techno-functional benefits that can advance the texture parameters of the final products [5].

Figure 1. *Traditional beverage Maksym.*

The nomadic lifestyle of Kyrgyz required the use of food products with a long shelf life. The lactic acid fermentation

process is widely used for the production of cereal beverages such as Jarma, Maksym and Bozo. For the production of Maksym, roasted and shredded cereals were used, usually wheat, barley and corn. It is characterized as a colloidal fluid with small grain particles, which has a slightly sour smell and brownish colour (Fig.1). Maksym was traditionally prepared in every household during the summer season and consumed chilled to relieve thirst and hunger. At least two decades before the company "Shoro" that first introduced Maksym as a commercial product was established, after which it became widely available all over the country. The company also entered China, in Kashgar, around the restaurant selling this beverage, local Kyrgyz and those who are in China only temporarily to work are joining [6, 7]. Currently, in Kyrgyzstan, Maksym is industrially produced by many enterprises. Methods and recipes of Maksym production differ from the region of Kyrgyzstan.

The traditional production method and recipe of Maksym are shown in Fig. 2. The general step is boiling the roasted and milled cereals, called "Talkan" in water (1:30 w/w) until starch gelatinization. For the preparation of "Talkan", cereals (wheat and barley) are peeled, cleaned from the husk, washed and dried. The roasting of cereals is carried out at 170–180°C until the brownish colour of the grain. Then they are cooled down to 30–40°C and ground in a millstone and sieved through a sieve with a pore diameter of 1 mm. To give the beverages a viscous consistency, roasted wheat flour with mutton fat is used. Water is added to the roasted wheat flour in small portions and boiled. After boiling, "Talkan" is added to the water-flour suspension thoroughly and boiled for about 50 minutes. After cooling to 25-30°C, 2% (w/v) of a previous batch of the beverage is added to the water-flour-talkan fluid. The fermentation is usually conducted at room temperature (about 25-30°C) for 12-14 hours and then cooled and stored at fridge temperature [7]. According to the Kyrgyz Standard Maksym contains 0.9 g/100 mL of proteins, 4.38 g/100 mL of carbohydrates, 0.08 mg/100 mL of vitamin B_1, 0.1 mg/100mL of vitamin B_2, 0.4 mg/100mL of vitamin PP, 0.59 g/100mL of ascorbic acid and 27 kcal/100 mL energy value [8].

The main problem of fermented alcohol-free beverages is the growth of microflora within the storage period. Fermented beverages have a limited shelf-life due to the growth of their own starter culture, unpleasant odours, browning, and bitterness, which, in turn negatively impact consumer perception [9]. Therefore, to track undesirable changes in fermented beverages, it is necessary to study some quality indicators during storage. In addition, it is important to determine the recommended maximum storage time during which a given product quality remains acceptable. Rheological parameters are a good indicator of structural changes in products containing starch and live microorganisms [10]. Consequently, an investigation of the rheological and sensory behaviour of the Kyrgyz ethnic beverage Maksym during storage is necessary. The producer guaranteed 30 days of storage, however, there is no information on the shelf-life of the opened Maksym in the refrigerator. Therefore, the aim of this study was to study changes in the consistency, microbiological and sensory properties of fermented beverages after opening the industrial-produced bottle. The research question was: How many days does the quality of the opened Maksym remain acceptable for consumers? The results will help predict the model for the shelf-life of Maksym and label the product by expiration date after the opening of the bottle.

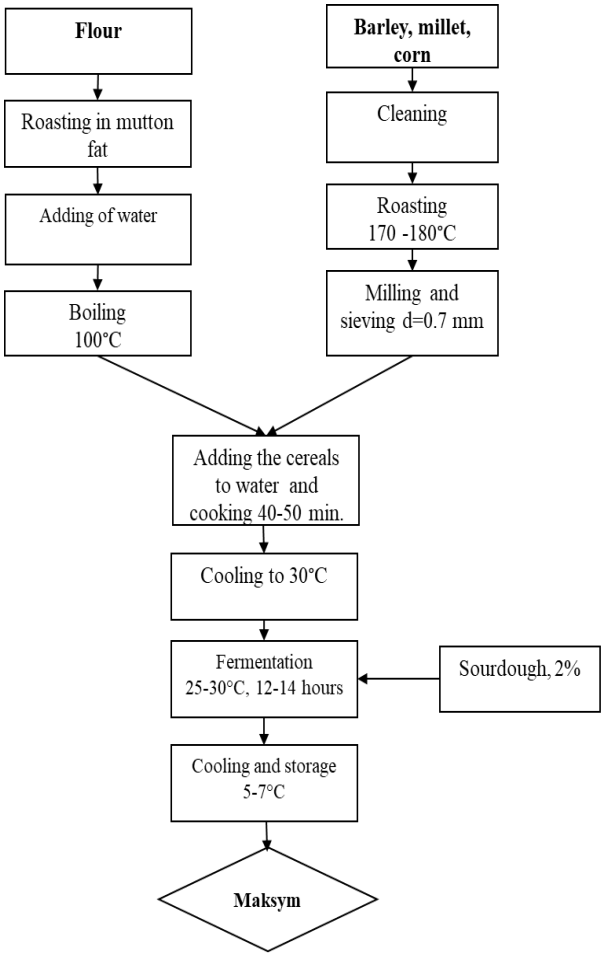

Figure 2. *Production scheme of Maksym.*

1. Materials and methods

1.1. Materials and Sample Preparation

Industrially produced fresh Maksym samples were obtained from a local market in Bishkek, Kyrgyzstan, and were refrigerated at 5°C.

pH meter (Mettler Toledo, Greifensee, Switzerland) was used for the determination of pH and titratable acidity of samples (AOAC method 981.12, 2019). The titratable acidity was given as the percentage of lactic acid in the beverage [11]. The determination of total soluble solids content was carried out

using a refractometer (Reichert Abbe Mark II Plus Refractometer, Reichert, Inc., NY, USA) at 20°C.

1.2. Microbiological analyses

For microbiological analyses 10 ml sample was taken under aseptic conditions and transferred into 90 ml of 0.9 % NaCl solution. After making serial dilutions, the samples were plated on selective media for both yeasts and lactic acid bacteria. For the isolation of yeasts Wort Agar (Merck, Germany) was used and plates were incubated at 27 °C for 5 days. Lactic acid bacteria were isolated using MRS Agar (Merck, Germany). Incubation was carried out at 30 °C for 5 days using the anaerobic incubation system Anaerocult® A (Merck, Germany) in an anaerobic jar [12]. Colonies were counted and the results were expressed as cfu/mL of the beverage. Three replicate counts were performed for each tray.

1.3. Rheological Measurements

The rheological properties of Kyrgyz ethnic beverage Maksym were measured at 5, 10, 20 and 30°C using rotational measurements using an MCR 302 rheometer (Anton Paar, Graz, Austria). The concentric cylinder geometry (CC27) was used as the working tool. The rheological data were analysed using the software Rheoplus 32 Multi 6 version 3.40. The flow curves were measured in the modes of increasing, holding and decreasing the shear rate from 0.1 to 100 1/s, for the measurement of time-dependent properties. To describe the sample's flow behaviour, the flow curves obtained from the 3rd interval were modelled using equations such as Newtonian, Ostwald-De-Waele, Herschel-Bulkley, and Casson [13].

1) Newtonian:

$$\tau = \eta\dot{\gamma} \quad (1)$$

2) Ostwald–de Waele (or Power-law):

$$\tau = k\dot{\gamma}^n \quad (2)$$

where k is the consistency index (Pa·s^n) and n is the flow behaviour index, $\dot{\gamma}$ is shear rate.

3) Herschel – Bulkley:

$$\tau = \tau_0 + k\dot{\gamma}^n \quad (3)$$

where τ_0 is yield stress, that is the stress at which the sample begins to flow or deform plastically.

4) Casson:

$$\tau^{0,5} = \tau_0^{0,5} + \eta_{Ca}\dot{\gamma}^{0,5} \quad (4)$$

where η_{Ca} is Casson's coefficient of viscosity.

The temperature dependence of Maksym's viscosity was expressed with the activation energy E_a and was calculated using the Arrhenius-type equation (Eq. 5, 6):

$$\eta(T) = A\exp\left(-\frac{E_a}{R\cdot T}\right) \quad (5)$$

$$\ln\eta = \ln A + \left(-\frac{E_a}{R}\right)\cdot\left(\frac{1}{T}\right) \quad (6)$$

Where A is the pre-exponential factor, R is the ideal gas constant (8.31 J/mol·K), T is the absolute temperature (K). E_a is the activation energy (J/mol) [14].

1.4. Evaluation of sensory properties

The evaluation of sensory properties changes during the storage period was conducted using an evaluation test covering mouthfeel, aroma, taste, acidic taste, and overall acceptability according to [10]. A five-point hedonic scale, from like extremely (5), like moderately (4), like a little (3), not sure (2), dislike a little (1) to dislike extremely (0) was used to assess the acceptance test and judged by a sensory group of 10 trained panellists [10, 15].

1.5. Statistical analysis

Each analysis was performed three times. Obtained data were analysed by the IBM statistical software SPSS 22 (SPSS Inc., Chicago, IL) using Tukey's post hoc tests and one-way analysis of variance (ANOVA) with a 95% confidence interval. A p-value < 0.05, was considered statistically significant.

2. Results and discussion

2.1. Chemical changes during storage

The pH of samples decreased with increasing storage time; with a starting value of 3.68, it decreased in 21 days to 3.62 (Fig. 3). After 21 days of cold storage, the total acidity of the samples slightly increased from 4.2 to 4.7 g/100 mL (Fig. 3), which indicates the continuance of acid maintenance during cold storage. According to previous studies, this is due to the prolongation of fermentation with lactic acid bacteria (LAB) during the storage period; a pH range of 3.6 to 4.9 allows LAB, which include probiotic microorganisms, to grow under usual conditions without damaging the product [16-18]. For mathematical modelling and prediction for 10 days of the change in solid content and acidity of the beverage during storage days, the polynomial regression analysis, and for pH - a linear regression analysis were carried out using the Excel MS Office program. The results are shown in Fig. 3.

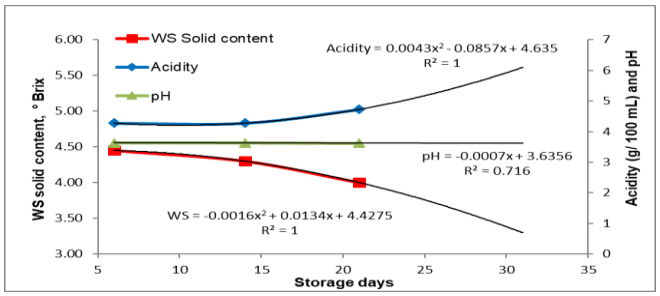

Figure 3. *Dependence of acidity, pH, and water-soluble solids content on storage days.*

The total soluble solids showed a slight decrease from 4.5 to 4.0 °Brix throughout the shelf life, and this was inversely proportional to the total acidity (Fig. 3). This change is associated with the metabolism of LAB and yeast cells. Lactic acid bacteria produce enzymes such as lipases, proteases, amylases, peptidases, esterases, ureases, polysaccharide degrading enzymes, and phenol oxidases [19]. The amylase enzymes produced by LAB break down insoluble starch molecules, making them soluble and subsequently usable by the same fermenting microorganisms such as *Saccharomyces cerevisiae* [17, 20].

2.2. Lactic acid bacteria enumeration

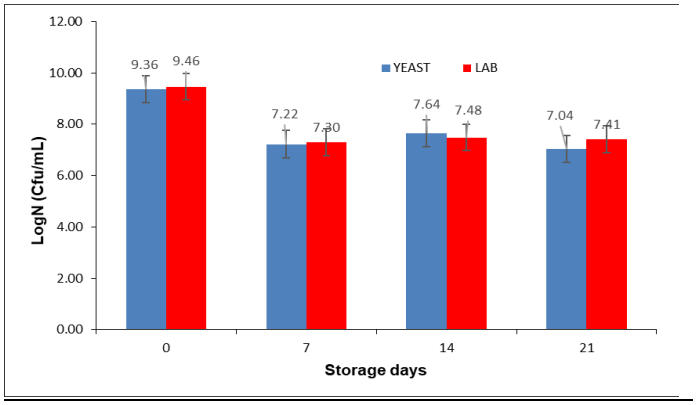

Figure 4. *Change in lactic acid bacteria (LAB) and yeast counts (cfu/mL) during the storage of fermented beverage Maksym.*

The microbiological characteristics of the final fermented product can be influenced by various factors, such as the ratio of starter cultures to food products, incubation time and temperature, agitation, and storage conditions [21]. The enumeration of lactic acid bacteria (LAB) and yeast number (cfu/mL) during the refrigerated storage of fermented beverage "Maksym" is shown in Fig.4. The amount of lactic acid bacteria (LAB) and yeast after production were 9.46 and 9.36 log cfu/mL, respectively. After 21 days the numbers of both starter cultures decreased to 7.41 and 7.04 log cfu/mL for LAB and yeast, respectively. The viability of yeast cells at the end of the shelf life period was slightly higher (78 %), compared to LAB (75%). In general, fermented cereal products contained LAB and mesophilic aerobic bacteria in the range of 5 to 9 log cfu/g [21]. The amount of LAB in some acidic beer products from Belgium, such as lambic and gueuze, ranged from 2 to 5 log cfu/g [22, 23]. For comparison, fermented dairy products contain LAB in the range of 1 to 10 log cfu/g [21]. According to [24] in Brazilian kefir containing yeast and LAB cells, the count of yeast was approximately 6 log cfu/mL and LAB group count was approximately 10 cfu/mL. They remained constant until the end of the storage period of 28 days. The amount of LAB cfu in khainak milk fermented by mesophilic starter cultures (*Lactococcus lactis* subsp. *lactis* and *L. lactis* subsp. *cremoris*) immediately after fermentation was also high at 9.42 log cfu/mL and decreased after 3 days of storage to 8.22 log cfu/mL [25].

2.3. Flow behaviour of the beverage Maksym

The flow curves: shear stress versus shear rate and viscosity curves: shear rate ($\dot{\gamma}$) versus dynamic viscosity (η) at 5°C for various storage periods: 7, 14, 21 days are shown in Fig. 5.

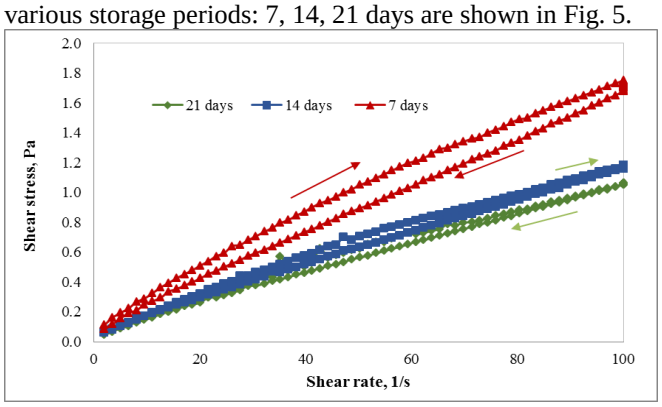

Figure 5. *Flow curves: shear-thinning and thixotropic behaviour of Maksym at 5°C.*

All shear stress vs. shear rate curves of Maksym represent shear-thinning behavior: a plot in which the apparent viscosity decreases with increasing shear rate. The viscosity of other Kyrgyz fermented cereal beverage Boza decreased as shear rate increased [10]. The two curves up (by increasing the shear rate) and down (decreasing shear rate) of Maksym samples did not overlap and led to the formation of a hysteresis loop (area). The downward curves were lower than the upward curves, indicating a thixotropic behaviour of the sample. The hysteresis area of Maksym at 5°C decreases with increasing storage time. This is the typical flow behaviour of starch-containing food and yogurts [15]. The shear stress will destroy the original structure, which will not recover as it moves down the curve, resulting in lower yield stress values [13]. The downward curves were used for regression analysis with the Newtonian, Herschel-Bulkley, Ostwald De-Waele, and Casson models to obtain parameters for inputting engineering calculations. The most suitable rheological model for describing Maksym flow was the Casson model. The calculated rheological model constants are presented in Table 1.

Table 1. *The rheological constants of Maksym according to Casson model (n=0.5)*

Days	T (°C)	τ_0 (Pa)	η_{Ca} Pa ·s	R^2	SD	A (Pa/s)	at shear rate of 50 s^{-1}
7	5	0.134	0.115	0.9996	0.01	11.30	0.028
	10	0.110	0.103	0.9999	0.01	4.63	0.022
	20	0.085	0.087	0.9999	0.00	2.54	0.016
	30	0.080	0.071	0.9988	0.00	0.45	0.016
14	5	0.113	0.096	0.9999	0.00	3.96	0.021
	10	0.077	0.090	1.0000	0.00	2.21	0.017
	20	0.058	0.077	1.0000	0.00	0.81	0.012
	30	0.049	0.068	0.9999	0.00	1.08	0.010
21	5	0.089	0.094	0.9995	0.00	3.30	0.019
	10	0.068	0.087	0.9999	0.00	0.39	0.015
	20	0.057	0.076	0.9999	0.00	0.29	0.012
	30	0.054	0.071	0.9989	0.00	1.95	0.011

* Mean values are given of three independent measurements; standard deviation is SD < 0.01.

Since the investigated samples have a small but measurable yield stress, defined as the minimum shear stress that must be applied to the material to initiate flow, mathematical models such as the Casson and Herschel-Bulkley models can be used and in terms of the correlation coefficient R^2, as well as the most suitable models of the dependence of shear stress on shear rate, the Casson and Herschel-Bulkley models outperformed other rheological models. However, the Casson model was superior to the Herschel-Bulkley model.

For the calculation of effective viscosity, the shear rate value was taken to be 50 s^{-1} as a mean of typical shear rate ranges under processing conditions such as stirring and swallowing beverages.

The values of effective viscosity and the yield stress (τ_0) measured at 5°C decreased from 0.028 to 0.019 Pa·s and 0.13 to 0.09 Pa, respectively. as the storage time increased from 7 to 21 days of storage. The pattern of decreasing rheological parameters with increasing storage time suggests complex carbohydrates such as starch. dextrin, etc., may hydrolyse as the yeast grows. Thus, the storage stability of the colloidal suspension will decrease. However, ANOVA analysis revealed that there is no significant difference in Casson's viscosity coefficient (η_{Ca}), yield stress values (τ_0), and effective viscosity (η_{eff}) of beverage Maksym within the storage time.

The values of yield stress (τ_0), effective viscosity (η_{eff}) and hysteresis area (A) of the samples decreased significantly with increasing temperature. ANOVA analysis also showed that these values of Maksym samples were significantly different ($p < 0.05$) when comparing temperatures at 5 and 30°C and differences are not statistically significant at 10 and 20°C. An Arrhenius-type equation (Eq. 4 and 5) was used to calculate flow activation energies for Maksym. The results of the calculation revealed that the activation energies of samples were 23.10; 19.92 and 14.94 kJ/mol at 7, 14, 21 days of storage, respectively. Correlation coefficients ranged from 0.973 to 0.992. The activation energy Ea is the energy barrier that must be overcome before the flow process is initiated [14]. Therefore, the decrease of activation energy during storage indicated the thinning of viscosity of the beverages Maksym. The activation energy of another Kyrgyz ethnic fermented beverage Bozo was found as 9.50 and 12.62 kJ/mol at 7 and 21 days of storage, respectively [10]. The activation energies of ghee samples stored at room and refrigerator temperatures were 26.3 kJ/mol and 29.9 kJ/mol [27], respectively, and the activation energy of Süzmö was 61.66 kJ/mol [28]. Lower activation energies (3.03 – 10.53 kJ/mol) at 5 – 65°C and 4 – 14°Brix were obtained for Josapine pineapple juice by [29]. Similar results for a malt wort of 21.17 kJ/mol and higher values for a hopped wort of 42.8 kJ/mol at 5 – 40°C were reported [30].

2.4. Sensory properties of beverage Maksym

Fig. 6 shows the sensory evaluation of the Maksym on different days of storage. In terms of mouthfeel, aroma, flavour, acidic taste, and overall acceptability after 7 days of storage, the panellists gave the highest scores. However, after 14 and 21 days of storage, the beverage was scored much

lower in all parameters. Acidic taste after 21 days of storage received the lowest rating. This observation is also consistent with the titratable acidity and pH analysis. These changes are due to the continuation of lactic acid and alcoholic fermentation, resulting in an increase in the content of lactic acid and ethyl alcohol, as well as carbon dioxide [31]. Since storage at refrigerator temperature does not stop the microbiological activity, the accumulation of metabolic by-products will continue.

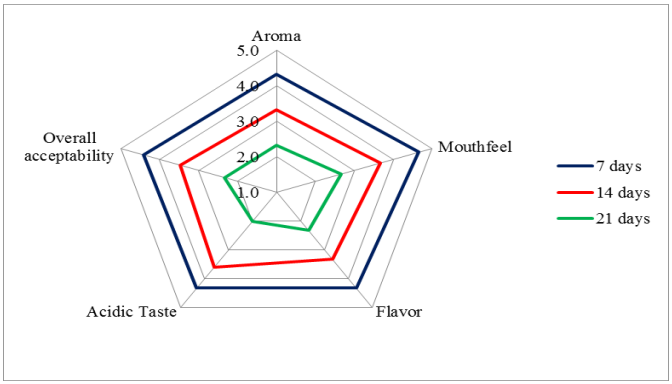

Figure 6. *Sensory evaluation of Maksym at different storage days.*

3. Conclusion

In this study, for the first time, the chemical, rheological and sensory properties of Kyrgyz ethnic cereal beverage Maksym were studied during storage. Research shows that there is an increase in acidity and a decrease in the total amount of soluble solids. The flow characteristics of Maksym during storage in the refrigerator also changed, which may be due to the hydrolysis of polysaccharides by LAB and yeast cells in the sample. Namely, Maksym's effective viscosity, the yield stress (τ_0), and Casson's coefficient of viscosity (η_{Ca}) decreased after 14 days of storage. However, these changes are statistically insignificant. Sensory properties investigated after 21 days of storage received the lowest score. Microbiological investigations have shown, that the number of lactic acid bacteria (LAB) and yeast after production were 9.46 and 9.36 log cfu/mL, respectively. After 21 days the viability of yeast cells at the end of the shelf life period was slightly higher (78 %), compared to LAB (75%). Thus, the shelf life of beverage Maksym after opening can be stated as 14 days. These rheological and sensory parameters provide food manufacturers with useful information on post-production storage parameters. Also, consumers can use the information to declare the quality of Maksym during refrigerated storage.

References

1. Köse E., Yücel U., "Chemical composition of Boza", Journal of Food Technology, 1(4), (2003), 191-193.
2. Arici M., Daglioglu O., "Boza: a lactic acid fermented cereal beverage as a traditional Turkish food", Food Reviews International, 18, (2002), 39-48.
3. Skovgaard N., "Lactic acid bacteria and bifidobacteria: Current progress in advanced research". pp 338-339. In: Sonomoto & Yokota (ed): International journal of food microbiology. Caister Academic Press, Amsterdam, 2011.
4. Prado F.C., Parada J.L., Pandey A., Soccol C.R., "Trends in non-dairy probiotic beverages", Food Research International, 41, (2008), 111-123.
5. De Vrese M., Schrezenmeir J., "Review Probiotics, prebiotics, and synbiotics". pp 1-66. In: Scheper T (ed): Advances in Biochemical Engineering/Biotechnology. Springer-Verlag Berlin Heidelberg, 2008.
6. Kokaislová P., Kokaisl P., "The Kyrgyz - Children of Manas", Nostalgie, Praha, 2009.
7. Smanalieva J., Iskakova J., Musulmanova M., "Milk-and cereal-based Kyrgyz ethnic foods", International Journal of Gastronomy and Food Science, 29, (2022), 100507.
8. Maksym and Jarma national drinks. General specifications, Kyrgyz Standard KMS 980:2005.
9. Stratford M., "Food and beverage spoilage yeasts", pp. 335-339. In: Querol, A. & Fleet G.H. (ed): Yeasts in food and beverages. Springer-Verlag, Berlin, 2006.
10. Iskakova J., Smanalieva J., Methner F-J., "Investigation of changes in rheological properties during processing of fermented cereal beverages", Journal of Food Sciences and Technology, 56(9), (2019), 3980-3987.
11. AACC "Official Methods of Analysis", 21st Edition - AOAC International, 2019.
12. Iskakova J., Hutzler M., Kemelov K., Grothusheitkamp D., Michel M., Methner F.J., "Screening a Bozo starter culture for potential application in beer fermentation", Journal of American Society of Brewing Chemists, 77, (2019), 54–61.
13. Rao M.A. "Rheology of fluid and semisolid foods", Principles and application. Aspen Publishers, Inc., Gaithersburg MD, 1999.
14. Mezger G.T. "The rheology handbook", Vincentz Network, Hannover, 2011.
15. Smanalieva J., Iskakova J., Fischer P., "Investigation of the prebiotic potential of rice varieties for *Lactobacillus acidophilus* bacteria", European Food Research and Technology, 247(7), (2021), 1815-1824.

16. Aportela-Palacios A., Sosa-Morales M.E., Vélezruiz J.F., "Rheological and physicochemical behavior of fortified yogurt, with fiber and calcium", Journal of Texture Studies, 36, (2005), 333-349.

17. Costa K.K.F.D., Soares Júnior M.S., Rosa S.I.R., Caliari M., Pimentel T.C., "Changes of probiotic fermented drink obtained from soy and rice byproducts during cold storage", LWT - Food Science and Technology, 78, (2017), 23-30.

18. Gupta S., Cox S., Abu-Ghannam N., "Process optimization for the development of a functional beverage based on lactic acid fermentation of oats", Biochemical Engineering Journal, 52(2–3), (2010), 199-204.

19. Padmavathi T., Bhargavi R., Priyanka P.R., Niranjan N.R., Pavitra P.V., "Screening of potential probiotic lactic acid bacteria and production of amylase and its partial purification", Journal of Genetic Engineering and Biotechnology, 16(2), (2018), 357-362.

20. Power R.F. "Enzymatic conversion of starch to fermentable sugars". pp 23-32. In: Jacques et al. (ed): The alcohol textbook, fourth edition. Nottingham University Press, Nottingham, 2003.

21. Rezac S., Kok C.R., Heermann M., Hutkins R., "Fermented foods as a dietary source of live organisms", Frontiers in Microbiology, 9, (2018), 1785.

22. Spitaels F., Kerrebroeck S., Snauwaert I., Aerts M., Landschoot A., Vuyst L.D., Vandamme P., "Microbiota and metabolites of aged bottled gueuze beers converge to the same composition", Food Microbiology, 47, (2015), 1–11.

23. Spitaels F., Wieme A. D., Janssens M., Aerts M., Daniel H. M., Van Landschoot A., Vuyst L.D., Vandamme P., "The microbial diversity of traditional spontaneously fermented lambic beer", PLoS ONE, 9, (2014), e95384.

24. Leite A.M.O., Leite D.C.A., Del Aguila E.M., Alvares T.S., Peixoto R.S., Miguel M.A.L., Silva J.T., Paschoalin V.M.F., "Microbiological and chemical characteristics of Brazilian kefir during fermentation and storage processes", Journal of Dairy Science, 96 (7), (2013), 4149-4159.

25. Elemanova R., Musulmanova M., Ozbekova Z., Usubalieva A., Adil Akai R., Deidiev A., Smanalieva J., "Rheological, microbiological and sensory properties of fermented khainak milk fermented with different starter cultures", International Dairy Journal, 134, (2022), 105453.

26. Genc M., Zorba M., Ova G., "Determination of rheological properties of boza by using physical and sensory analysis", Journal of Food Engineering, 52, 2002, 95-98.

27. Iskakova J., Smanalieva J., "Investigation of rheological behavior of Kyrgyz traditional food Sary mai", MANAS Journal of Engineering, 8(2), (2020), 84-89.

28. Iskakova J., Smanalieva J., "Determination of flow and viscoelastic properties of the Kyrgyz ethnic food "Süzmö" depending on temperature and moisture content", Trakya University Journal of Natural Sciences, 22(2), (2021), 199-205.

29. Shamsudin R., Wan Daud W.R., Takrif M.S., Hassan O., Ilicali, C., "Rheological properties of Josapine pineapple juice at different stages of maturity", International Journal of Food Science and Technology, 44, (2009), 757-762.

30. Travnicek P., Los J., Junga P., "Comparison of rheological properties of hopped wort and malt wort", Acta Universitatis Agriculturae et Silviculturae Mendelianae Brunensis, 63, (2015), 131-136.

31. Walker G.M., Stewart G.G., "Saccharomyces cerevisiae in the production of fermented beverages", Beverages 2(30), (2016), 1-12.

MANAS Journal of Engineering
ISSN 1694-7398 | e-ISSN 1694-7398

Volume 11, Issue 1, (2023) Pages 112-118
https://doi.org/10.51354/mjen.1149121

Computer based speed control application for universal motor

Sabir Rüstemli[1], Emin Ağralı[2]

[1] Department of Electrical and Electronics Engineering, Bitlis Eren University, Rahva Campus, Bitlis, Turkey, srustemli@beu.edu.tr, ORCID: 0000-0002-4957-1782

[2] Vocational School, Muş Alparslan University, Muş, Turkey, e.agrali@alparslan.edu.tr, ORCID: 0000-0002-0513-402X

ABSTRACT

In this study, speed control of alternative current (AC) universal motor is made in a computerized manner using PIC16F84A and PIC18F2550. AC universal motor speed control is realized by triggering the motor power circuit, triac with the phase angle control method by programming PIC16F84A. In the phase angle control method zero crossing points of AC line signal are detected by zero crossing detector and applied to the analog input of PIC16F84A. Zero crossing information applied to the microcontroller has provided phase control at a desired angle value in each alternance of the line. Motor speed control commands via computer are made by means of the control panel designed under Visual Basic 6.0 platform by using PIC18F2550 microcontroller based control card. Application results show that the speed control performed provides practical and easy control, is convenient, sensitive, and economic and also can immediately be adapted to different applications compared to the present analog control.

ARTICLE INFO

Research article

Received: 26.07.2022
Accepted: 12.12.2022

Keywords:
universal motor,
phase angle control,
visual basic,
PIC.

*Corresponding author

1. Introduction

Use of the electric motors which provide substantial efficiency in conversion of electric energy into mechanical energy is increasing day by day. Since Universal Motors out of electric motors can operate both with Alternative Current (AC) and Direct Current (DC), they are used in most of the household appliances and power tools today. Universal motors are preferred due to the properties thereof such as having high start-up and turning moments, ability of being operated at high speeds and manufactured in small powers. The method used in the speed control of the universal motors substantially affects the motor efficiency. One of the important conditions to optimize the motor efficiency is to determine a proper speed control method. Phase angle control method is commonly used in speed control of the universal motors. This method provides performing the control of the universal motors in wide speed range. Microcontrollers are considerably used in the motor drive circuits designed by using phase angle control method.

In this study, speed control of the AC universal washer motor is performed through the control panel designed under Visual Basic 6.0 platform based on the microcontroller. The study is performed in two stages as application and simulation. In the application part, drive card and control card to control the drive card are designed for the speed control of the motor. In the control system, speed information received from the tacho generator coupled to the motor shaft is monitored with Visual Basic 6.0 program control panel and speed change of the motor is instantaneously monitored in the computer screen. In line with the commands given to the control card with the control panel designed triac trigger angles are changed by means of drive card PIC microcontroller, input voltage of the motor is adjusted and the control thereof in a wide speed range is provided. In the simulation part, on the other hand, simulation of all of the circuits in the application is made with ISIS program, which is the circuit drawing, simulation and analysis program of PROTEUS, speed analysis of the universal motor in various excitation conditions is performed.

2. Material and methods

2.1. Unıversal Motors

Universal motor is an AC series motor with stator and rotor magnetic bodies thereof being composed of sheet packages. When separately fed from AC and DC sources with the same efficient voltage, universal motors exhibit similar speed and power output characteristics. The most common usage areas of these motors are small power household, workplace machine and devices [1]. Universal motor has excellent

properties. Compared to the induction motors, they are characterized with their high power regarding the size and weight thereof. Universal motor can be operated at a very good breakaway torque and extremely high speed (15 000-20 000 rpm) [2]. For a common use of the universal motor minimum energy consumption is very important. Therefore, universal motor high performance requirements have increasingly become important with a low-cost controller [3]. The best way of controlling the speed of a universal motor is to change the RMS value of the sinus function of AC input voltage. A higher RMS input voltage provides a higher motor speed [4]. Changing the RMS value of the sinus function of input voltage alternating current can simply be made using a triac serially connected AA source. Here, speed control can be performed adjusting the voltage applied to the motor by changing the triac firing angle [4]. In recent technology, power control is made with electronic circuits. Electronic control is preferred due to many advantages such as the elements being small in size, having a long life and providing computer control in automation [5]. In this study, BTA/BTB16-600B triac series is used as phase angle control power circuit element in the drive circuit. Triacs are semiconductor circuit elements which conduct bidirectional current, control high level load currents with small excitation current and operate at AC. Triac based power circuit is given in Fig. 1.

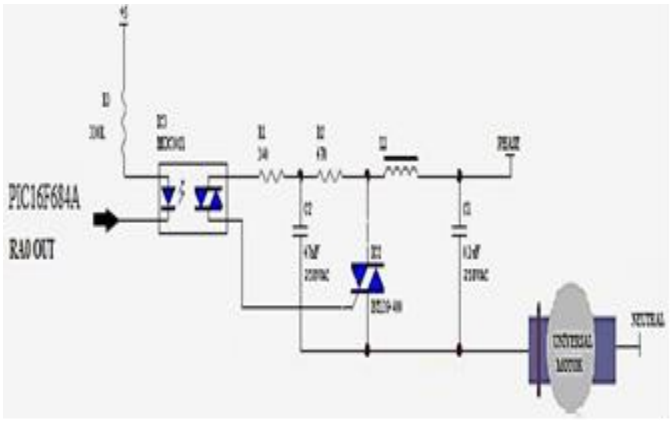

Figure 1. *Triac-based power circuit.*

Controller-based and speed-adjustable motor drives have also played an important role in the development of industrial automation [6].

Importance of the microcontrollers in the control of universal motors is increasing day by day. In the point of preferring the PIC microcontrollers, advantages of PICs compared to the other microcontrollers can be arranged as code efficiency, reliability, command set and speed [7]. The advantages provided by the computer programs in control systems are known to provide more professional control compared to the manual control systems. Computer program Visual Basic is a visual language having complex logics and forms which facilitate the designs of Windows compatible application. [8]. In this study, universal motor speed control is performed via computer. In line with the program written by forming necessary control elements with the use of drive card Visual Basic 6.0 program control panel, the control is performed. Control panel view of the designed control program is given in Fig. 2.

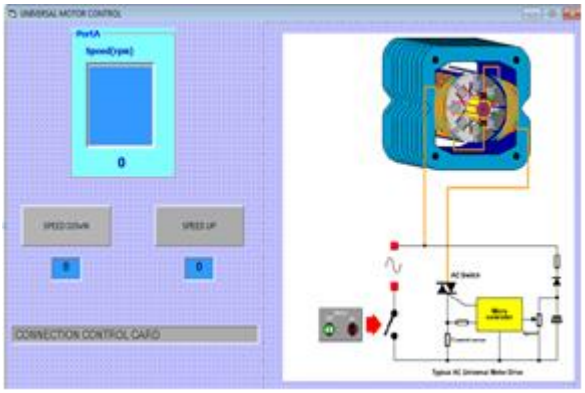

Figure 2. *Designed control panel.*

2.2. Speed Control of Universal Motor

The method used in the speed control of the universal motors substantially affects the motor efficiency. One of the important conditions to optimize the motor efficiency is to determine a proper speed control method. Motor drive systems designed depending on the speed control method affects the performance of the motor. Phase angle control method is commonly used in speed control of the universal motors. This method provides performing the control of the universal motors in wide speed range values. Microcontrollers are considerably used in the motor drive systems designed by using phase angle control method. Speed control of the universal motor connected to the AC source can simply be performed by using a triac connected to the motor in series. Speed control can be performed changing the voltage applied to the motor by changing the triac firing angle.

Varible Structure Systems (VSS) such as motor control, robotic manipulators and indefinite systems have an important place in the control of modern non-linear systems. However, there are some difficulties such as occurrence of numerous switches between the control bounds, which cannot be carried out by real controllers.

To overcome this problem, a thin boundary layer neighbouring the switching surface is introduced for smoothing out the control discontinuity [9].

In this study, speed control is made via computer using

PIC18F2550 based control card and PIC16F84A based drive card. It is cheaper to use PIC16F84A microcontroller for controlling the motor from the point of hardware [10]. Different reference frames can be used to model the motor: three phases frame (a,b,c), stationary frame (α,β) or synchronous frame (d,q). From the control point of view, the (d,q) reference frame is widely used [11]. Motor speed control is made using phase angle control in the drive system. Block diagram of the designed drive system is given in Fig. 3.

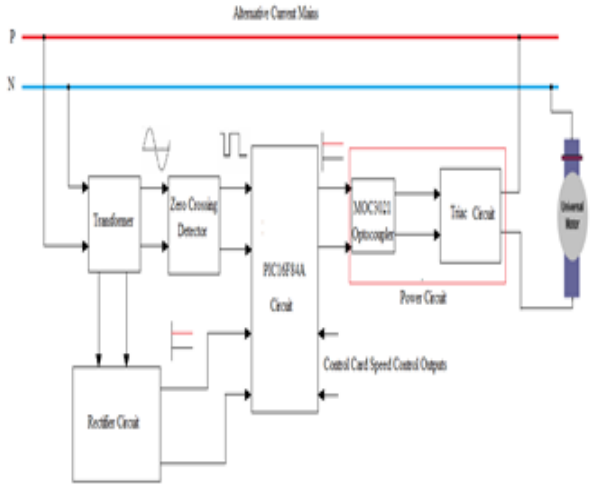

Figure 3. *Block diagram of the designed drive system*.

Zero crossing points of AC line should be detected in PIC based phase angle control systems. For this, a zero crossing detector is used in drive card. Zero crossing detector circuit used is given in Fig. 4.

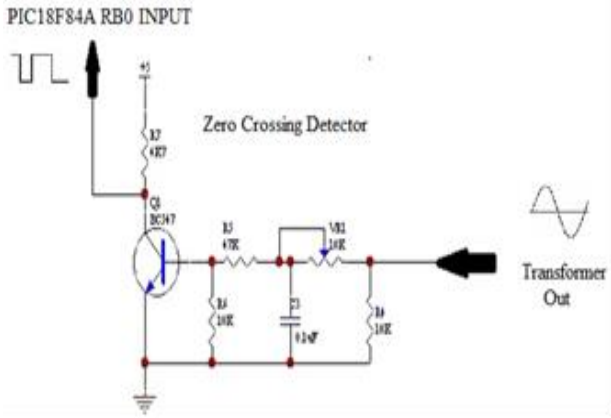

Figure 4. *Zero crossing detector circuit.*

In the speed control of universal motor application that proposed in this study, motor terminal voltage and triac terminal voltage changes are shown by oscilloscope measurements.

Oscilloscope probe connection of the voltage measurement of the universal motor excitation terminals and between A1-A2 terminals of triac in the drive circuit is given in Fig. 5.

Figure 5. *Oscilloscope probe connection.*

Various signals of the motor terminal voltage and the voltage between A1-A2 terminals of the triac monitored in the screen as a result of the measurements made with oscilloscope are given in figures 6, 7, 8 and 9.

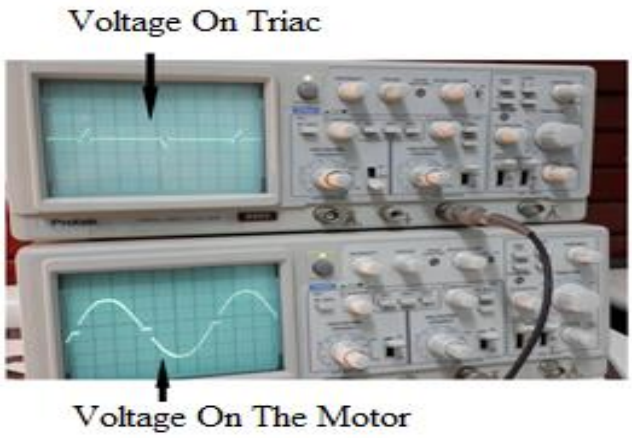

Figure 6. *Voltage between A1-A2 terminals of the triac and Motor terminal voltage when triac is triggered at the beginning of the alternance.*

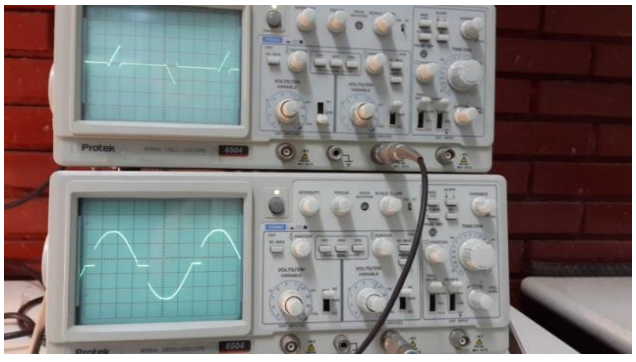

Figure 7. *Voltage between A1-A2 terminals of the triac and Motor*

terminal voltage when triac is triggered after 45o from beginning of the alternance.

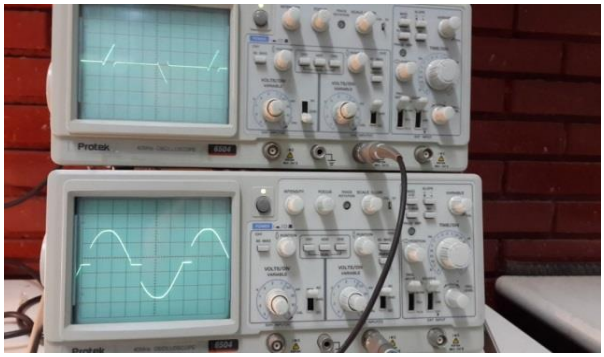

Figure 8. *Voltage between A1-A2 terminals of the triac and Motor terminal voltage when triac is triggered after 90o from beginning of the alternance.*

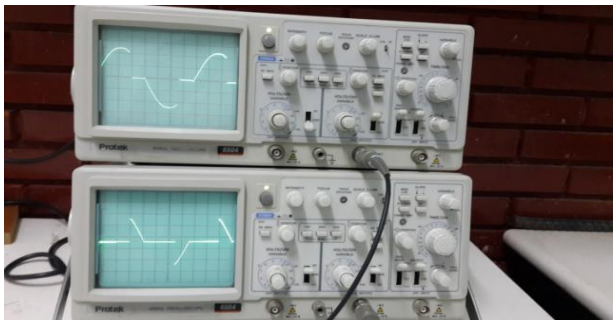

Figure 9. *Voltage between A1-A2 terminals of the triac and Motor terminal voltage when triac is triggered after 135o from beginning of the alternance.*

BTA16 triac used in the drive circuit is controlled with the phase angle control method and the voltage in the terminals of universal motor is adjusted as desired values and the speed control is performed. As long as the triac is not triggered, the current does not pass over the motor. While operating in AC voltage, triac is triggered at the start of each alternance and remains in transmission until the end of the alternance. However, in case triac is triggered toward the end of the alternance it will be cut until the time of triggering and a power loss occurs in the circuit. Triggering moment of the triac is adjusted with PIC16F84A and MOC3021 optocoupler in the circuit and efficient value of the voltage in the circuit is determined. As the triggering moment approaches to the end of alternance, power loss increases in the circuit and thus the motor speed will be reduced. As the triggering moment approaches to the start of alternance, however, a contrary situation is observed, transmission period of triac and accordingly motor speed increase [12].

2.3. Speed Control Sımulatıon of Unıversal Motor

In this study, universal motor speed control simulation is performed with ISIS PROTEUS program. Circuit diagram used in the simulation program is given in Fig. 10.

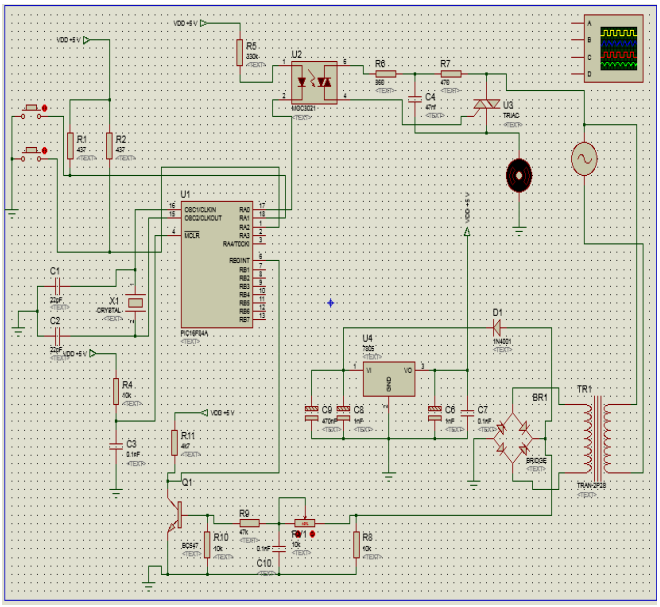

Figure 10. *Circuit diagram used in the simulation.*

In accordance with the commands given to the microcontroller in the simulation circuit of the drive card used in the application as seen in Fig. 10, line voltage, voltage of the load terminals and triac are measured by simulating the trigger pulse signal. In the simulation circuit, the load is controlled with the phase angle control method. Oscilloscope measurement in case of triggering the triac at the beginning of alternance based on the speed increase or speed decrease commands of the circuit line voltage simulated during zero crossing, line voltage signal, signal at the load terminals, triac gate signals are given in Fig. 11.

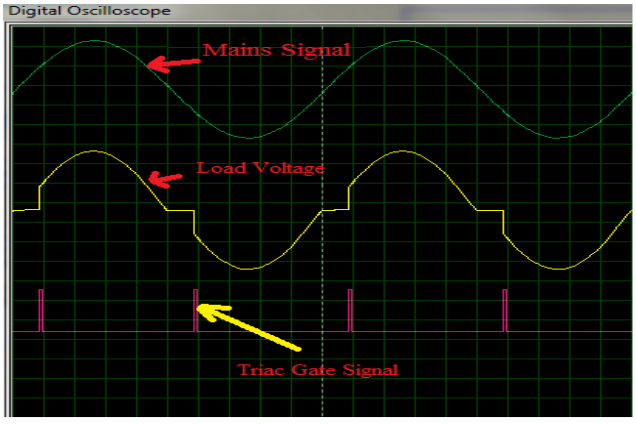

Figure 11. *Oscilloscope measurements when triac is triggered at the beginning of the alternance.*

Oscilloscope measurement in case of triggering the triac 45o after alternance started, line voltage signal, signal at the load terminals, triac gate signals are given in Fig. 12.

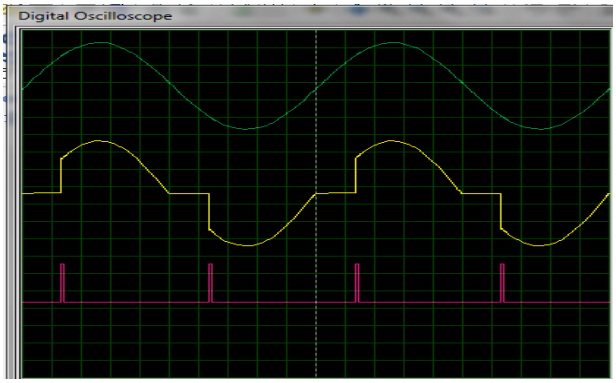

Figure 12 - *Oscilloscope measurements when triac is triggered after 45o from the beginning of the alternance.*

Oscilloscope measurement in case of triggering the triac 90o after alternance started, line voltage signal, signal at the load terminals, triac gate signals are given in Fig. 13.

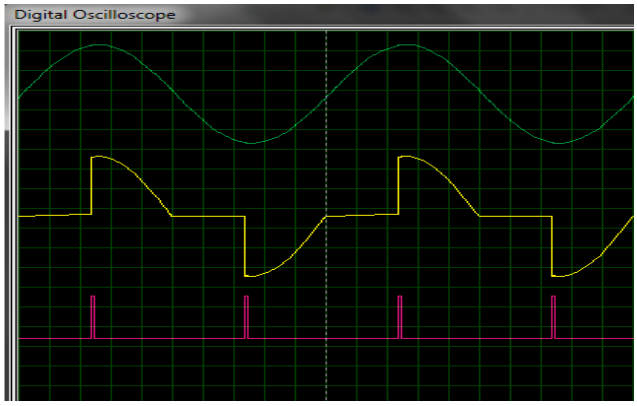

Figure 13 - *Oscilloscope measurements when triac is triggered after 90o from the beginning of the alternance.*

Oscilloscope measurement in case of triggering the triac 135o after alternance started, line voltage signal, signal at the load terminals, triac gate signals are given in Fig. 14.

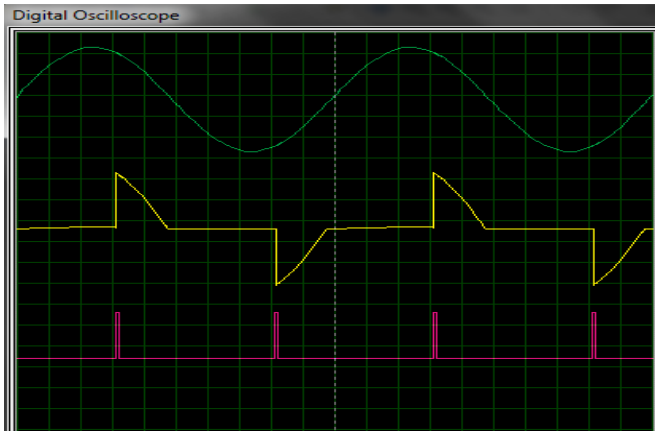

Figure 14 - *Oscilloscope measurements when triac is triggered after 135o from the beginning of the alternance.*

In this study, universal motor speed control is performed by means of Visual Basic 6.0 program. According with the program written by forming necessary control elements with the use of Visual Basic 6.0 program control panel, the control is performed. Control panel view of the designed control interface is given in Fig. 15.

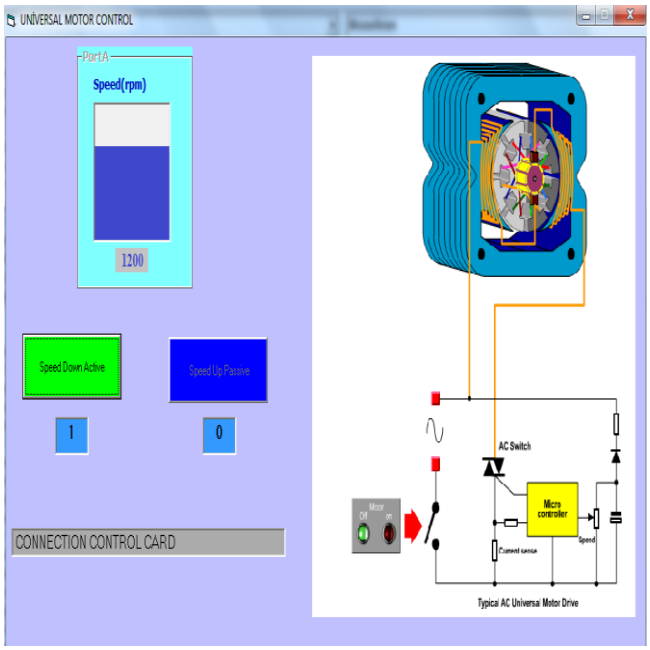

Figure 15 - *Control panel view of the designed control interface.*

As seen in the control panel of the designed control program in figure 15, dashboard instantaneously indicating the speed information of the motor and control buttons reducing or increasing the motor speed are provided. Each function of the control buttons provided in the control panel is defined in different colors, thereby the position of the control buttons is

visually understood better [13].

3. Results and discussions

In this study, universal motor speed control is performed via computer with drive card, control card and control program designed. Universal motor speed control is performed with phase angle control method. In the phase angle control application made with the circuit designed as a result of this method, motor terminal voltage signal oscilloscope measurement is observed to be close to the oscilloscope motor terminal voltage signals of the circuit simulated. Comparison of the application and simulation signal examples of the motor terminal voltage is given in Fig. 16 (a,b,c and d).

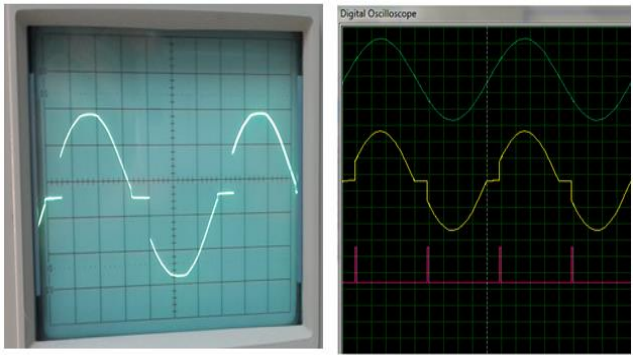

(a)

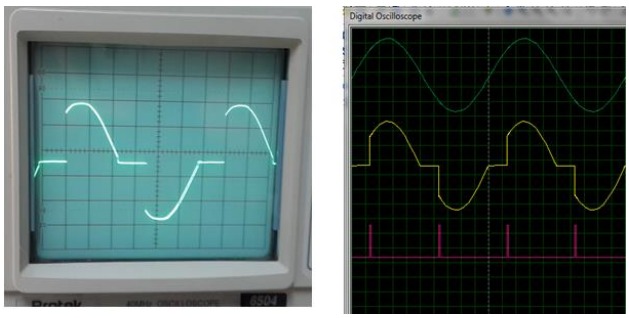

(b)

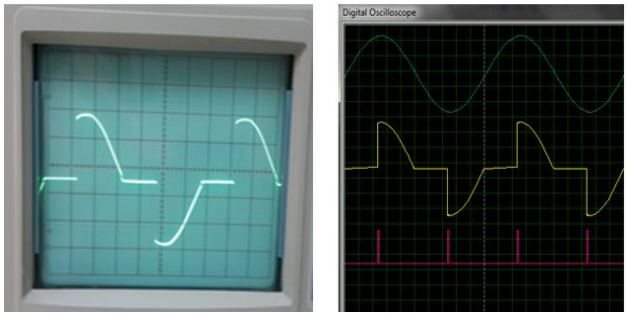

(c)

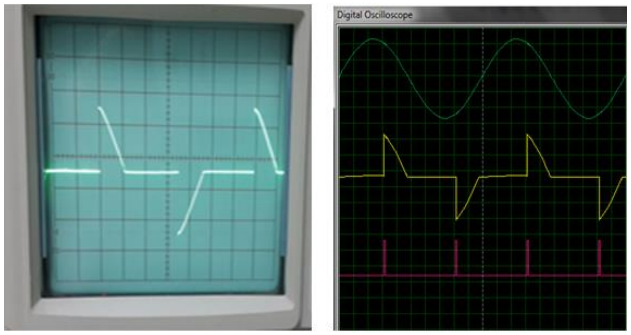

(d)

Figure 16 - *Comparison of the application and simulation of motor terminal voltage signals a) triac is triggered at the beginning of the alternance b) triac is triggered after 45o from the beginningof the alternance c) triac is triggered after 90o from the beginning of the alternance d) triac is triggered after 135º from the beginning of the alternance.*

As seen from the results of circuit application and simulation using PIC16F84A microcontroller and phase angle control method in the universal motor speed control, the motor is observed to have answered the commands given rapidly and be at desired values depending on the trigger angles in the motor terminal voltage measurements.

Control panel designed under Visual Basic 6.0 platform has provided the user with the opportunity of performing practical and easy control. Defining each function of each element provided in the control panel with colors and in writing, state of the functions are active or passive is provided visually in case of control. In this case, by facilitating the person controlling the control system to observe the relevant state of the system, a more professional control is provided. Moreover, while speed of the motor is controlled, motor speed information is indicated in the control panel and instant speed of the motor is known by the user, and thus in line with the motor speed information, the level of the control is provided to be known.

In this study, considering the method and circuit elements used, the cost can substantially be reduced as a faster control using less energy and less labor when compared to the manual control used in work and power tools is provided. When very big industrial systems are considered, this cost reduction may reach high rates and increase the profit rate.
With the study conducted, speed control of the universal motors, the use of which has significantly become common in the industrial applications is made with PIC 16F84 controller. It is shown that this and similar motor control applications can be made with PIC more simply and reliably.
Since this study provides incorporating more different systems, it has a developable structure. For instance, control

via internet can be developed to realize the objectives such as providing hand and power tools that can be controlled by mobile phones [14].

2. References

[1] G. Bal,, *Special Electrical Machinery*. ISBN 975 02 01574, Seçkin Publication, Ankara, TURKEY, 2006.

[2] J. Kaňuch, P Višnyi. "DC Drive For Universal Motor", *Technical University of Košice, Zeszyty Problemowe – Maszyny Elektryczne, Koszyce.* vol. 84, pp. 7-11, 2009.

[3] J. Yang, H. Li, Y. Qin, X. Yao, Y. Yuan, A. Guo, "Fuzzy Interfering Control of Universal Motor for Electromagnetic Nonlinearity", School of Information Science and Engineering, Lanzhou University, Lanzhou 730000,CHINA, 2009.

[4] S. J. Chapman, *Fundamentals of Electric Machinery,* ISBN: 9789754360691, Seçkin Publication, 746 Pages, İstanbul, TURKEY, 2005.

[5] A. Hughes, *Electric Motors and Drives Fundamentals. Types and Applications Third edition,* School of Electronic and Electrical Engineering, University of Leeds.684, ENGLAND, 2006.

[6] N. Abut, *Power Electronics*. Kocaeli University Engineering Faculty, Kocaeli, TURKEY, 2001.

[7] B. K. Bose, *Power Electronics and Variable Frequency Drives.* IEEE Press, 283, 13 February 1997.

[8] O. Kızılbey, *Sea Thermometer*, İstanbul Technical University, Electrical-Electronics Faculty, İstanbul, TURKEY, 2005.

[9] I. Senol, M. Demirtas, S. Rustemov and B. Gumus , "Position control of induction motor a new-bounded fuzzy sliding mode controller" *COMPEL - The international journal for computation and mathematics in electrical and electronic engineering,* vol. 24 no. 1 pp. 145-157, 2005.

[10] S. Rustemli, M. Yilmaz and M. Demirtas, "Ripple reduction at speed and torque of step motors used on a two-axis robot arm", *Robotics and Computer-Integrated Manufacturing,* vol. 26, pp. 759–767, 2010.

[11] M. Bourogaoui, H. Ben Attia Sethom, I. Slama-Belkhodja and H. Sammoud, "An Improved Sensorless IPMSM Control at Low speeds and Standstill for Washing Machine Drives Using dsPIC Technology", *CEAI*, vol. 17, no. 1, pp. 22-30, 2015.

[12] E. Ağralı, S. Rüstemli and S. Yıldız, "Alternative Current (AC) Supply Universal Motor Based on Computer Controlling Rate On Computer", *2016 INESEC,* pp. 308-316.

[13] S. Rüstemli, E. Ağralı and S. Yıldız, "Changing of Direction of Universal Motor Rotation by Using the Computer Supported PIC Controller", *2016 INESEC,* pp. 317-327.

[14] S. Rüstemli and E. Ağralı, "Computer Based Control of Universal Motor by Using PIC", *2016 ICNASE*, pp. 589-598.

MANAS Journal of Engineering
ISSN 1694-7398 | e-ISSN 1694-7398

Volume 11, Issue1, (2023) Pages 119-123
https://doi.org/10.51354/mjen. 12312751111111

The enhanced polymer-coated graphite anode electrodes for the electrooxidation of glucose

Aykut Caglar

Department of Chemical Engineering, Faculty of Engineering and Architectural Sciences, Eskisehir Osmangazi University, Eskişehir, 26040, Turkey, aykut_802@hotmail.com, ORCID: 0000-0002-0681-1096

ABSTRACT

In this study, poly(N-Isopropylacrylamide) (PNIPAM), poly(acrylamide) (PAAM), poly(acrylic acid) (PAAc), and poly(methacrylic acid) (PMAc) polymers are synthesized by radical polymerization method. The chemical composition and surface morphology of the PMAc polymer are examined by micro-Raman spectroscopy and scanning electron microscopy (SEM). The electrochemical measurements are examined by cyclic voltammetry (CV), chronoamperometry (CA), and electrochemical impedance spectroscopy (EIS) analyses for glucose (Glu) electrooxidation. The characterization analyses reveal that the polymer structure was formed. The electrochemical analysis results indicate that the PMAc/G electrode has higher catalytic activity, stability, and resistance compared to other electrodes with a specific activity of 1.7 mA/cm^2.

ARTICLE INFO

Research article

Received: 8.01.2023
Accepted: 14.02.2023

Keywords:
graphite,
polymer,
glucose,
electrooxidation

1. Introduction

Fuel cells are an alternative energy source that converts chemical energy into electrical energy, using clean, efficient, cheap, and low CO_2 emissions fuels [1, 2]. Recently, it is an energy source that has been the focus of attention of researchers in response to the problem of environmental pollution and increasing energy demand [3, 4]. Direct fuel cells using fuels such as formic acid [5, 6], methanol [7, 8], ethanol [9, 10], and glucose [11-13] are recognized as emerging power sources for electric vehicles and portable electronic devices. Glucose has recently attracted great interest in fuel cells, which are an alternative energy source, due to the high energy it contains. Glucose is an abundant monosaccharide in nature. Glucose oxidation has been realized as an electrochemical sensor for the control and rapid diagnosis of initial diabetes [14, 15]. Researchers have shown that when glucose is fed into direct fuel cells, it produces 24 electrons. However, it is difficult to break and oxidize since glucose has a very stable molecule. Therefore, it is mostly obtained gluconic acid and 2 electrons according to research [16].

Anode:

$C_6H_{12}O_6 + 2OH^- \longrightarrow C_6H_{12}O_7$ (gluconic acid) $+ H_2O + 2e^-$

Cathode:

$½O_2 + H_2O + 2e^- \longrightarrow 2OH^-$

Overall:

$C_6H_{12}O_6 + ½O_2 \longrightarrow C_6H_{12}O_7 + 12H_2O$

Materials such as carbon nanotube, graphene, graphite, carbon black, and carbon fibers have been used as carbon support for fuel cell systems [17-21]. The disadvantages of carbon support materials such as lower interaction and wear prevent parameters such as catalytic activity and durability [22]. Conducting polymers such as polyaniline, polypyrrole, poly(3,4-ethylene dioxythiophene), and poly-3-methyl thiophene have been utilized for fuel cell systems in literature studies [23-26]. Conductive polymers are promising materials as catalyst support or catalyst with advantages such as easy production, chemical stability, high electrical conductivity, and low cost [27]. Inamuddin and Kashmery [28] reported that they developed a graphene@polyanalin-TiO_2 composite for glucose biofuel cell anode applications. They found the current density of this composite by cyclic voltammetry analysis for glucose oxidation with glucose concentrations and glucose oxidase enzyme. Perveen et al [29] reported that they formed a composite material with polypropylene, which is a conductive polymer, iron oxide (Fe_3O_4), carbon nanotube (CNT), and Au, and immobilized it with ferritin and glucose oxidase and embedded it as a bioanode for glucose biofuel battery applications. Haque et al [30] investigated the activity of chitosan@reduced graphene-polyaniline composite

immobilized with ferritin/glucose oxidase enzyme for glucose oxidation by electrochemical analysis.

Table 1. *Summary of literature on electrocatalytic performances for Glu electrooxidation.*

Catalysts	Preperation Method	Specific Activity (mA/cm^2)	Ref.
PdIn/CNT	$NaBH_4$ reduction	0.97	[31]
Au-GtO	Electrodeposition	0.44	[32]
Pd/C	Water-in-oil microemulsion	0.92	[33]
Au@CF	One-pot route	2.00	[34]
Pd-N doped-G/ITO electrode	CVD and Electrodeposition	2.00	[35]

Herein, PNIPAM, PAAM, PAAc, and PMAc polymers were synthesized by the radical polymerization method for Glu electrooxidation. PMAc polymer was characterized by SEM and micro-Raman analysis. Furthermore, the activities, stability, and resistance of polymers were investigated by electrochemical analyses such as CV, CA, and EIS.

2. Experimental

2.1 Synthesis and Characterization

The radical polymerization method was used for the synthesis of polymers. The synthesis of polymers was carried out using N-Isopropylacrylamide, acrylamide, acrylic acid, and methacrylic acid as the monomer, methylene bisacrylamide as a crosslinker, N,N,N',N'-tetramethyl ethylenediamine as an accelerator, and ammonium persulfate as initiator. The distilled water, monomer, crosslinker, and accelerator materials were added and mixed into a vial, except for the initiator ammonium persulfate. Finally, the initiator was added and, after mixing, it was transferred to coat the graphite (G) which is the pencil tip. Thence, G pencil tip electrodes coated with polymer were obtained. SEM analysis was obtained with a Zeiss Sigma 300 instrument to examine the surface morphology of the polymer. Micro-Raman (WITech alpha 300R) analysis was applied to examine the bonds formed by atoms or molecules formed in the structure of the polymer.

2.2 Electrochemical Analysis

Electrochemical analyzes were performed with CV, CA, and EIS measurements using a CHI660-E potentiostat. This system was a three-electrode system such as a working electrode (polymer/graphite), reference electrode (Ag/AgCl), and counter electrode (Pt wire). All analyses were realized in 1 M KOH + 0.5 M Glu solution at room temperature. CV analyses were performed at a scan rate of 100 mV/s in the potential range of -0.65 ~ 0.65 V in 1 M KOH and 1 M KOH + 0.5 M Glu solutions. CA curves for the stability of polymers were performed at 0.6 V potentials during 1000 s in 1 M KOH + 0.5 M Glu. The electrochemical resistance of polymer/G electrodes was examined by EIS at 316 kHz-0.046 Hz frequency and 5 mV amplitude.

3. Results and Discussion

3.1 Physical Characterization

SEM analysis was obtained to examine the surface structure of the obtained polymer. Figure 1 shows SEM images of PMAc. As can be seen from Figure 1, it was observed that PMAc polymer structures were formed. Micro-Raman analysis was performed to examine the molecular structure of the polymer. The Raman spectrum of the PMAc polymer was given in Figure 2. Three main Raman peaks (D, G, and 2D) occur in Raman spectroscopy for PMAc polymer. The D band shows the irregularity in the carbon structure, while the G band reveals the relative graphitization degree [36]. Raman peaks at 1450 cm^{-1}, 1695 cm^{-1}, and 2939 cm^{-1} correspond to the D, G, and 2D bands, respectively. The I_D/I_G ratio was used to measure the disorder in the structure. The calculated I_D/I_G ratio for PMAc polymer was found to be 1.1. If the I_D/I_G ratio was greater than 1, it means that the polymer structure was disordered.

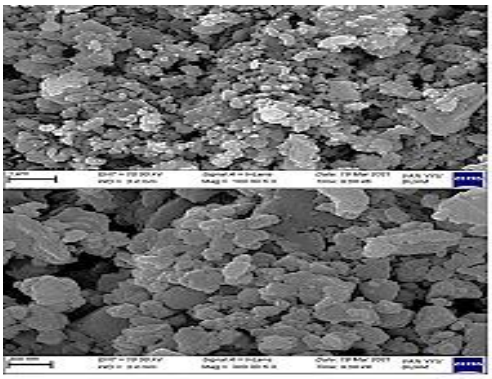

Figure 1. *SEM images of PMAc.*

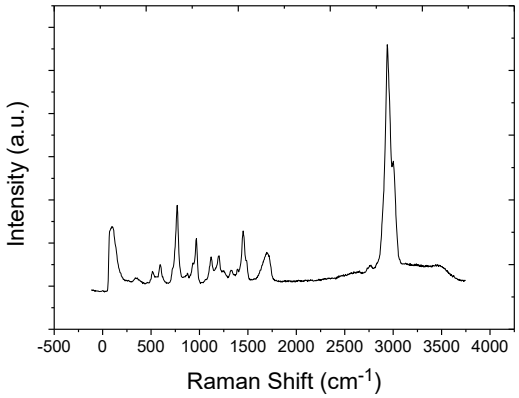

Figure 2. *Micro-Raman spectrum of PMAc*

3.2 Electrochemical Results

CA, CV, and EIS measurements were realized to investigate the electrochemical performance of the polymers. The catalytic activities of the polymers against Glu electrooxidation were determined by CV analyses. CV analyses of polymer electrodes were given in Figure 3(a, b). Although it contains high energy in its glucose structure, the current density was evaluated over the total current in the CV analysis, since it is difficult to decompose. The current densities of the G, PNIPAM/G, PMAc/G, PAAM/G, and PAAc/G polymer electrodes are 0.6 mA/cm^2, 1.6 mA/cm^2, 1.7 mA/cm^2, 0.5 mA/cm^2, and 0.9 mA/cm^2, respectively. The PMAc/G electrode exhibited the best catalytic activity compared to the others. In addition, when comparing two different solutions of 1 M KOH (1.2 mA/cm^2) and 1 M KOH + 0.5 M Glu (1.7 mA/cm^2) for PMAc/G electrode, the difference between them is due to fuel (glucose).

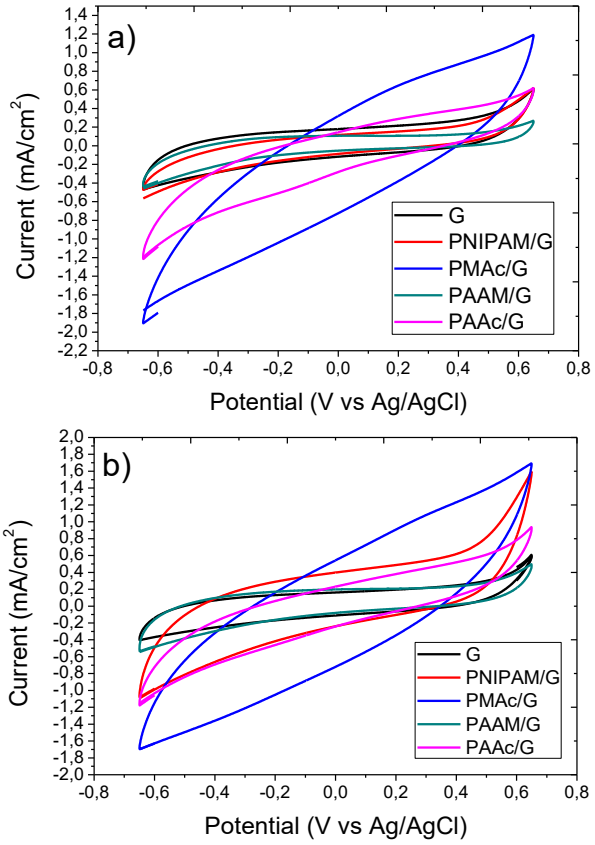

Figure 3. *CV analyses of (a) 1 M KOH and (b) 1 M KOH + 0.5 M Glu for polymer/G electrodes at a scan rate of 100 mV/s.*

CA and EIS analyses were performed to measure the stability and resistance of the polymer electrodes. Figures 4a and b illustrate the stability of the polymer electrodes for 1000 s at a potential of 0.6 V. The PMAc/G electrode was more active and stable than the other electrodes with a specific activity of 0.16 mA/cm^2 obtained after 1000 s. Figure 4c shows the Nyquist plots obtained from the EIS analysis at 0.6 V potential to examine the electrochemical resistance of the polymer electrodes. As the diameter of these plots decreases, the electrochemical resistance increases. PMAc electrode had the best electrochemical resistance as it had the lowest diameter compared to the others.

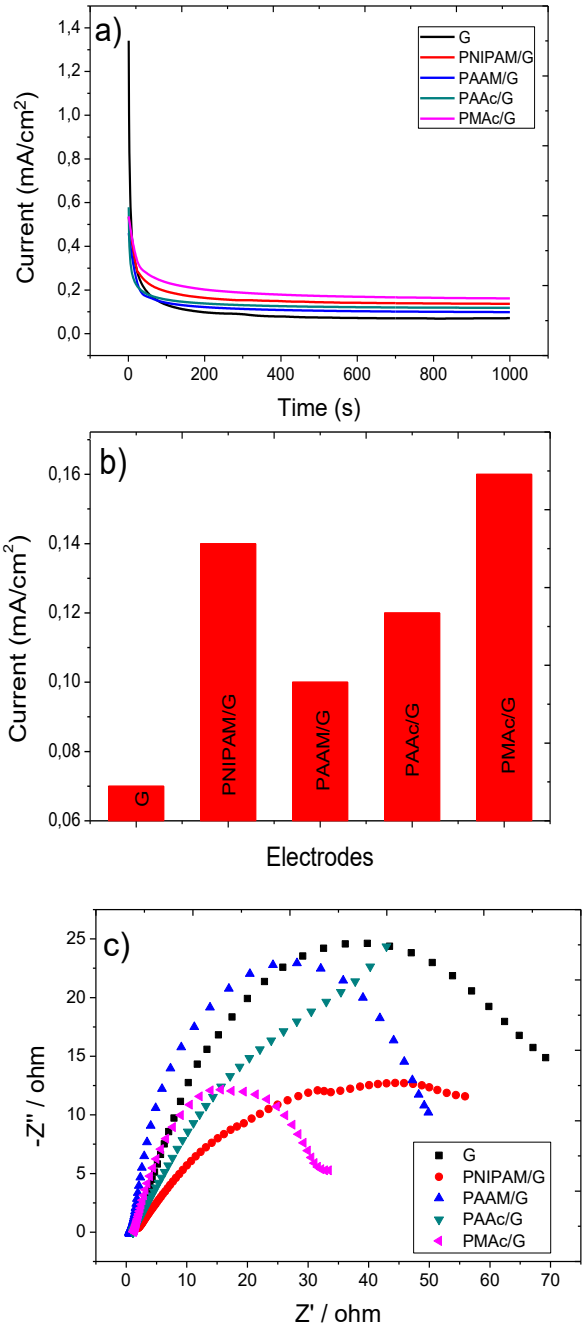

Figure 4. *(a) CA curves of polymer/G electrodes at 0.6 V potential, (b) specific activities after 1000 s, and (c) Nyquist plots of polymer/G electrodes at 0.6 V potential in 1 M KOH + 0.5 M Glu.*

4. Conclusion

The radical polymerization method was used for the synthesis of polymer electrodes. The activity, stability, and resistance of G, PNIPAM/G, PMAc/G, PAAM/G, and PAAc/G electrodes against Glu electrooxidation were investigated by CV, CA, and EIS analyses, respectively. Furthermore, the physical structure and morphology of the PMAc electrode were characterized by SEM and micro-Raman spectrum analyses. The characterization results showed that the polymer structure was formed. The PMAc electrode exhibited the best catalytic activity compared to other electrodes, with a specific activity of 1.7 mA/cm^2. In addition, it was observed that it had the best stability and resistance as a result of the CA and EIS analyses as in the CV analysis.

References

[1]. B. Ulas, A. Caglar, S. Yılmaz, U. Ecer, Y. Yilmaz, T. Sahan, H. Kivrak, Towards more active and stable PdAgCr electrocatalysts for formic acid electrooxidation: The role of optimization via response surface methodology, International Journal of Energy Research, 43 (2019) 8985-9000.

[2]. T. Avci Hansu, O. Sahin, A. Caglar, H. Kivrak, A remarkable Mo doped Ru catalyst for hydrogen generation from sodium borohydride: the effect of Mo addition and estimation of kinetic parameters, Reaction Kinetics, Mechanisms and Catalysis, 131 (2020) 661-676.

[3]. Z. Chen, X. Duan, W. Wei, S. Wang, B.-J. Ni, Recent advances in transition metal-based electrocatalysts for alkaline hydrogen evolution, Journal of Materials Chemistry A, 7 (2019) 14971-15005.

[4]. M. Cao, H. Cao, W. Meng, Q. Wang, Y. Bi, X. Liang, H. Yang, L. Zhang, M.-F. Lang, J. Sun, Nickel-copper oxide nanoflowers for highly efficient glucose electrooxidation, International Journal of Hydrogen Energy, 46 (2021) 28527-28536.

[5]. B. Ulas, A. Caglar, O. Sahin, H. Kivrak, Composition dependent activity of PdAgNi alloy catalysts for formic acid electrooxidation, J. Colloid Interface Sci., 532 (2018) 47-57.

[6]. A. Caglar, T. Sahan, M.S. Cogenli, A.B. Yurtcan, N. Aktas, H. Kivrak, A novel Central Composite Design based response surface methodology optimization study for the synthesis of Pd/CNT direct formic acid fuel cell anode catalyst, International Journal of Hydrogen Energy, 43 (2018) 11002-11011.

[7]. B. Ulas, A. Caglar, A. Kivrak, H. Kivrak, Atomic molar ratio optimization of carbon nanotube supported PdAuCo catalysts for ethylene glycol and methanol electrooxidation in alkaline media, Chemical Papers, 73 (2019) 425-434.

[8]. A. Çağlar, A. Aldemir, H. Kivrak, Alcohol electrooxidation study on carbon nanotube supported monometallic, Pt, Bi, and Ru catalysts, Fullerenes, Nanotubes and Carbon Nanostructures, 26 (2018) 863-870.

[9]. A. Caglar, H. Kivrak, Highly active carbon nanotube supported PdAu alloy catalysts for ethanol electrooxidation in alkaline environment, International Journal of Hydrogen Energy, 44 (2019) 11734-11743.

[10]. D. Atbas, A. Çağlar, H. Kivrak, A. Kivrak, Microwave Assisted Synthesis of Sn Promoted Pt Catalysts and Their Ethanol Electro-oxidation Activities, American Journal of Nanomaterials, 4 (2016) 8-11.

[11]. A. Caglar, D. Düzenli, I. Onal, I. Tezsevin, O. Sahin, H. Kivrak, A comparative experimental and density functional study of glucose adsorption and electrooxidation on the Au-graphene and Pt-graphene electrodes, International Journal of Hydrogen Energy, 45 (2020) 490-500.

[12]. A. Caglar, H. Kivrak, N. Aktas, A.O. Solak, Fabrication of Carbon-Doped Titanium Dioxide Nanotubes as Anode Materials for Photocatalytic Glucose Fuel Cells, Journal of Electronic Materials, 50 (2021) 2242-2253.

[13]. A. Caglar, T. Avci Hansu, O. Sahin, H. Kivrak, Fabrication of novel palladium-platinum based graphene/ITO electrodes and third metal addition effect through the glucose electrooxidation, Journal of Electroanalytical Chemistry, 918 (2022) 116505.

[14]. A. Caglar, B. Ulas, O. Sahin, H. Demir Kivrak, Few-layer graphene coated on indium tin oxide electrodes prepared by chemical vapor deposition and their enhanced glucose electrooxidation activity, Energy Storage, 1 (2019) e73.

[15]. A. Caglar, B. Ulas, O. Sahin, H. Kıvrak, Synthesis of in situ N-, S-, and B-doped few-layer graphene by chemical vapor deposition technique and their superior glucose electrooxidation activity, International Journal of Energy Research, 43 (2019) 8204-8216.

[16]. A. Brouzgou, S. Song, P. Tsiakaras, Carbon-supported PdSn and Pd_3Sn_2 anodes for glucose electrooxidation in alkaline media, Applied Catalysis B: Environmental, 158-159 (2014) 209-216.

[17]. J. Ryu, H.-S. Kim, H.T. Hahn, D. Lashmore, Carbon nanotubes with platinum nano-islands as glucose biofuel cell electrodes, Biosens. Bioelectron., 25 (2010) 1603-1608.

[18]. M. Irfan, X. Liu, S. Li, I.U. Khan, Y. Li, J. Wang, X. Wang, X. Du, G. Wang, P. Zhang, High-performance glucose fuel cell with bimetallic Ni–Co composite anchored on reduced graphene oxide as anode catalyst, Renewable Energy, 155 (2020) 1118-1126.

[19]. T. Ishimoto, Y. Hamatake, H. Kazuno, T. Kishida, M. Koyama, Theoretical study of support effect of Au catalyst for glucose oxidation of alkaline fuel cell anode, Applied Surface Science, 324 (2015) 76-81.

[20]. A. Eshghi, M. Kheirmand, Palladium nanoparticles supported on carbon black powder as an effective anodic catalyst for application in a direct glucose alkaline fuel cell, Iranian Journal of Hydrogen & Fuel Cell, 3 (2016) 11-17.

[21]. J.-S. Ye, Z.-T. Liu, C.-C. Lai, C.-T. Lo, C.-L. Lee, Diameter effect of electrospun carbon fiber support for the catalysis of Pt nanoparticles in glucose oxidation, Chemical Engineering Journal, 283 (2016) 304-312.

[22]. S. Ghosh, S. Das, M.E.G. Mosquera, Conducting Polymer-Based Nanohybrids for Fuel Cell Application, Polymers, 12 (2020) 2993.

[23]. S. Ghosh, T. Maiyalagan, R.N. Basu, Nanostructured conducting polymers for energy applications: towards a sustainable platform, Nanoscale, 8 (2016) 6921-6947.

[24]. K. Dutta, S. Das, D. Rana, P.P. Kundu, Enhancements of catalyst distribution and functioning upon utilization of conducting polymers as supporting matrices in DMFCs: a review, Polymer Reviews, 55 (2015) 1-56.

[25]. K. Dutta, P.P. Kundu, A review on aromatic conducting polymers-based catalyst supporting matrices for application in microbial fuel cells, Polymer Reviews, 54 (2014) 401-435.

[26]. L. Fan, T. Gao, Applications of nanoscale polypyrrole proton exchange membrane in microbial fuel cells, Int. J. Electrochem. Sci, 14 (2019) 470-480.

[27]. Q. Zhou, G. Shi, Conducting polymer-based catalysts, J. Am. Chem. Soc., 138 (2016) 2868-2876.

[28]. Inamuddin, H.A. Kashmery, Ternary graphene@polyaniline-TiO_2 composite for glucose biofuel cell anode application, International Journal of Hydrogen Energy, 44 (2019) 22173-22180.

[29]. R. Perveen, A. Nasar, S. Kanchi, H.A. Kashmery, Development of a ternerry condunting composite (PPy/Au/CNT@ Fe_3O_4) immobilized FRT/GOD bioanode for glucose/oxygen biofuel cell applications, International Journal of Hydrogen Energy, 46 (2021) 3259-3269.

[30]. A. Nasar, M.M. Rahman, Applications of chitosan (CHI)-reduced graphene oxide (rGO)-polyaniline (PAni) conducting composite electrode for energy generation in glucose biofuel cell, Sci. Rep., 10 (2020) 1-12.

[31]. O.F. Er, A. Caglar, H. Kivrak, Enhanced electrochemical glucose oxidation in alkaline solution over indium decorated carbon supported palladium nanoparticles, Mater. Chem. Phys., 254 (2020) 123318.

[32]. R.A. Escalona-Villalpando, M.P. Gurrola, G. Trejo, M. Guerra-Balcázar, J. Ledesma- García, L.G. Arriaga, Electrodeposition of gold on oxidized and reduced graphite surfaces and its influence on glucose oxidation, Journal of Electroanalytical Chemistry, 816 (2018) 92-98.

[33]. T. Rafaïdeen, S. Baranton, C. Coutanceau, Highly efficient and selective electrooxidation of glucose and xylose in alkaline medium at carbon supported alloyed PdAu nanocatalysts, Applied Catalysis B: Environmental, 243 (2019) 641-656.

[34]. A. Both Engel, M. Bechelany, O. Fontaine, A. Cherifi, D. Cornu, S. Tingry, One-Pot Route to Gold Nanoparticles Embedded in Electrospun Carbon Fibers as an Efficient Catalyst Material for Hybrid Alkaline Glucose Biofuel Cells, ChemElectroChem, 3 (2016) 629-637.

[35]. A. Caglar, D. Düzenli, I. Onal, I. Tezsevin, O. Sahin, H. Kivrak, A novel experimental and density functional theory study on palladium and nitrogen doped few layer graphene surface towards glucose adsorption and electrooxidation, J. Phys. Chem. Solids, 150 (2021) 109684.

[36]. T. Chhabra, J. Rohilla, V. Krishnan, Nanoarchitectonics of phosphomolybdic acid supported on activated charcoal for selective conversion of furfuryl alcohol and levulinic acid to alkyl levulinates, Molecular Catalysis, 519 (2022) 112135.

MANAS Journal of Engineering
ISSN 1694-7398 | e-ISSN 1694-7398

Volume 11, Issue 1, (2023) Pages 124-135
https://doi.org/10.51354/mjen.1242313

Novel CA-125 antigen determination in serum by electrochemical methods with onion oil-containing organo-hydrogels

Omer Faruk Er[1*], Duygu Alpaslan[1], Tuba Ersen Dudu[1], Hilal Kivrak[2,3]

[1]Van Yuzuncu Yil University, Faculty of Engineering, Department of Chemical Engineering, Van, 65000, Turkey, omerfaruker56@gmail.com, ORCID: 0000-0002-7179-726X, alpaslanduygu@yyu.edu.tr, ORCID: 0000-0002-6007-3397, tubaersendudu@yyu.edu.tr, ORCID: 0000-0001-5564-2834

[2]Eskisehir Osmangazi University, Faculty of Engineering and Architectural Sciences, Department of Chemical Engineering, Eskisehir, 26040, Turkey, hilaldemir.kivrak@ogu.edu.tr, ORCID: 0000-0001-8001-7854

[3]Eskisehir Osmangazi University, Translational Medicine Research and Clinical Center, Eskisehir, 26040, Turkey

ABSTRACT

CA-125 antigen is a glycoprotein that can be found at distinct levels in blood samples according to the phases of ovarian cancer. Herein, we designed novel onion oil-organo-hydrogels (OOHGs) to detect CA-125 antigen at high sensitivity and selectively via electrochemical methods. OOHGs produced are characterized by swelling analysis and Fourier Transform Infrared Spectroscopy (FT-IR). Cyclic voltammetry (CV), Electro impedance spectroscopy (EIS), and Differential pulse voltammetry (DPV) techniques in the potentiostat triple electron system are used for performing the electrochemical measurements. Performances and electron transfer resistances of OOHGs and OOHG+CA-125s are researched via CV and EIS, and the sensitivity properties such as LOD and LOQ of the sensor are determined via DPV. OOHG-2 among OOHGs produced exhibited the highest performance with 0.8151 mA/cm^2 (815.1 μA/cm^2) value at determining CA-125 in serum medium. Moreover, this electrode is found that exhibit a wide linear range like a 1-500 ng/mL concentration range. The limit of quantification (LOQ) and the lowest of detection (LOD) for the OOHG-2 electrode are calculated as 0.531 μU/mL and 0.265 μU/mL (S/N=3), respectively. Further, the CA-125 antigen of the OOHG-2 electrode in interference results is observed that can be detected with high selectivity. With these results, it can be noted that the OOHG-2 electrode holds great hope for detection ovarian cancer by electrochemical methods.

ARTICLE INFO

Research article

Received:25.01.2023
Accepted: 8.03.2023

Keywords:
MBA,
onion oil,
electrochemical sensor,
CA-125,
ovarian cancer

**Corresponding author:*

1. Introduction

Cancer markers could be proteins, mRNA, DNA, metabolites, and they are fabricated either by other tissues or the tumors themselves in response to conditions such as inflammation or the presence of cancer. Biomarkers may be found in cell lines, tissues, or a variety of body fluids such as nipple discharge, saliva, urine, and effusions. They are playing an important role in the screening of cancers, assessing prognosis, aiding in diagnosis, monitoring patients with cancer, and predicting response to treatment [1-3]. Biomarkers can be helpful in symptomatic patients in diagnosing whether the tumors are benign or malignant [4]. The development of strategies such as cost-effective, reliable, high-sensitivity monitoring, and strong detection for cancer screenings, cancer diseases are of great importance especially due to recurrence rates, potential lethality, and disease prevalence. Systems that can be developed over biomarkers in cancer screening offer great potential for early detection of cancer and personalized treatment methods [5-7].

Ovarian cancer is a gynecological disease with high mortality rates that all benign and malignant tumors occur from one of the germ cells, epithelial cells, and stromal cells, generally [8]. Ovarian cancer is one of the most difficult cancers to detect early due to the lack of symptoms, specific signs, and reliable screening methods. CA-125, which is a glycoprotein in the MUCIN-16 family, normal level in the blood between 0-35 U/mL, and molecular weight 200 kDa, is the only biomarker used in the screening, in the progression of the disease, and in the monitoring of relapses for ovarian cancer [9-11]. Distinct methods such as mass spectrometry [12], surface plasmon resonance [13], fluorescence [14], and colorimetry [15] have been used for the screening of ovarian cancer. While these methods have provided some benefits, they have some disadvantages such as low sensitivity, complex test procedures, and long detection time, which can greatly affect

sensitivity [16]. However, the electrochemical sensors (ESs) that use voltammetric, amperometric, impedimetric, or capacitive signals to characterize antigen and antibody binding are particularly promising for use in strong, free-label, sensitive, and rapid diagnostic fields [17-19]. Moreover, these sensors have superior properties such as low cost, fast response, and are easily miniaturized [20-22].

Recently, to increase sensitivities and selectivity's for CA-125 antigen of the electrochemical sensors (ESs) have been studied on materials such OHCOs [23], Ppy nanowire [24], CS–PDDA–PB nanoparticles [25], Ag-RGO/CysA-Au NPs [26], thionine/CA125/CNF/GCE [27], Au-VBG/BDD [28], and benzothiophene derivates [29-32]. In addition, Hasanzadeh et al. reported that developed an electrochemical sensor for the detection of CA-125 with Cys-AuNPs/ERGO probes, and they expressed that this sensor is exhibited high sensitivity and good stability to detect CA-125 with 0.1 U/mL LOQ value and at a wide concentration range as 0.1-400 U/mL linear range [33]. In another study, Zheng et al. reported that enhanced the electrochemical sensor with AuNP-PB-PtNP-PANI hydrogel material to detect CA-125 antigen, and this sensor was exhibited high sensitivity for determining CA-125 with quite a wide linear range among 0.01-5000 U/mL and low detection limit as 0.0044 U/mL values [34]. Apart from these studies, the features of distinct ESs summarized in the literature to detect CA-125 are given in Table 1.

Table 1. *Performances of dissimilar ESs reported in the literature for determining of CA-125 antigen.*

Biomarker	Sensor	LOD	Linear range	Ref.
CA-125	anti-CA125/Au–Thi-CPE	1.8 U/mL	10-30 U/mL	[35]
CA-125	MIP based Au-SPE	0.01 U/mL	0.01-500 U/mL	[36]
CA-125	M-Pt NPs	0.002 U/mL	0.05-20 U/mL	[37]
CA-125	GCE/FA@H-PANI@CS-HCl/Ab-Ag@Co_3O_4	0.25 pg/mL	0.001-25 ng/mL	[38]
CA-125	AgNPs-GQDs/Ab/BSA/Ag	0.01 U/mL	0.01-400 U/mL	[39]
CA-125	Au electrode	5.5 U/mL	10-100 U/mL	[40]
CA-125	MOF-808/CNT	0.0005 ng/mL	0.001-30 ng/mL	[41]
CA-125	ZnO NRs-Au NPs NHs based matrix	2.5 ng/μL	---	[42]
CA-125	OOHG-2	0.265 μU/mL	1-500 ng/mL	This study

The literature reported that studies were carried out on different materials to monitor the level of CA-125 antigen with different methods. However, studies on OOHGs weren't conducted on the follow-up of cancers. Herein, we enhanced an electrochemical sensor (ES) with onion oil-based OOHG's (Agar, glycerol, and MBA) for determining at high sensitivity and selectivity of CA-125 antigen in serum medium. Hydrogels are special kinds of polymers with tremendous capacity that can absorb large amounts of water, and these have used in many applications in technology and science. In particular, hydrogels offer great potential for applications in healthcare and diagnostic care due to their biodegradability, biocompatibility, and non-toxicity [43-46]. Organo-hydrogels can identify as hydrogels formed from synthetic or naturally derived molecules with physical or chemical crosslinkers [47-49]. Onion oil is contained at high concentrations from 3-((ethyltrisulfanyl)methyl)-3,4-dihydro-2H-thiopyran, 1,3-dipropyltrisulfane, and 1-methyl-2-propyldisulfane structures, and this oil is known properties as antibacterial, antitoxigenic, and antidermatophytic [50, 51].

2. Materials and Methods

All materials used in the realization of the measurements and the synthesis of OOHGs are given in detail in S1. The characterization methods and synthesis phases of OOHGs and fabricated steps of ESs with OOHGs have been given in S2 and S3. In addition, preparation steps of OOHGs for ESs were demonstrated in Fig. 1.

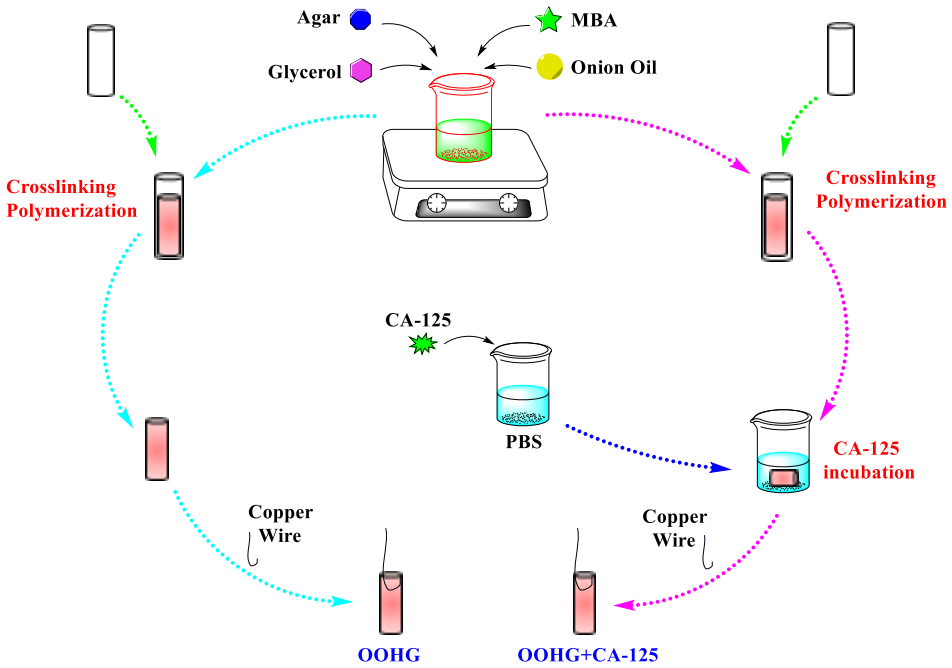

Figure 1. *Measurements and fabricate steps of ES prepared with onion oil-based OOHGs.*

Measurements for ES were performed with techniques such as EIS, CV, and DPV in potentiostat triple electrode system. CV measurements were firstly taken at 50 mV/s scan rate in pH: 7.4 PBS that contains 5.0 mM $Fe(CN)_6^{3-/4-}$ (prepared solution) over OOHGs and OOHG+CA-125s fabricated with CA-125 (500 ng/mL) for 30 min. OOHG-2+CA-125 electrode were exhibited the best activity in measurements taken over OOHG+CA-125s.

Secondary, CV measurements for the best concentration value were obtained at 50 mV/s scan rate in pH: 7.4 PBS that contains 5.0 mM $Fe(CN)_6^{3-/4-}$ (prepared solution) over OOHG-2+CA-125s produced with distinct amounts (1~5000 ng/mL) for 30 minutes. 500 ng/mL CA-125 amount value was determined as the best amount among concentrations prepared. Thirdly, CV measurements for the best incubation time were received at 50 mV/s scan rate in prepared solution over OOHG-2+CA-125s produced with CA-125 (500 ng/mL) during distinct incubation times among 10-90 min at room temperature. 30 min incubation time was found as the best time for incubation of CA-125 antigen over OOHG-2s.

To understand electrooxidation reaction between CA-125 antigen and OOHG-2, CV measurements at varying scan rates (5-1000 mV/s) and EIS measurements at varying potentials among -0.6~0.5 V were performed in prepared solution over OOHG-2+CA-125s produced with determined conditions (30 minute and 500 ng/mL CA-125).

To research properties such as LOD, LOQ, and linear range of ES, DPV measurements were taken in prepared solution over OOHG-2+CA-125s produced with different CA-125 amounts between 0.001~5000 ng/mL during 30 minutes.

The effects on the electrochemical reaction between CA-125 and OOHG-2 of structure molecules such as ascorbic acid, uric acid, dopamine, and glucose that found in serum medium were researched via CV technique at 50 mV/s scan rate and EIS technique at 0.2 potential in prepared solution+0.1 mM Ascorbic acid, prepared solution+2.5 mM Uric acid, prepared solution+0.1 mM Dopamine, prepared solution+4.7 mM Glucose, respectively. Measurements were performed over OOHG-2s and OOHG-2+CA-125s fabricated with determined conditions (30 minute and 500 ng/mL CA-125).

Finally, the effect on electrooxidation reaction among OOHG-2 and CA-125 antigen of the salts that found in serum medium were researched via EIS and CV. CV measurements at 50 mV/s scan rate and EIS measurements at 0.2 potential were performed in artificial and 0.9% isotonic NaCl serums over OOHG-2+CA-125 produced with determined conditions (30 minute and 500 ng/mL CA-125). Artificial serum was performed with $MgCl_2$ (1.6 mM), D-glucose (4.7 mM), $CaCl_2$ (5.0 mM), urea (2.5 mM), and KCl (4.5 mM).

3. Results and Discussion

CV measurements that performed in prepared solution at 50 mV/s scan rate over OOHGs and OOHG+CA-125 to detect CA-125 antigen in serum at room temperature were presented in Fig. 2. CV results, initially, were obtained over OOHGs produced in the absence of CA-125 antigen. Forward and backward peaks that express the electrooxidation process were not clearly observed, and the current densities on total currents were very lowest (Fig. 2a). Secondary, CV results were obtained on OOHGs produced by incubating CA-125 antigen. The maximum current density of OOHG-2 synthesized with 0.2 mL onion oil was high than the maximum current densities of OOHG-1 and OOHG-3 synthesized with 0.1 mL and 0.3 mL onion oil (Fig 2b). These

results show that 0.2 mL is the ideal onion oil amount in the OOHGs to can synthesize with the MBA crosslinker for the detection of CA-125. OOHG-2+CA-125 was exhibited the best electrochemical activity with 0.8151 mA/cm^2 (815.1 μA/cm^2) at 0.24 V of forward peak and 0.8258 mA/cm^2 (825.8 μA/cm^2) at -0.31 V of backward peak values (Fig. 2c). OOHG-3+CA-125 was shown lowest activity with 0.6461 mA/cm^2 (646.1 μA/cm^2) at 0.35 V of forward peak and 0.6212 mA/cm^2 (621.2 μA/cm^2) at -0.38 V of backward peak values (Fig. 2b). These results could say that was a higher performance than the studies for the detection of CA-125 antigen [40, 52, 53]. When comparing OOHG-2 and OOHG-2+CA-125, it can clearly see that OOHG-2 has a high activity to the CA-125 antigen (Fig. 2c).

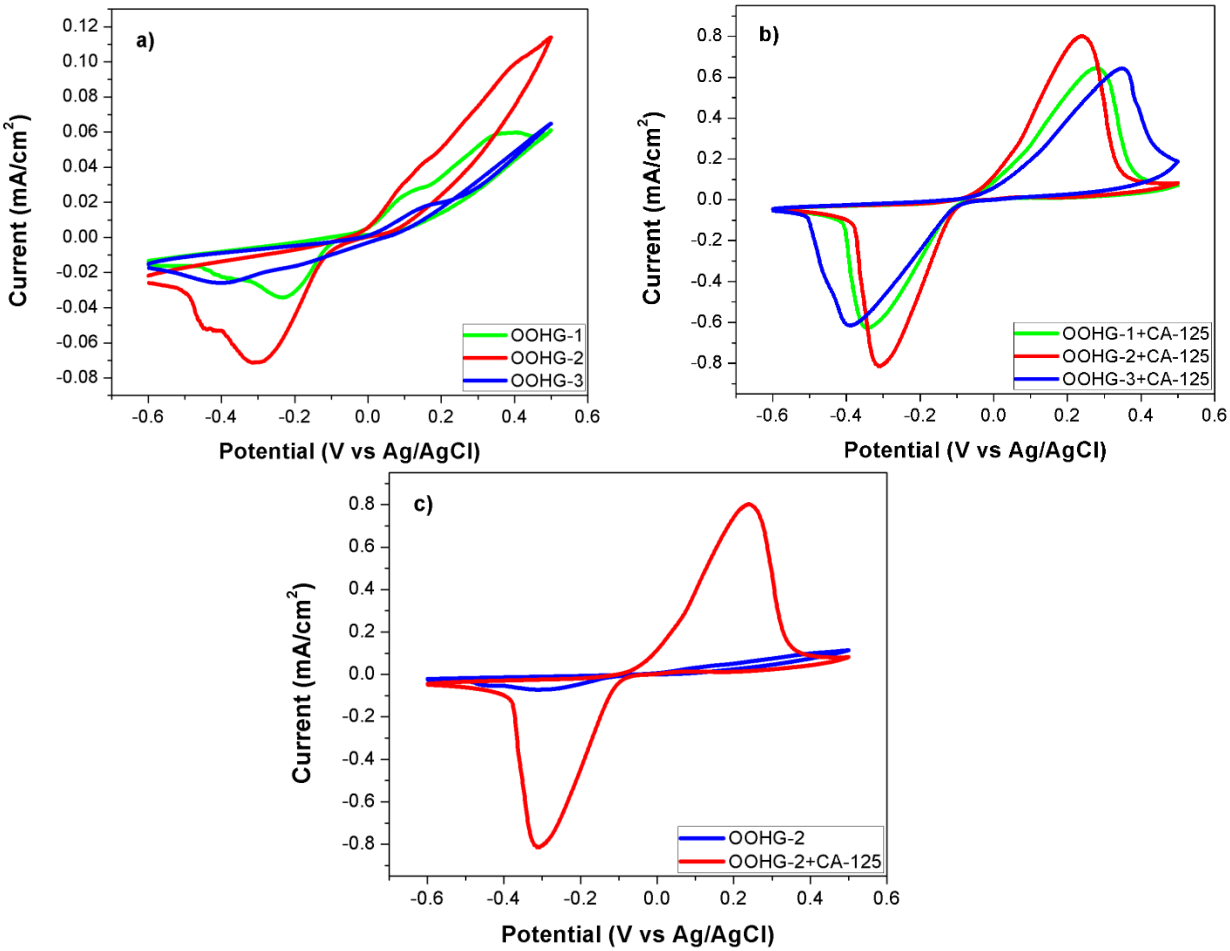

Figure 2. *CV results at 50 mV/s scan rate in prepared solution on a) OOHGs without CA-125 antigen, b) OOHG+CA-125s produced with determined conditions (30 minute and 500 ng/mL CA-125), and c) OOHG-2 and OOHG-2+CA-125 compare.*

To determine the optimum operating conditions of ES, CV measurements were received in prepared solution over OOHG-2+CA-125s produced with on distinct CA-125 concentrations and then distinct incubation times. All results are presented in Fig. 3. Concentration measurements were performed over OOHG-2+CA-125 produced with varying CA-125 amounts among 1~5000 ng/mL (Fig. 3a). Electrooxidation peaks were observed for all concentrations ratios. A gradual increase from 1 ng/mL to 500 ng/mL and a gradual decrease from 500 ng/mL to 5000 ng/mL were observed in maximum current densities. The highest the electrochemical activity was obtained on 500 ng/mL with 513.8 μA/cm^2 at 0.24 V of forward peak and 506.1 μA/cm^2 at -0.31 V of backward peak values. The incubation times measurements were taken over OOHG-2+CA-125 produced at varying times between 10-90 minutes (Fig. 3b). The lowest electrooxidation peaks were obtained in the measurements taken on the OOHG-2+CA-125 produced with 10 min and 90 min incubation times. The highest activity with 542.0 μA/cm^2 at 0.26 of forward peak and 513.3 μA/cm^2 at -0.32 of backward peak values was obtained from OOHG-2+CA-125 produced with 30 min. As a result, these data show that the determined conditions (30 minute and 500 ng/mL CA-125) for ES produced with OOHG-2.

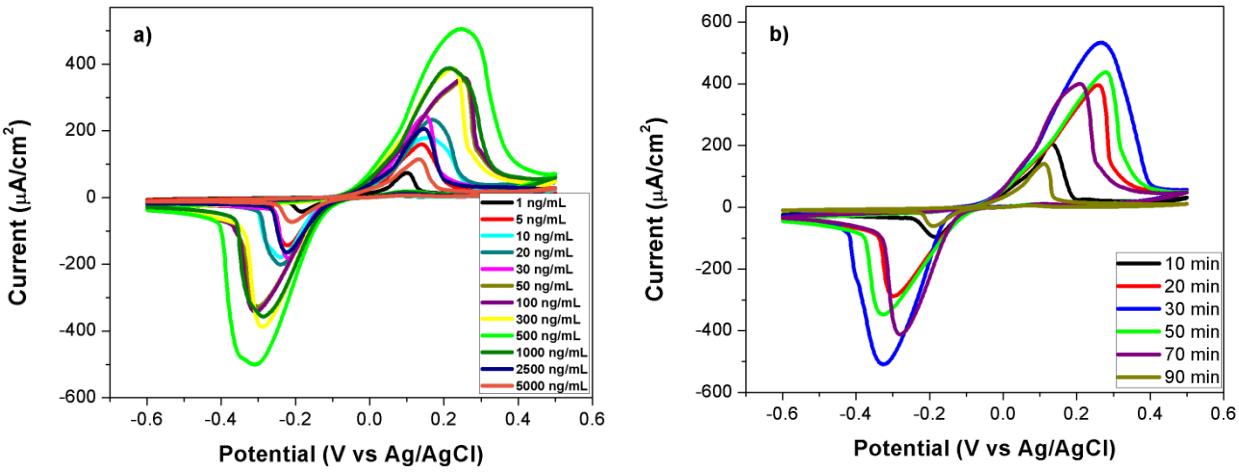

Figure 3. *CV results at 50 mV/s scan rate in prepared solution over a) OOHG-2+CA-125s produced with distinct CA-125 amounts (1~5000 ng/mL) for 30 minutes and b) OOHG-2+CA-125s produced with CA-125 (500 ng/mL) for distinct incubation times among 10 min and 90 min at room temperature.*

To investigate the electrooxidation process among OOHG-2 and CA-125 antigen, CV measurements at distinct scan rates and EIS measurements at distinct potentials were performed in prepared solution. CV results and the Nyquist plots obtained from EIS data are given in Fig. 4. OOHG-2+CA-125s that were used in measurements were produced at determined conditions (30 minute and 500 ng/mL CA-125). A gradual increase in the maximum current intensity from 5 mV/s to 1000 mV/s was observed in CV measurements taken at varying scan rates (5~1000 mV/s) (Fig. 4a). This regular increase indicates that a diffusion-controlled reaction has occurred over the OOHG-2 surface at the presence of CA-125 antigen. EIS is an electrochemical technique that expresses resistance to the flow of alternating current (AC). This technique is a powerful measurement method that can be used in a wide range of fields such as materials science, biology, medicine, and sensors. The Nyquist plots obtained from EIS data occurs a semi-circular area showing the charge transfer and linear sections, which expresses a diffusion-controlled process [54-58]. EIS measurements over OOHG-2+CA-125 were performed in prepared solution at varying potentials (-0.6~0.5 V) (Fig. 4b). When the diameter of the semicircles is large, the electron transfer resistance (Rct) is high, and when the diameter of the semicircles is small, the electron transfer resistance (Rct) is low also [59, 60]. It was seen a linear decrease in electron transfer resistance at potentials among -0.6~0.2 V, and a linear increase in electron transfer resistance at potentials between 0.2 V and 0.5 V. The lowest electron transfer resistance was observed on 0.2 potential. 0.2 potential was the potential at which the maximum current density was seen in the CV results. Therefore, EIS data and CV results are in agreement.

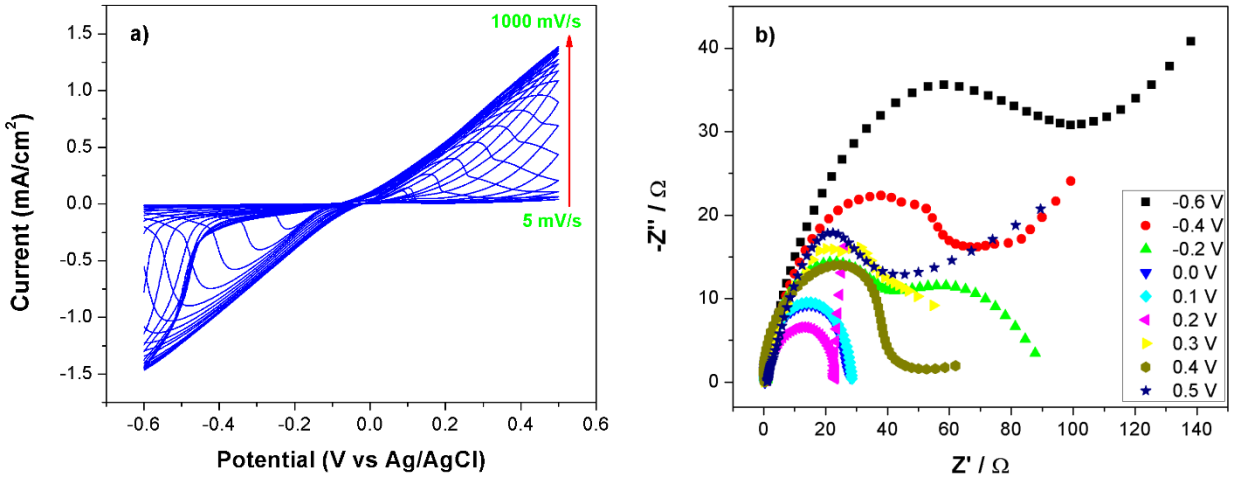

Figure 4. *a) CV results at distinct scan rates among 5 mV/s and 1000 mV/s and b) the Nyquist plots of EIS data at distinct potentials among -0.6 V and 0.5 V in prepared solution over OOHG-2+CA-125s produced determined conditions (30 minute and 500 ng/mL CA-125).*

Sensitivity of OOHG-2 electrodes produced with varying CA-125 concentrations for 30 minutes were investigated DPV technique. DPV plots that measurements received in prepared solution are presented in Figure 5a-c, and the calibration plots of concentration ratios vs. maximum current densities belonging DPV curves are demonstrated in Fig. 5d-e. As clearly seen in Fig. 5a and 5b, it could note that displayed a linear relationship among 1-500 ng/mL concentrations, and R^2 of this linear range was calculated as 0.9826. These concentration range value are wide a linear range than reported in the literature (Table 1). The limit of quantification (LOQ) and lowest detection limit (LOD) values for OOHG-2 electrode produced were determined by receiving measurements over 10 blank electrodes without CA-125 antigen, and these results of measurements are demonstrated in Figure 5f. LOD and LOQ values were calculated as 0.265 μU/mL and 0.531 μU/mL (S/N=3), respectively. LOD value that reckons for OOHG-2 electrode is lower than noticed in the literature (Table 1).

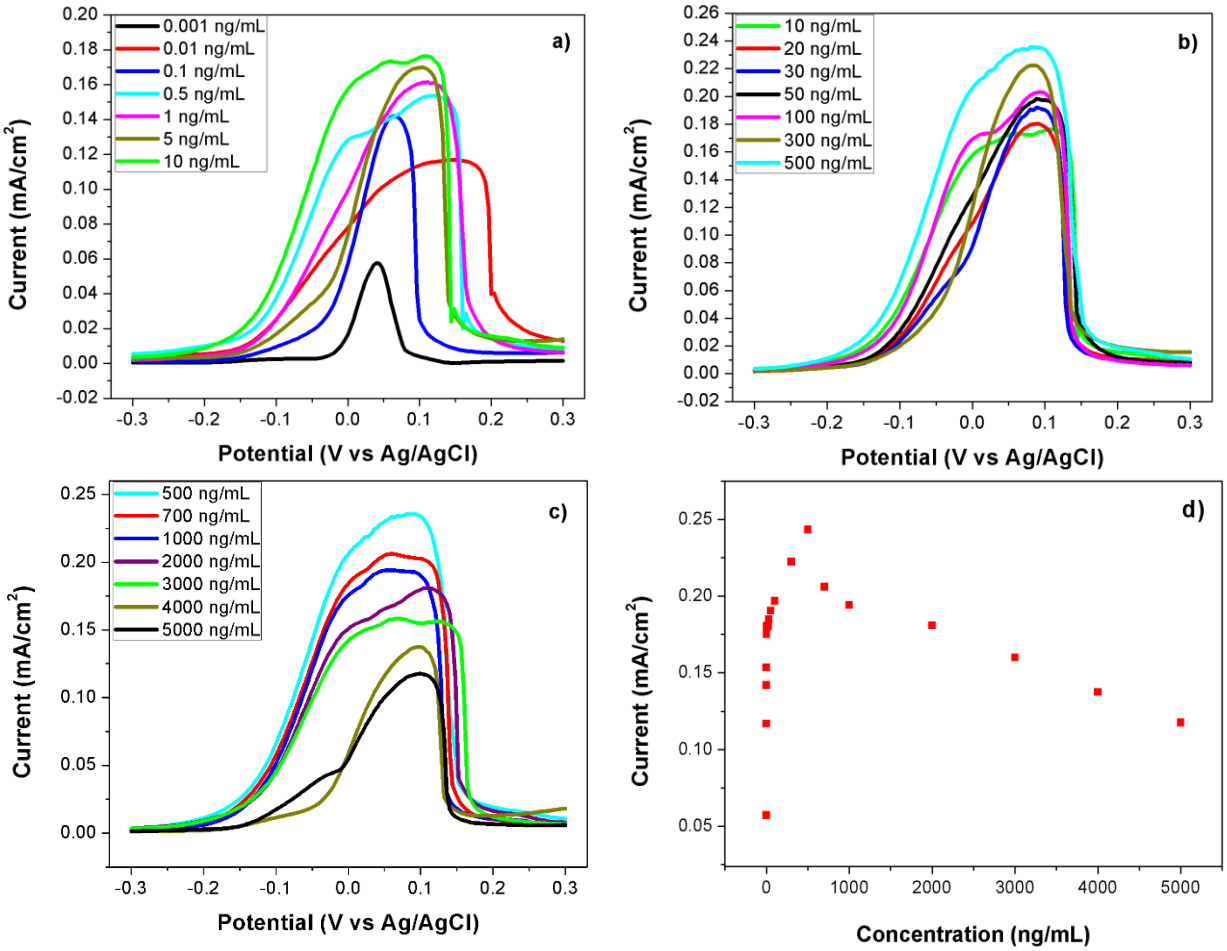

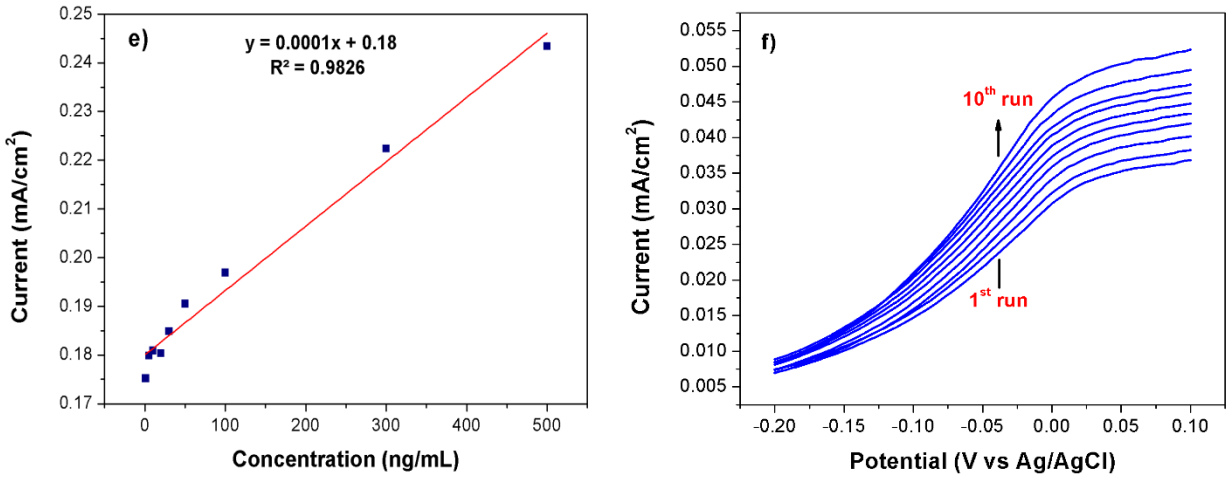

Figure 5. *DPV results at 50 mV amplitude in prepared solution over OOHG-2+CA-125 produced with distinct CA-125 amounts among a) 0.001-10 ng/mL, b) 10-500 ng/mL, c) 500-5000 ng/mL during 30 minutes, d-e) the calibration plots of maximum current densities vs. concentration ratios, and f) results of 10 blank measurements.*

Interference effects of structure molecules such as glucose, urea, dopamine, and ascorbic acid in serum over the electrooxidation process among OOHG-2 and CA-125 antigen were researched in distinct solutions prepared with urea, ascorbic acid, D-glucose, and dopamine. Measurements were performed with CV technique at 50 mV/s scan rate and EIS technique at 0.2 potential over OOHG-2s and OOHG-2+CA-125s produced at determined conditions (30 minute and 500 ng/mL CA-125). CV results and EIS data are presented in Fig.6 and Fig. 7, respectively. The electrooxidation peaks weren't seen in CV results that were achieved over OOHG-2s without CA-125 antigen (Fig. 6). One could see that causes a small increase over the maximum current densities of ascorbic acid, urea, and dopamine structures (Fig. 6a-c-d). It can be said that the glucose structure has almost no effect on the electrooxidation process (Fig. 6b). In addition, it was appeared that causes a slight shift towards the up field of dopamine structure and towards the downfield of the uric acid structure over potential (Fig. 6c-d). As a result, these structures may be clearly stated that there was no significant effect on the electrooxidation peaks of CA-125 antigen in CV results. Electron transfer resistances were high found according to the presence of CA-125 in the Nyquist plots obtained from EIS data at the absence of CA-125 antigen for all structures (Fig. 7). For all structures were no observed a significant difference in electron transfer resistances in the presence of CA-125 antigen, these results were in agreement with the CV results. All CV and EIS results prove that ascorbic acid, uric acid, glucose, and dopamine structures do not have any interference effects at the electrooxidation of CA-125 on OOHG-2 structure.

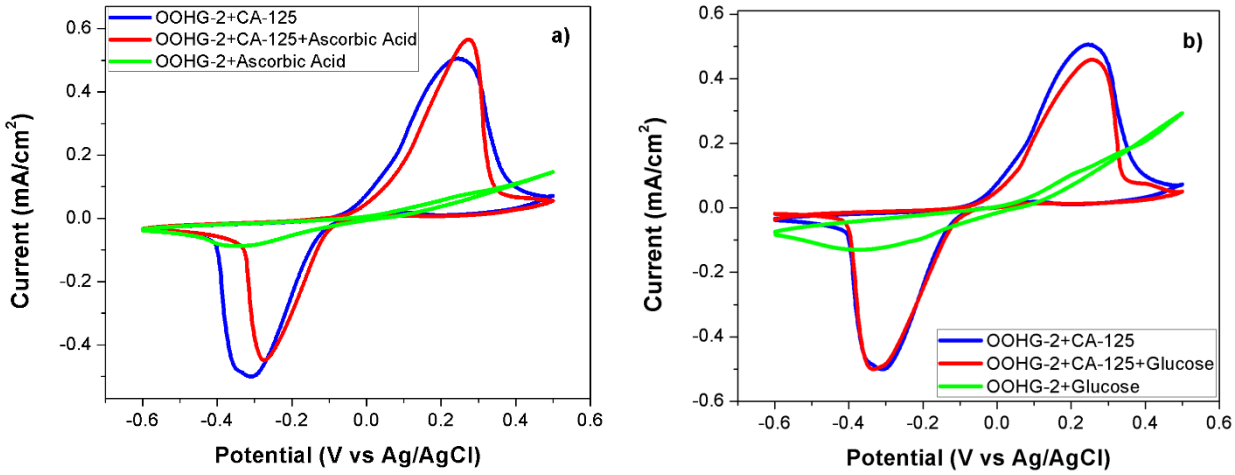

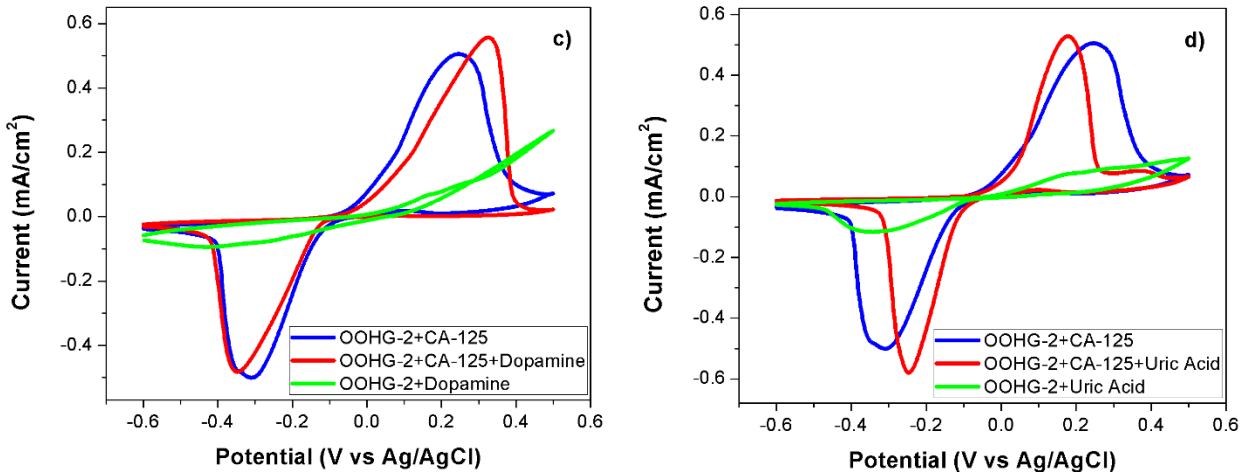

Figure 6. *CV results at 50 mV/s scan rate in a) prepared solution+Ascorbic acid, b) prepared solution+Glucose, c) prepared solution+Dopamine, and d) prepared solution+Uric acid over OOHG-2+CA-125 produced with determined conditions (30 minute and 500 ng/mL CA-125).*

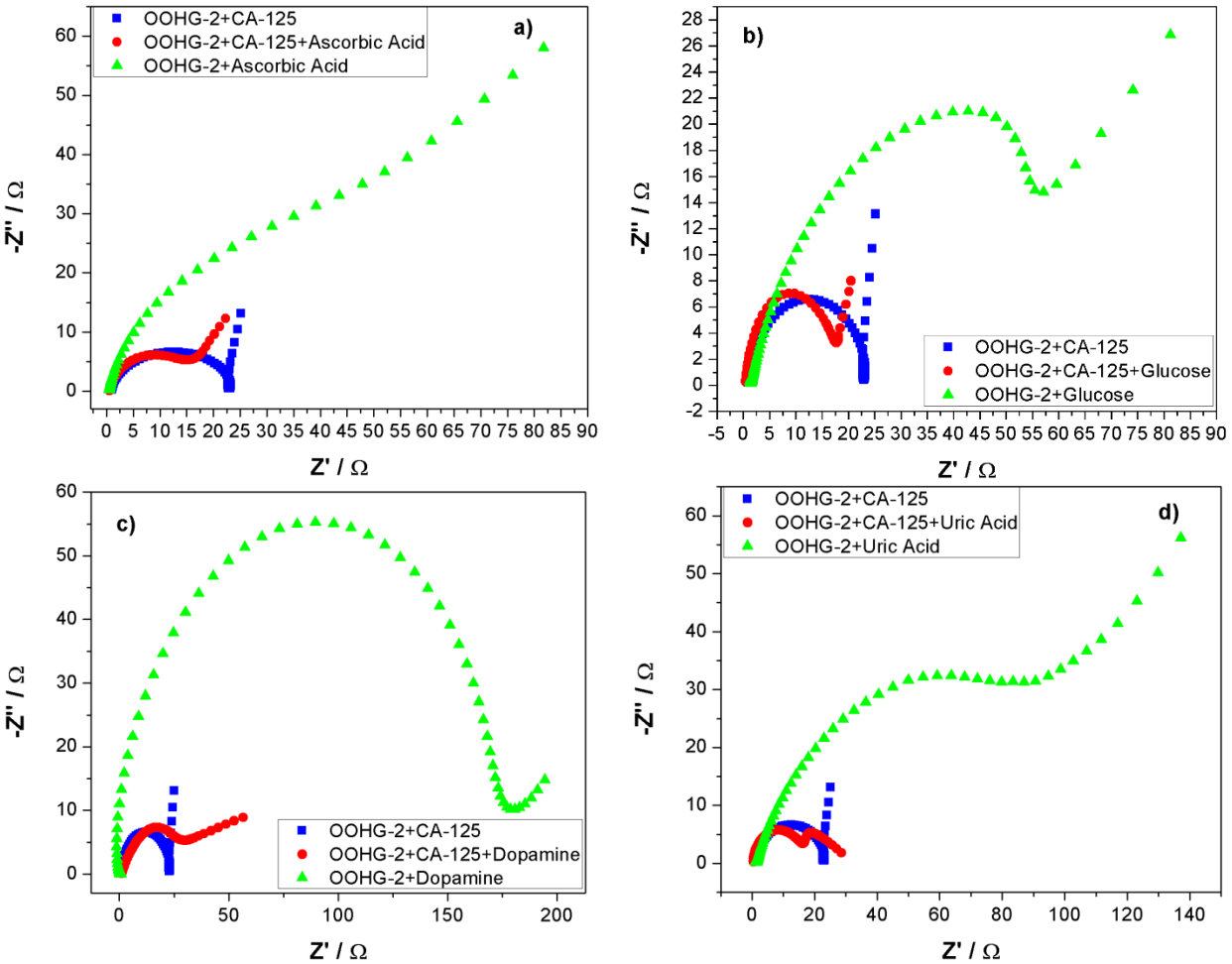

Figure 7. *The Nyquist plots of EIS data at 0.2 potential in a) prepared solution+Ascorbic acid, b) prepared solution+Glucose, c) prepared solution+Dopamine, and d) prepared solution+Uric acid over OOHG-2+CA-125 produced with determined conditions (30 minute and 500 ng/mL CA-125).*

Finally, the effect over the electrooxidation process among OOHG-2 and CA-125 of salts found in serum was examined in artificial and 0.9% isotonic NaCl serums via CV at 50 mV/s scan rate and EIS at 0.2 potential. OOHG-2+CA-125s that used in measurements were produced at determined conditions (30 minutes and 500 ng/mL CA-125). Results are given in Fig. 8. As clearly seen in Fig. 8a the salts in artificial and isotonic serums were found that don't have important effects over the electrooxidation reaction of CA-125. Likewise, the electron transfer resistances in these serum mediums were found that be very close to each other (Fig. 8b), and these data were compatible with CV results. As a result, CV results and EIS data prove that do not the effects over the electrooxidation process among OOHG-2 and CA-125 of the salts that found in serum medium.

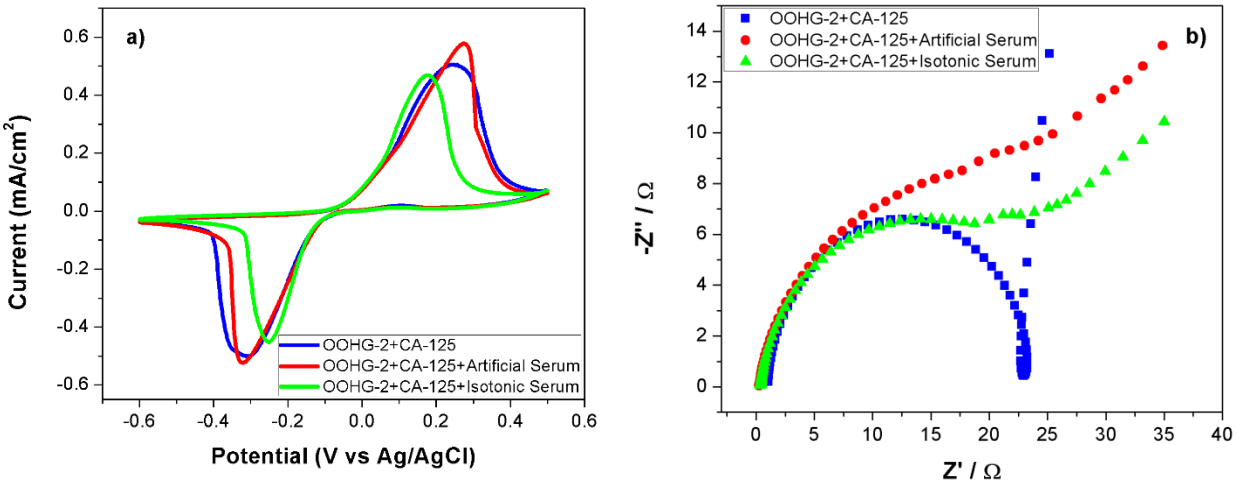

Figure 8. *a) CV results at 50 mV/s scan rate and b) the Nyquist plots of EIS data at 0.2 potential in artificial and isotonic serums over OOHG-2+CA-125 produced with determined conditions (30 minute and 500 ng/mL CA-125).*

4. Conclusions

In this study, onion oil-basic OOHGs were characterized by synthesizing to detect CA-125 in serum. FT-IR results and swelling tests were shown that OOHG structures synthesized successfully. Then, CA-125 at determined conditions was incubated over OOHG structures, and CV measurements were performed in the absence and presence of CA-125. While the electrooxidation peaks were not observed in measurements over OOHGs, Forward and backward peaks were clearly seen in measurements over OOHG+CA-125. OOHG-2+CA-125 among OOHGs prepared was displayed the highest performance with 0.8151 mA/cm^2 at 0.24 V of forward peak and 0.8258 mA/cm^2 at -0.31 V of backward peak values. Moreover, the linear range, LOD, and LOQ values for OOHG-2+CA-125 were found as 1-500 ng/mL concentrations (R^2 = 0.9826), 0.265 µU/mL, and 0.531 µU/mL, respectively. In addition, the electrooxidation peak belonging to CA-125 antigen was observed not affected in interference measurements of structures such as ascorbic acid, dopamine, glucose, and uric acid that could be found in the blood. These results show carries major hope for detecting at high sensitivity and selectivity, fast, and reliability of CA-125 in serum via electrochemical methods over OOHG-2 structure.

Acknowledgements

O. F. ER thanks for the scholarships the Scientific and Technological Research Council of Turkey (TUBITAK) (2211-A) and the Council of Higher Education (YOK) (100/2000) provide.

References

[1]. Kulasingam V., Diamandis EP., Strategies for discovering novel cancer biomarkers through utilization of emerging technologies, Nature clinical practice Oncology, 5, (2008), 588-99.

[2]. Hayes D.F., Bast R.C., Desch C.E., Fritsche Jr.H., Kemeny N.E., Jessup J.M., Tumor marker utility grading system: a framework to evaluate clinical utility of tumor markers, Journal of the National Cancer Institute, 88, (1996), 1456-66.

[3]. Duffy M., Clinical uses of tumor markers: a critical review, Critical reviews in clinical laboratory sciences, 38, (2001), 225-62.

[4]. Duffy M.J., Tumor markers in clinical practice: a review focusing on common solid cancers, Medical Principles and Practice, 22, (2013), 4-11.

[5]. Chikkaveeraiah B.V., Bhirde A.A., Morgan N.Y., Eden H.S., Chen X., Electrochemical immunosensors for detection of cancer protein biomarkers, ACS nano, 6, (2012), 6546-61.

[6]. Wulfkuhle J.D., Liotta L.A., Petricoin E.F., Proteomic applications for the early detection of cancer, Nature reviews cancer, 3, (2003), 267-75.

[7]. Kingsmore S.F., Multiplexed protein measurement: technologies and applications of protein and antibody arrays, Nature reviews Drug discovery, 5, (2006), 310-21.

[8]. Reid B.M., Permuth J.B., Sellers T.A., Epidemiology of ovarian cancer: a review, Cancer biology & medicine, 14, (2017), 9.

[9]. Majd S.M., Salimi A., Ultrasensitive flexible FET-type aptasensor for CA 125 cancer marker detection based on carboxylated multiwalled carbon nanotubes immobilized onto reduced graphene oxide film, Analytica chimica acta, 1000, (2018), 273-82.

[10]. Diaconu I., Cristea C., Hârceagă V., Marrazza G., Berindan-Neagoe I., Săndulescu R., Electrochemical immunosensors in breast and ovarian cancer, Clinica Chimica Acta, 425, (2013), 128-38.

[11]. Lahoud R., O'Shea A., El-Mouhayyar C., Atre I., Eurboonyanun K., Harisinghani M., Tumour markers and their utility in imaging of abdominal and pelvic malignancies, Clinical Radiology, 76, (2020), 99-107.

[12]. Wu S., Xu K., Chen G., Zhang J., Liu Z., Xie X., Identification of serum biomarkers for ovarian cancer using MALDI–TOF-MS combined with magnetic beads, International journal of clinical oncology, 17, (2012), 89-95.

[13]. Lamberti I., Scarano S., Esposito C.L., Antoccia A., Antonini G., Tanzarella C., Franciscis V.D., Minunni M., In vitro selection of RNA aptamers against CA125 tumor marker in ovarian cancer and its study by optical biosensing, Methods, 97, (2016), 58-68.

[14]. Chakkarapani S.K., Zhang P., Ahn S., Kang S.H., Total internal reflection plasmonic scattering-based fluorescence-free nanoimmunosensor probe for ultra-sensitive detection of cancer antigen 125, Biosensors and Bioelectronics, 81, (2016), 23-31.

[15]. Zhao Y., Zheng Y., Zhao C., You J., Qu F., Hollow PDA-Au nanoparticles-enabled signal amplification for sensitive nonenzymatic colorimetric immunodetection of carbohydrate antigen 125, Biosensors and Bioelectronics, 71, (2015), 200-6.

[16]. Soper J.T., Hunter V.J., Daly L., Tanner M., Creasman W.T., Bast Jr.RC., Preoperative serum tumor-associated antigen levels in women with pelvic masses, Obstetrics and gynecology, 75, (1990), 249-54.

[17]. Xu Q., Davis J.J., The diagnostic utility of electrochemical impedance, Electroanalysis, 26, (2014), 1249-58.

[18]. Bhalla V., Carrara S., Sharma P., Nangia Y., Suri C.R., Gold nanoparticles mediated label-free capacitance detection of cardiac troponin I, Sensors and Actuators B: Chemical, 161, (2012), 761-8.

[19]. Wang Y., Zhang Z., Jain V., Yi J., Mueller S., Sokolov J., Liu Z., Levon K., Rigas B., Rafailovich M.H., Potentiometric sensors based on surface molecular imprinting: Detection of cancer biomarkers and viruses, Sensors and Actuators B: Chemical, 146, (2010), 381-387.

[20]. Li T., Shu B., Jiang B., Ding L., Qi H., Yang M., Qu F., Ultrasensitive multiplexed protein biomarker detection based on electrochemical tag incorporated polystyrene spheres as label, Sensors and Actuators B: Chemical, 186, (2013), 768-73.

[21]. Kivrak H., Alal O., Atbas D., Efficient and rapid microwave-assisted route to synthesize Pt-MnOx hydrogen peroxide sensor, Electrochimica acta, 176, (2015), 497-503.

[22]. Kazıcı H.Ç., Caglar A., Aydogmus T., Aktas N., Kivrak H., Microstructured prealloyed Titanium-Nickel powder as a novel nonenzymatic hydrogen peroxide sensor, Journal of colloid and interface science, 530,(2018), 353-60.

[23]. Er O.F., Alpaslan D., Dudu T.E., Aktas N., Kivrak H., Novel Cacao oil-based organo-hydrogels to detect carcinoma antigen 125 in serum medium; synthesis, characterization, and electrochemical measurements, Materials Chemistry and Physics, 292, (2022), 126795.

[24]. Bangar M.A., Shirale D.J., Chen W., Myung N.V., Mulchandani A., Single conducting polymer nanowire chemiresistive label-free immunosensor for cancer biomarker, Analytical chemistry, 81, (2009), 2168-75.

[25]. Chen S., Yuan R., Chai Y., Xu Y., Min L., Li N., A new antibody immobilization technique based on organic polymers protected Prussian blue nanoparticles and gold colloidal nanoparticles for amperometric immunosensors, Sensors and Actuators B: Chemical, 135, (2008), 236-44.

[26]. Bahavarnia F., Saadati A., Hassanpour S., Hasanzadeh M., Shadjou N., Hassanzadeh A., Paper based immunosensing of ovarian cancer tumor protein CA 125 using novel nano-ink: a new platform for efficient diagnosis of cancer and biomedical analysis using microfluidic paper-based analytical devices (μPAD), International journal of biological macromolecules, 138, (2019), 744-54.

[27]. Wu L., Yan F., Ju H., An amperometric immunosensor for separation-free immunoassay of CA125 based on its covalent immobilization coupled with thionine on

carbon nanofiber, Journal of immunological methods, 322, (2007), 12-9.

[28]. Li H., Qin J., Li M., Li C., Xu S., Qian L., Yang B., Gold-nanoparticle-decorated boron-doped graphene/BDD electrode for tumor marker sensor, Sensors and Actuators B: Chemical, 302, (2020), 127209.

[29]. Er O.F., Kivrak H., Ozok O., Çelik S., Kivrak A., A novel electrochemical sensor for monitoring ovarian cancer tumor protein CA 125 on benzothiophene derivative based electrodes, Journal of Electroanalytical Chemistry, 904, (2021), 115854.

[30]. Er O.F., Kivrak H., Ozok O., Kivrak A., Novel 5-(2-phenylbenzo [b] thiophen-3-yl) furan-2-carbaldehyde based ovarian cancer carbohydrate antigen 125 electrochemical sensor, Materials Chemistry and Physics, 291, (2022), 126560.

[31]. Kivrak H., Er O.F., Ozok O., Celik S., Kivrak A., Synthesis and characterization of 4-(2-(4-methoxyphenyl) benzo [b] thiophen-3-yl) benzaldehyde for carbohydrate antigen 125 electrochemical detection and molecular docking modeling, Materials Chemistry and Physics, 281, (2022), 125951.

[32]. Er O.F., Kivrak H., Ozok O., Kivrak A., Superior and Novel Carbohydrate Antigen 125 Electrochemical Sensor Based on 4-(2-(Naphthalen-1-Yl) benzo [b] thiophen-3-Yl) benzaldehyde, Available at SSRN, (2021), 3863113.

[33]. Hasanzadeh M., Sahmani R., Solhi E., Mokhtarzadeh A., Shadjou N., Mahboob S., Ultrasensitive immunoassay of carcinoma antigen 125 in untreated human plasma samples using gold nanoparticles with flower like morphology: a new platform in early stage diagnosis of ovarian cancer and efficient management, International journal of biological macromolecules, 119, (2018), 913-25.

[34]. Zheng Y., Wang H., Ma Z., A nanocomposite containing Prussian Blue, platinum nanoparticles and polyaniline for multi-amplification of the signal of voltammetric immunosensors: highly sensitive detection of carcinoma antigen 125, Microchimica Acta, 184, (2017), 4269-77.

[35]. Tang D., Yuan R., Chai Y., Electrochemical immuno-bioanalysis for carcinoma antigen 125 based on thionine and gold nanoparticles-modified carbon paste interface, Analytica chimica acta, 564, (2006), 158-65.

[36]. Rebelo T.S., Costa R., Brandão A.T., Silva A.F., Sales M.G.F., Pereira C.M., Molecularly imprinted polymer SPE sensor for analysis of CA-125 on serum, Analytica chimica acta, 1082, (2019), 126-35.

[37]. Cui Z., Wu D., Zhang Y., Ma H., Li H., Du B., Wei Q., Ju H., Ultrasensitive electrochemical immunosensors for multiplexed determination using mesoporous platinum nanoparticles as nonenzymatic labels, Analytica chimica acta, 807, (2014), 44-50.

[38]. Ren X., Wang H., Wu D., Fan D., Zhang Y., Du B., Wei Q., Ultrasensitive immunoassay for CA125 detection using acid site compound as signal and enhancer, Talanta, 144, (2015), 535-41.

[39]. Jafari M., Hasanzadeh M., Solhi E., Hassanpour S., Shadjou N., Mokhtarzadeh A., Jouyban A., Mahboob S., Ultrasensitive bioassay of epitope of Mucin-16 protein (CA 125) in human plasma samples using a novel immunoassay based on silver conductive nano-ink: A new platform in early stage diagnosis of ovarian cancer and efficient management, International journal of biological macromolecules, 126, (2019), 1255-65.

[40]. Torati S.R., Kasturi K.C., Lim B., Kim C., Hierarchical gold nanostructures modified electrode for electrochemical detection of cancer antigen CA125, Sensors and Actuators B: Chemical, 243, (2017), 64-71.

[41]. Biswas S., Lan Q., Xie Y., Sun X., Wang Y., Label-Free Electrochemical Immunosensor for Ultrasensitive Detection of Carbohydrate Antigen 125 Based on Antibody-Immobilized Biocompatible MOF-808/CNT, ACS Applied Materials & Interfaces, 13, (2021), 3295-302.

[42]. Gasparotto G., Costa J.P.C., Costa P.I., Zaghete M.A., Mazon T., Electrochemical immunosensor based on ZnO nanorods-Au nanoparticles nanohybrids for ovarian cancer antigen CA-125 detection, Materials Science and Engineering: C, 76, (2017), 1240-7.

[43]. Mishra S.B., Mishra A.K., Polymeric hydrogels: A review of recent developments, Polymeric hydrogels as smart biomaterials, (2016), 1-17.

[44]. Dudu T.E., Alpaslan D., Aktas N., Application of Poly (Agar-Co-Glycerol-Co-Sweet Almond Oil) Based Organo-Hydrogels as a Drug Delivery Material, Journal of Polymers and the Environment, 30, (2021), 1-11.

[45]. Sahiner N., Alpaslan D., Metal-ion-containing ionic liquid hydrogels and their application to hydrogen production, Journal of Applied Polymer Science, 131, (2014), 40183.

[46]. Vázquez-González M., Willner I., Stimuli-Responsive Biomolecule-Based Hydrogels and Their Applications, Angewandte Chemie International Edition, 59, (2020), 15342-77.

[47]. Alpaslan D., Dudu T.E., Aktaş N., Synthesis and characterization of novel organo-hydrogel based agar, glycerol and peppermint oil as a natural drug carrier/release material, Materials Science and Engineering: C, 118, (2021), 111534.

[48]. Alpaslan D., Dudu T.E., Aktas N., Evaluation of poly (agar-co-glycerol-co-castor oil) organo-hydrogel as a controlled release system carrier support material, Polymer Bulletin, 79, (2021), 1-22.

[49]. Helgeson M.E., Moran S.E., An H.Z., Doyle P.S., Mesoporous organohydrogels from thermogelling photocrosslinkable nanoemulsions, Nature materials, 11, (2012), 344-52.

[50]. Zohri A-N., Abdel-Gawad K., Saber S., Antibacterial, antidermatophytic and antitoxigenic activities of onion (Allium cepa L.) oil, Microbiological research, 150, (1995), 167-72.

[51]. Lanzotti V., The analysis of onion and garlic, Journal of chromatography A, 1112, (2006), 3-22.

[52]. Taleat Z., Ravalli A., Mazloum-Ardakani M., Marrazza G., CA 125 immunosensor based on poly-anthranilic acid modified screen-printed electrodes, Electroanalysis, 25, (2013), 269-77.

[53]. Wu L., Chen J., Du D., Ju H., Electrochemical immunoassay for CA125 based on cellulose acetate stabilized antigen/colloidal gold nanoparticles membrane, Electrochimica Acta, 51, (2006), 1208-14.

[54]. Ciucci F., Modeling electrochemical impedance spectroscopy, Current Opinion in Electrochemistry, 13, (2019), 132-9.

[55]. ER Ö.F., Cavak A., Aldemir A., Kivrak H.D., Investigation of hydrazine electrooxidation performance of carbon nanotube supported Pd monometallic direct hydrazine fuel cell anode catalysts, MANAS Journal of Engineering, 8, (2020), 90-98.

[56]. Chang B-Y., Park S-M., Electrochemical impedance spectroscopy, Annual Review of Analytical Chemistryi, 3, (2010), 207-29.

[57]. Er O.F., Ulas B., Ozok O., Kivrak A., Kivrak H., Design of 2-(4-(2-pentyllbenzo [b] thiophen-3-yl) benzylidene) malononitrile based remarkable organic catalyst towards hydrazine electrooxidation, Journal of Electroanalytical Chemistry, 888, (2021), 115218.

[58]. Kivrak H., Selçuk K., Er O.F., Aktas N., Nanostructured electrochemical cysteine sensor based on carbon nanotube supported Ru, Pd, and Pt catalysts, Materials Chemistry and Physics, 267, (2021), 124689.

[59]. ER Ö.F., Ulaş B., Kivrak H.D., Remarkable bismuth-gold alloy decorated on MWCNT for glucose electrooxidation: the effect of bismuth promotion and optimization via response surface methodology, Turkish Journal of Chemistry, 45, (2021), 1173-88.

[60]. Kaya S., Yilmaz Y., Er O.F., Alpaslan D., Ulas B., Dudu T.E., Kivrak H., Highly Active RuPd Bimetallic Catalysts for Sodium Borohydride Electrooxidation and Hydrolysis, Journal of Electronic Materials, 51, (2021), 403-411.

MANAS Journal of Engineering
ISSN 1694-7398 | e-ISSN 1694-7398

Volume 11, Issue 1, (2023) Pages 136-144
https://doi.org/10.51354/mjen.1280304

Biotechnological valorization of sugar beet wastes into value-added products

Azhar Makambai kyzy, Aichurok Mazhitova*

Department of Food Engineering, Kyrgyz-Turkish Manas University, Bishkek 720038, Kyrgyz Republic, ajargida@gmail.com, aichurok.mazhitova@manas.edu.kg, ORCID: 0000-0003-2090-1116.

ABSTRACT

The sugar beet processing in the sugar production industry releases huge amounts of sugar beet pulp, lime residue, and molasses, which can be considered a valuable by-product as a source of cellulose, hemicellulose, and pectin. Sugar beet pulp is often used as a high-energy, low-protein supplement for ruminants to promote optimal rumen health and increase milk production. However, it cannot be used in large quantities and is thrown away, causing environmental pollution. Valorizing sugar beet processing wastes via biotechnological approaches into value-added products is cost-effective and eco-friendly. In this article, recent developments in the biotechnological valorization of sugar beet byproducts to produce biofuels, bioethanol, butanol, biomass and platform chemicals such as gluconic acid, lactic acid, rhamnolipid biosurfactant, and endo-polygalacturonase were reviewed, and the methods provide a way to save the environment. Several sugar beet processing plants in the Kyrgyz Republic can offer these methods as a roadmap for value-added production.

ARTICLE INFO

Review article

Received: 10.04.2023
Accepted: 11.06.2023

Keywords:
pulp,
lime residue,
organic acids,
biofuels,
biomass

**Corresponding Author*

1. Introduction

Research on sugar's history reveals that sugarcane was initially domesticated in Papua New Guinea. From there, it spread throughout the Pacific and eventually reached India, where crude forms of sugar were produced about 2000 years ago. In the mid-18th century, sugar beet was identified as a viable alternative source of sugar that could be cultivated in temperate regions. [1]. Recently, world sugar production has been approximately 160 Mt yearly, with a per capita consumption of about 23 kg. The chemical composition of commercial sugars produced from cane and beets is sucrose (over 99.5% in white crystalline sugar), even though the crops differ significantly in climatic requirements and photosynthesis pathways [2]. Beet sugar represents only 20% of the world's sugar production, with the other 80% produced from sugar cane [3]. Sugar beet (*Beta vulgaris*) is an important crop plant in central Europe for sugar production [4]. Due to the climatic conditions of growing sugar beet, it is grown more in Europe than in other countries. The European Union is the world's leading beet sugar producer, with approximately 50% of the total [3]. In Poland, about 11-12 x 10^9 kilograms of sugar beet is used each year to make white sugar [5]. As a byproduct of this process, around 5.5 x 10^8 kilograms of sugar beet bagasse (pulp) is obtained, along with lime residue and molasses which are considered waste materials [6]. The technology for producing sugar from beets and generated wastes is shown in Fig. 1.

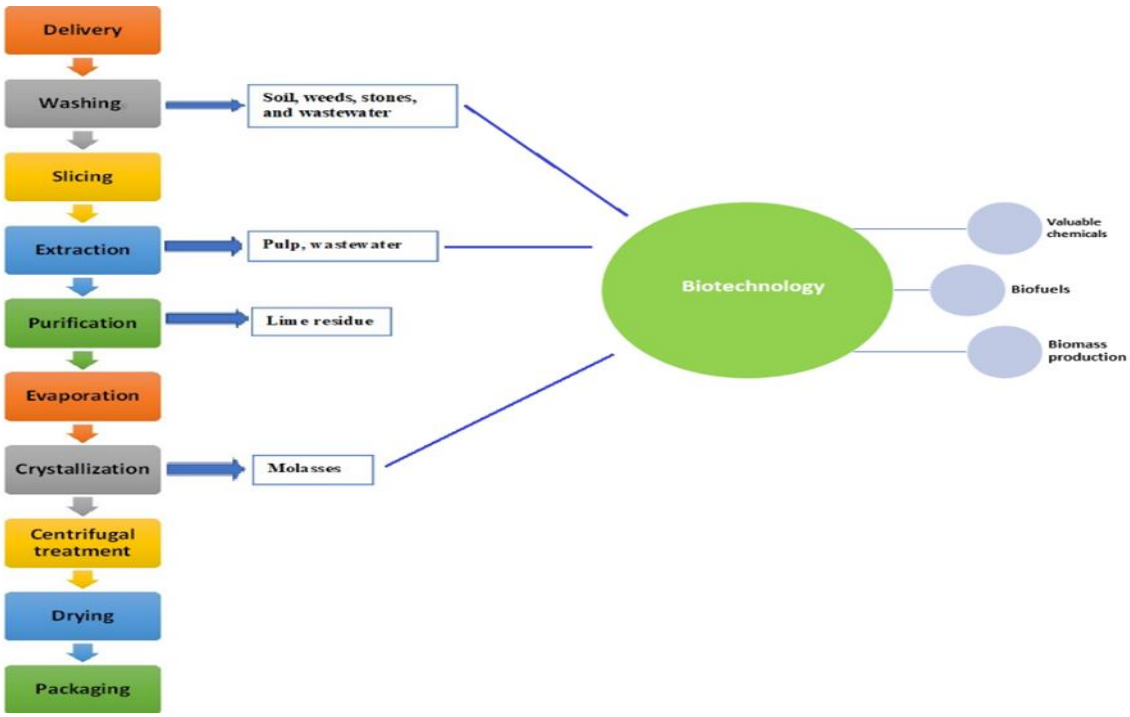

Figure 1. *Bioconversion of sugar industrial wastes into value-added products.*

Sugar beet pulp (SBP) is a highly fibrous sugar-depleted material produced after sugar is extracted from sugar beet [7]. SBP contains 20-30% cellulose and 18-36% hemicellulose (mainly arabinans), 20-32% pectin, 7-15% protein, and 1-4% lignin (dry weight basis) [8]. Pulp is a valuable cattle feed and supplies carbohydrates, proteins, and minerals. SBP (in dry, pelleted, or ensiled form) is often used as a high-energy, low-protein supplementary food for ruminants promoting optimum rumen conditions and boosting milk production [9].

The lime residue is the residual calcium carbonate precipitate left after the juice purification process, followed by the pressing process. It is a cake-like substance with approximately 70% dry substance (almost the same as soil). It consists of roughly 80% $CaCO_3$ in its dry substance (DS), 10% inorganic and insoluble organic compounds, and trace elements, such as selenium, zinc, and molybdenum.

Molasses is a thick solution that contains around 50% sucrose and 80% DS along with minerals, vitamins, and organic compounds. Due to its high sugar content and valuable nutrients, it is a popular choice for fermentation processes [7, 10]. It is commonly used in the animal feed industry, as well as in the production of yeast, citric acid, alcohol, rum, and pharmaceuticals [7, 11].

Food wastage has a huge carbon footprint, estimated at 3.3 billion tonnes of CO_2 equivalent to GHG (greenhouse gas) released into the atmosphere annually. The total volume of water used each year to produce lost or wasted food (250 km^3) is equivalent to the annual flow of Russia's Volga River, or three times the volume of Lake Geneva. Similarly, 1.4 billion hectares of land - 28% of the world's agricultural area - is used annually to produce lost or wasted food [12]. In terms of sugar production, traditional beet sugar processing causes environmental problems mainly due to the elaboration of large amounts of pulp, the consumption of large quantities of lime (which are transformed into sludge), the production of vinasse, and the consumption of energy and water [13].
Due to the huge amount of waste in the production of sugar from beets, it is of great interest to use it as a raw material for producing value-added chemicals such as gluconic acid [14], lactic acid [15], 2,3-butanediol [10], endo- polygalacturonase [16], rhamnolipid [17], propylene glycol [18], biofuels such as butanol [8], hydrogen [19], methane [20], ethanol [21], biomass such as microalgae *Chlorella* [22], single cell protein [23, 6] and sugar beet wastes used in the immobilization of microorganisms [24].

In the Kyrgyz Republic, beets are the only crop for sugar production. It is grown only in the Chui and Talas regions. According to the National Statistical Committee of the Kyrgyz Republic, the area dedicated to sugar beet cultivation decreased in 2022. In the previous year, the republic saw 10.2 thousand hectares of land sown, while in 2022, this decreased to 9.0 thousand hectares, marking an 11.3% decline. Despite this, a total of 468.1 thousand tons of sugar beets were harvested in 2022, with a yield of 518.1 centners per hectare, which is a significant increase of 28% compared to the previous year [25]. According to the Ministry of Economy of the Kyrgyz Republic, the main volume of sugar beet is processed by three enterprises, with an amount of 107.4 thousand tons in 2022. Unfortunately, the waste produced by the sugar industry is not effectively utilized. Currently, sugar producers sell fresh pulp to feed farm animals, but it must be used within 1-2 days due to its quick deterioration. Any

unused pulp is typically buried, leading to soil pollution and environmental damage. After a few weeks, the pulp undergoes oil fermentation, releasing butyric acid into nearby reservoirs.

This work aims to evaluate the biotechnological methods of obtaining value-added products to offer them as a "road map" in the utilization of sugar beet wastes in the Kyrgyz Republic.

2. Valuable chemicals from sugar beet waste

2.1 Gluconic acid

Gluconic acid and its salts are highly sought after for use in various industries such as pharmaceuticals, food, feed, textiles, and leather [26]. There are several methods to obtain gluconic acid, with most being chemical-based. However, there is increasing interest in fermentation as a preferred method for industrial production. In a recent study by Kelleci et al. (2022), three fermentation methods were tested: submerged, semisolid-state, and solid-state fermentations. The results showed that the most efficient method was semisolid-state fermentation, producing 0.354 g of gluconic acid per g of absolute solid substrate. The substrate used was SBP and sugar beet molasses, and it is noteworthy that gluconic acid was produced in situ. In addition, the authors found that $CaCO_3$ was a suitable neutralizer, and the required calcium carbonate can be obtained from the carbonation cake resulting from sugar juice treatment [14].

2.2 Lactic acid

Lactic acid and its derivatives, including salts and esters, have various applications in the food, polymer, and industrial sectors. They are commonly used in beverages, candies, meat, sauces, and as monomers for producing PLA, which is used to make cups, plates, and utensils. Additionally, lactic acid is utilized in metal plating, cosmetics, and the textile and leather industries [27]. During the fermentation process, lactic acid bacteria produce lactic acid, as demonstrated by a recent study that used *Lacticaseibacillus paracasei* NRRL B-4564 to produce lactic acid using sugar beet molasses [28]. It is worth noting that the MRS medium was modified by adding molasses, and the results were promising. The study found that waste substrate based on sugar beet molasses could substitute for expensive MRS broth as a source of nitrogen, vitamins, minerals, and fermentable sugars for the growth of LAB and LA production. However, another study used granules of SBP to obtain the highest LA concentration (30 g L−1) by *Lactiplantibacillus plantarum*, but pretreatment was required [15].

2.3 Rhamnolipid biosurfactant

Biological surface-active agents, also known as biosurfactants, are produced by various microorganisms and have unique properties such as lowering surface tension, increasing solubility of poorly soluble compounds, non-toxicity, non-allergenicity, and biodegradability [29]. One example of biosurfactant is the rhamnolipid, which is commonly produced by *Pseudomonas aeruginosa*. In a study by Onbasli and Aslim (2009), the same microorganism was used but with sugar beet molasses as a substrate [17]. It was found that *Pseudomonas* spp. can use molasses as a carbon source for rhamnolipid production without any pretreatment. The molasses was simply diluted with distilled water to the required concentration, the pH was adjusted to 7.0, and then sterilized in an autoclave.

2.4. Endo-polygalacturonase

It is crucial to note that endo-polygalacturonase (endo-PG), an enzyme derived from agroindustrial waste SBP, holds immense potential in various industrial applications. This enzyme serves as an efficient raw carbon source for breaking down industrial waste during urban waste disposal. A recent study by authors [16] conducted submerged fermentation using *A. niger* and *P. variotii* as fermentation agents, with SBP being dried and milled as the solitary pretreatment. The study demonstrated that SBP is a promising inducer for endo-PG production. However, it is imperative to test all types of fermentation conditions to determine the most effective method for producing commercial enzymes while optimizing the enzyme production and extraction methods from different industrial wastes. The results of this study have significant implications in the food, pharmaceutical, and other industrial sectors [16].

2.5 2,3-Butanediol

The chemical 2,3-Butanediol shows promise as a versatile substance with various potential uses such as in the production of printing inks, perfumes, synthetic rubber, fumigants, antifreeze agents, fuel additives, food products, and pharmaceuticals [30]. Recently, researchers [10] obtained 2,3-Butanediol through fermentation using *Bacillus amyloliquefaciens* TUL 308. The study found that sugar beet molasses was the most suitable carbon source for the synthesis of 2,3-Butanediol by the tested strain. This carbon source is not only cost-effective but also requires no pre-treatment before use.

3. Biofuels

3.1 Butanol

The relevance of biofuel has increased significantly in recent times due to the depletion of fossil fuel sources and their negative impact on the environment. In the current century, there is a growing interest in waste management and research on converting waste to green energy [31]. As a result, there is a need for crude oil that is environmentally friendly and provides energy similar to conventional diesel. Butanol is a liquid fuel that is considered a green energy and offers several advantages over ethanol, including an energy value similar to gasoline, lower corrosiveness, low vapor pressure, lower miscibility with water, high flash point, and easy transportation through existing pipelines. Additionally, it can

reduce hydrocarbon emissions by 95% and nitrogen oxides by 37% [8]. Butanol has the potential to address some of the infrastructure problems related to fuel cell use and can be dispersed through existing pipelines and filling stations. It offers a safer fuel with more hydrogen, making it a promising alternative energy source [32]. Table 1 displays the results of a study conducted by the authors [8], who used acetone-butanol-ethanol (ABE) fermentation to produce butanol. This process produces acetone, butanol, and ethanol in a 3:6:1 ratio, with butanol being the main product. The feedstock used for ABE fermentation was SBP and *Clostridium beijerinckii*. The scientists highlighted the significance of pretreatment and compared various methods such as dilute sulfuric acid pretreatment, autohydrolysis pretreatment at pH 4, and enzymatic hydrolysis. Autohydrolysis at pH 4 (120°C, 6% SBP (w/w), 5 minutes) was found to be the most effective pretreatment for enhancing overall sugar release yields in enzymatic hydrolysis and acetone and butanol yields in the fermentation process. It has advantages over conventional dilute acid pretreatment, such as higher solid recoveries, no washing needs, and lower use of chemicals. The authors claim that overall yields of 143.2 g ABE/kg SBP (62.3 g acetone and 80.9 g butanol) can be achieved.

3.2 Hydrogen

Hydrogen is a valuable commodity in various industries due to its versatility. It is not only highly efficient but also an eco-friendly fuel. When hydrogen is burned, it does not emit greenhouse gases, ozone-depleting chemicals, acid rain components, or any pollutants [33]. Moreover, it is often suggested as a safe fuel since it only produces water upon combustion [34]. In a study by authors [19], single-stage photofermentation was applied under anaerobic conditions using sugar beet molasses and *Rhodobacter capsulatus* JP91 as inoculum. Without any pretreatment, beet molasses yielded 10.5 mol H_2/mol sucrose, as shown in Table 1. Although two-stage systems were previously deemed the most efficient for hydrogen production, this paper carried out single-stage photofermentation, which saves space and energy. The single-stage system also produces more hydrogen at a low sugar concentration of 1 g sugar/L, which makes up for any deficiency in hydrogen production.

3.3 Methane

Organic waste, such as sugar beet wastes, can be effectively utilized for biogas production through anaerobic digestion. This process is currently the primary method for obtaining gas from organic waste. Anaerobic digestion occurs naturally in various environments, such as marshes, bogs, landfills, and dedicated digesters. It involves the conversion of organic waste into a combustible biogas, which can be used as a boiler or motor fuel, or even upgraded to pipeline quality [35]. Researchers have analyzed various scientific papers on sugar production waste and discovered positive outcomes. One study [36] examined the co-digestion of waste with SBP and wastewater using anaerobic seed culture from a municipal wastewater treatment plant as inoculum. The addition of wastewater led to an increase in methane production rate for the beet pulp, rather than an increase in ultimate biodegradability. Additionally, the wastewater replaced fresh water typically used as a diluent for pulp digestion. It's important to note that pretreatment is crucial for anaerobic digestion, which was also addressed in this study. This involved physically treating or cleaning the wastewater and drying and crushing the beet pulp. It's worth noting that not only is beet pulp utilized, which is typically used for animal feed, but also wastewater from sugar production that is often discarded. This helps save on the fresh water needed for fermentation. In a similar study, other experts [20] incorporated sugar beet waste as an extra carbon source in anaerobic co-digestors with cow and pig manure. It was found that the co-digestion with manure significantly reduced the inhibitory effect of volatile fatty acids at high organic loading rates, leading to a 70% and 31% increase in methane production for pig and cow manure co-digestion, respectively, compared to individual digestion of sugar beet byproducts.

3.4 Bioethanol

Bioethanol is a renewable biofuel made from various biomass materials that can be used as a sole fuel source or partial substitute for fossil fuels. Bioethanol production from agro-industrial byproducts, residues, and wastes is one example of sustainable energy production [21, 37]. Several studies have explored the production of bioethanol and identified effective processing methods. Dilute acid pretreatment, for instance, has been found to significantly improve the enzymatic hydrolysis and ethanol yield of SBP. Under the optimum conditions, the ethanol yield from pretreated SBP in a simultaneous saccharification and fermentation process using Escherichia coli KO11 was 0.4 g ethanol/g dry matter [21]. Additionally, ensiling SBP has been shown to increase its reducing sugar yield upon enzymatic hydrolysis, but it requires water washing. Authors report that ensiled SBP does not require sterilization for fermentation with *E. coli* KO11, and washing it decreases ethanol yield. This suggests that ensilage could be a useful method for storing and pretreating biomass to enhance biofuel yield [38]. In another study, researchers found that the liquid fraction obtained from the hydrolysis of SBP could be subjected to alcoholic fermentation, while the remaining solid residue and stillage were used for methane or hydrogen production [39]. Bioethanol fermentation using the coculture of *Saccharomyces cerevisiae* Ethanol Red and *Scheffersomyces stipitis* LOCK0047 resulted in 12.6 g/L ethanol, as shown in Table 1. The largest hydrogen yield (252 dm^3 H_2/kg VS) was achieved with sugar beet stillage (SBS) that underwent thermal pretreatment and had its inoculum pH adjusted, and the maximum methane yield was 444 dm3 CH_4/kg volatile solids (VS). As a result, the stillage obtained after alcoholic fermentation was not discarded but used as a raw material for the production of methane or hydrogen, making this process economically viable and environmentally friendly.

4. Biomass production

4.1 Microalgae Chlorella

The cultivation of *Chlorella* for producing biomass and derivative products is an industrial activity that has already been established commercially in several countries. The interest in these microalgae is due to their rapid growth and simple life cycles, allowing in-depth studies of their mechanisms and use as a food substitute in terms of their high protein, carotenoid, vitamin, and mineral contents [40]. *Chlorella* has a high protein content (58 g/100g) compared with wheat (13 g/100 g), chicken (24 g/100 g) and fish (18-24 g/100 g) [41]. Wang et al. (2019) conducted a study where they utilized SBP as an illustration of lignocellulosic biomass. This biomass was nonairtightly fermented with digested dairy manure to offer additional organic carbon sources for microalgae cultivation [22]. Additionally, the authors reported that *Chlorella* cultured in the 3-fold diluted hydrolysate demonstrated the best growth and nutrient reduction performance, in which case the final biomass density reached 2.17 g/L.

4.2 Single-cell protein

After distilling beet molasses to make alcohol, a dark brown liquid called vinasse is produced. This liquid is high in organic matter and salt content, making it difficult to dispose of and environmentally concerning [42, 23]. Unlike other sugar production wastes, beet vinasse is not often suitable for further processing. However, researchers have found that beet vinasse obtained after fermentation can be used to produce valuable single-cell protein and *Spirulina platensis* biomass. Single-cell protein is a type of protein extracted from cultivated microbial biomass that can be used to supplement diets by replacing costly conventional protein sources like soymeal and fishmeal [43]. In a study conducted by Coca et al. (2015), beet vinasse was used to supplement a mineral medium in a vertical airlift photobioreactor [23]. . The researchers noted that betaine, a nitrogenous compound found in beet vinasse, was completely removed from the broth due to its utilization as a nutrient source by the microalgae. Adding 1 g L^{-1} vinasse to the mineral medium significantly increased biomass and protein productivity compared to an unsupplemented medium. In another study, researchers [6] utilized SBP as a substrate for fed-batch cultivation of *C. tropicalis* to convert it into SCP. However, they highlighted the significance of pretreatment to ensure the culture is abundant in valuable components. The resulting biomass had a protein content of 52.3% of DM, indicating that SBP can be effectively utilized to produce yeast biomass that contains noteworthy amounts of SCP.

4.3 Immobilization agent

Cell immobilization refers to the process of preventing cells from moving either naturally or artificially [44]. This technique can be utilized to produce various value-added products, including biopharmaceuticals, bioplastics, biofuels, and bioremediation. Additionally, it can be employed in the development of biological biosensors for tissue regeneration in the medical field [45]. In a study on bioethanol production, *Saccharomyces cerevisiae* was immobilized using SBP [24]. The researchers found that this method enabled the rational use of intermediates and byproducts of sugar beet processing, contributing to the zero-waste goal. They achieved a maximum ethanol yield of 0.446 ± 0.017 g/g, with beet thick juice being the best substrate for ethanol production, requiring no nutrient supplementation. Autoclaving proved the supports to be both mechanically and chemically stable. The researchers confirmed that SBP was an ideal material for immobilizing *S. cerevisiae* due to its porosity, high water swelling capacity, biocompatibility, and high cell retention capacity. The immobilization method was deemed inexpensive, simple, and easy, with the exploited dried SBP supported with immobilized yeast cells potentially serving as a protein-enriched complement for animal feed. In a recent study [46], researchers explored a method for immobilizing *Leuconostoc mesenteroides* T3 using SBP, while utilizing beet molasses as a nutrient source for dextransucrase production. Dextransucrase (DS) enzymes, primarily secreted by *Leuconostoc*, *Streptococcus*, and *Lactobacillus* species, synthesize the majority of dextrans in nature [47]. The authors of the study [46] found that immobilizing the cells onto SBP enhances DS production. The results of the repeated batch fermentation experiment with Lc. mesenteroides T3 immobilized onto the SBP-NaOH carrier showed that four subsequent cycles could be performed with immobilized cells, until the productivity decreased by approximately 60%.

5 Conclusions

The field of biotechnology has gained prominence for its ability to extract valuable products from waste materials. In Europe, where there is a high volume of sugar production, sugar factories have found ways to recycle their waste as substrates, resulting in the creation of valuable products and energy. Various studies have integrated different types of agro-waste into a biorefining process, with sugar beet waste playing a crucial role as a carbon source. It's important to note that pretreatment is essential, but it's not always necessary, depending on the desired outcome. These findings demonstrate that seemingly useless sugar waste can be transformed into valuable products like biofuels, chemicals, immobilization agents, and biomass. These solutions can be implemented in sugar factories across the Kyrgyz Republic.

Table 1. *List of some value-added products using sugar beet byproducts as a fermentation substrate.*

Sugar beet wastes	Pretreatment	Pretreatment process	Method	Microorganism/Inoculum	Obtained value-added product	Ref.
Sugar beet molasses	No		Fermentation/three batch cultures	*Bacillus amyloliquefaciens* TUL 308	2,3-butanediol	[10]
SBP	Yes	Drying and milling to a powder	Submerged fermentation (static culture)	*Aspergillus niger, Paecilomyces variotii*	Endo-polygalacturonase	[16]
Sugar beet molases/distillery stillage	No	Sugar beet molasses were used as modified MRS media	Batch cultures, with shaking and under anaerobic conditions	*Lacticaseibacillus paracasei* NRRL B-4564	Lactic acid	[28]
SBP/sugar beet molasses	Yes	Drying	Semisolid state fermentation	*Aspergillus niger* NRRL-3	Gluconic acid	[14]
Sugar beet molasses	No		Fermentation in flasks	*Pseudomonas spp.*	Rhamnolipid biosurfactant	[17]
Sugar-beet pulp	Yes	Autohydrolysis at pH 4 (120 °C, 6% SBP (w/w), 5 minutes)	ABE fermentation (anaerobic fermentation)	*Clostridium beijerinckii*	Acetone, butanol	[8]
Sugar beet molasses	No		Single stage photofermentation (anaerobic conditions)	*Rhodobacter capsulatus* JP91	Hydrogen	[19]
SBP, sugar beet molasses	No		Anaerobic codigestion	Inoc1-municipal solid waste, Inoc2- the effluent from the reactor of single digestion	Methane	[20]
SBP, wastewater	Yes	Physical pretreatment/SBP was dried and homogenized to powder	Anaerobic mesophilic codigestion	Anaerobic seed culture from the municipal wastewater treatment plant	Methane	[36]
SBP	Yes	Dilute acid pretreatment and Enzymatic hydrolysis	SSF (solid-state fermentation)	*E. coli* KO11	Fuel ethanol	[21]
SBP	Yes	Enzymatically depolymerization	Bioethanol fermentation, anaerobic digestion, dark fermentation	*Saccharomyces cerevisiae* Ethanol Red, and *Scheffersomyces stipitis*/Sewage sludge	Bioethanol, methane, hydrogen	[39]
SBP	Yes	Anaerobic digestion dairy manure	Nonairtight fermentation	*Chlorella* seeds	*Chlorella*	[22]
Sugar beet vinasse	No		Fermentation in a vertical airlift tubular photobioreactor	*Spirulina platensis*	Single cell protein	[23]
SBP	Yes	Enzymatic hydrolysis	Fed-batch cultivation	*Candida tropicalis* LOCK 0007	Single cell protein	[6]
SBP	Yes	Drying	Repeated batch ethanol fermentation	*Saccharomyces cerivisiae*	Bioethanol	[24]
SBP/sugar beet molasses	Yes	Alkaline pretreatment with NaOH of SBP	Fermentation in Erlenmeyer flasks	*Leuconostoc mesenteroides T3*	Dextransucrase (DS)	[46]

References

[1]. Cheesman O. D., "History of sugar production", in Environmental Impacts of Sugar Production the Cultivation and Processing of Sugarcane and Sugar Beet. Cambridge, MA: CABI, 2004, pp. 2.

[2]. Biancardi E., "Sugar beet", in Root and tuber crops, McGrath J. M., Panella L. W., Lewellen R. T., Stevanato, P., 1st ed. New York: Springer, 2010, pp. 173-219.

[3]. European Commission, "Agriculture and rural development," in Crop productions and plant-based products: https://agriculture.ec.europa.eu/farming/crop-productions-and-plant-based-products/sugar_en

[4]. Lange C., Holtgräwe D., Schulz B., Weisshaar B., Himmelbauer, H., "Construction and characterization of a sugar beet (Beta vulgaris) fosmid library", Genome, 51 (2008), pp. 948-951.

[5]. FAO statistical database: Sugar beet production in Poland in 2012

[6]. Patelski P., Berlowska J., Dziugan P., Pielech-Przybylska K., Balcerek M., Dziekonska U., Kalinowska H., "Utilization of sugar beet bagasse for the biosynthesis of yeast SCP", Journal of Food Engineering, 167 (2015), pp. 32-37.

[7]. FAO Investment Centre Division, "Sugar Beet White Sugar". Rome, Italy: Agribusiness handbook, 2009, pp. 9-14.

[8]. Bellido C., Infante C., Coca M., González-Benito G., Lucas S., García-Cubero M. T., "Efficient acetone–butanol–ethanol production by Clostridium beijerinckii from sugar beet pulp", Bioresource technology, 190 (2015), pp. 332-338.

[9]. Habeeb A. A. M., Gad A. E., El-Tarabany A. A., Mustafa M. M., Atta M. A. A., "Using of sugar beet pulp by-product in farm animals feeding", International Journal of Scientific Research in Science and Technology, 3 (2017), pp. 107-120.

[10]. Sikora B., Kubik C., Kalinowska H., Gromek E., Białkowska A., Jędrzejczak-Krzepkowska M., Turkiewicz M., "Application of byproducts from food processing for production of 2,3-butanediol using Bacillus amyloliquefaciens TUL 308", Preparative Biochemistry and Biotechnology, 46 (2016), pp. 610-619.

[11]. Duraisam R., Salelgn K., Berekete, A. K., "Production of beet sugar and bioethanol from sugar beet and it bagasse: a review", International Journal of Engineering Trends and Technology, 43(2017), pp. 222-233.

[12]. FAO, "Food wastage footprint Impacts on natural resources", Summary report, 2013, https://www.fao.org/news/story/en/item/196402/icode/

[13]. Vaccari G., Tamburini E., Sgualdino G., Urbaniec K., Klemeš J., "Overview of the environmental problems in beet sugar processing: possible solutions", Journal of Cleaner Production, 13 (2005), pp. 499-507.

[14]. Kelleci K., Altundoğan H. S., Tanyıldızı M. Ş., "Valorization of Beet-Processing Sugar Factory by-Products for in situ Gluconic Acid Production by using Aspergillus Niger Fermentation", Sugar Tech (2022), pp. 410–421.

[15]. Marzo C., Díaz A. B., Caro I., & Blandino A., "Valorization of fungal hydrolysates of exhausted sugar beet pulp for lactic acid production", Journal of the Science of Food and Agriculture, 101(2021), pp. 4108-4117.

[16]. Almowallad S. A., Aljobair M. O., Alkuraieef A. N., Aljahani A. H., Alsuhaibani A. M., Alsayadi M. M., "Utilization of agro-industrial orange peel and sugar beet pulp wastes for fungal endo-polygalacturonase production", Saudi Journal of Biological Sciences, 29(2022), pp. 963-969.

[17]. Onbasli D., Aslim B., "Biosurfactant production in sugar beet molasses by some *Pseudomonas spp*.", Journal of Environmental Biology, 30 (2009), pp. 161-163.

[18]. Berlowska J., Binczarski M., Dudkiewicz M., Kalinowska H., Witonska I. A., Stanishevsky A. V., "A low-cost method for obtaining high-value biobased propylene glycol from sugar beet pulp", RSC Advances, 5 (2015), pp. 2299-2304.

[19]. Keskin T., Hallenbeck P. C., "Hydrogen production from sugar industry wastes using single-stage photofermentation", Bioresource Technology, 112 (2012), pp. 131-136.

[20]. Aboudi K., Gómez-Quiroga X., Álvarez-Gallego C. J., Romero-García L. I., "Insights into anaerobic codigestion of lignocellulosic biomass (sugar beet byproducts) and animal manure in long-term semicontinuous assays", Applied Sciences, 10 (2020), pp. 5126.

[21]. Zheng Y., Lee C., Yu C., Cheng Y. S., Zhang R., Jenkins B. M., VanderGheynst, J. S., "Dilute acid pretreatment and fermentation of sugar beet pulp to ethanol", Applied Energy, 105 (2013), pp. 1-7.

[22]. Wang L., Chen L., Wu S. X., Ye J., "Nonairtight fermentation of sugar beet pulp with anaerobically digested dairy manure to provide acid-rich hydrolysate for mixotrophic microalgae cultivation", Bioresource technology, 278 (2019), pp. 175-179.

[23]. Coca M., Barrocal V. M., Lucas S., González-Benito G., García-Cubero M. T., "Protein production in Spirulina platensis biomass using beet vinasse-supplemented culture media", Food and Bioproducts Processing, 94 (2015), pp. 306-312.

[24]. Vučurović V. M., Razmovski R. N. (2012). "Sugar beet pulp as support for Saccharomyces cerivisiae immobilization in bioethanol production", Industrial Crops and Products, 39 (2012), pp. 128-134.

[25]. Retrieved May 31, 2023, from http://stat.kg/

[26]. Прахова М. С., Выборнова Т. В., Шарова, Н. Ю., "Биосинтез лимонной и глюконовой кислот микромицетом Aspergillus niger", Сборник: Научное обеспечение инновационных технологий производства и хранения сельскохозяйственной и пищевой продукции, (2014), стр. 94-98. / Praxova M. S., Vjbornova T. V., SHarova, N. YU., "Biosintez limonnoy i glükonovoy kislot mikromicetom Aspergillusniger", Sbornik: Nauchnoe obespechenie innovacionnjx texnologiy proizvodstva i xraneniq sel'skoxozqystvennoy i piwevoy produkcii, (2014), str. 94-98.

[27]. Chahal S. P., Starr J. N., "Lactic acid", Ullmann's encyclopedia of industrial chemistry, 20 (2000), pp. 219-225.

[28]. Mladenović D. D., Djukić-Vuković A. P., Kocić-Tanackov S. D., Pejin J. D., Mojović, L. V., "Lactic acid production on a combined distillery stillage and sugar beet molasses substrate", Journal of Chemical Technology & Biotechnology, 91(2016), pp. 2474-2479.

[29]. Helmy Q., Gustiani S., Mustikawati A. T., "Application of rhamnolipid biosurfactant for biodetergent formulation", in IOP Conference Series: Materials Science and Engineering (Vol. 823, No. 1, p. 012014), 2020, April, pp. 1-7.

[30]. Białkowska A. M., "Strategies for efficient and economical 2,3-butanediol production: new trends in this field", World Journal of Microbiology and Biotechnology, 32 (2016), pp. 1-14.

[31]. Sen B., Aravind J., Kanmani P., Lay C. H., "State of the art and future concept of food waste fermentation to bioenergy", Renewable and Sustainable Energy Reviews, 53 (2016), pp. 547-557.

[32]. Huang W. C., Ramey D. E., Yang, S. T., "Continuous production of butanol by *Clostridium acetobutylicum* immobilized in a fibrous bed bioreactor", Applied Biochemistry and Biotechnology, 115 (2004), pp. 887-898.

[33]. Zhu G., Liu C., Li J., Ren N., Liu L., Huang, X., "Fermentative hydrogen production from beet sugar factory wastewater treatment in a continuous stirred tank reactor using anaerobic mixed consortia", Frontiers of Environmental Science & Engineering, *7*(2013), pp. 143-150.

[34]. Nandi R., Sengupta S., "Microbial production of hydrogen: an overview", Critical reviews in microbiology, 24(1998), pp. 61-84.

[35]. Buekens A., "Energy recovery from residual waste by means of anaerobic digestion technologies", In Conference: "The future of residual waste management in Europe", 2005, November, pp. 17-18.

[36]. Alkaya E., Demirer, G. N., "Anaerobic mesophilic codigestion of sugar-beet processing wastewater and beet-pulp in batch reactors", *Renewable Energy*, *36* (2011), pp. 971-975.

[37]. Vučurović D., Bajić B., Vučurović V., Jevtić-Mučibabić R., & Dodić, S., "Bioethanol Production from Spent Sugar Beet Pulp—Process Modeling and Cost Analysis", MDPI, Fermentation, 8 (2022), pp. 114.

[38]. Zheng Y., Yu C., Cheng Y. S., Lee C., Simmons C. W., Dooley T. M., VanderGheynst J. S., "Integrating sugar beet pulp storage, hydrolysis and fermentation for fuel ethanol production", Applied Energy, 93 (2012), pp. 168-175.

[39]. Berlowska J., Pielech-Przybylska K., Balcerek M., Cieciura W., Borowski S., Kregiel D., "Integrated bioethanol fermentation/anaerobic digestion for valorization of sugar beet pulp", Energies, 10 (2017), pp. 1255.

[40]. Silva J., Alves C., Pinteus S., Reboleira J., Pedrosa R., Bernardino S., "Chlorella", in Nonvitamin and nonmineral nutritional supplements, Academic Press, (2019), pp. 187-193.

[41]. Katiyar R., Gurjar B. R., Biswas S., Pruthi V., Kumar N., Kumar, P., "Microalgae: an emerging source of energy based bioproducts and a solution for environmental issues", Renewable and Sustainable Energy Reviews, 72 (2017), pp. 1083-1093.

[42]. Madejón E., López R., Murillo J. M., Cabrera F., "Agricultural use of three (sugar-beet) vinasse composts: effect on crops and chemical properties of a Cambisol soil in the Guadalquivir river valley (SW Spain)", Agriculture, ecosystems & environment, 84 (2001), pp. 55-65.

[43]. Ravindra P., "Value-added food: Single cell protein", Biotechnology advances, 18 (2000), pp. 459-479.

[44]. Tampion J., Tampion M. D., "Immobilized cells: principles and applications", Cambridge University Press, 5, (1987), pp. 1.

[45]. Lapponi M. J., Méndez M. B., Trelles J. A., Rivero C. W., "Cell immobilization strategies for biotransformations". *Current Opinion in Green and Sustainable Chemistry, 33 (2022)*, pp. 100565.

[46]. Miljković M. G., Davidović S. Z., Carević M. B., Veljović Đ. N., Mladenović D. D., Rajilić-Stojanović M. D., Dimitrijević-Branković S. I., "Sugar beet pulp as *Leuconostoc mesenteroides* T3 support for enhanced dextransucrase production on molasses", Applied biochemistry and biotechnology, 180 (2016), pp. 1016-1027.

[47]. Naessens M., Cerdobbel A. N., Soetaert W., Vandamme E. J., "*Leuconostoc dextransucrase* and *dextran*: production, properties and applications", Journal of Chemical Technology & Biotechnology: International Research in Process, Environmental & Clean Technology, 80 (2005), pp. 845-860.

MANAS Journal of Engineering
ISSN 1694-7398 | e-ISSN 1694-7398

Volume 11, Issue 1, (2023) Pages 145-153
https://doi.org/10.51354/mjen.1288413

Antibiotic residuals removal via novel fabricated hydrogel from 2-hydroxyethyl methacrylate and sodium methacrylate

Urmat Zholdoshbek uulu[1,*], Sinan Akgol[2], Nahit Aktas[1]

[1] Kyrgyz-Turkish Manas University, Faculty of Engineering, Department of Chemical Engineering, Bishkek, Kyrgyzstan, 2151y05003@manas.edu.kg, ORCID: 0009-0007-2219-8870

[2] Ege University, Faculty of Science, Department of Biochemistry, Izmir, Turkey.

ABSTRACT

In this study, poly(2-hydroxyethyl-sodium methacrylate) (p(HEMA-SMA)) hydrogels were synthesized as a novel adsorbent to remove antibiotic residues from environmental samples. [p(HEMA-SMA)] co-polymers were synthesized by the free radical photopolymerization method. Synthesized hydrogels were characterized by different methods such as Fourier-transform infrared spectroscopy (FTIR), elemental and scanning electron microscope (SEM), and surface area calculations. The average size surface area of the synthesized hydrogels were 1.515 µm. Penicillin G (Pen. G) was used as the sample antibiotic for the adsorption process. The absorption of the drugs was studied under different environmental conditions. Medium pH, temperature, and hydrogel concentration were varied to achieve the highest absorption. The specific adsorption value (Qmax) of p(HEMA-SMA) copolymers was found 303.03mg/g for Penicillin G at the 0,35 mg/mL of initial Pen. G concentration. In conclusion, we suggest a novel microstructure, selective, low-cost adsorption polymeric material for the removal of Pen. G as the template antibiotic.

ARTICLE INFO

Technical Brief

Received: 28.04.2023
Accepted: 23.05.2023

Keywords:
removal of penicillin G,
copolymer,
sorption isotherm

**Corresponding Author*

1. Introduction

Antibiotics are secondary metabolites or semi-synthetic or synthetic derivatives that can inhibit or kill pathogenic microorganisms. According to the classification based on their chemical structure, β-lactam antibiotics, macrolides, aminoglycoside, and tetracycline are the four main antibiotic groups. β-lactam antibiotics are the most extensively used for antibacterial activity with low side effects. β-lactam antibiotics involve in carbapenem, Pen.G, monobactams, andcephalosporins. β-lactam antibiotics have a common ring structure [16].

Pen. G is one of the most commonly used β-lactam antibiotics, which is used effectively for the prevention and treatment of bacterial infection. The versatility of Pen. G has made it a choice for many applications, including agriculture and human health. However, the widespread use of antibiotics in animal husbandry may lead to residues in food which can stimulate allergic reactions in some hypersensitive individuals [17][25].

Antibiotics are rapidly losing their potency due to overuse or wrong use in human and animal health, known as antibiotic resistance. There are three major mechanisms in bacteria that make themselves resistant to β-lactam antibiotics. The first mechanism of β-lactam resistance is the production of β-lactamase which degrades β-lactam antibiotics before they reach the targets. The third mechanism is to prevent the β-lactam antibiotic from reaching the target by altering the permeability of the outer membrane or increasing the efflux pump activity [16]. Antibiotics were used as antimicrobial drug and as a result of unnecessary, wrong, and excessive antibiotic using, through the pharmaceutical companies, hospitals, and municipal waste, many antibiotics waste passes the environment and water [6]. Antibiotic residues in environment may also be responsible for the increase of the risk of development and spread of antibiotic resistance, posing a potential threat to public health, since they can be released into the environment after their application [14]. Therefore, it is important to minimize the inappropriate use of antibiotics and to detect the antibiotic residues in wastewater, and animal products such as milk, meat, and eggs [20].

In recent years, antibiotics have been detected in the effluent of pharmaceutical companies and hospitals, municipal wastewater, surface water, and groundwater. For the

determination of samples, liquid and mass chromatograhy techniques are frequently used [11][22]. In order to protect the public health, a rapid, accurate, and specific method is requested for the isolation and determination of penicillin G in food such as milk and environmental water [19][23][1].

In the current study, microstructure, selective, lowcost molecularly adsorption polymeric systems were produced using Pen.G as a template molecule for leading to improved away from the antibiotics. Firstly, Pen.G adsorption poly (2-hydroxyethyl methacrylate-sodium methacrylate) hydrogels were prepared by photopolymerization method.

Fourier-transform infrared spectroscopy (FTIR), elemental analysis, scanning electron microscopy (SEM), and surface area calculations were used for the characterization of hydrogels. Optimization studies of penicillin G adsorption on p(HEMA-SMA) hydrogels was investigated at different conditions and adsorption isotherms were calculated. Selectivity, specificity, and reusability studies were performed. According to all those interrelationships, we aimed to develop a nanomaterial that can be used for several purpose such as determination, purification and removal of Pen. G.

2. Materials and method

2.1. Materials

Pen.G, was obtained from biochemistry department at Ege University. In addition, 2-hydroxyethyl methacrylate (HEMA), sodium methacrylate (SMA) ethylene glycol di-methacrylate (EGDMA), 2,2-Dimethoxy-2-phenylacetone-phenone (DMPA) and other chemicals were obtained from Sigma Chemical Co (st.louis, USA).

2.2. Synthesis p(HEMA-SMA) copolymer.

Prior to the polymerization process, the template HEMA (2.5 mL), SMA (100 mg in 2 mL DW), and EGDMA (0.1 mL) were mixed in 50 mL bottom flat flaks for 5 min. Then, 5.4 mL of DMPA(25 mg) solution added the mixture as the initiator in the beaker to initiate the polymerization reaction. The flask was kept under the ultraviolet and polymer formation was observed in 3-5 min [15].

The prepared hydrogels were washed several times with deionized water. After washing, it was dryed at 30 °C in the oven for 24 hours and stored for further utilization. was used as an adsorption agent so that the template molecule of Pen.G, could be removed from the hydrogel structure at 6 h. This treatment was continued until the penicillin G could not be determined in the adsorption solution [5][4],**Ошибка! Источник ссылки не найден.**,[9] (Eq. (1)):

$$\text{Removal of penicillin G \%} = \frac{C_i - C_f}{C_i} * 100 \quad (1)$$

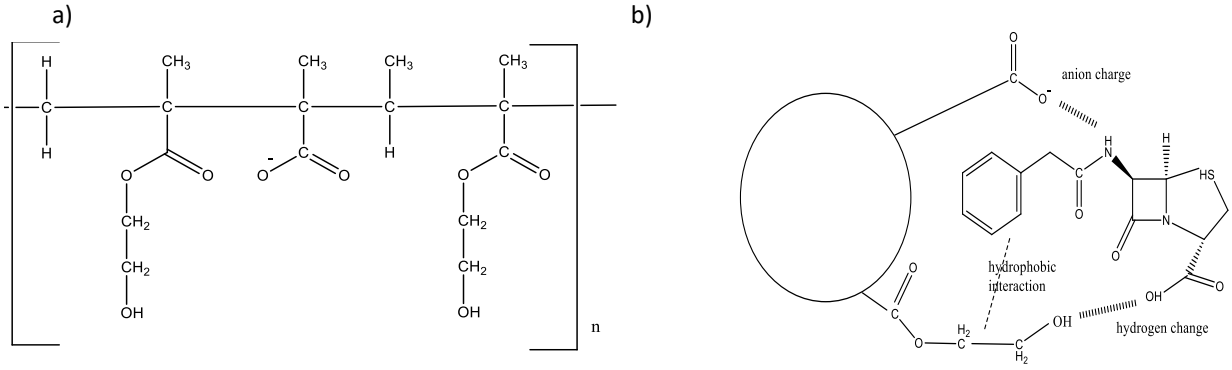

Figure 1. *a Molecular structure of p(HEMA-SMA).b. Penicillin G adsorption of p(HEMA-SMA) copolymer*.

C_{inital} initial concentration of penicillin G (ppm)

C_{final} the remaining amount of Penicillin G

Characteriation of penicillin G adsorption p(HEMA-MA) copolymers.For the chracterization of penicillin G adsorption p(HEMA-SMA) copolymers, SEM, FT-IR, elemental analysis, and surface area calculations were performed. Adsobtion studies of penicillin G p(HEMA-SMA) copolymers.

Pen.G adsorption on the p(HEMA-SMA) hydrogels were investigated with different parameters. The effects of time, pH, the initial Pen. G concentration, and temperature on adsorption were also investigated. For this reason, the initial concentration of Pen. G was changed between 100 and 350 ppm, and the pH of the solution was also changed between 2.0 and 12. For investigating of the effect of time, the experiments were performed in the range of 0 and 300 min and the experiments for the effect of temperature were studied in the range of 4 °C and 55 °C. At the end of the equilibrium time, the hydrogels were removed from the solutions with centrifugation. The adsorption amount of Pen. G was obtained by measuring the difference between the initial and the final Pen G concentration in the solution with UV spectrophotometry analysis (Fig. 2).

Pen.G measurements were monitored with UV-vis spectrophotometer analysis and 290 nm wavelength in UV-vis spectrophotometer detector was selected. The calibration graph was prepared in standard solutions (in water) at a range of 100 to 350 ppm.

The Q values were calculated with the following equation (Eq. (2)). It also should be noticed that all adsorption curves are averages of at least triplicated experiments.

$$Q=[\frac{(C_i-C_f)}{m}]*V \quad [\frac{Pen.G\ (mg)}{dry\ hydrogel\ (g)}] \tag{2}$$

Q is the hydrogel adsorption capacity of Pen. G on p(HEMA-SMA) hydrogels (mg/g), C_i is the initial concentrations of Pen. G in the solution (ppm), C_f is the final concentration of Pen. G in the solution (ppm), and V is the volume of the aqueous phase (mL). The calibration curve was prepared with the Pen. G solution concentration between 100 and 350 ppm.

2.4. Adsorption isotherms

Adsorption isotherm is used to characterize the interaction of each molecule with the adsorbent. The adsorption isotherm provides an association between the concentration of molecules in the solution and the amount of adsorbed molecules in the solid phase when the two phases are in equilibrium. In this context, Langmuir and Freundlich adsorption isotherms were calculated.

The Langmuir adsorption model assumes that there is a certain number of defined adsorption sites, each of which is capable of binding only one molecule. It is assumed that the energy levels of these regions are equal and far away from each other by the adsorbed molecules. The Langmuir adsorption model is defined as follows (Eq. (3)):

$$Q=\frac{Q_{max}bC_d}{(1+bC_d)} \tag{3}$$

Here, Q is the amount of Pen. G removed (mg/g), C_d is the equilibrium concentration (mg/L), b is the Langmuir constant (mL/mg), and Q_{max} is the maximum adsorption capacity (mg/g). By linearizing of the equations,

$$Q = [\frac{1}{Q_{max}}] = [\frac{1}{Q_{max}b}](\frac{1}{C_d}) \tag{4}$$

equality is achieved. When $[1/C_d]$ is plotted against to $[1/Q]$, the y axis of the line gives the cut point $[1/Q_{max}]$ and the slope of the line gives $1/Q_{max}.b$.

The Freundlich adsorption model, which is another commenly used adsorption model, accepts the exponential adsorption system in contrast to the Langmuir adsorption model. After the initial surface adsorption, it shows the strong soluble-soluble interaction with the condensation effect.

The Freundlich adsorption model is defined as (Eq. (5)):

$$Q = K_F C_{eq}(\frac{1}{n}) \tag{5}$$

Here, K_F and n are the Freundlich constants. $1/n$ indicates the surface heterogeneity and takes values ranging from 0 to 1. K_F, Freundlich constant. The adsorption constant, which indicates the size of the adsorption capacity, depends on the temperature, the adsorbent, and the adsorbed compound. n, Freundlich constant, is degree of adsorption which shows the severity of adsorption. As the value approaches, surface heterogeneity increases [21], [7] [2]. By linearizing the logarithm of the equations:

$$\ln Q=\ln K_F+(\frac{1}{n})\ln C_{eq} \tag{6}$$

equality is achieved. When $\ln C_{eq}$ is plotted against $\ln Q$, $\ln K_F$ is the value ofcut off point of the y-axis and (1/n) is the value of slope of the line.

The Temkin isotherm assumes linear decrease of heat adsorption while ignoring extremely low and very high concentration. It also assumes uniform distribution of bounding energy up to some maximum bonding energy. It is expressed by Eq. (7) below.

$$q_e=(\frac{RT}{b})\ln AT+(\frac{RT}{b})\ln C_e \tag{7}$$

where q_e is the amount of adsorbate adsorbed at equilibrium (mg/g), C_e is concentration of adsorbate in solution at equilibrium (mg/L).

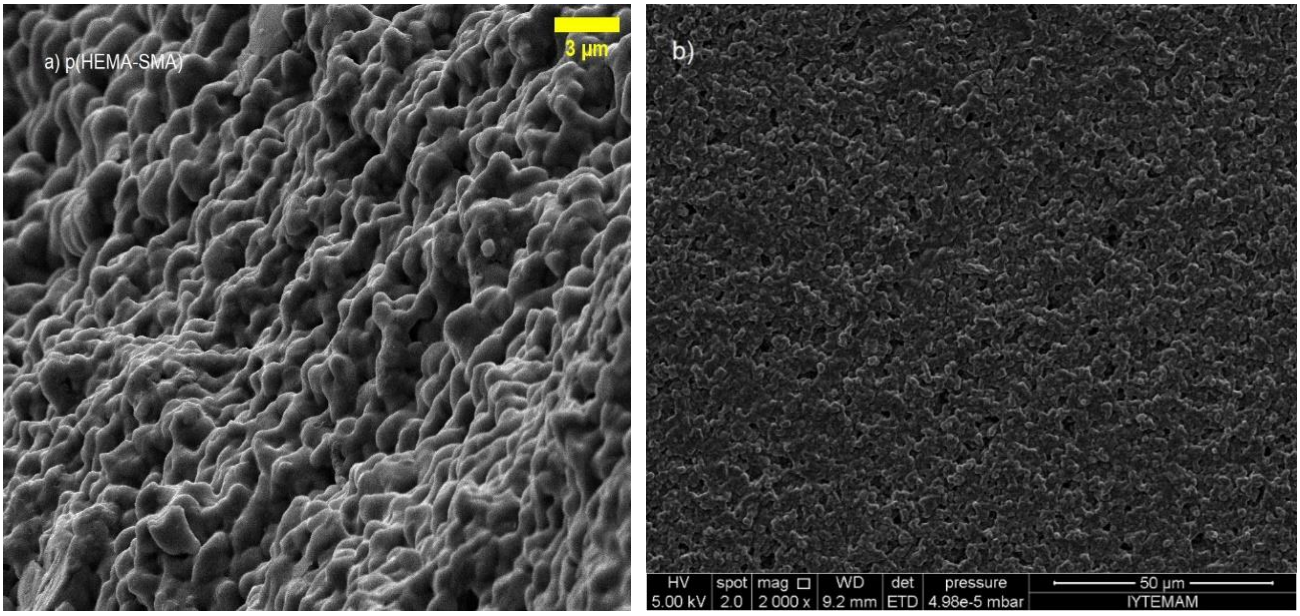

Figure 2. *The SEM images of the p(HEMA-SMA) copolymers with (in the scale of 3 µm), b (in the scale of 50 µm)*

B is a constant related to the heat of adsorption and it is defined by the expression B = RT/*b*, *b* is the Temkin constant (J/mol), *T* is the absolute temperature (K), *R* is the gas constant (8.314 J/ mol K), and *A* is the Temkin isotherm constant (L/g). From the plot of q_e vs. lnCe, *B* and *A* can be calculated from the slopes (*B*) and intercepts (BlnA) respectively [10].

3. Results

Adsorption yield of the Pen. G p (HEMA-SMA) copolymer.

After adsorption at 6 hr, temperature 40 °C removal of Pen. G 69%, utilizing the equation (Eq. (1)).

Characterization of p(HEMA-SMA) copolymers.

In this study p(HEMA-SMA) copolymers were characterized using FTIR, elemental and SEM, and surface area calculations.

The morphological structure of p(HEMA-SMA) copolimers was determined by SEM. As shown in Fig. 2, penicillin p(HEMA-SMA) hydrogels include spherical particles.

As seen in the FTIR spectrum (Fig. 3), the p(HEMA) (A) and p(HEMA-SMA) (B) structures have characteristic hydrogen-bonded alcohol, -OH,

tensile vibration band around 3451 cm−1. By way of the incorporation of the SMA monomer into the polymer structure, the intensity of the tensile vibration band of the hydrogen-bonded alcohol, OH, increased according to the p(HEMA). This may be due to the fact that -C-O^- stretching vibrations in the structure of the p (HEMA-SMA) copolymer also have vibrations around 3300– 3400 cm−1. FTIR spectrum of the p(HEMA-SMA) has -C-O^- stretching vibrations around (1277-1160) cm^{-1}. However, this vibration is not seen in the FTIR spectrum of p(HEMA). This is also an indication that the SMA co-monomer incorporate into the polymer structure. In addition, the extra -C═O groups from the SMA monomer in the p(HEMA-SMA) structure caused the -C═O stretching vibration observed around 1728 cm^{-1} in the p(HEMA-SMA) structures severely.

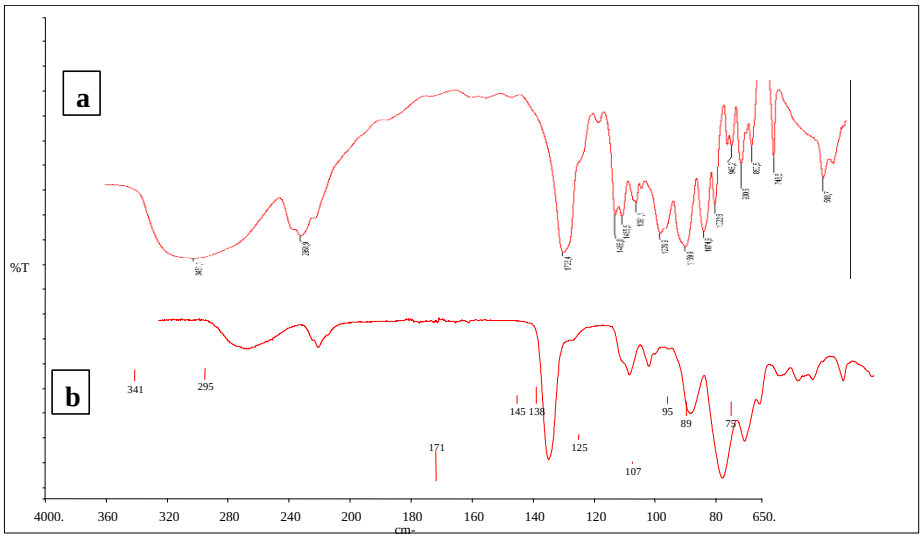

Figure 3. *FTIR spectra of p(HEMA-SMA) copolymer, b p(HEMA) co-polymers.*

The time-dependent Pen.G adsorption on p(HEMA-SMA) copolymers was shown in Fig. 1b. As seen from Fig. 6, the adsorption amount of Pen.G was increased by the time of progress, and the saturation levels were reached within 300 min. Also, the maximum adsorption of Pen.G was found as 29.93 mg/g. The effect of the initial concentration of penicillin G on the adsorption of Pen.G on the copolymer is given in Fig. 7. As seen from the graph, the amount of Pen.G adsorbed per unit mass by the micropolymers increased with increasing concentration of Pen.G in the solution. Also, at a concentration of about 350 ppm Pen.G, it reached a high adsorption capacity. In addition, 29.93 mg/g Pen.G adsorption at the initial concentration of 0.350 mg/mL penicillin G per unit mass of the p(HEMA-SMA) copolymer is associated surface area of the microstructure.

Also, the homogeneous distribution of molecular specific wells to Pen.G and the anionic character of the SMA functional monomer significantly increased the Pen.G adsorption of the copolymer by increasing the affinity to Pen.G.

Increasing the initial concentration of Pen.G raises the concentration difference (ΔC), which is the driving force for adsorption. Furthermore, Pen.G adsorption capacity is also increased by the increase of the driving force.

When the concentration-dependent adsorption curve is examined, it appears that the adsorption is compatible with the Freundlich model. The Freundlich isotherm is derived by assuming exponentially increasing adsorption, with adsorption where the hydrophobic interaction predominates, and multiple adsorption behavior is expected [21].

The change in adsorption capacity of the Pen.G copolymer is given in Fig. 6. The effect of Pen.G adsorption on the temperature was studied at (4–55) °C. It was observed that from the obtained graph, the Pen.G adsorption capacity of the co-polymer increased until 40 °C with increasing temperature values.

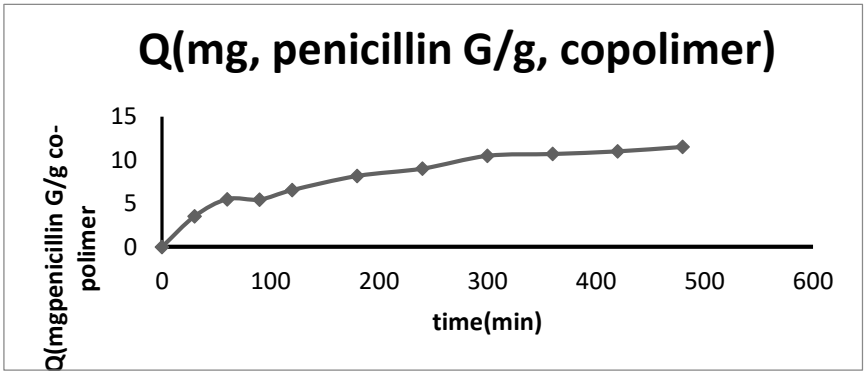

Figure 4. *The effect of time on Pen.G adsorption ($C_{initial}$: 350ppm Pen G; pH= 2.0 acid buffer; 20 °C)*

According to the [ΔG = (ΔH-TΔS)] theory, the interaction increases with temperature. Where ΔH can be positive or negative, control of ΔG is achieved by a positive entropy change. For this, increasing entropy is achieved with heat. However, there are also weak interactions with hydroxyl groups on the HEMA surface, such as hydrogen bonds and van der Waals interactions. The van der Waals interaction forces seen in hydrophobic interactions have also been observed in other studies that have been associated with increased temperature [8]. With this theory, the raising Pen. G adsorption of the co-polymer with increasing temperature up to a certain temperature can be explained. However, penicillin G adsorption is decreased at high temperatures after 40 °C. It is known that the lactam ring of beta-lactam antibiotics is chemically very unstable and is not resistant to acid, temperature, and beta-lactamase enzyme [26].

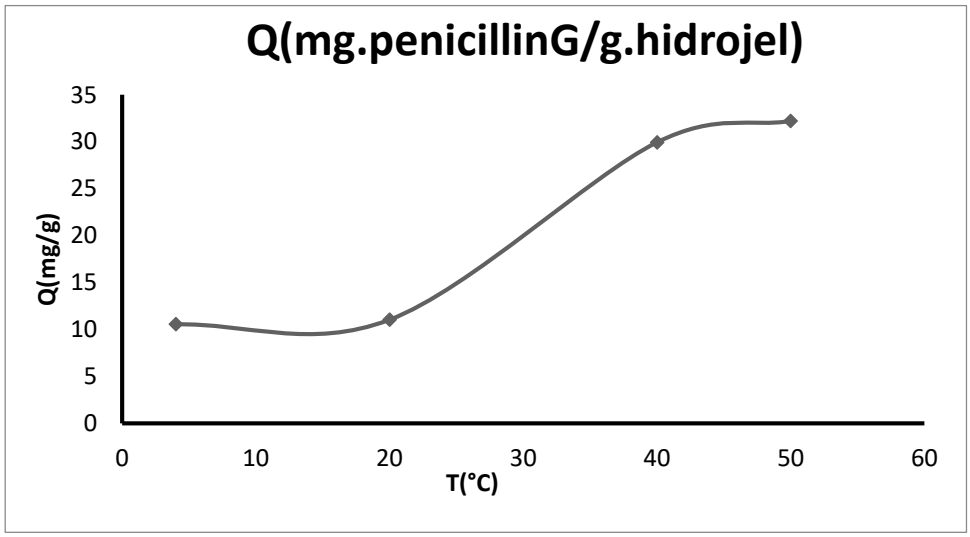

Figure 5. *The effect of initial concentration on Pen G adsorption (pH = 2.0 acid buffer; 20 °C; 300 min)*

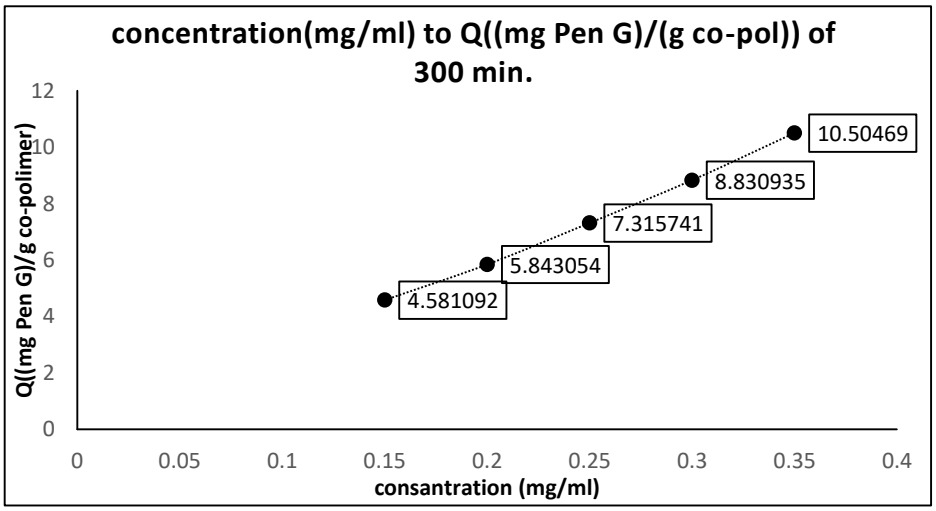

Figure 6. *Effect of temperature on Pen G adsorption ($C_{initial}$: 0.35 mg/mL Pen G; pH=2.0 ortho-phosphoric acid buffer; 300 min)*

In connection with this, the decrease in adsorption of penicillin G in the copolymer is significant due to the β-lactam ring which may be unstable and degradable at high temperatures.

As a result, shown in the graph, the effect of temperature change on penicillin G adsorption of the copolymer can be supported thermodynamically.

The apparent increase in penicillin G adsorption capacity on synthesized copolymers with increasing temperature and followed by a decrease in adsorption by degradation of penicillin G structure at high temperatures indicates and supports binding between the hydrophobic ligand alanine and penicillin G. The apparent increase in penicillin G adsorption capacity on synthesized co-polymers with increasing

temperature and followed by an increase in adsorption of penicillin G at high temperatures indicates and supports binding between the hydrophobic ligand alanine and penicillin G.

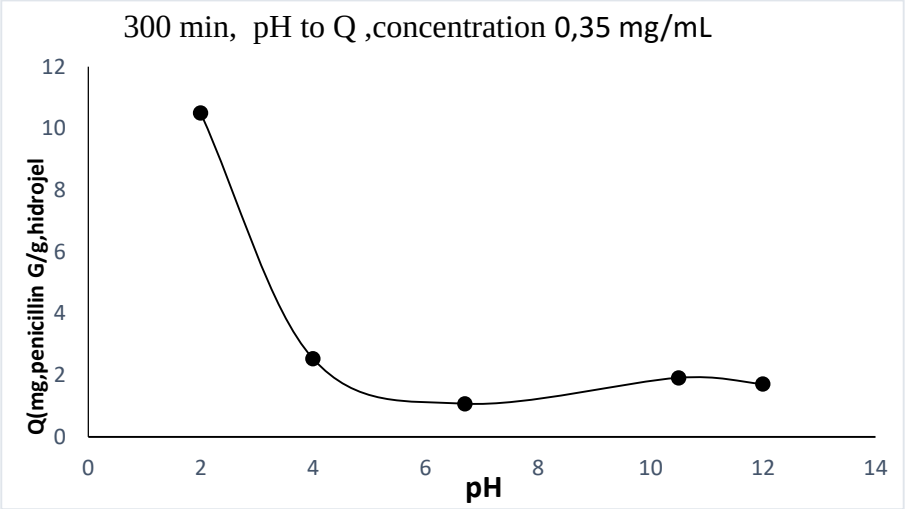

Figure 7. *Effect of pH on Pen G adsorption ($C_{initial}$: 0,35 mg/mL; pH 2.0, 4.0, 6.7,10.5,12.0 ortho-phosphoric acid buffer, 20 °C; 300 min*)

3.1. Adsorption isotherms

The adsorption isotherm of the penicillin G p(HEMA-SMA) copolymer was determined from the initial adsorption effect of penicillin G concentration. The results of the calculations show that the correlation value R^2 = 0.9948 indicates that the adsorption corresponds to the Freundlich adsorption model.

When the concentration-dependent adsorption curve is examined, it is seen that the adsorption is compatible with the Freundlich model. The classical Freundlich adsorption model accepts the exponential adsorption system as opposed to the Langmuir adsorption model. After the initial surface adsorption, it exhibits a strong solute-solute interaction with the condensation effect. The Freundlich isotherm is derived assuming an exponential increasing adsorption, in other words, multiphase adsorption behavior is expected for

As seen in Fig. 7, penicillin G adsorption of p(HEMA-SMA) co-polymer is pH dependent. Penicillin G adsorption capacity of the co-polymer increases as the acidic region moves to the basic region. The maximum penicillin G adsorption was found to be 10.50 mg/g in pH 2.0 ortho-phosphoric acid buffer. heterogeneous amorphous surfaces [21] [2]. The 1/n coefficient in the equation shows this feature. There is heterogeneous distribution of discrete interaction regions.

Freundlich equation is an exponential function of the amount of adsorbent adsorbed on the adsorbent surface. The Freundlich isotherm is generally used for adsorption from liquid solutions. Freundlich isotherm is based on approaches and can be thought of as the sum of the distributions of Langmuir adsorption isotherms. Freundlich isoterm does not predict saturation of the bonding surface by solvated [3], [7].

Adsorption of antibiotics, steroids, and hormones onto commonly used adsorbents follows this isotherm. Reversed phase and hydrophobic interaction type adsorption are usually followed by Freundlich type isotherm. Like the Langmuir equation, the Freundlich isotherm equation does not apply Henry's law at low concentrations and a stable constant adsorbent value cannot be obtained after equilibration [18]. In the initial

Table 1. *Langmuir, Freundlich and Temkin adsorption isotherm constants*

experimental	**Langmuir constants**			**Freundlich costants**			**Temkin costants**			**Shape of izotherm**
Q_{ex}(mg/g)	Q_{max}(mg/g	b(ml/mg)	R^2	K_f	n	R^2	A(L/g)	B(j/mol)	R^2	0<R<1
29.93	303.03	0.0033	0.9933	0.04709	1.0098	0.9948	1.00	347.435	0.9761	

4. Conclusions

In this study, a HEMA-based micro-size, the highly selective, environmentally friendly, and cost-effective polymeric system has been developed for the first time in the literature. These copolymers have the potential to use direct determination and purification of penicillin G which is widely used for antimicrobial agents or growth factors in animal breeding from environmental wastes and food products. Antibiotic residue analysis is a problem in countries in terms of public health. In this study, the synthesized copolymer, which has a molecular memory, can be used to separate, purify, and determine the target molecule penicillin G from environmental wastes and food products. Moreover, the copolymer provides reasonable specificity, ease, reliability, and quick response to the specific molecule. This polymeric system is a convenient method with high adsorption capacity, allowing easy and rapid analysis without the need for a ligand system. In this context, it is necessary to use only the advantageous aspects of the use of antibiotics which is an integral part of public health to detect the essential removal of adverse effects and to minimize antibiotic residues in environmental pollution. The synthesized copolymers can provide a promising method for control of the different pharmaceutical residues caused by the use of high doses of antibiotics.

(Table 1). Temkin equation is excellent for predicting the gasphase equilibrium, conversely complex adsorption systems including the liquid-phase adsorption isotherms are usually not penicillin G concentration experiment, *Q*max was obtained as 303.03 mg/g; in the Freundlich adsorption model equation, the *n* value was calculated as 1.0098 and the *K*f value as 0.04709 appropriate to be represented [7]. In the Temkin adsorption model equation, the *A* value was calculated as 1.00 and the *B* value as 347.435 and R^2 as 0.9761 (Table 1).

References

[1] Aqda, T. G., Behkami, S., Raoofi, M., & Bagheri, H. (2019). Graphene oxide-starch-based micro-solid phase extraction of antibiotic residues from milk samples. *Journal of Chromatography A, 1591*, 7–14.

[2] Ayawei, N., Ebelegi, A. N., & Wankasi, D. (2017). Modelling and interpretation of adsorption isotherms. *Journal of Chemistry, 2017*, 1–11.

[3] Bulut, Y., Gözübenli, N., & Aydın, H. (2007). Equilibrium and kinetics studies for adsorption of direct blue 71 from aqueous solution by wheat shells. *Journal of Hazardous Materials, 144*, 300–306pp.

[4] Congur, G., Senay, H., Turkcan, C., Canavar, E., Erdem, A., & Akgol, S. (2013). Estrone specific molecularly imprinted polymeric nanospheres: Synthesis, characterization and applications for electrochemical sensor development. *Combinatorial Chemistry & High Throughput Screening, 16*(7), 503–510.

[5] Çorman, M. E., & Akgöl, S. (2012). Preparation of molecular imprinted hydrophobic polymeric nanoparticles havingstructural memories for lysozyme recognition. *Artificial Cells, Blood Substitutes, and Biotechnology, 40*(4), 245–255.

[6] Dincer, S., & Yigittekin, E. S. (2017). Spreading of antibiotic resistance with wastewater. *Biological Wastewater Treatment and Resource*

[7] Foo, K. Y., & Hameed, B. H. (2010). Insights into the modeling of adsorptionisothermsystems. *Chemical Engineering Journal, 156*(1), 2–10.

[8] Ghose, S., Hubbard, B. B., & Cramer, S. M. (2005). Protein interactions in hydrophobic charge induction chromatography (HCIC). *Biotechnology Progress, 21*, 498pp.

[9] Inanan, T., Tüzmen, N., Akgöl, S., & Denizli, A. (2016). Selective cholesterol adsorption by molecular imprinted polymeric nanospheres and application to GIMS. *International Journal of Biological Macromolecules, 92*, 451–460.

[10] Inyinbor, A. A., Adekola, F. A., & Olatunji, G. A. (2016). Kinetics, isotherms and thermodynamic modeling of liquid phase adsorption of Rhodamine B dye onto Raphia hookerie fruit epicarp. *Water Resources and Industry, 15*, 14–27.

[11] Joshi, S. (2002). HPLC separation of antibiotics present in formulated and unformulated samples. *Journal of Pharmaceutical and Biomedical Analysis, 28*(5), 795–809.

[12] Kamranifar, M., Allahresani, A., & Naghizadeh, A. (2019). Synthesis and characterizations of a novel CoFe2O4@ CuS magnetic nanocomposite and investigation of its efficiency for photocatalytic degradation of penicillin G antibiotic in simulated wastewater. *Journal of Hazardous Materials, 366*, 545–555.

[13] Koch, C., Poghossian, A., Schöning, M. J., & Wege, C. (2018). Penicillin detection by tobacco mosaic virus-assisted colorimetric biosensors. *Nanotheranostics, 2*(2), 184–196.

[14] Kraemer, S. A., Ramachandran, A., & Perron, G. G. (2019). Antibiotic pollution in the environment: from

microbial ecology to public policy. *Microorganisms, 7*(6), 180.

[15] Kuru, C. İ., Türkcan, C., Uygun, M., Okutucu, B., & Akgöl, S. (2014). Preparation and characterization of silanized poly(HEMA) nanopolymers for recognition of sugars. *Artificial Cells, Nanomedicine, and Biotechnology, 44*, 835–841.

[16] Lingzhi, L., Haojie, G., Dan, G., Hongmei, M., Yang, L., Mengdie, J., Chengkun, Z., & Xiaohui, Z. (2018). The role of two-component regulatory system in β-lactam antibiotics resistance. *Microbiological Research, 215*, 126–129.

[17] Lobanovska, M., & Pilla, G. (2017). Focus: Drug development: Penicillin's discovery and antibiotic resistance: Lessons for the future? *The Yale Journal of Biology and Medicine, 90*(1), 135.

[18] Malkoç, E. (2006). Ni(II) removal from aqueous solutions using cone biomass of Thuja orientalis. *Journal of Hazardous Materials, 137*, 899–908pp.

[19] Moreno-González, D., Rodríguez-Ramírez, R., del Olmo-Iruela, M., & García-Campaña, A. M. (2017). Validation of a new method based on salting-out assisted liquid-liquid extraction and UHPLC-MS/MS for the determination of betalactam antibiotics in infant dairy products. *Talanta, 167*, 493–498.

[20] Okocha, R. C., Olatoye, I. O., & Adedeji, O. B. (2018). Food safety impacts of antimicrobial use and their residues in aquaculture. *Public Health Reviews, 39*(1), 1–22.

[21] Paulino, A. T., Minasse, F. A. S., Guilherme, M. R., Reis, A. V., Muniz, E. C., & Nozaki, J. (2006). Novel adsorbent based on silkworm chrysalides for removal of heavy metals from wastewaters. *Journal of Colloid and Interface Science, 301*, 479–487pp.

[22] Pinder, N., Brenner, T., Swoboda, S., Weigand, M. A., & HoppeTichy, T. (2017). Therapeutic drug monitoring of beta-lactam antibiotics–influence of sample stability on the analysis of piperacillin, meropenem, ceftazidime and flucloxacillin by HPLC-UV. *Journal of Pharmaceutical and Biomedical Analysis, 143*, 86–93.

[23] Samanidou, V., Michaelidou, K., Kabir, A., & Furton, K. G. (2017). Fabric phase sorptive extraction of selected penicillin antibiotic residues from intact milk followed by high performance liquid chromatography with diode array detection. *Food Chemistry, 224*, 131–138.

[24] Türkmen, D., Bereli, N., Çorman, M. E., Shaikh, H., Akgöl, S., & Denizli, A. (2014). Molecular imprinted magnetic nanoparticles for controlled delivery of mitomycin C. *Artificial Cells, Nanomedicine, and Biotechnology, 42*(5), 316–322.

[25] Willms, I. M., Yuan, J., Penone, C., Goldmann, K., Vogt, J., Wubet, T., Schöning, I., Schrumpf, M., Buscot, F., & Nacke, H. (2020). Distribution of medically relevant antibiotic resistance genes and Mobile genetic elements in soils of temperate forests and grasslands varying in land use. *Genes, 11*(2), 150.

[26] Yin, J., Meng, Z., Du, M., Liu, C., Song, M., & Wang, H. (2010). Pseudo-template molecularly imprinted polymer for selective screening of trace β-lactam antibiotics in river and tap water. *Journal of Chromatography. A, 33*, 5420–5426pp.

MANAS Journal of Engineering
ISSN 1694-7398 — e-ISSN 1694-7398

Volume 11 (Issue 1) (2023) Pages 154-157
https://doi.org/10.51354/mjen.1186550

Finding Solutions to Undamped and Damped Simple Harmonic Oscillations via Kashuri Fundo Transform

Fatma Aybike Çuha[1]*, **Haldun Alpaslan Peker**[2]

[1]Graduate School of Natural and Applied Sciences, Selçuk University, Konya, Türkiye, fatmaaybikecuha@gmail.com, ORCID: 0000-0002-7227-2086,
[2]Department of Mathematics, Faculty of Science, Selçuk University, Konya, Türkiye, pekera@gmail.com, ORCID: 0000-0002-1654-6425

ABSTRACT

Differential equations are expressions that are frequently encountered in mathematical modeling of laws or problems in many different fields of science. It can find its place in many fields such as applied mathematics, physics, chemistry, finance, economics, engineering, etc. They make them more understandable and easier to interpret, by modeling laws or problems mathematically. Therefore, solutions of differential equations are very important. Many methods have been developed that can be used to reach solutions of differential equations. One of these methods is integral transforms. Studies have shown that the use of integral transforms in the solutions of differential equations is a very effective method to reach solutions. In this study, we are looking for a solution to damped and undamped simple harmonic oscillations modeled by linear ordinary differential equations by using Kashuri Fundo transform, which is one of the integral transforms. From the solutions, it can be concluded that the Kashuri Fundo transform is an effective method for reaching the solutions of ordinary differential equations.

ARTICLE INFO

Research article

Received: 9.10.2022
Accepted: 27.01.2023

Keywords: Kashuri Fundo transform, inverse Kashuri Fundo transform, undamped simple harmonic oscillation, damped simple harmonic oscillation, differential equation

**Corresponding author*

1. Introduction

Differential equations are mathematical models that are encountered in many different fields of applied sciences and include one or more functions and their derivatives [1]. Generally, laws and problems in physics, chemistry, biology, engineering, economics, finance and many other fields are expressed using differential equations. Although it is one of the subjects that applied mathematics is mostly studied, differential equations have been encountered in every field that is intertwined with mathematics in a professional sense. The principles used in the formation of many inventions that make our lives easier in daily life include differential equations [1, 2].

Simple harmonic oscillation (SHO), which is one of the advanced physics subjects, is also one of the principles modeled with differential equations. Simple harmonic oscillation (SHO) logically comes after linear oscillation and circular oscillation [3]. This oscillation has a special periodic motion. In mechanical systems, as the system moves, a restoring force is created that can do both positive and negative work. In SHO, the restoring force on the moving object is directly proportional to the displacement magnitude of the object. This indicates that the oscillation is linear. Especially in linear oscillators, the oscillation frequency is independent of amplitude. In order to physically represent linear oscillators correctly, a special damping force is defined that draws energy from the oscillator. In mechanical oscillators, this force is due to friction. Such oscillators are called damped oscillators. Damped or undamped oscillations can be driven by external forces [3–5].

Many different methods have been used in modeling

damped and undamped simple harmonic oscillations, in mechanics and in reaching the solutions of differential equations that appear in many different fields. One of these methods is integral transforms [6]. Integral transforms allow the solutions of differential equations to be reached more easily and without dealing with complicated operations. There are many different integral transforms available [7–12]. The Kashuri Fundo transform, which we have used in this study, is one of these transforms [13]. When the literature is examined, many studies are encountered in which Kashuri Fundo transform is used to reach the solution of differential equations [14–22]. In this study, we sought a solution for damped and undamped simple harmonic oscillations by using Kashuri Fundo transform.

2. Kashuri Fundo Transform

2.1. Definition of Kashuri Fundo Transform

Definition 1. We consider functions in the set F defined as [13],

$$F = \Big\{ f(t) | \exists M, k_1, k_2 > 0, \quad \text{such that} \quad |f(t)| \leqslant M e^{\frac{|t|}{k_i^2}}, \quad \text{if} \quad t \in (-1)^i \times [0, \infty) \Big\}$$

For a function belonging to the set F, M must be finite number. k_1, k_2 may be finite or infinite.

Definition 2. Kashuri Fundo transform defined on the set F and denoted by the operator $\mathscr{K}(.)$ is defined as [13],

$$\mathscr{K}[f(t)](v) = A(v) = \frac{1}{v} \int_0^\infty e^{\frac{-t}{v^2}} f(t)\, dt, \quad t \geqslant 0, \quad -k_1 < v < k_2 \quad (1)$$

The Kashuri Fundo transform expressed by (1) can also be expressed as [13],

$$\mathscr{K}[f(t)](v) = A(v) = v \int_0^\infty e^{-t} f(v^2 t)\, dt$$

Inverse Kashuri Fundo transform is denoted by $\mathscr{K}^{-1}[A(v)] = f(t), t \geq 0$.

Definition 3. A function $f(t)$ is said to be of exponential order $\frac{1}{k^2}$, if there exist positive constants T and M such that, $|f(t)| \leq M e^{\frac{-t}{k^2}}$, for all $t \geq T$ [13].

Theorem 1. (Sufficient Conditions for Existence of Kashuri Funfo Transform) If $f(t)$ is piecewise continuous on $[0, \infty)$ and of exponential order $\frac{1}{k^2}$, then $\mathscr{K}[f(t)](v)$ exists for $|v| < k$ [13].

2.2. Some Properties of Kashuri Fundo Transform

Theorem 2. (Linearity Property) Let $f(t), g(t) \in F$ be functions whose Kashuri Fundo integral transforms exists and c be a constant. Then [13],

$$\mathscr{K}[(f+g)(t)](v) = \mathscr{K}[f(t)](v) + \mathscr{K}[g(t)](v)$$

$$\mathscr{K}[(cf)(t)](v) = c\mathscr{K}[f(t)](v)$$

Theorem 3. (Kashuri Fundo Transform of The Derivatives of The Function $f(t)$) Let's assume that the Kashuri Fundo transform of $f(t) \in F$ is $A(v)$. Then [13],

$$\mathscr{K}[f'(t)](v) = \frac{A(v)}{v^2} - \frac{f(0)}{v} \quad (2)$$

$$\mathscr{K}[f''(t)](v) = \frac{A(v)}{v^4} - \frac{f(0)}{v^3} - \frac{f'(0)}{v} \quad (3)$$

$$\mathscr{K}[f^{(n)}(t)](v) = \frac{A(v)}{v^{2n}} - \sum_{k=0}^{n-1} \frac{f^{(k)}(0)}{v^{2(n-k)-1}} \quad (4)$$

Theorem 4. (First Translation Theorem) Let's assume that the Kashuri Fundo transform of $f(t) \in F$ is $A(v)$. Then [13],

$$\mathscr{K}[e^{at} f(t)] = \left(\frac{1}{\sqrt{1 - av^2}} \right) A\left[\frac{v}{\sqrt{1 - av^2}} \right] \quad (5)$$

2.3. Kashuri Fundo Transform of Some Special Functions

Table 1: Kashuri Fundo Transform of Some Special Functions [13, 23]

$f(t)$	$\mathscr{K}[f(t)] = A(v)$
1	v
t	v^3
t^n	$n! v^{2n+1}$
e^{at}	$\frac{v}{1-av^2}$
$sin(at)$	$\frac{av^3}{1+a^2v^4}$
$cos(at)$	$\frac{v}{1+a^2v^4}$
$sinh(at)$	$\frac{av^3}{1-a^2v^4}$
$cosh(at)$	$\frac{v}{1-a^2v^4}$
t^α	$\Gamma(\alpha+1) v^{2\alpha+1}$
$\sum_{k=0}^{n} a_k t^k$	$\sum_{k=0}^{n} k! a_k v^{2k+1}$

3. Application of Kashuri Fundo Transform to The Equation of Simple Harmonic Oscillation

3.1. Undamped Simple Harmonic Oscillation

The undamped simple harmonic oscillation is mathematically modeled as [3–5]

$$y''(x) + \omega_0^2 y(x) = 0 \tag{6}$$

where $\omega_0 = \sqrt{\frac{k}{m}}$ and is called the natural angular frequency. m is a inertial mass of the object and k is a spring constant.

Having applied bilaterally the Kashuri Fundo transform to the differential equation of undamped simple harmonic oscillation, we acquire

$$\mathcal{K}[y''(x)] + \omega_0^2 \mathcal{K}[y(x)] = 0 \tag{7}$$

Rearranging the equation (7) using the equation (3), we get

$$A(v) = \frac{v^4}{1+\omega_0^2 v^4}\left(\frac{f(0)+v^2 f'(0)}{v^3}\right) \tag{8}$$

If we assume that $f(0) = c_1$ and $f'(0) = c_2$ here (c_1, c_2 are constants), and arranging this equation to apply the inverse Kashuri Fundo transform, we get

$$A(v) = \frac{c_1 v}{1+\omega_0^2 v^4} + \frac{c_2 v^3}{1+\omega_0^2 v^4} \tag{9}$$

Having applied bilaterally the inverse Kashuri Fundo transform to the equation (9), using table 1, we acquire

$$y(x) = c_1 \cos(\omega_0 x) + \frac{c_2}{\omega_0}\sin(\omega_0 x) \tag{10}$$

which is a sinusoidal function.

3.2. Damped Simple Harmonic Oscillation

The damped simple harmonic oscillation is mathematically modeled as [3–5]

$$y''(x) + \frac{b}{m}y'(x) + \omega_0^2 y(x) = 0 \tag{11}$$

where $\omega_0 = \sqrt{\frac{k}{m}}$ is called the natural angular frequency and b is called the damping coefficient. m is a inertial mass of the object and k is a spring constant.

Having applied bilaterally the Kashuri Fundo transform to the differential equation of damped simple harmonic oscillation with initial conditions $y(0) = 1$ and $y'(0) = 0$, we acquire

$$\mathcal{K}[y''(x)] + \frac{b}{m}\mathcal{K}[y'(x)] + \omega_0^2 \mathcal{K}[y(x)] = 0 \tag{12}$$

Rearranging the equation (12) using the equations (2), (3) and initial conditions, we get

$$A(v) = \frac{v + \frac{b}{m}v^3}{1 + \frac{b}{m}v^2 + \omega_0^2 v^4} \tag{13}$$

We need to get the equation (13) into the form that can be applied the inverse Kashuri Fundo transform. If we rearrange the equation (13) for this, we obtain

$$A(v) = \frac{v\left(1+\frac{b}{2m}v^2\right)}{\left(1+\frac{b}{2m}v^2\right)^2 + \omega_1^2 v^4} + \frac{b}{2m\omega_1}\frac{\omega_1 v^3}{\left(1+\frac{b}{2m}v^2\right)^2 + \omega_1^2 v^4} \tag{14}$$

where $\omega_1 = \sqrt{\omega_0^2 - \frac{b^2}{4m^2}}$.

Having applied bilaterally the inverse Kashuri Fundo transform to the equation (14), using the equation (5), we acquire

$$y(x) = e^{-(\frac{b}{2m})x}cos(\omega_1 x) + \frac{b}{2m\omega_1}e^{-(\frac{b}{2m})x}sin(\omega_1 x) \tag{15}$$

which is also a sinusoidal function.

4. Conclusion

At the beginning of the study, we mentioned the importance of differential equations for science. The more clear and uncomplicated the steps taken while reaching the solutions of these equations, which are so important for science, the sooner and more clearly the result can be revealed. In this study, we have based on damped and undamped simple harmonic oscillations modeled by ordinary differential equations. We examined the Kashuri Fundo transform through these models. As a result of the applied steps, it was concluded that the Kashuri Fundo transform is a simple and effective method for reaching the solutions of ordinary differential equations.

References

[1] Zill D.G., A First Course in Differential Equations with Modeling Applications, 11th ed. Cengage Learning, 2017.

[2] Hairer E., Norsett S.P. and Wanner G., Solving Ordinary Differential Equations I: Nonstiff Problems, Berlin, New York: Springer-Verlag, 1993.

[3] Hand L.N. and Finch J.D., Analytical Mechanics, Cambridge, UK: Cambridge University Press, 1998.

[4] Fowles G.R. and Cassiday G.L., Analytical Mechanics, 7th ed. Brooks/Cole, 2004.

[5] Fasano A. and Marmi S., Analytical Mechanics, USA: Oxford University Press, 2006.

[6] Debnath L. and Bhatta D., Integral Transforms and Their Applications, 2nd ed. Boca Raton, FL: Chapman and Hall/CRC, 2007.

[7] Bracewell R.N., The Fourier Transform and Its Applications, 3rd ed. New York, USA: McGraw-Hill, 1986.

[8] Widder D.V., The Laplace Transform. Princeton, USA: Princeton University Press, 1946.

[9] Watugala G.K., "Sumudu Transform: A New Integral Transform to Solve Differential Equations and Control Engineering Problems", International Journal of Mathematical Education in Science and Technology, 24, (1993), 35-43.

[10] Al-Omari S.K.Q., "On the Application of Natural Transforms", International Journal of Pure and Applied Mathematics, 85(4), (2013), 729-744.

[11] Elzaki T.M., "The New Integral Transform 'Elzaki Transform'", Global Journal of Pure and Applied Mathematics, 7(1), (2011), 57-64.

[12] Maitama S., Zhao W., "New Integral Transform: Shehu Transform a Generalization of Sumudu and Laplace Transform for Solving Differential Equations", International Journal of Analysis and Applications, 17(2), (2019), 167-190.

[13] Kashuri A., Fundo A., "A New Integral Transform", Advances in Theoretical and Applied Mathematics, 8(1), (2013), 27-43.

[14] Kashuri A., Fundo A., Liko R., "On Double New Integral Transform and Double Laplace Transform", European Scientific Journal, 9(33), (2013), 1857–7881.

[15] Shah K., Singh T., "A Solution of the Burger's Equation Arising in the Longitudinal Dispersion Phenomenon in Fluid Flow through Porous Media by Mixture of New Integral Transform and Homotopy Perturbation Method", Journal of Geoscience and Environment Protection, 3, (2015), 24-30.

[16] Kashuri A., Fundo A., Liko R. "New Integral Transform For Solving Some Fractional Differential Equations", International Journal of Pure and Applied Mathematics, 103(4), (2015), 675-682.

[17] Shah K., Singh T., "The Mixture of New Integral Transform and Homotopy Perturbation Method for Solving Discontinued Problems Arising in Nanotechnology", Open Journal of Applied Sciences, 5, (2015), 688-695.

[18] Fundo A., Kashuri A., Liko R., "New Integral Transform in Caputo Type Fractional Difference Operator", Universal Journal of Applied Science, 4(1), (2016), 7-10.

[19] Güngör N., "Solving Convolution Type Linear Volterra Integral Equations with Kashuri Fundo Transform", Journal of Abstract and Computational Mathematics, 6(2), (2021), 1-7.

[20] Peker H.A., Cuha F.A., "Application of Kashuri Fundo Transform and Homotopy Perturbation Methods to Fractional Heat Transfer and Porous Media Equations", Thermal Science, 26(4A), (2022), 2877-2884.

[21] Cuha F.A., Peker H.A., "Solution of Abel's Integral Equation by Kashuri Fundo Transform", Thermal Science, 26(4A), (2022), 3003-3010.

[22] Peker H. A., Cuha F. A., Peker B., "Solving Steady Heat Transfer Problems via Kashuri Fundo Transform", Thermal Science, 26(4A), (2022), 3011-3017.

[23] Subartini B., Sumiati I., Sukono, Riaman, Sulaiman I.M., "Combined Adomian Decomposition Method with Integral Transform", Mathematics and Statistics, 9(6), (2021) 976-983.

MANAS Journal of Engineering
ISSN 1694-7398 — e-ISSN 1694-7398

Volume 11 (Issue 1) (2023) Pages 158-165
https://doi.org/10.51354/mjen.1233063

The Solution and Dynamic Behaviour of Difference Equations of Twenty-First Order

Burak Oğul[1]*, Dağıstan Şimşek[2], Tarek Fawzi Ibrahim[3]

[1] Department of Management Informations Systems, School of Applied Sciences, Istanbul Aydin University, Istanbul 34295, Turkey, burakogul@aydin.edu.tr, ORCID: 0000-0002-3264-4340

[2]Department of Engineering Basic Scieneces, Faculty of Engineering and Natural Sciences, Konya Technical University, Konya 42250, Turkey, dsimsek@ktun.edu.tr, ORCID: 0000-0003-3003-807X

[3]Department of Mathematics, Faculty of Sciences and Arts (Mahayel Aser), King Khalid University, Saudi Arabia, tfoze@kku.edu.sa, ORCID: 0000-0002-6895-3268

ABSTRACT

We explore the dynamics of adhering to rational difference formula

$$\psi_{m+1} = \frac{\psi_{m-20}}{\pm 1 \pm \psi_{m-2}\psi_{m-5}\psi_{m-8}\psi_{m-11}\psi_{m-14}\psi_{m-17}\psi_{m-20}}, \quad m \in \mathbb{N}_0$$

where the initials are arbitrary nonzero real numbers. Specifically, we examine global asymptotically stability. Additionally, we provide examples and solutions graphs of some special cases.

ARTICLE INFO

Research article

Received: 12.01.2023
Accepted: 30.03.2023

Keywords: Equilibrium point, solution of difference equation, stability, boundedness, global asymptotic stability

**Corresponding author*

1. Introduction

Our objective in this paper is to check out the actions of the solution of the adhering to nonlinear difference formula

$$\psi_{m+1} = \frac{\psi_{m-20}}{\pm 1 \pm \psi_{m-2}\psi_{m-5}\psi_{m-8}\psi_{m-11}\psi_{m-14}\psi_{m-17}\psi_{m-20}}, \tag{1}$$

$m \in \mathbb{N}_0$, where the initials are real numbers. Additionally, we obtain these types of solutions.

Just recently there has been an expanding rate of interest in researching rational difference equations and also their qualitative properties.

Ahmed et al., in [2] discovered a collection of first order sine-type difference equations that are constructively solvable in closed form, and they provided a general solution to each of the equations.

Aloqeili, [6] has actually gotten the solutions to

$$\psi_{m+1} = \frac{\psi_{m-1}}{a - \psi_m\psi_{m-1}}.$$

Elsayed [14] got the solution of

$$\psi_{m+1} = \frac{\psi_{m-5}}{-1 + \psi_{m-2}\psi_{m-5}}.$$

In [17] Ibrahim et al., explored the boundedness and global stability of a nonlinear generalized high-order difference equation with delay.

Khan et. al. in [18], investigated the second-order nonlinear difference equation's local stability, attractor, periodicity feature, and boundedness solutions. Finally, the resulting findings are quantitatively validated.

Rahaman et. al., In light of Zadeh's expansion principle, they gave a new perspective on the fuzzy difference equation in [22].

Stevic et. al., [26] investigated a nonlinear second-order difference equation that significantly extends several previous equations. Their primary finding is that the difference equation may be solved in closed form. There are also several applications of the main result provided.

Yalcinkaya, [29] studied the existence, boundedness, and asymptotic behavior of positive solutions to the fuzzy difference equation,

$$\psi_{m+1} = \frac{A\psi_{m-1}}{1+\psi_{m-2}^{p}}, m \in \mathbf{N_0}$$

where (ψ_m) is a sequence of positive fuzzy numbers, A and the initial conditions ψ_{-j} are positive fuzzy numbers and p is a positive integer.

Soykan, et al., the binomial transform of the generalized third-order Jacobsthal sequence is established in [27]. They also describe the binomial transform of four special cases of third-order Jacobsthal sequences: the binomial transform of the third-order Jacobsthal, the binomial transform of the third-order Jacobsthal-Lucas, the modified third-order Jacobsthal-Lucas, and the binomial transform of the third-order Jacobsthal-Perrin. Furthermore, they investigated their characteristics in greater depth.

2. First Equation

In this part we give the solutions of

$$\psi_{m+1} = \frac{\psi_{m-20}}{1+\psi_{m-2}\psi_{m-5}\psi_{m-8}\psi_{m-11}\psi_{m-14}\psi_{m-17}\psi_{m-20}}, \quad m \in \mathbb{N}_0, \qquad (2)$$

where the initials are arbitrary real numbers.

Theorem 1. *Let $\{x_m\}_{m=-20}^{\infty}$ be a solution of Eq. 2. Then for $m \in \mathbb{N}_0$*

$$\psi_{21m+1} = \frac{A_{20}\prod_{i=0}^{m-1}(1+7iA_2A_5A_8A_{11}A_{14}A_{17}A_{20})}{\prod_{i=0}^{m}(1+(7i+1)A_2A_5A_8A_{11}A_{14}A_{17}A_{20})},$$

$$\psi_{21m+2} = \frac{A_{19}\prod_{i=0}^{m-1}(1+7iA_1A_4A_7A_{10}A_{13}A_{16}A_{19})}{\prod_{i=0}^{m}(1+(7i+1)A_1A_4A_7A_{10}A_{13}A_{16}A_{19})},$$

$$\psi_{21m+3} = \frac{A_{18}\prod_{i=0}^{m-1}(1+7iA_0A_3A_6A_9A_{12}A_{15}A_{18})}{\prod_{i=0}^{m}(1+(7i+1)A_0A_3A_6A_9A_{12}A_{15}A_{18})},$$

$$\psi_{21m+4} = \frac{A_{17}\prod_{i=0}^{m}(1+(7i+1)A_2A_5A_8A_{11}A_{14}A_{17}A_{20})}{\prod_{i=0}^{m}(1+(7i+2)A_2A_5A_8A_{11}A_{14}A_{17}A_{20})},$$

$$\psi_{21m+5} = \frac{A_{16}\prod_{i=0}^{m}(1+(7i+1)A_1A_4A_7A_{10}A_{13}A_{16}A_{19})}{\prod_{i=0}^{m}(1+(7i+2)A_1A_4A_7A_{10}A_{13}A_{16}A_{19})},$$

$$x_{21n+6} = \frac{A_{15}\prod_{i=0}^{m}(1+(7i+1)A_0A_3A_6A_9A_{12}A_{15}A_{18})}{\prod_{i=0}^{m}(1+(7i+2)A_0A_3A_6A_9A_{12}A_{15}A_{18})},$$

$$\psi_{21m+7} = \frac{A_{14}\prod_{i=0}^{m}(1+(7i+2)A_2A_5A_8A_{11}A_{14}A_{17}A_{20})}{\prod_{i=0}^{m}(1+(7i+3)A_2A_5A_8A_{11}A_{14}A_{17}A_{20})},$$

$$\psi_{21m+8} = \frac{A_{13}\prod_{i=0}^{m}(1+(7i+2)A_1A_4A_7A_{10}A_{13}A_{16}A_{19})}{\prod_{i=0}^{m}(1+(7i+3)A_1A_4A_7A_{10}A_{13}A_{16}A_{19})},$$

$$\psi_{21m+9} = \frac{A_{12}\prod_{i=0}^{m}(1+(7i+2)A_0A_3A_6A_9A_{12}A_{15}A_{18})}{\prod_{i=0}^{m}(1+(7i+3)A_0A_3A_6A_9A_{12}A_{15}A_{18})},$$

$$\psi_{21m+10} = \frac{A_{11}\prod_{i=0}^{m}(1+(7i+3)A_2A_5A_8A_{11}A_{14}A_{17}A_{20})}{\prod_{i=0}^{m}(1+(7i+4)A_2A_5A_8A_{11}A_{14}A_{17}A_{20})},$$

$$\psi_{21m+11} = \frac{A_{10}\prod_{i=0}^{m}(1+(7i+3)A_1A_4A_7A_{10}A_{13}A_{16}A_{19})}{\prod_{i=0}^{m}(1+(7i+4)A_1A_4A_7A_{10}A_{13}A_{16}A_{19})},$$

$$\psi_{21n+12} = \frac{A_9\prod_{i=0}^{m}(1+(7i+3)A_0A_3A_6A_9A_{12}A_{15}A_{18})}{\prod_{i=0}^{m}(1+(7i+4)A_0A_3A_6A_9A_{12}A_{15}A_{18})},$$

$$\psi_{21m+13} = \frac{A_8\prod_{i=0}^{m}(1+(7i+4)A_2A_5A_8A_{11}A_{14}A_{17}A_{20})}{\prod_{i=0}^{m}(1+(7i+5)A_2A_5A_8A_{11}A_{14}A_{17}A_{20})},$$

$$\psi_{21m+14} = \frac{A_7\prod_{i=0}^{m}(1+(7i+4)A_1A_4A_7A_{10}A_{13}A_{16}A_{19})}{\prod_{i=0}^{m}(1+(7i+5)A_1A_4A_7A_{10}A_{13}A_{16}A_{19})},$$

$$\psi_{21n+15} = \frac{A_6\prod_{i=0}^{m}(1+(7i+4)A_0A_3A_6A_9A_{12}A_{15}A_{18})}{\prod_{i=0}^{m}(1+(7i+5)A_0A_3A_6A_9A_{12}A_{15}A_{18})},$$

$$\psi_{21m+16} = \frac{A_5\prod_{i=0}^{m}(1+(7i+5)A_2A_5A_8A_{11}A_{14}A_{17}A_{20})}{\prod_{i=0}^{m}(1+(7i+6)A_2A_5A_8A_{11}A_{14}A_{17}A_{20})},$$

$$\psi_{21m+17} = \frac{A_4\prod_{i=0}^{m}(1+(7i+5)A_1A_4A_7A_{10}A_{13}A_{16}A_{19})}{\prod_{i=0}^{m}(1+(7i+6)A_1A_4A_7A_{10}A_{13}A_{16}A_{19})},$$

$$\psi_{21m+18} = \frac{A_3\prod_{i=0}^{m}(1+(7i+5)A_0A_3A_6A_9A_{12}A_{15}A_{18})}{\prod_{i=0}^{m}(1+(7i+6)A_0A_3A_6A_9A_{12}A_{15}A_{18})},$$

$$\psi_{21m+19} = \frac{A_2\prod_{i=0}^{m}(1+(7i+6)A_2A_5A_8A_{11}A_{14}A_{17}A_{20})}{\prod_{i=0}^{m}(1+(7i+7)A_2A_5A_8A_{11}A_{14}A_{17}A_{20})},$$

$$\psi_{21m+20} = \frac{A_1\prod_{i=0}^{m}(1+(7i+6)A_1A_4A_7A_{10}A_{13}A_{16}A_{19})}{\prod_{i=0}^{m}(1+(7i+7)A_1A_4A_7A_{10}A_{13}A_{16}A_{19})},$$

$$\psi_{21m+21} = \frac{A_0\prod_{i=0}^{m}(1+(7i+6)A_0A_3A_6A_9A_{12}A_{15}A_{18})}{\prod_{i=0}^{m}(1+(7i+7)A_0A_3A_6A_9A_{12}A_{15}A_{18})}.$$

where, $\psi_{-20} = A_{20}, \psi_{-19} = A_{19}, \ldots, \psi_{-1} = A_1, \psi_0 = A_0$.

Proof Suppose that $m > 0$ and that our assumption holds for $m-1$. That is,

$$\psi_{21m-20} = \frac{A_{20}\prod_{i=0}^{m-2}(1+7iA_2A_5A_8A_{11}A_{14}A_{17}A_{20})}{\prod_{i=0}^{m-1}(1+(7i+1)A_2A_5A_8A_{11}A_{14}A_{17}A_{20})},$$

$$\psi_{21m-19} = \frac{A_{19}\prod_{i=0}^{m-2}(1+7iA_1A_4A_7A_{10}A_{13}A_{16}A_{19})}{\prod_{i=0}^{m-1}(1+(7i+1)A_1A_4A_7A_{10}A_{13}A_{16}A_{19})},$$

$$\psi_{21m-18} = \frac{A_{18}\prod_{i=0}^{m-2}(1+7iA_0A_3A_6A_9A_{12}A_{15}A_{18})}{\prod_{i=0}^{m-1}(1+(7i+1)A_0A_3A_6A_9A_{12}A_{15}A_{18})},$$

$$\psi_{21m-17} = \frac{A_{17}\prod_{i=0}^{m-1}(1+(7i+1)A_2A_5A_8A_{11}A_{14}A_{17}A_{20})}{\prod_{i=0}^{m-1}(1+(7i+2)A_2A_5A_8A_{11}A_{14}A_{17}A_{20})},$$

$$\psi_{21m-16} = \frac{A_{16}\prod_{i=0}^{m-1}(1+(7i+1)A_1A_4A_7A_{10}A_{13}A_{16}A_{19})}{\prod_{i=0}^{m-1}(1+(7i+2)A_1A_4A_7A_{10}A_{13}A_{16}A_{19})},$$

$$\psi_{21m-15} = \frac{A_{15}\prod_{i=0}^{m-1}(1+(7i+1)A_0A_3A_6A_9A_{12}A_{15}A_{18})}{\prod_{i=0}^{m-1}(1+(7i+2)A_0A_3A_6A_9A_{12}A_{15}A_{18})},$$

$$\psi_{21m-14} = \frac{A_{14}\prod_{i=0}^{m-1}(1+(7i+2)A_2A_5A_8A_{11}A_{14}A_{17}A_{20})}{\prod_{i=0}^{m-1}(1+(7i+3)A_2A_5A_8A_{11}A_{14}A_{17}A_{20})},$$

$$\psi_{21m-13} = \frac{A_{13}\prod_{i=0}^{m-1}(1+(7i+2)A_1A_4A_7A_{10}A_{13}A_{16}A_{19})}{\prod_{i=0}^{m-1}(1+(7i+3)A_1A_4A_7A_{10}A_{13}A_{16}A_{19})},$$

$$\psi_{21m-12} = \frac{A_{12}\prod_{i=0}^{m-1}(1+(7i+2)A_0A_3A_6A_9A_{12}A_{15}A_{18})}{\prod_{i=0}^{m-1}(1+(7i+3)A_0A_3A_6A_9A_{12}A_{15}A_{18})},$$

$$\psi_{21m-11} = \frac{A_{11}\prod_{i=0}^{m-1}(1+(7i+3)A_2A_5A_8A_{11}A_{14}A_{17}A_{20})}{\prod_{i=0}^{m-1}(1+(7i+4)A_2A_5A_8A_{11}A_{14}A_{17}A_{20})},$$

$$\psi_{21m-10} = \frac{A_{10}\prod_{i=0}^{m-1}(1+(7i+3)A_1A_4A_7A_{10}A_{13}A_{16}A_{19})}{\prod_{i=0}^{m-1}(1+(7i+4)A_1A_4A_7A_{10}A_{13}A_{16}A_{19})},$$

$$\psi_{21m-9} = \frac{A_9\prod_{i=0}^{m-1}(1+(7i+3)A_0A_3A_6A_9A_{12}A_{15}A_{18})}{\prod_{i=0}^{m-1}(1+(7i+4)A_0A_3A_6A_9A_{12}A_{15}A_{18})},$$

$$\psi_{21m-8} = \frac{A_8\prod_{i=0}^{m-1}(1+(7i+4)A_2A_5A_8A_{11}A_{14}A_{17}A_{20})}{\prod_{i=0}^{m-1}(1+(7i+5)A_2A_5A_8A_{11}A_{14}A_{17}A_{20})},$$

$$\psi_{21m-7} = \frac{A_7\prod_{i=0}^{m-1}(1+(7i+4)A_1A_4A_7A_{10}A_{13}A_{16}A_{19})}{\prod_{i=0}^{m-1}(1+(7i+5)A_1A_4A_7A_{10}A_{13}A_{16}A_{19})},$$

$$\psi_{21m-6} = \frac{A_6\prod_{i=0}^{m-1}(1+(7i+4)A_0A_3A_6A_9A_{12}A_{15}A_{18})}{\prod_{i=0}^{m-1}(1+(7i+5)A_0A_3A_6A_9A_{12}A_{15}A_{18})},$$

$$\psi_{21m-5} = \frac{A_5\prod_{i=0}^{m-1}(1+(7i+5)A_2A_5A_8A_{11}A_{14}A_{17}A_{20})}{\prod_{i=0}^{m-1}(1+(7i+6)A_2A_5A_8A_{11}A_{14}A_{17}A_{20})},$$

$$\psi_{21m-4}=\frac{A_4\prod_{i=0}^{m-1}(1+(7i+5)A_1A_4A_7A_{10}A_{13}A_{16}A_{19})}{\prod_{i=0}^{m-1}(1+(7i+6)A_1A_4A_7A_{10}A_{13}A_{16}A_{19})},$$
$$\psi_{21m-3}=\frac{A_3\prod_{i=0}^{m-1}(1+(7i+5)A_0A_3A_6A_9A_{12}A_{15}A_{18})}{\prod_{i=0}^{m-1}(1+(7i+6)A_0A_3A_6A_9A_{12}A_{15}A_{18})},$$
$$\psi_{21m-2}=\frac{A_2\prod_{i=0}^{m-1}(1+(7i+6)A_2A_5A_8A_{11}A_{14}A_{17}A_{20})}{\prod_{i=0}^{m-1}(1+(7i+7)A_2A_5A_8A_{11}A_{14}A_{17}A_{20})},$$
$$\psi_{21m-1}=\frac{A_1\prod_{i=0}^{m-1}(1+(7i+6)A_1A_4A_7A_{10}A_{13}A_{16}A_{19})}{\prod_{i=0}^{m-1}(1+(7i+7)A_1A_4A_7A_{10}A_{13}A_{16}A_{19})},$$
$$\psi_{21m}=\frac{A_0\prod_{i=0}^{m-1}(1+(7i+6)A_0A_3A_6A_9A_{12}A_{15}A_{18})}{\prod_{i=0}^{m-1}(1+(7i+7)A_0A_3A_6A_9A_{12}A_{15}A_{18})}.$$

Now, using the main 2, one has

$$\psi_{21m+1}=\frac{\psi_{21m-20}}{1+\psi_{21m-2}\psi_{21m-5}\psi_{21m-8}\psi_{21m-11}\psi_{21m-14}\psi_{21m-17}\psi_{21m-20}},$$

Hence, we have

$$\psi_{21m+1}=\frac{A_{20}\prod_{i=0}^{m-1}(1+7iA_2A_5A_8A_{11}A_{14}A_{17}A_{20})}{\prod_{i=0}^{m}(1+(7i+1)A_2A_5A_8A_{11}A_{14}A_{17}A_{20})}.$$

Other relations can be proved similarly way.

Theorem 2. *Eq. 2 has unique equilibrium point which is the number zero and this equilibrium isn't locally asymptotically stable. Also $\overline{\psi}$ is non hyperbolic.*

Proof For the equilibrium points of Eq. 2, we can write

$$\overline{\psi}=\frac{\overline{\psi}}{1+\overline{\psi}^7}.$$

Then

$$\overline{\psi}+\overline{\psi}^8=\overline{\psi},\quad \overline{\psi}^8=0.$$

Thus the equilibrium point of Eq. 2 is $\overline{\psi}=0$.
So,

$$f(l,o,t,w,\alpha,\beta,\gamma)=\frac{l}{1+lotw\alpha\beta\gamma}$$

$$f_l(l,o,t,w,\alpha,\beta,\gamma)=\frac{1}{(1+lotw\alpha\beta\gamma)^2},\quad f_o(l,o,t,w,\alpha,\beta,\gamma)=\frac{-l^2tw\alpha\beta\gamma}{(1+lotw\alpha\beta\gamma)^2},$$
$$f_t(l,o,t,w,\alpha,\beta,\gamma)=\frac{-l^2ow\alpha\beta\gamma}{(1+lotw\alpha\beta\gamma)^2},\quad f_w(l,o,t,w,\alpha,\beta,\gamma)=\frac{-l^2ot\alpha\beta\gamma}{(1+lotw\alpha\beta\gamma)^2}$$
$$f_\alpha(l,o,t,w,\alpha,\beta,\gamma)=\frac{-l^2owt\beta\gamma}{(1+lotw\alpha\beta\gamma)^2},\quad f_\beta(l,o,t,w,\alpha,\beta,\gamma)=\frac{-l^2ot\alpha w\gamma}{(1+lotw\alpha\beta\gamma)^2},$$
$$f_\gamma(l,o,t,w,\alpha,\beta,\gamma)=\frac{-l^2ot\alpha w\beta}{(1+lotw\alpha\beta\gamma)^2}.$$

We have

$$f_l(\overline{\psi},\overline{\psi},\overline{\psi},\overline{\psi},\overline{\psi},\overline{\psi},\overline{\psi})=1,\quad f_o(\overline{\psi},\overline{\psi},\overline{\psi},\overline{\psi},\overline{\psi},\overline{\psi},\overline{\psi})=-1,$$
$$f_t(\overline{\psi},\overline{\psi},\overline{\psi},\overline{\psi},\overline{\psi},\overline{\psi},\overline{\psi})=-1,\quad f_w(\overline{\psi},\overline{\psi},\overline{\psi},\overline{\psi},\overline{\psi},\overline{\psi},\overline{\psi})=-1,$$
$$f_\alpha(\overline{\psi},\overline{\psi},\overline{\psi},\overline{\psi},\overline{\psi},\overline{\psi},\overline{\psi})=-1,\quad f_\beta(\overline{\psi},\overline{\psi},\overline{\psi},\overline{\psi},\overline{\psi},\overline{\psi},\overline{\psi})=-1,$$
$$f_\gamma(\overline{\psi},\overline{\psi},\overline{x},\overline{x},\overline{\psi},\overline{\psi},\overline{\psi})=-1.$$

We confirm our results with the following numerical examples.

Example 1. *Assume that*

$\psi_{-20}=0.3,\ \psi_{-19}=0.35,\ \psi_{-18}=0.4,\ \psi_{-17}=0.87,\ \psi_{-16}=0.86,$
$\psi_{-15}=0.85,\ \psi_{-14}=1.84,\ \psi_{-13}=0.96,\ \psi_{-12}=0.82,\ \psi_{-11}=0.81,$
$\psi_{-10}=0.8,\ \psi_{-9}=0.79,\ \psi_{-8}=0.78,\ \psi_{-7}=1.77,\ \psi_{-6}=0.76,$
$\psi_{-5}=0.75,\ \psi_{-4}=0.9,\ \psi_{-3}=0.73,\ \psi_{-2}=0.72,\ \psi_{-1}=0.91,$
$\psi_0=0.7,$

See figure 1

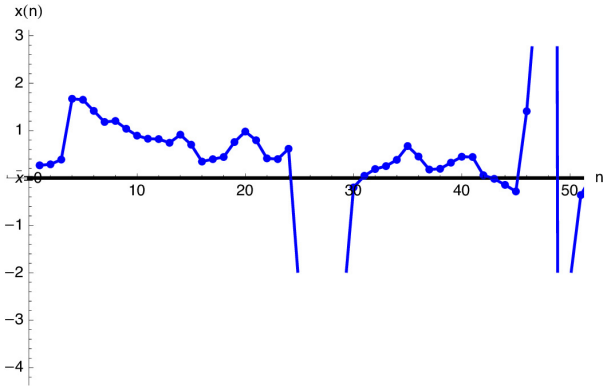

Figure 1

Example 2. *Assume that,*

$\psi_{-20}=0.5,\ \psi_{-19}=0.3,\ \psi_{-18}=0.42,\ \psi_{-17}=0.83,\ \psi_{-16}=0.81,$
$\psi_{-15}=0.85,\ \psi_{-14}=1.84,\ \psi_{-13}=0.91,\ \psi_{-12}=0.81,\ \psi_{-11}=0.84,$
$\psi_{-10}=0.342,\ \psi_{-9}=0.79,\ \psi_{-8}=0.78,\ \psi_{-7}=1.77,\ \psi_{-6}=0.76,$
$\psi_{-5}=0.75,\ \psi_{-4}=0.9,\ \psi_{-3}=0.73,\ \psi_{-2}=0.72,\ \psi_{-1}=0.91,$
$\psi_0=0.7,$

See figure 2.

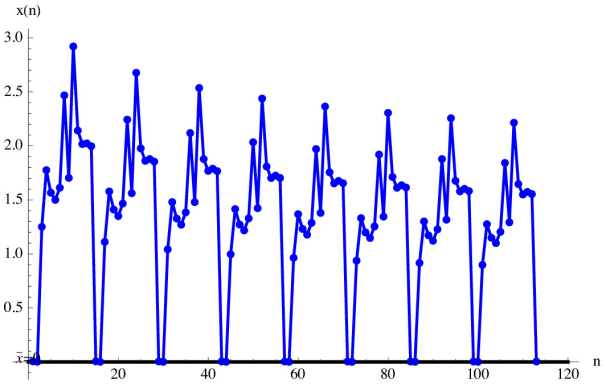

Figure 2

3. The Equation $\psi_{m+1}=\frac{\psi_{m-20}}{1-\psi_{m-2}\psi_{m-5}\psi_{m-8}\psi_{m-11}\psi_{m-14}\psi_{m-17}\psi_{m-20}}$

We deal with the difference equation

$$\psi_{m+1}=\frac{\psi_{m-20}}{1-\psi_{m-2}\psi_{m-5}\psi_{m-8}\psi_{m-11}\psi_{m-14}\psi_{m-17}\psi_{m-20}}\quad m\in\mathbb{N}_0. \tag{3}$$

Theorem 3. *Let $\{\psi_m\}_{m=-20}^{\infty}$ be a solution of Eq. 3 Then for $m\in\mathbb{N}_0$*

$$\psi_{21m+1}=\frac{A_{20}\prod_{i=0}^{m-1}(1-7iA_2A_5A_8A_{11}A_{14}A_{17}A_{20})}{\prod_{i=0}^{m}(1-(7i+1)A_2A_5A_8A_{11}A_{14}A_{17}A_{20})},$$
$$\psi_{21m+2}=\frac{A_{19}\prod_{i=0}^{m-1}(1-7iA_1A_4A_7A_{10}A_{13}A_{16}A_{19})}{\prod_{i=0}^{m}(1-(7i+1)A_1A_4A_7A_{10}A_{13}A_{16}A_{19})},$$
$$\psi_{21m+3}=\frac{A_{18}\prod_{i=0}^{m-1}(1-7iA_0A_3A_6A_9A_{12}A_{15}A_{18})}{\prod_{i=0}^{m}(1-(7i+1)A_0A_3A_6A_9A_{12}A_{15}A_{18})},$$
$$\psi_{21m+4}=\frac{A_{17}\prod_{i=0}^{m}(1-(7i+1)A_2A_5A_8A_{11}A_{14}A_{17}A_{20})}{\prod_{i=0}^{m}(1-(7i+2)A_2A_5A_8A_{11}A_{14}A_{17}A_{20})},$$

$$\psi_{21m+5}=\frac{A_{16}\prod_{i=0}^{m}(1-(7i+1)A_1A_4A_7A_{10}A_{13}A_{16}A_{19})}{\prod_{i=0}^{m}(1-(7i+2)A_1A_4A_7A_{10}A_{13}A_{16}A_{19})},$$
$$\psi_{21m+6}=\frac{A_{15}\prod_{i=0}^{m}(1-(7i+1)A_0A_3A_6A_9A_{12}A_{15}A_{18})}{\prod_{i=0}^{m}(1-(7i+2)A_0A_3A_6A_9A_{12}A_{15}A_{18})},$$
$$\psi_{21m+7}=\frac{A_{14}\prod_{i=0}^{m}(1-(7i+2)A_2A_5A_8A_{11}A_{14}A_{17}A_{20})}{\prod_{i=0}^{m}(1-(7i+3)A_2A_5A_8A_{11}A_{14}A_{17}A_{20})},$$
$$\psi_{21m+8}=\frac{A_{13}\prod_{i=0}^{m}(1-(7i+2)A_1A_4A_7A_{10}A_{13}A_{16}A_{19})}{\prod_{i=0}^{m}(1-(7i+3)A_1A_4A_7A_{10}A_{13}A_{16}A_{19})},$$
$$\psi_{21m+9}=\frac{A_{12}\prod_{i=0}^{m}(1-(7i+2)A_0A_3A_6A_9A_{12}A_{15}A_{18})}{\prod_{i=0}^{m}(1-(7i+3)A_0A_3A_6A_9A_{12}A_{15}A_{18})},$$
$$\psi_{21m+10}=\frac{A_{11}\prod_{i=0}^{m}(1-(7i+3)A_2A_5A_8A_{11}A_{14}A_{17}A_{20})}{\prod_{i=0}^{m}(1-(7i+4)A_2A_5A_8A_{11}A_{14}A_{17}A_{20})},$$
$$\psi_{21m+11}=\frac{A_{10}\prod_{i=0}^{m}(1-(7i+3)A_1A_4A_7A_{10}A_{13}A_{16}A_{19})}{\prod_{i=0}^{m}(1-(7i+4)A_1A_4A_7A_{10}A_{13}A_{16}A_{19})},$$
$$\psi_{21m+12}=\frac{A_{9}\prod_{i=0}^{m}(1-(7i+3)A_0A_3A_6A_9A_{12}A_{15}A_{18})}{\prod_{i=0}^{m}(1-(7i+4)A_0A_3A_6A_9A_{12}A_{15}A_{18})},$$
$$\psi_{21m+13}=\frac{A_{8}\prod_{i=0}^{m}(1-(7i+4)A_2A_5A_8A_{11}A_{14}A_{17}A_{20})}{\prod_{i=0}^{m}(1-(7i+5)A_2A_5A_8A_{11}A_{14}A_{17}A_{20})},$$
$$\psi_{21m+14}=\frac{A_{7}\prod_{i=0}^{m}(1-(7i+4)A_1A_4A_7A_{10}A_{13}A_{16}A_{19})}{\prod_{i=0}^{m}(1-(7i+5)A_1A_4A_7A_{10}A_{13}A_{16}A_{19})},$$
$$\psi_{21m+15}=\frac{A_{6}\prod_{i=0}^{m}(1-(7i+4)A_0A_3A_6A_9A_{12}A_{15}A_{18})}{\prod_{i=0}^{m}(1-(7i+5)A_0A_3A_6A_9A_{12}A_{15}A_{18})},$$
$$\psi_{21m+16}=\frac{A_{5}\prod_{i=0}^{m}(1-(7i+5)A_2A_5A_8A_{11}A_{14}A_{17}A_{20})}{\prod_{i=0}^{m}(1-(7i+6)A_2A_5A_8A_{11}A_{14}A_{17}A_{20})},$$
$$\psi_{21m+17}=\frac{A_{4}\prod_{i=0}^{m}(1-(7i+5)A_1A_4A_7A_{10}A_{13}A_{16}A_{19})}{\prod_{i=0}^{m}(1-(7i+6)A_1A_4A_7A_{10}A_{13}A_{16}A_{19})},$$
$$\psi_{21m+18}=\frac{A_{3}\prod_{i=0}^{m}(1-(7i+5)A_0A_3A_6A_9A_{12}A_{15}A_{18})}{\prod_{i=0}^{m}(1-(7i+6)A_0A_3A_6A_9A_{12}A_{15}A_{18})},$$
$$\psi_{21m+19}=\frac{A_{2}\prod_{i=0}^{m}(1-(7i+6)A_2A_5A_8A_{11}A_{14}A_{17}A_{20})}{\prod_{i=0}^{m}(1-(7i+7)A_2A_5A_8A_{11}A_{14}A_{17}A_{20})},$$
$$\psi_{21m+20}=\frac{A_{1}\prod_{i=0}^{m}(1-(7i+6)A_1A_4A_7A_{10}A_{13}A_{16}A_{19})}{\prod_{i=0}^{m}(1-(7i+7)A_1A_4A_7A_{10}A_{13}A_{16}A_{19})},$$
$$\psi_{21n+21}=\frac{A_{0}\prod_{i=0}^{m}(1-(7i+6)A_0A_3A_6A_9A_{12}A_{15}A_{18})}{\prod_{i=0}^{m}(1-(7i+7)A_0A_3A_6A_9A_{12}A_{15}A_{18})}.$$

where, $\psi_{-20}=A_{20}$, $\psi_{-19}=A_{19}$, ..., $\psi_{-1}=A_1$, $\psi_0=A_0$.

Proof Theorem 3 proof can be obtained similar way to Theroem 1.

Theorem 4. *Eq. 3 has a unique equilibrium point* $\overline{\psi}=0$, *which isn't locally asymptotically stable.*

Proof Theorem 4 proof can be obtained similar way to Theroem 2.

For confirming the outcomes of this section, we take into consideration mathematical instances which stand for various kind of solutions to (3).

Example 3. *Figure 3 gives the behavior when,*

$\psi_{-20}=0.4$, $\psi_{-19}=0.42$, $\psi_{-18}=0.43$, $\psi_{-17}=0.44$, $\psi_{-16}=0.45$,
$\psi_{-15}=0.46$, $\psi_{-14}=0.47$, $\psi_{-13}=0.48$, $\psi_{-12}=0.49$, $\psi_{-11}=0.5$,
$\psi_{-10}=0.51$, $\psi_{-9}=0.52$, $\psi_{-8}=0.53$, $\psi_{-7}=0.54$, $\psi_{-6}=0.55$,
$\psi_{-5}=0.56$, $\psi_{-4}=0.57$, $\psi_{-3}=0.58$, $\psi_{-2}=0.59$, $\psi_{-1}=0.6$,
$\psi_0=0.61$

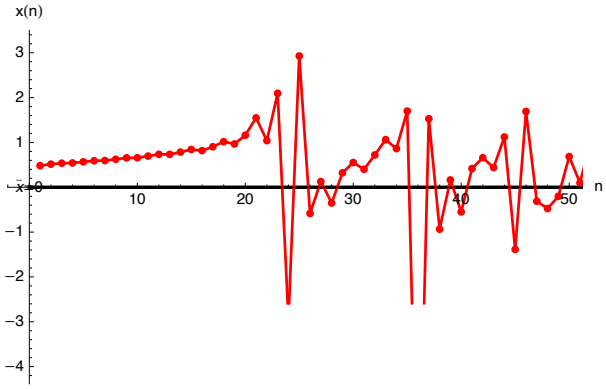

Figure 3

Example 4. *Figure 4 gives the behavior when,*

$\psi_{-20}=0.8$, $\psi_{-19}=0.65$, $\psi_{-18}=0.43$, $\psi_{-17}=0.44$, $\psi_{-16}=0.45$,
$\psi_{-15}=0.46$, $\psi_{-14}=0.47$, $\psi_{-13}=0.48$, $\psi_{-12}=0.49$, $\psi_{-11}=0.5$,
$\psi_{-10}=0.51$, $\psi_{-9}=0.52$, $\psi_{-8}=0.53$, $\psi_{-7}=0.54$, $\psi_{-6}=0.55$,
$\psi_{-5}=0.56$, $\psi_{-4}=0.57$, $\psi_{-3}=0.74$, $\psi_{-2}=0.75$, $\psi_{-1}=0.76$,
$\psi_0=0.77$

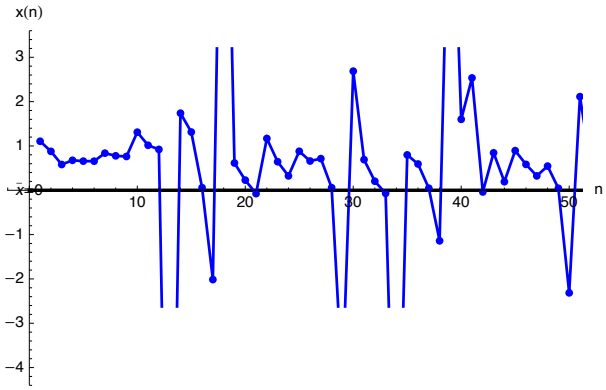

Figure 4

4. The Equation $\psi_{m+1}=\frac{\psi_{m-20}}{-1+\psi_{m-2}\psi_{m-5}\psi_{m-8}\psi_{m-11}\psi_{m-14}\psi_{m-17}\psi_{m-20}}$

In this part, we study

$$\psi_{m+1}=\frac{\psi_{m-20}}{-1+\psi_{m-2}\psi_{m-5}\psi_{m-8}\psi_{m-11}\psi_{m-14}\psi_{m-17}\psi_{m-20}},\quad m\in\mathbb{N}_0, \tag{4}$$

where the initial conditions are arbitrary nonzero real numbers with

$\psi_{m-2}\psi_{m-5}\psi_{m-8}\psi_{m-11}\psi_{m-14}\psi_{m-17}\psi_{m-20}\neq 1$.

Theorem 5. *Let* $\{\psi_m\}_{m=-20}^{\infty}$ *be a solution of difference equation 4. Then for,* $m=0,1,2,\ldots$

$$\psi_{42m+1}=\frac{A_{20}}{-1+A_2A_5A_8A_{11}A_{14}A_{17}A_{20}},$$
$$\psi_{42m+2}=\frac{A_{19}}{-1+A_1A_4A_7A_{10}A_{13}A_{16}A_{19}},$$
$$\psi_{42m+3}=\frac{A_{18}}{-1+A_0A_3A_6A_9A_{12}A_{15}A_{18}},$$
$$\psi_{42m+4}=A_{17}(-1+A_2A_5A_8A_{11}A_{14}A_{17}A_{20}),$$
$$\psi_{42m+5}=A_{16}(-1+A_1A_4A_7A_{10}A_{13}A_{16}A_{19}),$$
$$x_{42n+6}=A_{15}(-1+A_0A_3A_6A_9A_{12}A_{15}A_{18}),$$

$$\psi_{42m+7}=\frac{A_{14}}{-1+A_2A_5A_8A_{11}A_{14}A_{17}A_{20}},$$
$$\psi_{42m+8}=\frac{A_{13}}{-1+A_1A_4A_7A_{10}A_{13}A_{16}A_{19}},$$
$$\psi_{42m+9}=\frac{A_{12}}{-1+A_0A_3A_6A_9A_{12}A_{15}A_{18}},$$
$$\psi_{42m+10}=A_{11}(-1+A_2A_5A_8A_{11}A_{14}A_{17}A_{20}),$$
$$\psi_{42m+11}=A_{10}(-1+A_1A_4A_7A_{10}A_{13}A_{16}A_{19}),$$
$$x_{42n+12}=A_9(-1+A_0A_3A_6A_9A_{12}A_{15}A_{18}),$$
$$\psi_{42m+13}=\frac{A_8}{-1+A_2A_5A_8A_{11}A_{14}A_{17}A_{20}},$$
$$\psi_{42m+14}=\frac{A_7}{-1+A_1A_4A_7A_{10}A_{13}A_{16}A_{19}},$$
$$\psi_{42m+15}=\frac{A_6}{-1+A_0A_3A_6A_9A_{12}A_{15}A_{18}},$$
$$\psi_{42m+16}=A_5(-1+A_2A_5A_8A_{11}A_{14}A_{17}A_{20}),$$
$$\psi_{42m+17}=A_4(-1+A_1A_4A_7A_{10}A_{13}A_{16}A_{19}),$$
$$x_{42n+18}=A_3(-1+A_0A_3A_6A_9A_{12}A_{15}A_{18}),$$
$$\psi_{42m+19}=\frac{A_2}{-1+A_2A_5A_8A_{11}A_{14}A_{17}A_{20}},$$
$$\psi_{42m+20}=\frac{A_1}{-1+A_1A_4A_7A_{10}A_{13}A_{16}A_{19}},$$
$$\psi_{42m+21}=\frac{A_0}{-1+A_0A_3A_6A_9A_{12}A_{15}A_{18}},$$

$$\psi_{42m+22}=A_{20},\quad \psi_{42m+23}=A_{19},\quad \psi_{42m+24}=A_{18},\quad \ldots,\quad \psi_{42m+40}=A_2,$$
$$\psi_{42m+41}=A_1,\quad \psi_{42m+42}=A_0,$$

Proof Suppose

$$\psi_{42m-41}=\frac{A_{20}}{-1+A_2A_5A_8A_{11}A_{14}A_{17}A_{20}},$$
$$\psi_{42m-40}=\frac{A_{19}}{-1+A_1A_4A_7A_{10}A_{13}A_{16}A_{19}},$$
$$\psi_{42m-39}=\frac{A_{18}}{-1+A_0A_3A_6A_9A_{12}A_{15}A_{18}},$$
$$\psi_{42m-38}=A_{17}(-1+A_2A_5A_8A_{11}A_{14}A_{17}A_{20}),$$
$$\psi_{42m-37}=A_{16}(-1+A_1A_4A_7A_{10}A_{13}A_{16}A_{19}),$$
$$\psi_{42m-36}=A_{15}(-1+A_0A_3A_6A_9A_{12}A_{15}A_{18}),$$
$$\psi_{42m-35}=\frac{A_{14}}{-1+A_2A_5A_8A_{11}A_{14}A_{17}A_{20}},$$
$$\psi_{42m-34}=\frac{A_{13}}{-1+A_1A_4A_7A_{10}A_{13}A_{16}A_{19}},$$
$$\psi_{42m-33}=\frac{A_{12}}{-1+A_0A_3A_6A_9A_{12}A_{15}A_{18}},$$
$$\psi_{42m-32}=A_{11}(-1+A_2A_5A_8A_{11}A_{14}A_{17}A_{20}),$$
$$\psi_{42m-31}=A_{10}(-1+A_1A_4A_7A_{10}A_{13}A_{16}A_{19}),$$
$$x_{42n-30}=A_9(-1+A_0A_3A_6A_9A_{12}A_{15}A_{18}),$$
$$\psi_{42m-29}=\frac{A_8}{-1+A_2A_5A_8A_{11}A_{14}A_{17}A_{20}},$$
$$\psi_{42m-28}=\frac{A_7}{-1+A_1A_4A_7A_{10}A_{13}A_{16}A_{19}},$$
$$\psi_{42m-27}=\frac{A_6}{-1+A_0A_3A_6A_9A_{12}A_{15}A_{18}},$$
$$\psi_{42m-26}=A_5(-1+A_2A_5A_8A_{11}A_{14}A_{17}A_{20}),$$
$$\psi_{42m-25}=A_4(-1+A_1A_4A_7A_{10}A_{13}A_{16}A_{19}),$$
$$\psi_{42m-24}=A_3(-1+A_0A_3A_6A_9A_{12}A_{15}A_{18}),$$
$$\psi_{42m-23}=\frac{A_2}{-1+A_2A_5A_8A_{11}A_{14}A_{17}A_{20}},$$
$$\psi_{42m-22}=\frac{A_1}{-1+A_1A_4A_7A_{10}A_{13}A_{16}A_{19}},$$
$$\psi_{42m-21}=\frac{A_0}{-1+A_0A_3A_6A_9A_{12}A_{15}A_{18}},$$

$$\psi_{42m-20}=A_{20},$$
$$\psi_{42m-19}=A_{19},\quad \psi_{42m-18}=A_{18},$$
$$\psi_{42m-17}=A_{17},\quad \psi_{42m-16}=A_{16},$$
$$\psi_{42m-15}=A_{15},\quad \psi_{42m-14}=A_{14},$$
$$\vdots\qquad\qquad \vdots$$
$$\psi_{42m-5}=A_5,\quad \psi_{42m-4}=A_4,$$
$$\psi_{42m-3}=A_3,\quad \psi_{42m-2}=A_2,$$
$$\psi_{42m-1}=A_1,\quad \psi_{42m}=A_0,$$

Now, it follows from 4 that

$$\psi_{42m+1}=\frac{\psi_{42m-20}}{-1+\psi_{42m-2}\psi_{42m-5}\psi_{42m-8}\psi_{42m-11}\psi_{42m-14}\psi_{42m-17}\psi_{42m-20}}$$

Then, we have

$$\psi_{21m+1}=\frac{A_{20}}{-1+A_2A_5A_8A_{11}A_{14}A_{17}A_{20}}.$$

Other relations can be given by the same way.

Theorem 6. *Eq. 4 has three equilibrium points which are* $0,\pm\sqrt[7]{2}$*, and these equilibrium points aren't locally asymptotically stable.*

Proof Theorem 6 can be obtained similar way to proofs Theorem 2.

Example 5. *Figure 5 gives the behavior with*

$$\psi_{-20}=0.8,\quad \psi_{-19}=0.65,\quad \psi_{-18}=0.43,\quad \psi_{-17}=0.44,\quad \psi_{-16}=0.45,$$
$$\psi_{-15}=0.46,\quad \psi_{-14}=0.47,\quad \psi_{-13}=0.48,\quad \psi_{-12}=0.49,\quad \psi_{-11}=0.5,$$
$$\psi_{-10}=0.51,\quad \psi_{-9}=0.52,\quad \psi_{-8}=0.53,\quad \psi_{-7}=0.54,\quad \psi_{-6}=0.55,$$
$$\psi_{-5}=0.56,\quad \psi_{-4}=0.57,\quad \psi_{-3}=0.74,\quad \psi_{-2}=0.75,\quad \psi_{-1}=0.76,$$
$$\psi_0=0.77$$

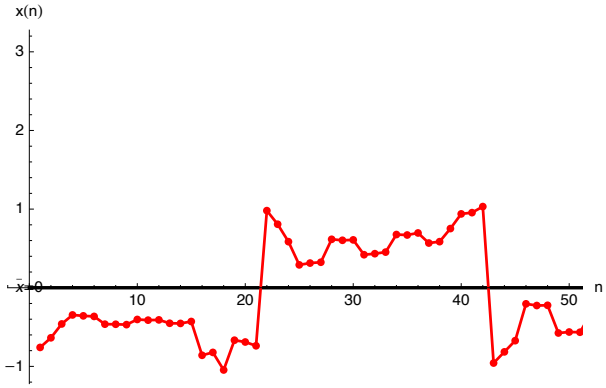

Figure 5

Example 6. *Figure 6 gives the behavior with*

$$\psi_{-20}=0.79,\quad \psi_{-19}=0.65,\quad \psi_{-18}=0.41,\quad \psi_{-17}=0.44,\quad \psi_{-16}=0.45,$$
$$\psi_{-15}=0.465,\quad \psi_{-14}=0.472,\quad \psi_{-13}=0.48,\quad \psi_{-12}=0.494,\quad \psi_{-11}=0.5,$$
$$\psi_{-10}=0.513,\quad \psi_{-9}=0.52,\quad \psi_{-8}=0.53,\quad \psi_{-7}=0.54,\quad \psi_{-6}=0.55,$$
$$\psi_{-5}=0.953,\quad \psi_{-4}=0.94,\quad \psi_{-3}=0.74,\quad \psi_{-2}=0.75,\quad \psi_{-1}=0.76,$$
$$\psi_0=0.77$$

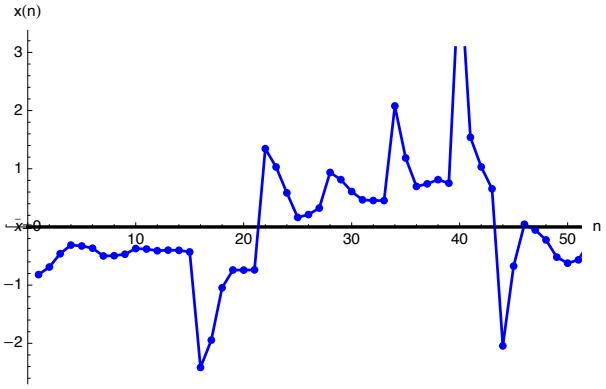

Figure 6

5. The Equation $\frac{\psi_{m-20}}{-1-\psi_{m-2}\psi_{m-5}\psi_{m-8}\psi_{m-11}\psi_{m-14}\psi_{m-17}\psi_{m-20}}$,

In this section, we find the solutions of

$$\frac{\psi_{m-20}}{-1-\psi_{m-2}\psi_{m-5}\psi_{m-8}\psi_{m-11}\psi_{m-14}\psi_{m-17}\psi_{m-20}}, \quad m \in \mathbb{N}_0, \tag{5}$$

where the initial conditions are arbitrary nonzero real numbers with
$\psi_{m-2}\psi_{m-5}\psi_{m-8}\psi_{m-11}\psi_{m-14}\psi_{m-17}\psi_{m-20} \neq -1$.

Theorem 7. *Let $\{\psi_m\}_{m=-20}^{\infty}$ be a solution of 5.*

$$\psi_{42m+1} = \frac{-A_{20}}{1+A_2A_5A_8A_{11}A_{14}A_{17}A_{20}}, \qquad \psi_{42m+2} = \frac{-A_{19}}{1+A_1A_4A_7A_{10}A_{13}A_{16}A_{19}},$$
$$\psi_{42m+3} = \frac{-A_{18}}{1+A_0A_3A_6A_9A_{12}A_{15}A_{18}}, \qquad \psi_{42m+4} = -A_{17}(1+A_2A_5A_8A_{11}A_{14}A_{17}A_{20}),$$
$$\psi_{42m+5} = -A_{16}(1+A_1A_4A_7A_{10}A_{13}A_{16}A_{19}), \qquad \psi_{42m+6} = -A_{15}(1+A_0A_3A_6A_9A_{12}A_{15}A_{18}),$$
$$\psi_{42m+7} = \frac{-A_{14}}{1+A_2A_5A_8A_{11}A_{14}A_{17}A_{20}}, \qquad \psi_{42m+8} = \frac{-A_{13}}{1+A_1A_4A_7A_{10}A_{13}A_{16}A_{19}},$$
$$\psi_{42m+9} = \frac{-A_{12}}{1+A_0A_3A_6A_9A_{12}A_{15}A_{18}}, \qquad \psi_{42m+10} = -A_{11}(1+A_2A_5A_8A_{11}A_{14}A_{17}A_{20}),$$
$$\psi_{42m+11} = -A_{10}(1+A_1A_4A_7A_{10}A_{13}A_{16}A_{19}), \qquad x_{42n+12} = -A_9(1+A_0A_3A_6A_9A_{12}A_{15}A_{18}),$$
$$\psi_{42m+13} = \frac{-A_8}{1+A_2A_5A_8A_{11}A_{14}A_{17}A_{20}}, \qquad \psi_{42m+14} = \frac{-A_7}{1+A_1A_4A_7A_{10}A_{13}A_{16}A_{19}},$$
$$\psi_{42m+15} = \frac{-A_6}{1+A_0A_3A_6A_9A_{12}A_{15}A_{18}}, \qquad \psi_{42m+16} = -A_5(1+A_2A_5A_8A_{11}A_{14}A_{17}A_{20}),$$
$$\psi_{42m+17} = -A_4(1+A_1A_4A_7A_{10}A_{13}A_{16}A_{19}), \qquad \psi_{42m+18} = -A_3(1+A_0A_3A_6A_9A_{12}A_{15}A_{18}),$$
$$\psi_{42m+19} = \frac{-A_2}{1+A_2A_5A_8A_{11}A_{14}A_{17}A_{20}}, \qquad \psi_{42m+20} = \frac{-A_1}{1+A_1A_4A_7A_{10}A_{13}A_{16}A_{19}},$$
$$\psi_{42m+21} = \frac{-A_0}{1+A_0A_3A_6A_9A_{12}A_{15}A_{18}}, \qquad \psi_{42m+22} = A_{20},$$
$$\psi_{42m+23} = A_{19}, \qquad \psi_{42m+24} = A_{18},$$
$$\psi_{42m+25} = A_{17}, \qquad \psi_{42m+26} = A_{16},$$
$$\psi_{42m+27} = A_{15}, \qquad \psi_{42m+28} = A_{14},$$
$$\vdots \qquad \vdots$$
$$\psi_{42m+36} = A_6, \qquad \psi_{42m+37} = A_5,$$
$$\psi_{42m+38} = A_4, \qquad \psi_{42m+39} = A_2,$$
$$\psi_{42m+41} = A_1, \qquad \psi_{42m+42} = A_0,$$

where the initial conditions are arbitrary nonzero real numbers with
$\psi_{m-2}\psi_{m-5}\psi_{m-8}\psi_{m-11}\psi_{m-14}\psi_{m-17}\psi_{m-20} \neq -1$.

Proof Theorem 7 can be obtained similar way to Theorem 5.

Theorem 8. *Eq. 5 has three equilibrium point which are $0, \pm\sqrt[5]{-2}$ and these equilbrium points aren't locally asymptotically stable.*

Proof Theorem 8 can be obtained similar way to Theorem 2.

Example 7. *See 7 for the initials*

$\psi_{-20} = 0.8$, $\psi_{-19} = 0.65$, $\psi_{-18} = 0.43$, $\psi_{-17} = 0.44$, $\psi_{-16} = 0.45$,
$\psi_{-15} = 0.46$, $\psi_{-14} = 0.9$, $\psi_{-13} = 0.91$, $\psi_{-12} = 0.92$, $\psi_{-11} = 0.5$,
$\psi_{-10} = 0.51$, $\psi_{-9} = 0.52$, $\psi_{-8} = 0.53$, $\psi_{-7} = 0.54$, $\psi_{-6} = 0.55$,
$\psi_{-5} = 0.95$, $\psi_{-4} = 0.94$, $\psi_{-3} = 0.74$, $\psi_{-2} = 0.75$, $\psi_{-1} = 0.76$,
$\psi_0 = 0.77$

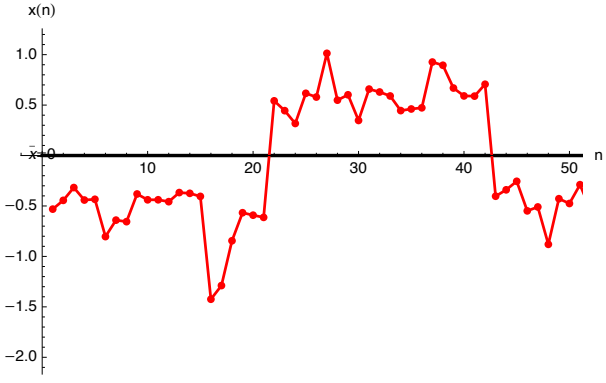

Figure 7

Example 8. *We consider*

$\psi_{-20} = 0.8$, $\psi_{-19} = 0.65$, $\psi_{-18} = 0.43$, $\psi_{-17} = 0.44$, $\psi_{-16} = 0.45$,
$\psi_{-15} = 0.46$, $\psi_{-14} = 0.9$, $\psi_{-13} = 0.91$, $\psi_{-12} = 0.92$, $\psi_{-11} = 0.5$,
$\psi_{-10} = 0.51$, $\psi_{-9} = 0.87$, $\psi_{-8} = 0.53$, $\psi_{-7} = 0.54$, $\psi_{-6} = 0.88$,
$\psi_{-5} = 0.95$, $\psi_{-4} = 0.94$, $\psi_{-3} = 0.74$, $\nu_{-2} = 0.96$, $\psi_{-1} = 0.76$,
$\psi_0 = 0.77$

See figure 8

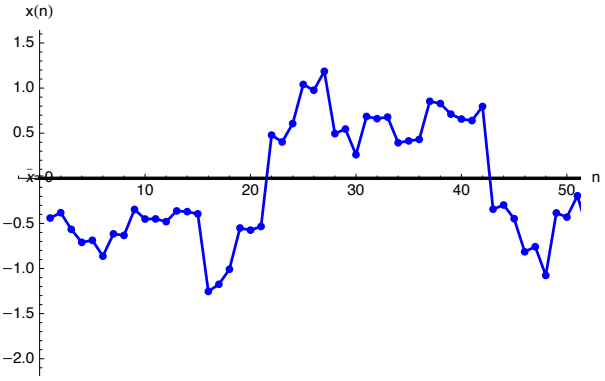

Figure 8

6. Conclusion

We study the behavior of the difference equation

$$\psi_{m+1} = \frac{\psi_{m-20}}{\pm 1 \pm \psi_{m-2}\psi_{m-5}\psi_{m-8}\psi_{m-11}\psi_{m-14}\psi_{m-17}\psi_{m-20}}$$

where the initials are positive real numbers. Local stability is discussed. More- over,we get the solution of some special cases.Finally, some numerical examples are given.

References

[1] Abdelrahman M.A.E, Moaaz O., "On the New Class of The Nonlinear Rational Difference Equations," Electronic Journal of Mathematical Analysis and Applications, 6 (1), 117-125, (2018).

[2] Ahmed A.E.S., Iričanin B., Kosmala W., Stević S., Smarda Z, "Note on constructing a family of solvable sine-type difference equations," Advances in Difference Equations, 2021(1), 1-11, (2021).

[3] Agarwal R.P., "Difference Equations and Inequalities," Marcel Dekker, New York, 1992, 2nd edition, 2000.

[4] Agarwal R.P.and Elsayed E.M., "Periodicity and stability of solutions of higher order rational difference equation," Advanced Studies in Contemporary Mathematics, 17(2), 181-201, (2008).

[5] Agarwal R.P.and Elsayed E.M., "On the solution of fourth-order rational recursive sequence," Advanced Studies in Contemporary Mathematics, 20(4), 525-545 (2010).

[6] Aloqeili M., "Dynamics of a rational difference equation," Applied Mathematics and Computation, 176(2), 768-774, (2006).

[7] Amleh A.M., Grove G.A., Ladas G., Georgiou, D.A., "On the recursive sequence $y_{m+1} = \alpha + \frac{y_{m-1}}{y_m}$," J. of Math. Anal. App. 233, 790-798 (1999).

[8] Belhannache F., Touafek N., Abo-Zeid, R., "On a higher-order rational difference equation," J. Appl. Math. Informatics, 34(5-6), 369-382, (2016).

[9] Bilgin A., Kulenović M.R.S., "Global asymptotic stability for discrete single species population models," Discrete Dynamics in Nature and Society, 2017. Article ID 5963594, 15.

[10] Cinar C., "On the positive solutions of the difference equation $\psi_{m+1} = \frac{a\psi_{m-1}}{1+b\psi_m\psi_{m-1}}$," J. of App. Math. Comp., 156(2), 587-590 (2004).

[11] Cinar C., Mansour T., Yalcinkaya I., On the difference equation of higher order," Utilitas Mathematica, 92, 161-166 (2013).

[12] Das S.E., Bayram M., "On a system of rational difference equations," World Applied Sciences Journal, 10(11), 1306-1312 (2010).

[13] DeVault R., Ladas G., Schultz S.W., "On the recursive sequence $\psi_{m+1} = \frac{A}{\psi_m} + \frac{1}{\psi_{m-2}}$," Proc.Amer. Math. Soc.126 (11) 3257-3261 (1998).

[14] Elsayed E.M., "On The Difference Equation $\psi_{m+1} = \frac{\psi_{m-5}}{-1+\psi_{m-2}\psi_{m-5}}$," Inter. J. Contemp. Math. Sci., 3 (33) 1657-1664, (2008).

[15] Gibbons C.H., Kulenovic M.R.S., Ladas G., "On the recursive sequence $\frac{\alpha+\beta\psi m-1}{\chi+\beta\psi m-1}$," Math. Sci. Res. Hot-Line, 4(2), 1-11 (2000).

[16] Ibrahim T.F., Khan A.Q., Ogul, B., Şimşek, D., "Closed-Form Solution of a Rational Difference Equation," Mathematical Problems in Engineering, 2021.

[17] Ibrahim T.F., Khan A.Q., Ibrahim, A., "Qualitative behavior of a nonlinear generalized recursive sequence with delay," Mathematical Problems in Engineering, (2021).

[18] Khan A.Q., El-Metwally H., "Global dynamics, boundedness, and semicycle analysis of a difference equation," Discrete Dynamics in Nature and Society, (2021).

[19] Kocic V.L., Ladas G., "Global behavior of nonlinear difference equations of higher order with applications," volume 256 of Mathematics and its Applications, Kluwer Academic Publishers Group, Dordrecht, 1993.

[20] Kulenovic M.R.S., Ladas G., Sizer W.S., "On the recursive sequence $\frac{\alpha\psi_m+\beta\psi_{m-1}}{\chi\psi_m+\beta\psi_{m-1}}$," Math. Sci. Res.Hot-Line, 2(5), 1-16 (1998).

[21] Kulenovic M.R.S., Ladas G., "Dynamics of second order rational difference equations" Chapman & Hall/CRC, Boca Raton, FL, 2002. With open problems and conjectures.

[22] Rahaman M., Mondal S.P., Algehyne E.A., Biswas A., Alam S, "A method for solving linear difference equation in Gaussian fuzzy environments," Granular Computing, 7(1), 63-76, (2021).

[23] Simsek D., Abdullayev F.G., "On the Recursive Sequence $\psi_{m+1} = \frac{\psi_{m-(k+1)}}{1+\psi_m\psi_{m-1}\ldots\psi_{m-k}}$," Journal of Mathematical Sciences, 234(1), 73-81 (2018) .

[24] Simşek D., Ogul B., Cinar C., "Solution of the rational difference equation $\psi_{m+1} = \frac{\psi_{m-17}}{1+\psi_{m-5}\psi_{m-11}}$," Filomat, 33(5), 1353-1359, (2019).

[25] Stevic S., "A note on periodic character of a higher order difference equation," Rostock. Math. Kolloq., 61 2-30, (2006).

[26] Stevic S., Iricanin B., Kosmala W., Smarda Z., "On a nonlinear second-order difference equation," Journal of Inequalites and Applications, 2022(1), (2022).

[27] Soykan Y., Taşdemir E., Göcen M, "Binomial transform of the generalized third-order Jacobsthal sequence, Asian-European Journal of Mathematics, (2022).

[28] Taşdemir E., "On the global asymptotic stability of a system of difference equations with quadratic terms," Journal of Applied Mathematics and Computing, 1-15, (2020).

[29] Yalcinkaya İ., Çalışkan V., Tollu D.T., "On a nonlinear fuzzy difference equation," Communications Faculty of Sciences University of Ankara Series A1 Mathematics and Statistics, 71(1), 68-78, (2022).